

Cover Page



Universiteit Leiden



The handle <http://hdl.handle.net/1887/36380> holds various files of this Leiden University dissertation

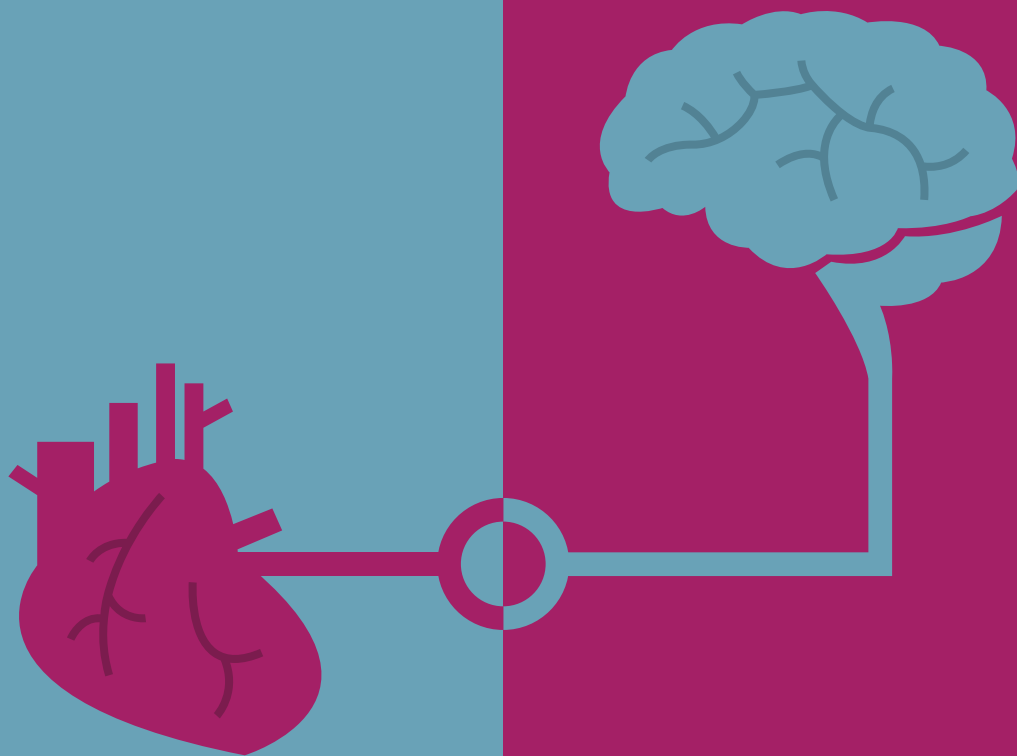
Author: Kooijman, Sander

Title: Neural control of lipid metabolism and inflammation : implications for atherosclerosis

Issue Date: 2015-11-18

NEURAL
CONTROL
OF LIPID
METABOLISM AND
INFLAMMATION

IMPLICATIONS FOR
ATHEROSCLEROSIS



SANDER KOOIJMAN

NEURAL CONTROL OF LIPID METABOLISM AND INFLAMMATION
IMPLICATIONS FOR ATHEROSCLEROSIS

SANDER KOOIJMAN

Neural control of lipid metabolism and inflammation: implications for atherosclerosis
2015, Sander Kooijman

ISBN: 978-94-6233-112-9

Layout by Textcetera, Den Haag
Printed by Gildeprint, Enschede

All rights are reserved. No part of this publication may be reproduced, stored, or transmitted
in any form or by any means, without permission of the copyright owners.

NEURAL CONTROL OF LIPID METABOLISM AND INFLAMMATION

IMPLICATIONS FOR ATHEROSCLEROSIS

Proefschrift

Ter verkrijging van de graad van Doctor aan de Universiteit Leiden, op gezag van Rector Magnificus prof. mr. C.J.J.M. Stolker, volgens besluit van het College voor Promoties te verdedigen op woensdag 18 november 2015 klokke 13.45 uur

door

Sander Kooijman

Geboren te 's-Gravenhage
in 1987

Promotores: Prof. dr. P.C.N. Rensen
Prof. dr. ir. L.M. Havekes

Promotiecommissie: Prof. dr. J.A.P. Willems van Dijk
Prof. dr. J.H. Meijer
Prof. dr. A. Kalsbeek (NIH, Amsterdam)
Prof. dr. J.A. Romijn (AMC, Amsterdam)
Prof. dr. P. Schrauwen (MUMC, Maastricht)

Het onderzoek dat aan dit proefschrift ten grondslag ligt is mogelijk gemaakt door een subsidie van de Nederlandse Hartstichting (NHS-2009T038).

TABLE OF CONTENTS

Chapter 1	General introduction and outline	7
PART I		
Chapter 2	Inhibition of the central melanocortin system decreases brown adipose tissue activity <i>J Lipid Res (2014) 55: 2022-32</i>	23
Chapter 3	Central GLP-1 receptor signalling accelerates clearance of triacylglycerol and glucose by activating brown adipose tissue in mice <i>Diabetologia (2015) in press</i>	47
Chapter 4	Prolonged daily light exposure increases body fat mass through attenuation of brown adipose tissue activity <i>Proc Natl Acad Sci USA (2015) 112: 6748-53</i>	65
Chapter 5	Daily and seasonal encoding of rhythms in brown adipose tissue activity <i>In preparation</i>	89
Chapter 6	Peripheral cannabinoid 1 receptor blockade activates brown adipose tissue and diminishes dyslipidemia and obesity <i>FASEB J (2014) 28: 5361-75</i>	107
PART II		
Chapter 7	Hematopoietic $\alpha 7$ nicotinic acetylcholine receptor deficiency increases inflammation and platelet activation status, but does not aggravate atherosclerosis <i>J Thromb Haemost (2015) 13: 126-35</i>	139
Chapter 8	Splenic denervation does not aggravate atherosclerotic lesion development in APOE*3-Leiden.CETP transgenic mice <i>Am J Physiol Heart Circ Physiol (2015) 309: H646-54</i>	161

Chapter 9	General discussion and future perspectives	179
Chapter 10	Summary	195
	Nederlandse samenvatting	199
	List of publications	205
	Curriculum vitae	207

Cardiovascular disease (CVD) is currently the leading cause of death worldwide (1). While mortality rates are declining in high-income countries, CVD morbidity and mortality rapidly increase in low- and middle-income countries. Although CVD usually affects the elderly, the antecedents of CVD including atherosclerosis, begin in early life. CVD may be prevented by behavioral adjustments including exercise, healthy eating and avoidance of smoking, thereby reducing the development of dyslipidemia and inflammation, the two main risk factors for atherosclerotic lesion development. Current pharmaceutical approaches in the treatment of atherosclerosis mainly aim at correcting dyslipidemia through reduction of plasma cholesterol levels. However, although statins effectively reduce low-density lipoprotein-cholesterol (LDL-C), only about 25-30% of all cardiovascular events are prevented by this treatment (2). Accumulating evidence indicates a prominent role of the autonomic nervous system (ANS) in the regulation of lipid metabolism as well as inflammation, but the consequences for atherosclerosis development and the potential for novel treatment strategies are still unclear (**Figure 1**).

Autonomic nervous system control of homeostatic activity

From reports describing the effects of lesioning discrete brain nuclei, through to studies of genetically engineered animal models and human genetic disorders, the primacy of the central nervous system (CNS) in the control and coordination of homeostasis is clear. The hypothalamus in particular is critical in sensing and

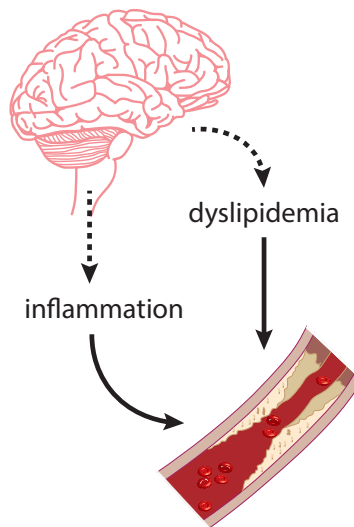


Figure 1 – Dysregulation of the inflammatory response and lipid metabolism by the autonomic nervous system may result in atherosclerotic lesion development.

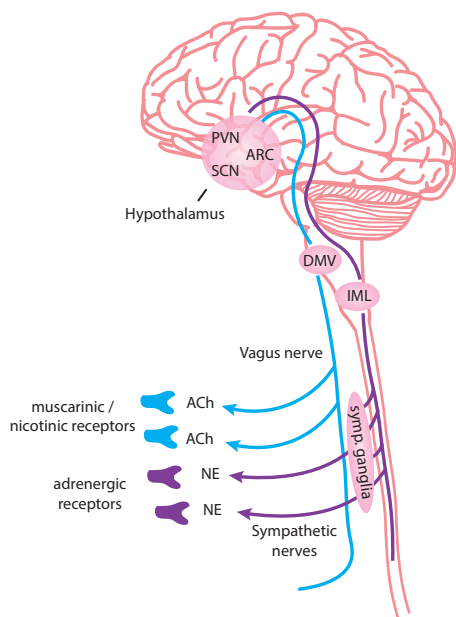


Figure 2 – Hypothalamic projection onto the autonomic nervous system. See text for details. In purple sympathetic pathways, in blue parasympathetic pathways. Ach, acetyl choline; ARC, arcuate nucleus; DMV, dorsal motor nucleus of the vagus; IML, intermediolateral column of the thoracic spinal cord; NE, norepinephrine; PVN, paraventricular nucleus; SCN, suprachiasmatic nucleus.

integrating signals from the periphery and effecting appropriate physiological changes to maintain homeostasis. Classically, this has been viewed in terms of the neuroendocrine control system resulting from processing of hypothalamic signals projected to the pituitary. More recently, the hypothalamic control over the ANS has been increasingly recognized as a potent modulator of homeostatic activity in peripheral tissues.

Separate populations of pre-autonomic nerve fibers residing from hypothalamic nuclei relay to either parasympathetic or sympathetic nuclei in the brain stem and spinal cord, respectively (**Figure 2**). The efferent parasympathetic signal is conveyed via preganglionic cells in the dorsal motor nucleus of the vagus (DMV). The DMV is directly connected by the vagal nerve to ganglion cells, without involvement of the spinal cord. Postganglionic parasympathetic nerves project on target organs and use acetylcholine (ACh) as their main neurotransmitter, which acts on muscarinic and nicotinic cholinergic receptors. On the other hand, sympathetic nerve fibers arise from the intermediolateral (IML) column of the thoracic spinal cord and project onto the chain of sympathetic ganglia located just outside of the spinal cord. In turn, sympathetic ganglia give rise to postsynaptic sympathetic nerve fibers that subsequently innervate the target organ. In general, sympathetic

neurons transmit their signal by releasing norepinephrine (NE) from their nerve endings. NE subsequently binds to adrenergic receptors located at the postsynaptic membrane on the target organ. At least nine subtypes of adrenergic receptors, divided into three major classes, have been identified: $\alpha_{1[A/B/D]}$ -adrenergic receptors, $\alpha_{2[A/B/C]}$ -adrenergic receptors, and $\beta_{[1/2/3]}$ -adrenergic receptors.

In addition to the hypothalamic control of both the sympathetic and parasympathetic nervous system, the ANS regulation of homeostatic activity involves certain reflexes, including the cholinergic anti-inflammatory reflex. Changes in homeostasis, e.g. the release of pro-inflammatory cytokines, are sensed by afferent peripheral nerve fibers that project directly onto efferent nerve fibers within the spinal cord or DMV, resulting in direct (de-)activation of efferent nerve signaling, without involvement of the hypothalamus or other brain regions.

Hypothalamic control of energy homeostasis

Before the ANS regulation of lipid metabolism can be discussed in more detail, I first have to elaborate on the role of the hypothalamus in energy homeostasis, which is a balance between energy intake and energy expenditure. It should be noted that several hypothalamic nuclei control both energy intake as well as peripheral energy expenditure, indicating the close interplay between these processes.

The arcuate nucleus (ARC) of the hypothalamus, in particular, plays an important role in energy metabolism. Within the ARC, two neuronal populations, cocaine- and amphetamine-regulated transcript (CART)/pro-opiomelanocortin (POMC)-expressing neurons and neuropeptide Y (NPY)/Agouti-related protein (AgRP)-expressing neurons, oppositely regulate energy balance (3). Activation of CART/POMC neurons leads to the production of α -melanocyte-stimulating hormone (α -MSH), which in turn stimulates the melanocortin (MC) receptors within the paraventricular nucleus (PVN) to promote satiety and induce a catabolic state of the body. In contrast, activation of NPY/AgRP neurons promotes food intake and an anabolic state, partly because AgRP acts as an endogenous antagonist for the melanocortin receptors and hereby directly inhibits the actions of CART/POMC-expressing neurons. Mutations and polymorphism within genes involved in this central melanocortin system are associated with the development of obesity and related metabolic disorders (4). Interestingly, variants in and near the melanocortin 4 receptor gene are not only associated with obesity, but also with reduced energy expenditure, suggesting that the melanocortin system directly regulates energy metabolism in peripheral organs. However, the exact mechanism remains unknown.

A second example and probably underappreciated regulator of energy balance is the central biological clock, located in the suprachiasmatic nucleus (SCN), which orchestrates diurnal and seasonal rhythms. Neuronal firing within the SCN is synchronized by light exposure, resulting in a high electrical activity during

the day and low activity during the night. The SCN subsequently signals to other hypothalamic nuclei and peripheral organs via regulation of hormonal output, *e.g.* rhythmic secretion of pituitary hormones and melatonin output, and via the ANS (5), together resulting in diurnal rhythms in metabolic processes. Disturbances in circadian rhythmicity, *e.g.* by shift-work or light pollution, are associated with obesity and related disorders including cancer and CVD (6). Causality in many of these associations still remain to be confirmed in animal studies or randomized-controlled clinical trials.

Hypothalamic control of lipid metabolism via the autonomic nervous system

Energy balance comprises energy intake and expenditure of mainly glucose and lipids (triglycerides; TG). The role of the ANS in the regulation of glucose metabolism has been firmly established (reviewed in (7)), however, considerably fewer studies have focused on its role in TG metabolism.

Important players in TG metabolism include the liver and intestines (production), white adipose tissue (WAT) (storage), heart and skeletal muscle (combustion to generate ATP), and brown adipose tissue (BAT) (combustion towards heat), the collective action of which determine plasma TG levels. While all of these organs are innervated by sympathetic nerve fibers (8), the role for parasympathetic nerves in WAT is less clear (9) and even appear to be absent in BAT (10).

Hepatic sympathetic innervation stimulates very low-density lipoprotein (VLDL)-triglyceride (TG) production (reviewed in (11)), while sympathetic denervation reduces VLDL-TG secretion (12). This reduction in VLDL-TG secretion upon sympathetic denervation was only observed in fasted rats, a situation in which lipids become the key substrate for energy metabolism. Conversely, neuropeptides that are increased upon positive energy balance reduce hepatic VLDL-TG production and hepatic parasympathetic denervation in obese Zucker rats results in elevated plasma cholesterol levels (reviewed in (13)).

Just as in liver, sympathetic innervation of WAT results in secretion of lipids to be used as substrate for energy metabolism. β_2 -adrenergic signaling induces phosphorylation of adipose tissue TG lipase (ATGL), hormone-sensitive lipase (HSL), and perilipins, ultimately resulting in lipolysis of stored TG and subsequent secretion of fatty acids into the circulation (reviewed in (14)). Long-term adrenergic stimulation of WAT additionally results in transdifferentiation of white adipocytes into beige/bright adipocytes (15).

In general, increased sympathetic outflow toward BAT (*e.g.*, following a cold stimulus) results in increased clearance and combustion of TG into heat (16). As BAT is an important topic of this thesis, I will provide a detailed description of BAT physiology. Upon sympathetic nerve fiber activity, NE is released and binds to

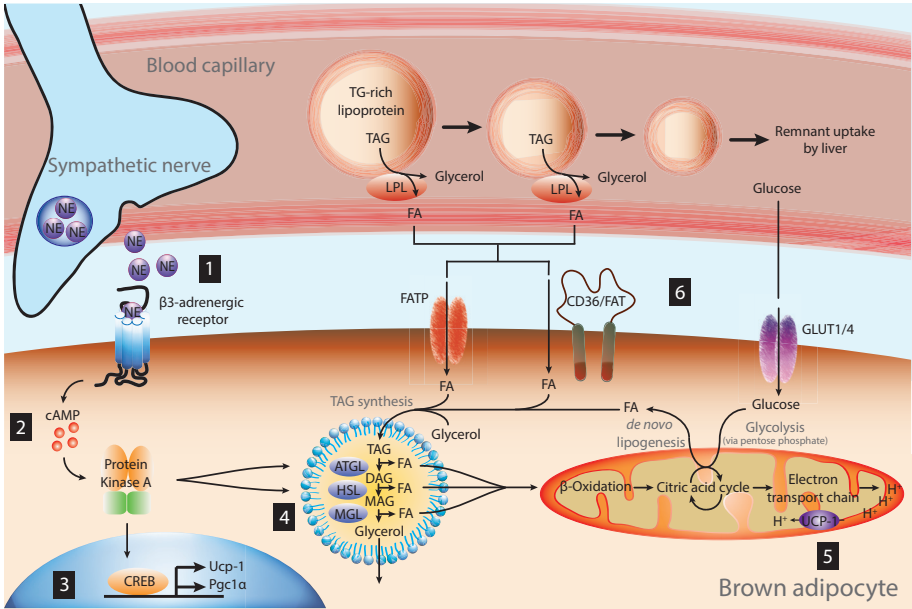


Figure 3 – Sympathetic innervation of brown adipose tissue and subsequent combustion of TG into heat. See text for details.

β -adrenergic receptors on brown adipocytes (**Figure 3**; step 1). Of the three subtypes of β -adrenergic receptors, the β 3-adrenergic receptor is the most significant in mature brown adipocytes from at least rodents. Binding of norepinephrine (*i.e.* noradrenalin) to the β 3-adrenergic receptor results in activation of its coupled stimulatory G-protein, after which adenylyl cyclase stimulates the formation of cyclic adenosine monophosphate (cAMP). cAMP activates protein kinase A (PKA), resulting in two important downstream effects (**Figure 3**; step 2). First, PKA stimulates phosphorylation of transcription factors that enhance expression and synthesis of uncoupling protein-1 (UCP-1) (**Figure 3**; step 3). Furthermore, PKA phosphorylates and activates intracellular HSL, resulting in increased intracellular lipolysis and, consequently, an increased flux of FAs toward the mitochondria to be combusted (**Figure 3**; step 4). In addition, FAs may bind to a hydrophobic binding pocket on the UCP-1 protein, resulting in its conformational change. This results in uncoupling between the respiratory chain and ATP synthase by proton leakage from the mitochondrial innermembrane space into the matrix leading to heat production instead of ATP (**Figure 3**; step 5). Finally, intracellular lipid stores need to be replenished by the uptake of glucose, FAs and triglyceride (TG)-derived FAs from plasma (**Figure 3**; step 6).

Because of its ability to combust large amounts of TG into heat, BAT is an appealing target for treatment of obesity, dyslipidemia and related disorders. Cold exposure and β_3 -adrenergic receptor agonists were found to activate human BAT resulting in lower plasma TG and increased energy expenditure (17,18). Unfortunately, to my knowledge, until now no sympathomimetic drugs have been developed that stimulate human BAT without marked effects on the cardiovascular system, indicating the need for alternative pharmaceutical targets.

Control of inflammatory responses by reflexes of the autonomic nervous system

The hypothalamus-pituitary-adrenal (HPA) axis, which controls glucocorticoid release, is probably the most well-established neuroimmunomodulatory pathway. While the systemic control exerted by the HPA axis takes place over hours, inflammatory control by the ANS can control peripheral inflammation more rapidly and directly. Stimulation of peripheral C-afferent fibers, upon acute peripheral inflammation, releases excitatory amino acids (e.g. glutamate) in the spinal cord, which then binds to *N*-methyl-D-aspartate (NMDA) receptors to decrease adenosine release by efferent fibers (reviewed in (19)). Adenosine has an anti-inflammatory effect in the periphery by binding to A_{2A} -receptors on neutrophils and to A_1 -receptors on nerve fibers within the spinal cord that inhibit NMDA receptor activation (20). Thus, acute inflammation results in further amplification of pro-inflammatory responses via the so-called dorsal root reflexes (**Figure 4**; item 1).

Subsequently, cytokines released at the inflammatory site may activate afferent fibers of the vagus nerve, resulting in an anti-inflammatory reflex. The afferent arm of the cholinergic reflex routes through the DMV to finally stimulate the release of ACh, the main neurotransmitter released by terminal vagal fibers, which activates nicotinic receptors composed of the $\alpha 7$ subunit on immune cells (reviewed in (21)). Interruption of this homeostatic mechanism in vagotomized animals aggravates inflammation (22). In animals with an intact vagal nerve, this reflex operates to reduce the release of pro-inflammatory cytokines in the periphery, thereby contributing to the homeostasis of the system by reducing inflammation (**Figure 4**; item 2).

The sympathetic nervous system (SNS) also exerts complex control on inflammation. The sympathetic neurotransmitter NE directly influences activation of CD4⁺ T cells during initial stages of inflammation (23). In later phases, the net effect of the SNS is anti-inflammatory and can be enhanced by the β -adrenergic agonists (24).

The development of atherosclerosis is considered as a chronic low-grade inflammatory disease. In particular serum concentrations of pro-inflammatory cytokines IL-1 β , TNF α and IL-6 have been proposed as predictors for future cardiovascular events (reviewed in (25)). Large clinical trials are now underway with

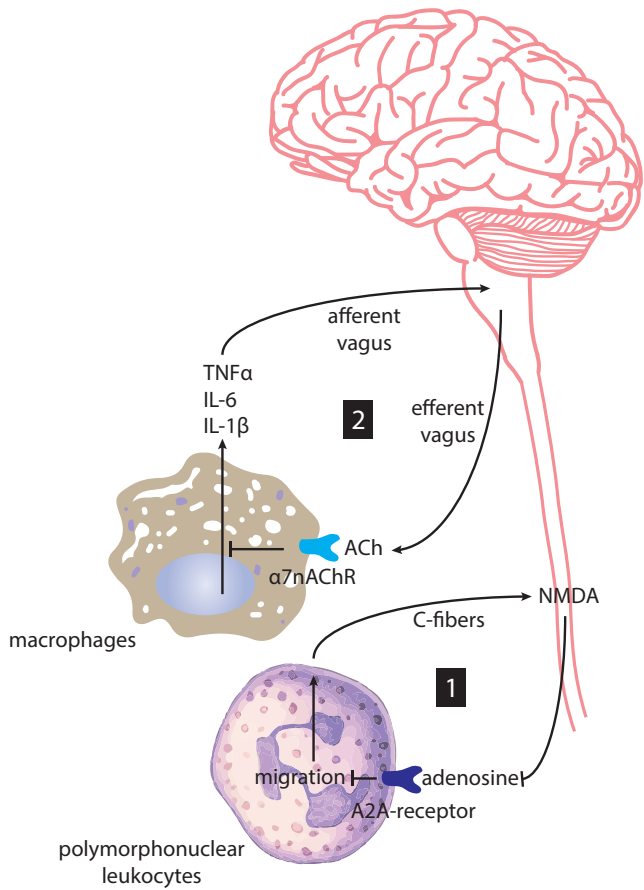


Figure 4 – Autonomic nervous system regulation of inflammatory responses; dorsal root reflex (1) and cholinergic anti-inflammatory reflex (2). See text for details.

agents that lead to reduced inflammation, investigating the effect on cardiovascular events as clinical end-point. Despite the clear primacy and big attention for the inflammatory status during atherosclerotic lesion development and cardiovascular events, little is known about the consequences of interfering with the inflammatory reflexes of the autonomic nervous system.

Interplay between lipid metabolism and inflammation; potential consequences for atherosclerosis development

Dyslipidemia is often accompanied by low-grade systemic inflammation, which is characterized by increased presence of cytokines and other markers of inflammation in the circulation. Cholesterol, fatty acids and modified lipids can directly activate inflammatory pathways. In addition, circulating (modified) lipoproteins modulate the activity of leukocytes. *Vice versa*, pro-inflammatory signaling (*i.e.* cytokines) in pre-clinical models directly affects lipid metabolism. Whereas the main lipid-lowering drugs including statins, fibrates and niacin all have potent anti-inflammatory actions, the lipid-modulating actions of anti-inflammatory agents appear to be less straightforward (reviewed in [26]).

Another compound with a dual mode of action is adenosine. As mentioned before adenosine has an anti-inflammatory effect in the periphery by binding to A_{2A} -receptors on neutrophils. Additionally, adenosine is released upon sympathetic innervation of BAT and WAT, resulting in activation of brown adipocytes and browning of white adipocytes, respectively. Treatment of mice with A_{2A} agonists prevents diet-induced obesity (DIO) and improves glucose tolerance [27]. Yet, the possible beneficial effects of A_{2A} agonists on CVD remain to be determined.

Interactions between lipid metabolism and inflammatory pathways do have direct consequences for the development of atherosclerosis as seen for example with salicylates. Salicylates belong to the NSAIDs (non-steroidal anti-inflammatory drugs) and are frequently used for prevention and treatment CVD, due to their anti-inflammatory activity by inhibiting the pro-inflammatory transcription factor NF- κ B function through activation of 5' AMP-activated protein kinase (AMPK) [28]. Interestingly, besides its role in the control of inflammation, AMPK is crucial in maintaining cellular energy homeostasis. The net effect of AMPK activation is uptake and combustion of nutrients to increase cellular energy availability. Controversially, activation of AMPK by *e.g.* metformin [29] or salsalate [30] in BAT also enhances uncoupled respiration, resulting in a loss of energy. Taken together, salicylate drugs may potentiate a dual action in the treatment of both type II diabetes and atherosclerosis as they not only reduce inflammation [31], but also improve glucose tolerance, whole-body energy expenditure [32] and induce an anti-atherogenic lipoprotein profile [31].

Outline of this thesis

The aim of the present thesis is to gain more insight in the ANS regulation of lipid metabolism and inflammation, and the potential consequences for the development of atherosclerosis. Part I of this thesis focuses on regulation of lipid metabolism by the ANS, with special attention for BAT as an emerging pharmacological target for therapy.

Since the melanocortin system has been linked to energy expenditure in addition to the regulation of food intake, and the underlying mechanism is as yet unknown, in **Chapter 2**, the direct effects of inhibition of the central melanocortin system on lipid metabolism were evaluated. Next we determined in **Chapter 3** the potential beneficial effects of activating the central melanocortin system by intracerebroventricular (ICV) infusion of glucagon-like peptide-1 (GLP-1) on the activation of BAT, restoration of dyslipidemia and the reduction of DIO.

Interestingly, many genes involved in lipid metabolism and inflammation are expressed in a circadian manner. Disturbances in circadian rhythmicity by *e.g.* light pollution or shiftwork are associated with human obesity and CVD. The aim of the study described in **Chapter 4** was to specifically determine the potentially harming effects of prolonged daily light exposure, as perceived by the SCN, on lipid metabolism and adiposity in mice. Subsequently, in **Chapter 5**, we determined the daily rhythm in lipid metabolism and the differences that may occur between seasons considering the change in daily light exposure.

The endocannabinoid system is a group of neuromodulatory lipids and their receptors in the brain that are involved in a variety of metabolic processes including appetite and energy expenditure. Interestingly, the cannabinoid receptors are not only expressed in CNS, but also on peripheral tissues, including BAT. In **Chapter 6**, we determined the effects of cannabinoid 1 receptor (CB1R) blockade on brown fat activation, reversal of dyslipidemia and DIO. Additionally, we discriminated between direct peripheral and indirect central effects of CB1R antagonism.

Part II of this thesis describes studies on the regulation of inflammation by the ANS, with focus on the anti-inflammatory reflex. During this reflex, binding of Ach to $\alpha 7$ nAChR and subsequent intracellular signaling results in transcriptional repression of pro-inflammatory genes. In **Chapter 7**, we investigated the consequences of hematopoietic $\alpha 7$ nAChR deficiency on the development of inflammation, platelet reactivity and atherosclerosis. Since the nerves involved in the anti-inflammatory reflex mainly project towards the spleen, in **Chapter 8**, we investigated the effects of selective parasympathetic and sympathetic denervation of the spleen on inflammation and atherosclerotic plaque development.

Finally, the results from these studies and their therapeutic implications are discussed in **Chapter 9**.

References

1. Finegold, J. A., Asaria, P., & Francis, D. P. (2013) Mortality from ischaemic heart disease by country, region, and age: statistics from World Health Organisation and United Nations. *Int J Cardiol* 168, 934-945.
2. Pignone, M., Phillips, C., & Mulrow, C. (2000) Use of lipid lowering drugs for primary prevention of coronary heart disease: meta-analysis of randomised trials. *BMJ* 321, 983-986.
3. Simpson, K. A., Martin, N. M., & Bloom, S. R. (2009) Hypothalamic regulation of food intake and clinical therapeutic applications. *Arq Bras Endocrinol Metabol* 53, 120-128.
4. Girardet, C. & Butler, A. A. (2014) Neural melanocortin receptors in obesity and related metabolic disorders. *Biochim Biophys Acta* 1842, 482-494.
5. Buijs, R. M., la Fleur, S. E., Wortel, J. *et al.* (2003) The suprachiasmatic nucleus balances sympathetic and parasympathetic output to peripheral organs through separate preautonomic neurons. *J Comp Neurol* 464, 36-48.
6. Payne, R. B. (1995) Circadian rhythmic variations in serum concentrations of clinically important lipids. *Clin Chem* 41, 120.
7. Kalsbeek, A., Bruinstroop, E., Yi, C. X. *et al.* (2010) Hypothalamic control of energy metabolism via the autonomic nervous system. *Ann NY Acad Sci* 1212, 114-129.
8. Tiniakos, D. G., Lee, J. A., & Burt, A. D. (1996) Innervation of the liver: morphology and function. *Liver* 16, 151-160.
9. Bartness, T. J. (2002) Dual innervation of white adipose tissue: some evidence for parasympathetic nervous system involvement. *J Clin Invest* 110, 1235-1237.
10. Bartness, T. J., Vaughan, C. H., & Song, C. K. (2010) Sympathetic and sensory innervation of brown adipose tissue. *Int J Obes (Lond)* 34 Suppl 1, S36-S42.
11. Bruinstroop, E., Fliers, E., & Kalsbeek, A. (2014) Hypothalamic control of hepatic lipid metabolism via the autonomic nervous system. *Best Pract Res Clin Endocrinol Metab* 28, 673-684.
12. Bruinstroop, E., la Fleur, S. E., Ackermans, M. T. *et al.* (2013) The autonomic nervous system regulates postprandial hepatic lipid metabolism. *Am J Physiol Endocrinol Metab* 304, E1089-E1096.
13. Kalsbeek, A., Bruinstroop, E., Yi, C. X. *et al.* (2014) Hormonal control of metabolism by the hypothalamus-autonomic nervous system-liver axis. *Front Horm Res* 42, 1-28.
14. Bartness, T. J. & Song, C. K. (2007) Thematic review series: adipocyte biology. Sympathetic and sensory innervation of white adipose tissue. *J Lipid Res* 48, 1655-1672.
15. Nedergaard, J. & Cannon, B. (2014) The browning of white adipose tissue: some burning issues. *Cell Metab* 20, 396-407.
16. Boon, M. R., Bakker, L. E., Meinders, A. E. *et al.* (2013) [Brown adipose tissue: the body's own weapon against obesity?]. *Ned Tijdschr Geneesk* 157, A5502.
17. Cypess, A. M., Weiner, L. S., Roberts-Toler, C. *et al.* (2015) Activation of Human Brown Adipose Tissue by a beta3-Adrenergic Receptor Agonist. *Cell Metab* 21, 33-38.
18. van Marken Lichtenbelt, W. D., Vanhomerig, J. W., Smulders, N. M. *et al.* (2009) Cold-activated brown adipose tissue in healthy men. *N Engl J Med* 360, 1500-1508.
19. Waldburger, J. M. & Firestein, G. S. (2010) Regulation of peripheral inflammation by the central nervous system. *Curr Rheumatol Rep* 12, 370-378.
20. Cronstein, B. N. (1994) Adenosine, an endogenous anti-inflammatory agent. *J Appl Physiol* (1985) 76, 5-13.
21. Tracey, K. J. (2002) The inflammatory reflex. *Nature* 420, 853-859.
22. Borovikova, L. V., Ivanova, S., Zhang, M. *et al.* (2000) Vagus nerve stimulation attenuates the systemic inflammatory response to endotoxin. *Nature* 405, 458-462.
23. Straub, R. H., Rauch, L., Fassold, A. *et al.* (2008) Neuronally released sympathetic neurotransmitters stimulate splenic interferon-gamma secretion from T cells in early type II collagen-induced arthritis. *Arthritis Rheum* 58, 3450-3460.

24. Malfait, A. M., Malik, A. S., Marinova-Mutafchieva, L. *et al.* (1999) The beta2-adrenergic agonist salbutamol is a potent suppressor of established collagen-induced arthritis: mechanisms of action. *J Immunol* 162, 6278-6283.
25. Ridker, P. M. & Luscher, T. F. (2014) Anti-inflammatory therapies for cardiovascular disease. *Eur Heart J* 35, 1782-1791.
26. van Diepen, J. A., Berbee, J. F., Havekes, L. M. *et al.* (2013) Interactions between inflammation and lipid metabolism: relevance for efficacy of anti-inflammatory drugs in the treatment of atherosclerosis. *Atherosclerosis* 228, 306-315.
27. Gnad, T., Scheibler, S., von, K., I *et al.* (2014) Adenosine activates brown adipose tissue and recruits beige adipocytes via A2A receptors. *Nature* 516, 395-399.
28. Steinberg, G. R., Dandapani, M., & Hardie, D. G. (2013) AMPK: mediating the metabolic effects of salicylate-based drugs? *Trends Endocrinol Metab* 24, 481-487.
29. Geerling, J. J., Boon, M. R., van der Zon, G. C. *et al.* (2014) Metformin lowers plasma triglycerides by promoting VLDL-triglyceride clearance by brown adipose tissue in mice. *Diabetes* 63, 880-891.
30. van Dam, A. D., Nahon, K. J., Kooijman, S. *et al.* (2015) Salsalate activates brown adipose tissue in mice. *Diabetes* 64, 1544-1554.
31. de Vries-van der Weij, Toet, K., Zadelaar, S. *et al.* (2010) Anti-inflammatory salicylate beneficially modulates pre-existing atherosclerosis through quenching of NF-kappaB activity and lowering of cholesterol. *Atherosclerosis* 213, 241-246.
32. Meex, R. C., Phielix, E., Moonen-Kornips, E. *et al.* (2011) Stimulation of human whole-body energy expenditure by salsalate is fueled by higher lipid oxidation under fasting conditions and by higher oxidative glucose disposal under insulin-stimulated conditions. *J Clin Endocrinol Metab* 96, 1415-1423.

2

INHIBITION OF THE CENTRAL MELANOCORTIN SYSTEM DECREASES BROWN ADIPOSE TISSUE ACTIVITY

Sander Kooijman

Mariëtte R. Boon

Edwin T. Parlevliet

Janine J. Geerling

Vera van de Pol

Johannes A. Romijn

Louis M. Havekes

Illiana Meurs

Patrick C.N. Rensen

Abstract

2

The melanocortin system is an important regulator of energy balance and MC4R deficiency is the most common monogenic cause of obesity. We investigated whether the relationship between melanocortin system activity and energy expenditure is mediated by brown adipose tissue (BAT) activity. Therefore, female APOE*3-Leiden.CETP transgenic mice were fed a Western-type diet for 4 weeks and infused intracerebroventricularly with the MC3/4R antagonist SHU9119 or vehicle for 2 weeks. SHU9119 increased food intake (+30%), body fat (+50%) and decreased energy expenditure by reduction in fat oxidation (-42%). In addition, SHU9119 impaired the uptake of VLDL-TG by BAT. In line with this, SHU9119 decreased uncoupling protein-1 levels in BAT (-60%) and induced large intracellular lipid droplets, indicative of severely disturbed BAT activity. Finally, SHU9119-treated mice pair-fed to the vehicle-treated group still exhibited these effects, indicating that MC4R inhibition impairs BAT activity independent of food intake. These effects were not specific to the APOE*3-Leiden.CETP background as SHU9119 also inhibited BAT activity in wild-type mice. We conclude that inhibition of central MC3/4R signaling impairs BAT function, which is accompanied by reduced energy expenditure thereby promoting adiposity. We anticipate that activation of MC4R is a promising strategy to combat obesity by increasing BAT activity.

Introduction

The hypothalamus is important in the regulation of energy balance. Activation of pro-opiomelanocortin neurons, *e.g.* by insulin or leptin, induces secretion of α -melanocyte-stimulating hormone, which in turn stimulates melanocortin -3 and -4 receptors (MC3R/MC4R) within the paraventricular nucleus to cause a negative energy balance (1). Accordingly, activation of central MC4R in rodent models results in anorexia and weight loss (2), whereas blockade or targeted gene disruption induces hyperphagia and obesity, even on regular chow diet (3,4). Loss-of-function mutations in MC4R are the most common monogenic form of obesity in humans and are associated with severe obesity in childhood (5). In addition, recent meta-analyses of genome-wide association studies identified common variants near MC4R to influence fat mass, obesity and obesity risk (6,7). These observations support an essential role for the melanocortin system in the regulation of energy homeostasis across mammalian species.

In addition to the effects of the melanocortin system on food intake, this system also affects energy balance via other pathways. This notion is supported by the observation that pharmacological inhibition of central MC4R by intracerebroventricular (*i.c.v.*) administration of the synthetic MC3/4R antagonist SHU9119 still increases body fat in pair-fed rats (8). Moreover, the peripheral effects of the central melanocortin system involves alterations in the activity of the sympathetic nervous system (SNS), as *i.c.v.* administration of the MC3/4R agonist MTII dose-dependently increases renal sympathetic activity in mice (9). Furthermore, ablation of neurons that produce agouti-related protein (AgRP), the endogenous antagonist for MC4R, in mice changes autonomic output into metabolic organs, accompanied by a changed respiratory exchange ratio (RER) indicating altered nutrient combustion (10). Additionally, chronic *i.c.v.* SHU9119 treatment in rats increases the RER (8), indicative of reduced lipid utilization. Interestingly, variants near and in the MC4R gene in humans are not only associated with an increased RER (8), but also with reduced total energy expenditure (EE) (11,12), underscoring the importance of the melanocortin system in the regulation of EE.

A recently discovered and highly important contributor to EE is brown adipose tissue (BAT). BAT contributes to EE by combusting high amounts of TG into heat, a process mediated by uncoupling protein-1 (UCP-1) (13). Interestingly, MC4R expressing neurons project onto BAT (14), indicating that BAT may mediate the association between MC4R signaling and EE. Therefore, the aim of this study was to evaluate the role of the melanocortin system in BAT activity. For this purpose, we inhibited melanocortin receptor signaling using the MC3/4R antagonist SHU9119 in APOE*3-Leiden.CETP transgenic mice, a well-established model for human-like lipoprotein metabolism.

Materials & Methods

2

Animals and diet

Female APOE*3-Leiden.CETP mice on a C57Bl/6J background (15) were bred at our institutional animal facility and housed under standard conditions with a 12-12 h light-dark cycle with *ad libitum* access to food and water unless stated otherwise. From 12-22 weeks after birth, mice were fed a Western-type diet containing 15% (w/w) cacao butter and 0.1% cholesterol (AB Diets, Woerden, The Netherlands) for the duration of the study, to increase plasma levels of apoB-containing lipoproteins thereby inducing a more human-like lipoprotein profile. After 4 weeks of run-in diet, mice were randomized into groups that received i.c.v. administration of artificial cerebrospinal fluid (vehicle) or SHU9119 (5 nmol/day; Bachem, Bubendorf, Germany) in vehicle during 14-17 days. Since SHU9119 induces hyperphagia (3), the effect of SHU9119 on BAT activity independent of food intake was also investigated by using an additional SHU9119-treated group that was pair-fed (SHU9119-pf) to the vehicle-treated group. To achieve pair-feeding, food intake of the *ad libitum* fed mice was monitored daily and pair-fed mice received surgery one day behind the control mice. The pair-feeding regimen consisted of giving the mice the average daily consumed food amount by the control mice, just before onset of darkness. To investigate the effect of SHU9119 independent of dyslipidemia induced by Western-type feeding of APOE*3-Leiden.CETP mice, a second experiment was performed using 15-week old male wild-type C57Bl/6J mice (Charles River, USA) that were housed under similar conditions, while being fed a regular chow diet. After 2 weeks of acclimatization, mice were randomized into three groups receiving, e.g. vehicle, SHU9119 and SHU9119-pf for 15 days. All animal experiments were approved by the institutional ethics committee on animal care and experimentation at Leiden University Medical Center.

Surgical procedure

For continuous i.c.v. administration of SHU9119 vs. vehicle, mice were sedated using a mixture of dexmedetomidine (0.5 mg/kg), midazolam (5 mg/kg) and fentanyl (0.05 mg/kg), and cannulas (Brain Infusion Kit 3, ALZET Cupertino, CA, USA) were stereotactically placed in the left lateral ventricle of the brain (coordinates: -0.45 mm anteroposterior, -1.00 mm lateral and 2.50 mm dorsoventral from bregma). Osmotic mini-pumps (Model 1004, Alzet, CA) attached to the cannula via a catheter were implanted subcutaneously on the back slightly posterior to the scapulae. The skin was sutured and the sedation was antagonized with a mixture of antiparnezol (2.5 mg/kg), flumanezil (0.5 mg/kg) and naloxon (1.2 mg/kg). Buprenorphine (0.9 µg) was used as pain killer. After the surgery, mice were housed individually and food intake and body weight were monitored on a daily basis. By filling the catheters with

vehicle, mice were allowed to recover for four days before actually receiving the assigned treatment for 17 days (collection of organs or VLDL production) or 14 days (indirect calorimetry and VLDL clearance).

Body composition

After 17 days of treatment, body composition (lean mass and fat mass) was determined in conscious mice using an EchoMRI-100 (EchoMRI, Houston, Texas).

Indirect calorimetry

During the first 5 days of treatment, oxygen uptake ($\dot{V} O_2$), carbon dioxide production ($\dot{V} CO_2$) and physical activity were measured in fully automatic metabolic cages (LabMaster System, TSE Systems, Bad Homburg, Germany). The average RER, EE, carbohydrate and fat oxidation rates were calculated as described previously (16).

Liver lipid staining and content

Liver samples were perfused with PBS, collected, snap frozen and stored at -80°C . Sections of $10\ \mu\text{m}$ were cut, fixed in 4% paraformaldehyde and stained with Oil-red-O and Mayer's hematoxylin. Lipids were extracted according to a modified protocol from Bligh and Dyer (17). In short, small liver pieces were homogenized in ice-cold methanol ($10\ \mu\text{L}/\text{mg}$ tissue). $1.8\ \text{mL}$ of $\text{CH}_3\text{OH}:\text{CHCl}_3$ (3:1, vol/vol) was added to $45\ \mu\text{L}$ of homogenate. After vigorous mixing and centrifugation, the supernatant was dried and suspended in 2% Triton X-100. Concentrations of hepatic TG, total cholesterol (TC) and phospholipids (PL) were measured using commercially available enzymatic kits for TG (11488872, Roche Diagnostics, Germany), TC (11489232, Roche Diagnostics, Mannheim, Germany) and PL (3009, Instruchemie, Delfzijl, the Netherlands). Liver lipids were expressed per milligram of protein, which was determined using the BCA protein assay kit (Thermo Scientific, Rockford, IL, USA).

VLDL production

After 17 days of treatment, after 4 h of fasting (from 8.00 h to 12.00 h), the VLDL production rate was assessed. Mice were sedated using a mixture of ventranquil (6.25 mg/kg), dormicum (6.25 mg/kg), and fentanyl (0.31 mg/kg). Subsequently, mice were injected intravenously (i.v.) with $100\ \mu\text{L}$ PBS containing $150\ \mu\text{Ci}$ Tran ^{35}S label to measure *de novo* apoB synthesis and blood samples were taken via tail bleeding ($t=0$). 30 min after injection of the Tran ^{35}S label, the mice received an i.v. injection of 500 mg of tyloxapol (Triton WR-1339, Sigma Aldrich, Germany) per kg body weight as 10% (w/w) solution in PBS, to block VLDL-TG clearance by lipoprotein lipase (LPL)-mediated TG hydrolysis. Additional blood samples were taken at $t=15$, 30, 60 and 90 min after tyloxapol injection and used for determination of plasma TG concentration. After 120 min, the mice were exsanguinated via the retro-orbital

plexus. VLDL was isolated from serum after density gradient ultracentrifugation and counted for incorporated ^{35}S -activity. VLDL particle size was determined using a Zetasizer (Malvern Instruments, Malvern, UK) and VLDL lipid composition was determined as described above.

VLDL clearance experiment

Glycerol tri[^3H]oleate ([^3H]TO) and [^{14}C]cholesteryl oleate ([^{14}C]CO) double-labeled VLDL-like emulsion particles (80 nm) were prepared as previously described (18). After 14 days of i.c.v. SHU9119 or vehicle treatment, mice were fasted for 4 h (from 8.00 h to 12.00 h) and injected i.v. with the radiolabeled emulsion particles (1.0 mg TG in 200 μL PBS) via the tail vein. At time points $t=2, 5, 10$ and 15 min after injection, blood was taken from the tail vein to determine the serum decay of both radiolabels. Immediately after the last blood withdrawal, mice were euthanized by cervical dislocation and perfused with ice-cold PBS for 5 min. Organs were harvested, weighed, and the uptake of ^3H and ^{14}C radioactivity was determined.

BAT histology

After 17 days of SHU9119 treatment, a part of interscapular BAT (iBAT) was fixed in 4% paraformaldehyde in PBS (pH 7.4) for 24 h, dehydrated and embedded in paraffin. 10 μm sections were cut, rehydrated and stained with Mayer's hematoxylin and eosin. To determine sympathetic activation of BAT a tyrosine hydroxylase (TH) staining was performed. To this end, sections were rehydrated and incubated 15 min with 10 mM citrate buffer (pH 6.0) at 120°C for antigen retrieval. Sections were cooled on ice, washed in PBS and PBS 0.1% Tween and incubated with 5% BSA/PBS for 60 min at room temperature. This was followed by overnight incubation with 1:2000 anti-TH (Abcam) primary antibody at 4°C. Next, sections were incubated with secondary antibody (anti-rabbit antibody, DAKO enVision TM) and stained with Nova Red. Nuclei were counterstained with Mayer's haematoxylin and sections were mounted on glass slides. Percentage of area positive for TH staining was quantified using Image J software.

BAT Western blot analysis

Another part of BAT was snap frozen and stored at -80°C. These BAT samples were homogenized in RIPA buffer, centrifuged and protein concentration was determined using the BCA protein assay kit (Thermo Scientific, Rockford, IL, USA). Samples were diluted and denatured for 5 min at 95°C after adding Laemmli Sample Buffer (1:1, vol/vol; Serva, Heidelberg, Germany). Proteins within homogenates (1 μg protein for UCP1 and 15 μg for p-CREB) were separated on a 10% SDS-page gel and subsequently transferred onto blotting membrane. The blotting membranes were then washed with PBS+0.1% Tween (PBS+T), blocked with 5% milk powder in PBS+T and incubated

O/N at 4°C with the first antibody (anti-UCP-1 rabbit polyclonal; Ab U6382, Sigma Aldrich or anti-p-CREB; Cell). After washing (PBS-T) the second antibody (anti-rabbit IgG HRP conjugate; 1:5,000; Promega, Madison, WI, USA) was added. After another wash with PBS-T and PBS, SuperSignal Western Blot Enhancer (Thermo Scientific, Rockford, IL, USA) was added to the blotting membranes after which they were analyzed with Bio-Rad Quantity One.

BAT gene expression analysis

A part of iBAT from wild-type C57Bl/6J mice treated with vehicle or SHU9119, was snap frozen and stored at -80°C for gene expression analysis and protein analysis (see above). Total RNA was isolated using TriPure (Roche) according to the manufacturer's instructions. 1 µg of total RNA was reverse-transcribed using M-MLV reverse transcriptase (Promega, Madison, WI, USA). Real-time PCR was carried out on a CFX96 PCR machine (Bio-Rad) using IQ SYBR-Green Supermix (Bio-Rad). Melt curve analysis was included to assure a single PCR product was formed. Expression levels were normalized using β 2-microglobulin as housekeeping gene.

Body temperature

In four wild-type C57Bl/6J mice per group, temperature transponders (IPTT-300, BMDS) were implanted subcutaneously in the clavicular region. Every three days body temperature was recorded using a compatible Smart Probe (BMDS).

Statistical analysis

Differences between groups were determined using independent sample T-tests for normally distributed data and Mann-Whitney U tests for non-normal distributed data. Serum decay in the VLDL clearance experiment was analyzed using repeated measurements ANOVA with a Tukey's Post-Hoc test. Probability values less than 0.05 were considered statistically significant. Data are presented as means \pm SEM.

Results

SHU9119 increases body weight and fat mass independent of food intake

APOE*3-Leiden.CETP mice were treated i.c.v. with SHU9119 or vehicle for 17 days. In *ad libitum* fed mice, throughout the treatment period, SHU9119 consistently increased food intake (on average 4.04 ± 0.21 vs. 3.18 ± 0.13 g/day, $p < 0.01$) (**Figure 1A**), concomitantly with an increased body weight gain (after 17 days: 6.68 ± 0.58 vs. 0.70 ± 0.14 g, $p < 0.001$). Obviously, SHU9119 also increased body weight in pair-fed mice when compared to vehicle-treated mice (4.14 ± 0.45 vs. 0.70 ± 0.14 g, $p < 0.01$) (**Figure 1B**) indicating that the SHU9119-induced weight gain is independent of food

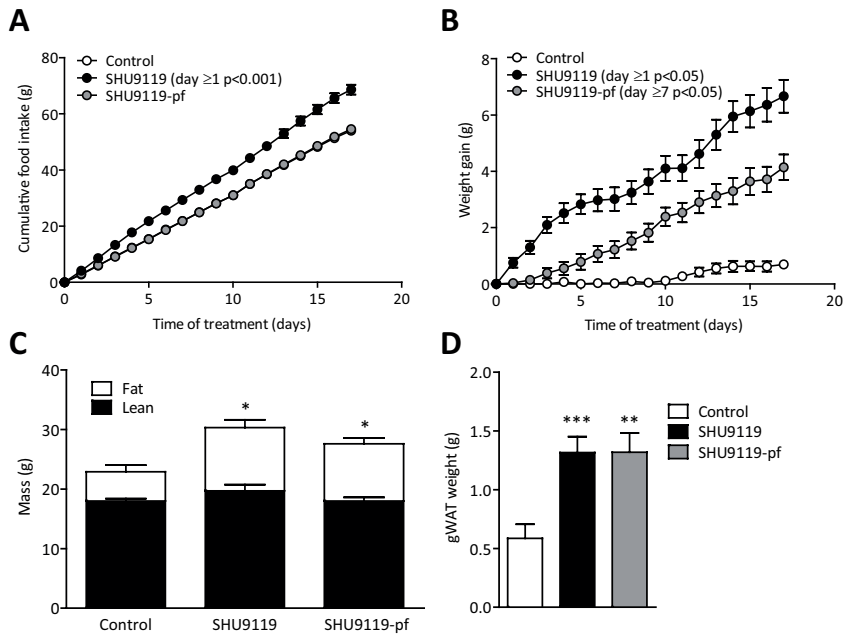


Figure 1 – SHU9119 increases body weight and fat mass independent of food intake. APOE*3-Leiden.CETP mice were treated intracerebroventricularly with vehicle (n=21) or SHU9119 (5 nmol/day) while being fed *ad libitum* (n=21) or being pair-fed (pf) to the vehicle-treated group (n=22). Food intake (**A**) and body weight gain (**B**) were monitored on a daily basis. After 17 days of treatment, lean and fat mass were measured in a random selection of the mice (n=3-4 per group) using EchoMRI (**C**). Part of the mice were used for the collection of organs, and weight of gonadal white adipose tissue was determined (n=10-11 per group) (**D**). Values are means \pm SEM. *p<0.05, **p<0.01, ***p<0.001 compared to control.

intake. Determination of body composition using EchoMRI revealed that SHU9119 increased body weight under both *ad libitum* feeding and pair-fed conditions due to a selective increase in fat mass (10.6 \pm 1.2 and 9.6 \pm 1.0 vs. 4.9 \pm 1.1 g, p<0.05) (**Figure 1C**). The SHU9119-induced increase in body weight and fat mass was accompanied by an increase in gonadal white adipose tissue (gWAT) weight, both in *ad libitum* feeding conditions (+124%; 1.32 \pm 0.13 vs. 0.59 \pm 0.12 g, p<0.001) and pair-fed conditions (+124%; 1.32 \pm 0.16 vs. 0.59 \pm 0.12 g, p<0.01) (**Figure 1D**). SHU9119 increased plasma TG levels in pair-fed mice, while it decreased total cholesterol levels in both *ad libitum* and pair-fed mice (**Supplemental Figure 1**).

In a first experiment, we did observe a large increase in plasma TG levels upon 17 days of SHU9119 treatment under *ad libitum* conditions (**Supplemental Figure 1A**), which would be consistent with reduced uptake of TG by BAT. However, in a subsequent

study the SHU9119-induced increase in plasma TG only reached significance under pair-fed conditions (**Supplemental Figure 1B**).

SHU9119 reduces whole body fat oxidation independent of food intake

Since SHU9119 induced fat accumulation independent of food intake, we reasoned that SHU9119 likely affected EE. Therefore, we next assessed the effect of SHU9119 on energy metabolism. Fully automated metabolic cages were used during the first 5 days of treatment in order to prevent a potential confounding effect of differences in body weight. Indeed, in *ad libitum* fed mice, SHU9119 decreased EE (-10%; 23.7 ± 0.3 vs. 26.4 ± 0.2 cal/h/g fat-free mass [FFM], $p < 0.05$) (**Figure 2A**) and increased RER (0.92 ± 0.01 vs. 0.88 ± 0.00 $p < 0.01$) (**Figure 2B**). These effects were not caused by an effect on carbohydrate oxidation (**Figure 2C**) but rather by a large reduction in fat oxidation (-43%; 5.1 ± 1.0 vs. 8.9 ± 0.3 cal/h/g FFM, $p < 0.001$) (**Figure 2D**). SHU9119 also reduced activity of the animals (-46%; 67 ± 6 vs. 123 ± 5 A.U., $p < 0.05$; **Figure 2E**). Strikingly, the effects of SHU9119 in pair-fed mice, as compared to the control group, were essentially similar as in *ad libitum* fed mice with respect to EE (23.9 ± 0.1 cal/h/g FFM; $p < 0.01$), RER (0.91 ± 0.01 ; $p < 0.01$), fatty acid oxidation (5.3 ± 0.5 cal/h/g FFM; $p < 0.001$) and activity (75 ± 3 A.U.; $p < 0.05$). Apparently, SHU9119 reduced EE, because of reduced fat oxidation and independent of food intake, as well as a lower locomotor activity.

SHU9119 induces hepatic steatosis due to increased food intake

Since the liver is an important player in TG storage and secretion, we evaluated the effect of SHU9119 on liver weight and TG content as well as on hepatic VLDL-TG secretion. SHU9119 induced hepatomegaly as evidenced by increased liver weight (+85%; 2.17 ± 0.11 vs. 1.17 ± 0.06 g, $p < 0.001$) (**Figure 3A**) and aggravated hepatic steatosis, as shown by a selective increase in liver TG (+57%; 689 ± 33 vs. 439 ± 37 nmol/mg protein, $p < 0.001$) (**Figure 3B**) and neutral lipid staining (**Figure 3C**). However, the effects of SHU9119 on the liver were fully attributed to the induction of hyperphagia, as hepatomegaly and hepatic steatosis were not induced under pair-fed conditions (**Figure 3A-D**). SHU9119 did not affect the VLDL-TG production rate in mice that were either fed *ad libitum* (3.39 ± 0.14 mmol/L/h) or pair-fed (3.61 ± 0.37 mmol/L/h) as compared to control mice (3.59 ± 0.29 mmol/L/h) (**Figure 3D,E**). The VLDL-apoB production rate was slightly decreased in SHU9119-treated mice, but not in pair-fed SHU9119-treated mice (**Figure 3F**). In line with these observations, SHU9119 did not affect VLDL particle size (**Figure 3G**), VLDL composition (**Figure 3H**), or hepatic expression of the genes *Apob*, *Mttp*, *Dgat2* involved in VLDL synthesis (not shown). Taken together, SHU9119 induced hepatic steatosis secondary to its induction of hyperphagia and without affecting VLDL-TG secretion.

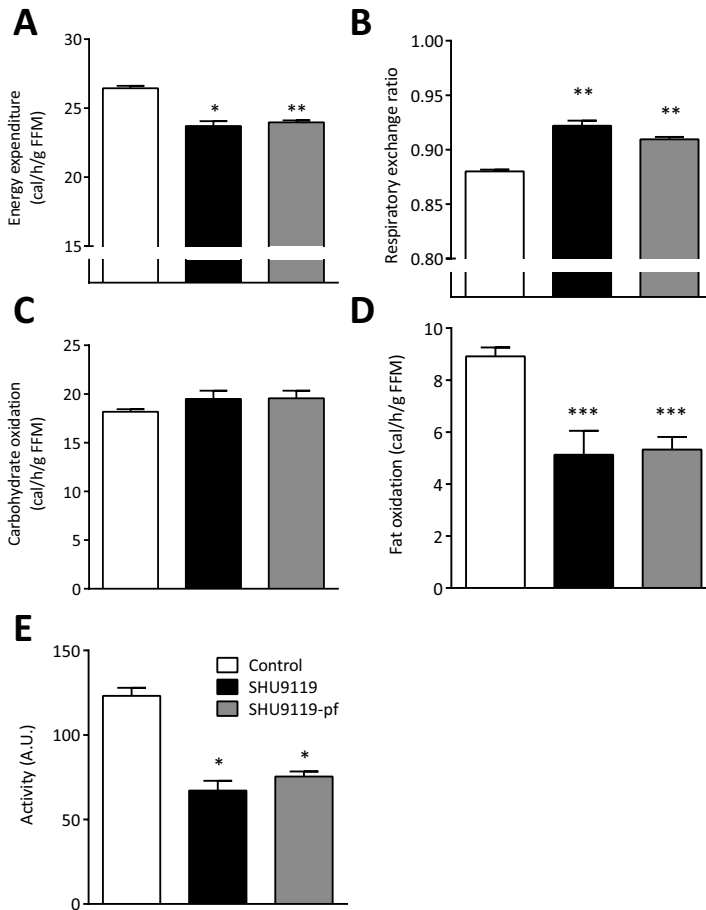


Figure 2 – SHU9119 lowers energy expenditure by reducing fat oxidation independent of food intake. APOE*3-Leiden.CETP mice were treated intracerebroventricularly with vehicle (n=9) or SHU9119 (5 nmol/day) while being fed *ad libitum* (n=6) or being pair-fed (pf) to the vehicle-treated group (n=9). During the first 5 days of treatment, mice were housed in fully automated metabolic cages. Energy expenditure (**A**), respiratory exchange ratio (**B**), carbohydrate oxidation (**C**) and fat oxidation (**D**) were calculated from O₂ uptake and CO₂ excretion. Values are means ± SEM. *p<0.05, **p<0.01, ***p<0.001 compared to control.

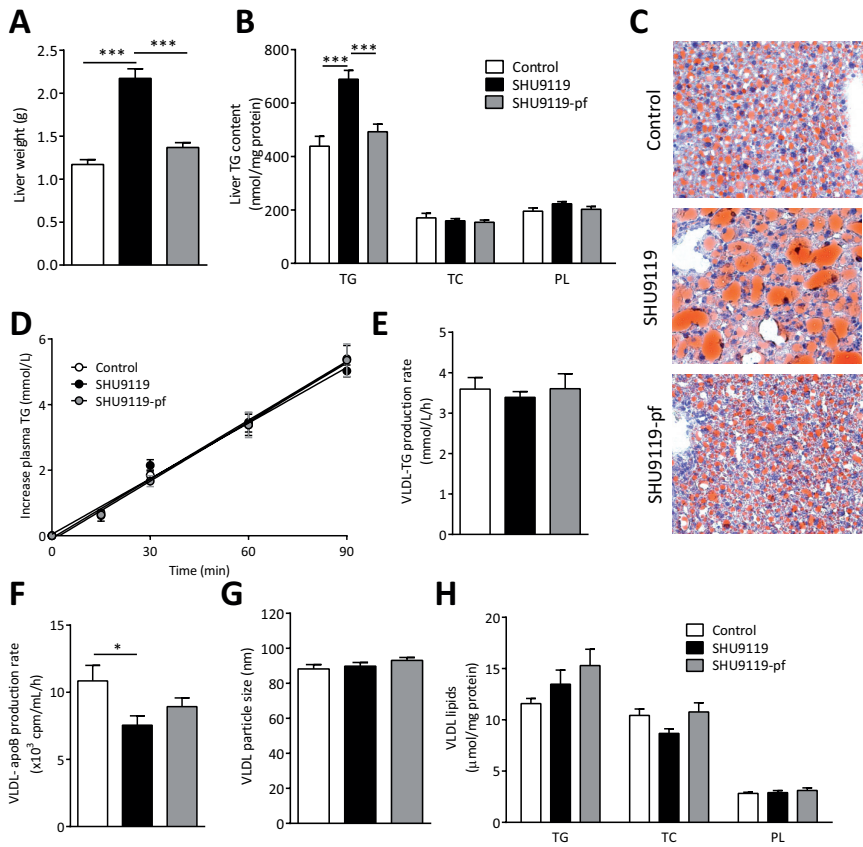


Figure 3 – SHU9119 induces hepatomegaly and steatosis only in *ad libitum* fed mice. APOE*3-Leiden.CETP mice were treated intracerebroventricularly with vehicle (n=21) or SHU9119 (5 nmol/day) while being fed *ad libitum* (n=21) or being pair-fed (pf) to the vehicle-treated group (n=20). After 17 days of treatment, part of the mice were sacrificed (n=10-11 per group) to collect organs and determine liver weight (A), and to determine liver content of triglycerides (TG), total cholesterol (TC) and phospholipids (PL) (B). Frozen liver samples were sectioned and stained with a neutral lipid staining (Oil-red-O) and hematoxylin, and representative pictures are shown (C). The remaining mice (n=8-10 per group) were 4 h fasted, consecutively injected with Trans³⁵S label and tyloxapol, and blood samples were drawn up to 90 min after tyloxapol injection. Plasma TG concentration was determined and plotted as the increase in plasma TG relative to t=0 (D). The rate of TG production was calculated from the slopes of the curves from the individual mice (E). After 120 min, the total VLDL fraction was isolated by ultracentrifugation and the rate of newly synthesized VLDL-ApoB was determined (F). The VLDL fractions were assayed for particle size (G) and lipid content (H). Values are means ± SEM. *p<0.05, ***p<0.001 compared to control.

SHU9119 induces brown adipose tissue dysfunction independent of food intake

Since BAT strongly contributes to fat oxidation and total energy expenditure, we subsequently determined the effect of SHU9119 treatment on BAT function. SHU9119 treatment increased BAT weight in *ad libitum* fed mice (+50%; 0.15 ± 0.01 vs. 0.10 ± 0.01 g, $p < 0.01$) and tended to increase BAT weight in pair-fed animals (+24%; 0.13 ± 0.01 g, $p = 0.06$) (**Figure 4A**). Strikingly, SHU9119 dramatically increased intracellular lipid droplet size in BAT in both *ad libitum* fed and pair-fed mice (**Figure 4B**), along with reduced sympathetic innervation of BAT as evidenced by reduced tyrosine hydroxylase (*i.e.* the rate-limiting enzyme in norepinephrine synthesis) (-53%; $p < 0.001$ and -43%; $p < 0.001$) (**Figure 4C-D**) and reduced phosphorylation of CREB (-22%; $p < 0.05$ and -15%; n.s.) (**Figure 4E**), a downstream target of $\beta 3$ -adrenergic signaling. Accordingly, largely reduced UCP-1 protein levels in BAT (-61%; $p < 0.001$ and -61%, $p < 0.001$) were observed (**Figure 4F**). These data imply that SHU9119 decreases BAT activity independent of food intake, likely due to lower sympathetic innervation of BAT, and this may result in decreased burning of intracellularly stored TG and, as a consequence, larger intracellular lipid droplet size.

To assess the capacity of BAT to take up VLDL-TG, we next determined the effect of SHU9119 on the kinetics of *i.v.* injected [^3H]TO and [^{14}C]CO double-labeled VLDL-like emulsion particles after 14 days of treatment. SHU9119 impaired the plasma decay of [^3H]TO (**Figure 4G**) and [^{14}C]CO (**Figure 4I**) under *ad libitum* fed conditions, and that of [^{14}C]CO under pair-fed conditions (**Figure 4I**). At 15 min after injection, the distribution of radiolabels over the organs was assessed. In control mice, the uptake of [^3H]TO-derived activity by BAT ($31.6 \pm 8.0\%$ /g) was much higher than the uptake by liver (~4-fold), muscle (~25-fold) and WAT (~25-fold), indicating that BAT is highly metabolically active compared to other organs. Interestingly, SHU9119 tended to selectively decrease the uptake of [^3H]TO by BAT in the *ad libitum* fed group, and significantly did so in mice pair-fed to the control group (-57%; $13.7 \pm 1.9\%$ of injected dose/g; $p < 0.05$) (**Figure 4H**), most likely as a consequence of reduced hydrolysis of VLDL-TG. Indeed, in the control group, as compared to the ^3H -label, the uptake of the ^{14}C -label was much lower in BAT (~10-fold), muscle (~4-fold), heart (~3-fold) and WAT (~3-fold), while the uptake of ^{14}C -label was higher in liver (~3-fold). This pattern is compatible with selective delipidation of the VLDL-like emulsion particles in plasma by the LPL-expressing tissues (*i.e.* uptake of ^3H activity), with subsequent uptake of the core remnant by the liver (*i.e.* uptake of ^{14}C activity). SHU9119 treatment tended to reduce the uptake of [^{14}C]CO in the liver of both *ad libitum* fed mice (-20%; $20.8 \pm 3.6\%$ /g; $p = 0.11$) and pair-fed mice (-11%; $23.1 \pm 1.5\%$ /g; $p = 0.25$) as compared to the control group ($26.1 \pm 2.1\%$ /g), whereas it decreased the uptake of [^{14}C]CO by BAT (*ad libitum* fed: -39%; $p = 0.24$; pair-fed: -57%; $p < 0.01$) (**Figure 4J**).

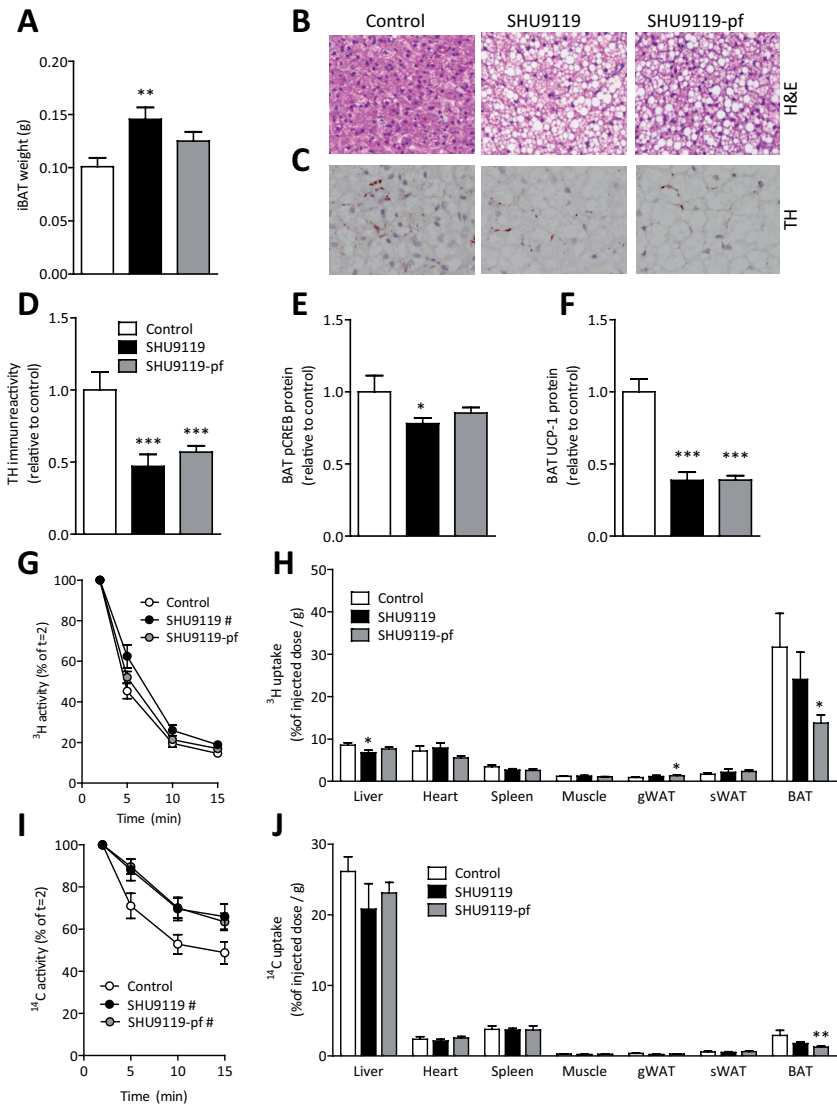


Figure 4 – SHU9119 causes malfunction of brown adipose tissue. APOE³-Leiden.CETP mice were treated intracerebroventricularly with vehicle (n=21) or SHU9119 (5 nmol/day) while being fed *ad libitum* (n=21) or being pair-fed (pf) to the vehicle-treated group (n=22). After 17 days of treatment, part of the mice were sacrificed (n=10-11 per group) and interscapular brown adipose tissue (iBAT) was quantitatively removed. iBAT was examined for weight (**A**), morphology, as assessed by hematoxylin and eosin (H&E) staining, (**B**) and tyrosine hydroxylase (TH) content (**C,D**). In iBAT, protein content of phosphorylated CREB (**E**) and UCP-1 (**F**) were determined. In a second experiment, after 14 days of i.c.v. treatment with vehicle (n=8) or SHU9119 (5 nmol/day) while being fed *ad libitum* (n=5) or being pf to the vehicle-treated group (n=9), mice were 4h fasted and consecutively injected with [³H]TO and [¹⁴C]CO-labeled VLDL-like emulsion particles. Plasma [³H]TO (**G**) and [¹⁴C]CO (**H**) were determined at the indicated time points and plotted relative to the dosage at t=2 min. At 15 min after injection, organs were isolated and uptake of the ³H-activity (**I**) and ¹⁴C-activity (**J**) was determined. Values are means ± SEM. #p<0.05, *p<0.05, **p<0.01, ***p<0.001 compared to control.

SHU9119 also induces brown adipose tissue dysfunction independent of dyslipidemia

To investigate the inhibitory effects of SHU9119 on BAT activity independent of dyslipidemia induced by Western-type diet feeding in APOE*3-Leiden.CETP mice, we next repeated experiments in wild-type mice that were fed a regular chow diet. Again, SHU9119 consistently increased food intake (on average 4.97 ± 0.29 vs. 4.10 ± 0.26 g/day, $p < 0.05$) (**Figure 5A**) accompanied by an increase in body weight gain (5.43 ± 0.58 vs. 0.21 ± 0.24 g, $p < 0.001$) (**Figure 5B**). As with the APOE*3-Leiden.CETP mice, administration of SHU9119 in wild-type mice increased body weight gain in pair-fed animals (1.29 ± 0.32 g, $p < 0.05$) (**Figure 5B**), due to a selective increase in fat mass (**Figure 5C**). Histological analysis revealed increased lipid accumulation in BAT upon SHU9119 treatment (**Figure 5D**), especially in the *ad libitum* fed mice in which 51±14% of the total area consisted of lipids ($p < 0.001$) (**Figure 5E**). In addition, SHU9119 tended to reduce tyrosine hydroxylase content in BAT in both *ad libitum* and pair-fed mice (-32% and -42%, respectively) (**Figure 5F**), accompanied by reduced phosphorylation of CREB (-32%, $p < 0.01$ and -52%, $p < 0.001$ respectively) (**Figure 5G**), supporting reduced sympathetic innervation of BAT. Again, SHU9119 markedly reduced UCP-1 protein content in BAT in both *ad libitum* and pair-fed mice (-54%, $p < 0.001$ and -64%, $p < 0.001$ respectively) (**Figure 5H**). SHU9119 resulted in lower body temperature in both *ad libitum* (35.9 ± 0.32 °C, $p < 0.01$), and pair-fed (35.6 ± 0.47 °C, $p < 0.05$) animals as compared to vehicle treated mice (36.7 ± 0.46 °C) (**Figure 5I-J**), which is in line with reduced BAT thermogenesis. We next assessed the capacity of BAT to take up VLDL-TG upon SHU9119 treatment. Again, SHU9119 lowered uptake of [³H]TO-derived activity from VLDL-like emulsion particles by BAT In *ad libitum* fed mice compared to vehicle treated animals (-80%; $p < 0.001$). Interestingly, in pair fed animals this effect was not observed (**Figure 5K**). Accordingly, gene expression of the lipolytic enzyme *Lpl* was decreased in *ad libitum* fed mice (-70%; $p < 0.001$), but not in pair fed mice (**Figure 5L**). These data suggest that lower local hydrolysis of TG-rich lipoprotein like particles may well underlie the lower uptake of TG by BAT upon SHU9119 treatment. Altogether, SHU9119 inhibits BAT activity in both hyperlipidemic APOE*3-Leiden.CETP mice and normolipidemic wild-type mice.

Discussion

The melanocortin system is an important regulator of energy balance and MC4R deficiency is the most common monogenic cause of obesity. BAT recently emerged as an important player in energy expenditure by combusting high amounts of TG towards heat. In addition, MC4R expressing neurons project onto BAT (14). Hence, the association between MC4R and energy expenditure may be mediated by BAT. In the current study we aimed to evaluate the direct effect of the melanocortin system

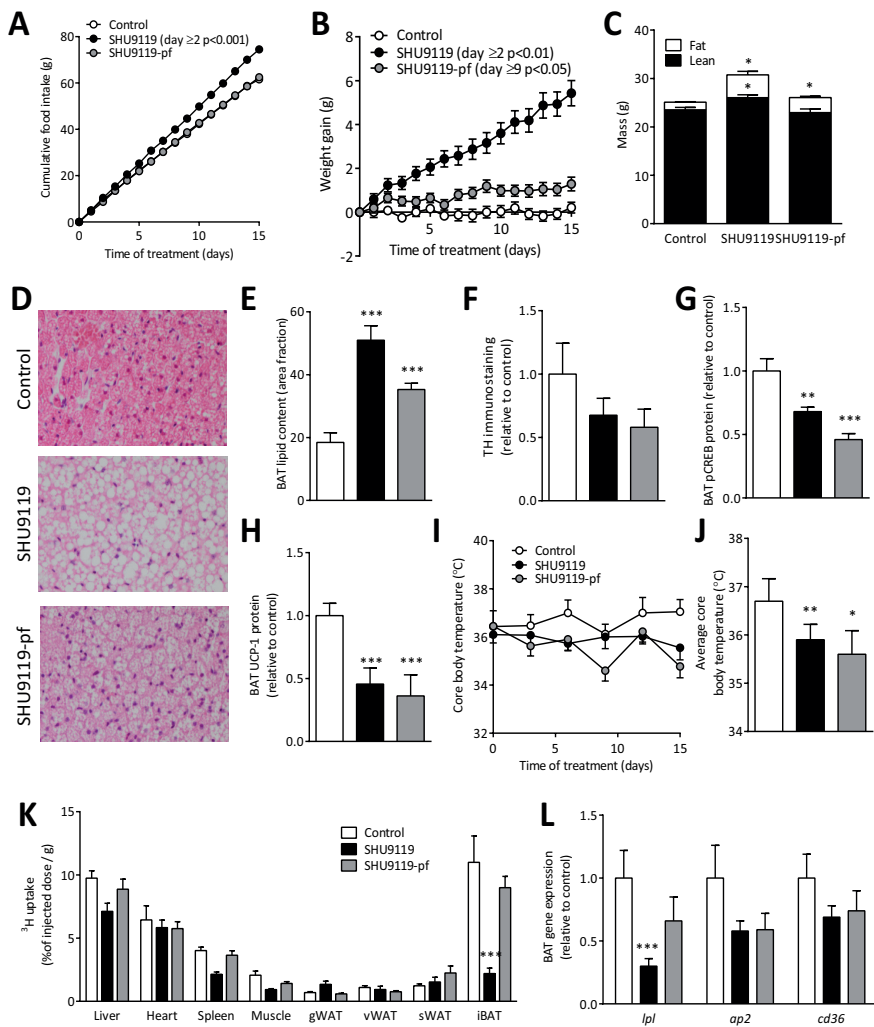


Figure 5 – SHU9119 induces brown adipose tissue dysfunction independent of dyslipidemia. Wild-type C57Bl/6J mice were treated intracerebroventricularly with vehicle (n=9) or SHU9119 (5 nmol/day) while being fed *ad libitum* (n=10) or being pair-fed (pf) to the vehicle-treated group (n=9). Food intake (A) and body weight (B) were monitored on a daily basis. After 15 days, body composition was determined using echo-MRI (C). Core body temperature was measured every 3 days using subcutaneously implanted temperature transponder (D) and average core body temperature was calculated (E). On histological level tyrosine hydroxylase (TH) immunoreactivity was determined (F) and BAT protein levels of phosphorylated CREB (G) and UCP-1 (H) were measured using Western blots. Before scarification, after 4h of fasting, mice were injected with 3 H]TO-labeled VLDL-like emulsion particles and organs were isolated 15 min after injection. Uptake of the 3 H-activity (I) was determined. On BAT, an H&E staining (J) was performed to quantify lipid content (K) and on frozen sections were used to determine gene expression (L). Values are means \pm SEM. *p<0.05, **p<0.05, ***p<0.001 compared to control.

on BAT activity. For this purpose, we inhibited the central melanocortin system using the MC3/4R synthetic antagonist SHU9119 in APOE*3-Leiden.CETP mice. We found that i.c.v. administration of SHU9119 decreased EE and BAT activity, concomitant with selectively impaired uptake of TG from plasma by BAT, independent of food intake.

Both in *ad libitum* as well in pair-fed conditions, SHU9119 treatment increased body weight and WAT mass. These data are in line with those of Nogueiras *et al.* (8), who attributed weight gain and adiposity upon SHU9119 treatment to an increase in both lipid uptake as well as TG synthesis for storage in WAT. Accordingly, we found enhanced uptake of TG by gWAT after a bolus injection of double-labeled VLDL-like emulsion particles. Though the increase in TG uptake by gWAT may have seemed small when expressed per gram tissue, the total depot of gWAT may contribute to a marked absolute TG uptake by the tissue. We also showed that in *ad libitum* fed conditions, SHU9119 induced ectopic lipid deposition in the liver, manifested by hepatomegaly and hepatic steatosis. Hepatic steatosis did not develop in pair-fed mice, indicating that this effect is a direct consequence of SHU9119-induced hyperphagia. Similar effects on the liver are observed after 4 days of i.c.v. SHU9119 treatment in rats (19) and in MC4R deficient mice, which in addition develop steatohepatitis when fed a high-fat diet and have therefore been proposed as a novel mouse model for non-alcoholic steatohepatitis (NASH) (20). Although hepatic steatosis could promote the secretion of hepatic lipid as VLDL (21), SHU9119 did not increase the VLDL-TG production, VLDL-size or composition of newly synthesized VLDL. Our data corroborate those of Stafford *et al.*(22) who showed that a single i.c.v. injection of 15 µg SHU9119 does not affect VLDL-TG production in rats. Of note, ApoB production was decreased in *ad libitum* fed SHU9119 treated animals, which may be the consequence of the hepatic steatosis. These data corroborate previous observations that steatosis, by inducing ER stress, inhibits the hepatic production of apoB100 (23), which can result in production of large lipid-rich VLDL particles (24).

Because SHU9119 was able to increase body adiposity independent of a change in food intake, we reasoned that SHU9119 reduced EE. Indeed, by performing studies with metabolic cages we confirmed that inhibition of the central melanocortin system reduced EE. Besides decreasing locomotor activity, SHU9119 selectively reduced fat oxidation, whereas carbohydrate oxidation remained unaffected. This reduction in fat oxidation and total EE occurred independently of food intake and before changes in body weight were observed, indicative of a causal relation between reduced energy expenditure and the induction of obesity. Likewise, a previous study has shown that 7 days of i.c.v. injections with SHU9119 in rats increased the RER and thereby decreased fat utilization independent of food intake (8). As locomotor activity was not affected in that study, reduced fat oxidation may be dominant over the effect of decreased locomotor activity in the decrease in EE. In addition, MC4R-deficient humans also display an increase in RER (8). Taken together, we suggest that, in

general, inhibition of the melanocortin system results in a shift towards decreased metabolic use of lipids leading to elevated fat deposition in WAT.

Since BAT is a highly active metabolic tissue involved in EE and regulation of weight gain, we next proposed that the reduction in fat oxidation could be largely attributed to decreased activity of BAT. Indeed, in both *ad libitum* and pair-fed conditions in Western-type diet fed APOE*3-Leiden.CETP mice, analysis of BAT revealed that SHU9119 largely increased intracellular lipid stores and decreased the protein level of the UCP-1, both indicative of reduced BAT activity (25). These data corroborate previous findings showing that chronic i.c.v. treatment of *ad libitum* fed rats with SHU9119 lowered BAT temperature during the night (26). Moreover, 7 daily i.c.v. injections of AgRP, the endogenous antagonist for MC4R, decreased *Ucp1* gene expression in pair-fed rats (27), while acute i.c.v. injections of GLP-1, which indirectly stimulates MC4R, increased BAT thermogenesis by increasing activity of the sympathetic fibers towards BAT (28). Accordingly, since the activity of BAT is dependent on SNS outflow from the hypothalamus (29,30), reduced sympathetic output from the hypothalamus towards BAT is the likely mechanism by which inhibition of the central melanocortin system reduced BAT activity. We observed reduced sympathetic output towards BAT as evidenced by decreased levels of tyrosine hydroxylase, the rate limiting enzyme in norepinephrine synthesis, and decreased phosphorylation of CREB, a downstream target of β 3-adrenergic signaling, in BAT upon SHU9119 treatment. Thus, these data support a major role for BAT in the reduced EE and enhanced weight gain of central MC4R inhibition. However, based on these data, we cannot exclude the involvement of other metabolic tissues such as liver and WAT in the development of the disadvantageous metabolic phenotype.

Interestingly, in the Western type diet-fed APOE*3-Leiden.CETP mice we provided evidence that SHU9119 lowered both β -oxidation and VLDL-TG uptake by BAT, while lipid accumulation was markedly enhanced. This suggests that the lower β -oxidation upon SHU9119 treatment was more pronounced than the reduced VLDL-TG uptake by the tissue. It would make physiological sense if the reduction in VLDL-TG uptake by BAT occurred as a secondary mechanism to compensate for the diminished TG combustion by the tissue. Indeed, this is supported by the study performed in chow-fed wild-type C57Bl/6J mice. While both the *ad libitum* fed and pair-fed animals developed marked lipid accumulation in BAT upon SHU9119 treatment, only the *ad libitum* fed mice exhibited lower TG uptake by BAT. Of note, the lipid accumulation in BAT was less pronounced in the chow pair-fed C57Bl6/J mice as compared to the Western-type diet pair-fed APOE*3-Leiden.CETP mice, perhaps due to the lower fat content of the chow diet. It is, therefore, likely that especially brown adipocytes that become saturated with lipids lower their TG uptake as a secondary mechanism, for instance by downregulation of *Lpl* expression resulting in lower VLDL-TG hydrolysis.

Indeed, in the study with C57Bl6/J mice *Lpl* was downregulated only in the SHU9119 mice that were fed *ad libitum*.

Recently, Bartelt *et al.* (13) identified BAT as a major organ involved in plasma VLDL-TG clearance, with 24 hours of cold induction resulting in normalisation of plasma TG levels in hypertriglyceridemic mice. To investigate the effects of decreased BAT activity on plasma lipid levels, dyslipidemic APOE*3-Leiden.CETP mice were used in the first set of experiments. In a first experiment, we did observe a large increase in plasma TG levels upon 17 days of SHU9119 treatment under *ad libitum* conditions (**Supplemental Figure 1A**), which would be consistent with reduced uptake of TG by BAT. However, in a subsequent study the SHU9119-induced increase in plasma TG only reached significance under pair-fed conditions (**Supplemental Figure 1B**). Likewise, i.c.v. infusion of the MC4R synthetic antagonist HS104 also failed to increase plasma TG levels in pair-fed rats (31). It should be noted that MC4R deficient mice have only modestly increased plasma TG levels compared to control mice (+30%) (32), implying that partial inhibition of MC4R by SHU9119 may be insufficient to significantly increase plasma TG levels. In heterozygous MC4R-deficient subjects, plasma TG levels are increased (1.7 vs. 1.3 mmol/L) (33), indicating that the melanocortin system does play a role in the regulation of plasma VLDL-TG levels in humans.

Recently, Perez-Tilve *et al.* (34) demonstrated that inhibition of the central melanocortin neurons by either ghrelin or SHU9119 in wild-type mice increased circulating cholesterol, related to a decreased hepatic expression of SR-BI involved in the selective hepatic uptake of HDL-cholesteryl esters. In our study in APOE*3-Leiden.CETP mice with a human-like lipoprotein metabolism, SHU9119 did not rather decrease total cholesterol levels (**Supplemental Figure 1**) despite decreased hepatic SR-BI expression (**Supplemental Figure 2**). This is likely due to the expression of human CETP that provides an alternative route for the clearance of HDL-cholesterol, as CETP expression in SR-BI-deficient mice also precludes an increase in HDL-cholesterol (35). In addition, this could be related to an increased output of cholesterol in the feces as well as a somewhat reduced output of cholesterol from the liver within VLDL. Likewise, humans with heterozygous MC4R deficiency also do not have increased cholesterol levels (33), pointing to a species-dependent effect of MC4R function on HDL-cholesterol levels.

In conclusion, inhibition of central MC3/4R signaling by SHU9119 reduces BAT activity thereby reducing the uptake and combustion of VLDL-TG by BAT. As a consequence, excess lipids are stored in WAT (**Figure 6**). We anticipate that MC4R agonists that are currently in development to combat obesity, increase energy expenditure through activation of BAT.

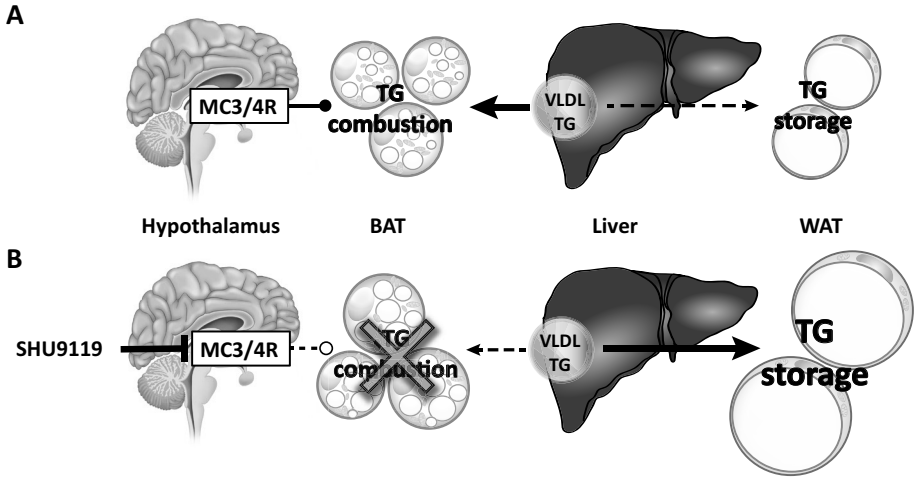


Figure 6 – Proposed model of the effect of SHU9119 on peripheral triglyceride metabolism. Under physiological conditions MC3/4R signalling is required for basal combustion of VLDL-derived triglycerides (TG) in brown adipose tissue (BAT), preventing storage of excess TG in WAT (A). Inhibition of central MC3/4R signaling by SHU9119 reduces BAT activity, thereby reducing the uptake and combustion of VLDL-TG by BAT. As a consequence, excess TG is stored in WAT, independent of SHU9119-induced hyperphagia (B).

Acknowledgements

We acknowledge the support from 'the Netherlands CardioVascular Research Initiative: the Dutch Heart Foundation, Dutch Federation of University Medical Centers, the Netherlands Organisation for Health Research and Development and the Royal Netherlands Academy of Sciences' for the GENIUS project 'Generating the best evidence-based pharmaceutical targets for atherosclerosis' (CVON2011-19). PCN Rensen is an Established Investigator of the Netherlands Heart Foundation (grant 2009T038).

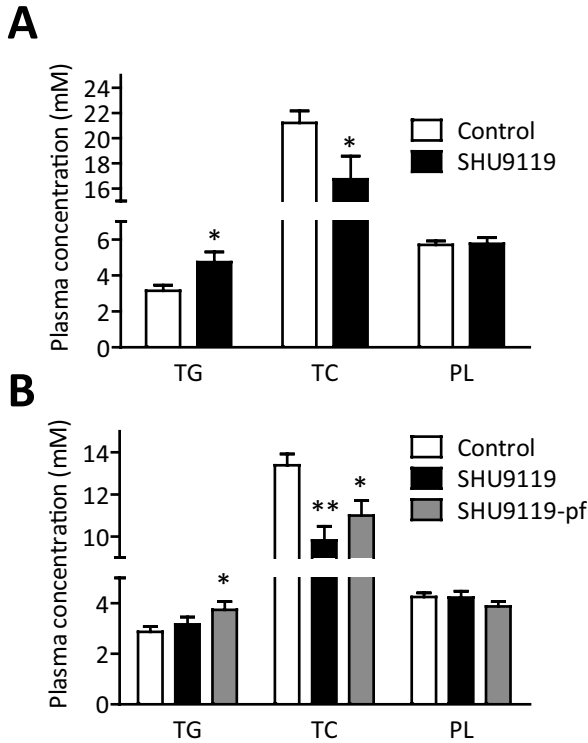
References

- Garfield, A. S., Lam, D. D., Marston, O. J. *et al.* (2009) Role of central melanocortin pathways in energy homeostasis. *Trends Endocrinol Metab* 20, 203-215.
- Nargund, R. P., Strack, A. M., & Fong, T. M. (2006) Melanocortin-4 receptor (MC4R) agonists for the treatment of obesity. *J Med Chem* 49, 4035-4043.
- Fan, W., Boston, B. A., Kesterson, R. A. *et al.* (1997) Role of melanocortinergic neurons in feeding and the agouti obesity syndrome. *Nature* 385, 165-168.
- Huszar, D., Lynch, C. A., Fairchild-Huntress, V. *et al.* (1997) Targeted disruption of the melanocortin-4 receptor results in obesity in mice. *Cell* 88, 131-141.
- Farooqi, I. S., Keogh, J. M., Yeo, G. S. *et al.* (2003) Clinical spectrum of obesity and mutations in the melanocortin 4 receptor gene. *N Engl J Med* 348, 1085-1095.
- Loos, R. J., Lindgren, C. M., Li, S. *et al.* (2008) Common variants near MC4R are associated with fat mass, weight and risk of obesity. *Nat Genet* 40, 768-775.
- Xi, B., Chandak, G. R., Shen, Y. *et al.* (2012) Association between common polymorphism near the MC4R gene and obesity risk: a systematic review and meta-analysis. *PLoS One* 7, e45731.
- Nogueiras, R., Wiedmer, P., Perez-Tilve, D. *et al.* (2007) The central melanocortin system directly controls peripheral lipid metabolism. *J Clin Invest* 117, 3475-3488.
- Rahmouni, K., Haynes, W. G., Morgan, D. A. *et al.* (2003) Role of melanocortin-4 receptors in mediating renal sympathoactivation to leptin and insulin. *J Neurosci* 23, 5998-6004.
- Joly-Amado, A., Denis, R. G., Castel, J. *et al.* (2012) Hypothalamic AgRP-neurons control peripheral substrate utilization and nutrient partitioning. *EMBO J* 31, 4276-4288.
- Cole, S. A., Butte, N. F., Voruganti, V. S. *et al.* (2010) Evidence that multiple genetic variants of MC4R play a functional role in the regulation of energy expenditure and appetite in Hispanic children. *Am J Clin Nutr* 91, 191-199.
- Krakoff, J., Ma, L., Kobes, S. *et al.* (2008) Lower metabolic rate in individuals heterozygous for either a frameshift or a functional missense MC4R variant. *Diabetes* 57, 3267-3272.
- Bartelt, A., Bruns, O. T., Reimer, R. *et al.* (2011) Brown adipose tissue activity controls triglyceride clearance. *Nat Med* 17, 200-205.
- Voss-Andreae, A., Murphy, J. G., Ellacott, K. L. *et al.* (2007) Role of the central melanocortin circuitry in adaptive thermogenesis of brown adipose tissue. *Endocrinology* 148, 1550-1560.
- Westerterp, M., van der Hoogt, C. C., de, H. W. *et al.* (2006) Cholesteryl ester transfer protein decreases high-density lipoprotein and severely aggravates atherosclerosis in APOE*3-Leiden mice. *Arterioscler Thromb Vasc Biol* 26, 2552-2559.
- Van Klinken, J. B., van den Berg, S. A., Havekes, L. M. *et al.* (2012) Estimation of activity related energy expenditure and resting metabolic rate in freely moving mice from indirect calorimetry data. *PLoS One* 7, e36162.
- BLIGH, E. G. & DYER, W. J. (1959) A rapid method of total lipid extraction and purification. *Can J Biochem Physiol* 37, 911-917.
- Rensen, P. C., Herijgers, N., Netscher, M. H. *et al.* (1997) Particle size determines the specificity of apolipoprotein E-containing triglyceride-rich emulsions for the LDL receptor versus hepatic remnant receptor in vivo. *J Lipid Res* 38, 1070-1084.
- Wiedmer, P., Chaudhary, N., Rath, M. *et al.* (2012) The HPA axis modulates the CNS melanocortin control of liver triacylglyceride metabolism. *Physiol Behav* 105, 791-799.
- Itoh, M., Suganami, T., Nakagawa, N. *et al.* (2011) Melanocortin 4 receptor-deficient mice as a novel mouse model of nonalcoholic steatohepatitis. *Am J Pathol* 179, 2454-2463.
- Adiels, M., Taskinen, M. R., Packard, C. *et al.* (2006) Overproduction of large VLDL particles is driven by increased liver fat content in man. *Diabetologia* 49, 755-765.

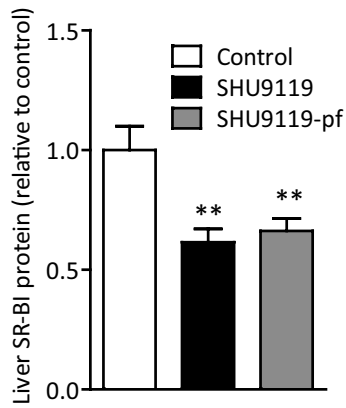
22. Stafford, J. M., Yu, F., Printz, R. *et al.* (2008) Central nervous system neuropeptide Y signaling modulates VLDL triglyceride secretion. *Diabetes* 57, 1482-1490.
23. Ota, T., Gayet, C., & Ginsberg, H. N. (2008) Inhibition of apolipoprotein B100 secretion by lipid-induced hepatic endoplasmic reticulum stress in rodents. *J Clin Invest* 118, 316-332.
24. Werner, A., Havinga, R., Bos, T. *et al.* (2005) Essential fatty acid deficiency in mice is associated with hepatic steatosis and secretion of large VLDL particles. *Am J Physiol Gastrointest Liver Physiol* 288, G1150-G1158.
25. Carobbio, S., Rosen, B., & Vidal-Puig, A. (2013) Adipogenesis: new insights into brown adipose tissue differentiation. *J Mol Endocrinol*
26. Verty, A. N., Allen, A. M., & Oldfield, B. J. (2010) The endogenous actions of hypothalamic peptides on brown adipose tissue thermogenesis in the rat. *Endocrinology* 151, 4236-4246.
27. Small, C. J., Kim, M. S., Stanley, S. A. *et al.* (2001) Effects of chronic central nervous system administration of agouti-related protein in pair-fed animals. *Diabetes* 50, 248-254.
28. Lockie, S. H., Heppner, K. M., Chaudhary, N. *et al.* (2012) Direct control of brown adipose tissue thermogenesis by central nervous system glucagon-like peptide-1 receptor signaling. *Diabetes* 61, 2753-2762.
29. Bartness, T. J., Vaughan, C. H., & Song, C. K. (2010) Sympathetic and sensory innervation of brown adipose tissue. *Int J Obes (Lond)* 34 Suppl 1, S36-S42.
30. Morrison, S. F., Madden, C. J., & Tupone, D. (2012) Central control of brown adipose tissue thermogenesis. *Front Endocrinol (Lausanne)* 3.
31. Baran, K., Preston, E., Wilks, D. *et al.* (2002) Chronic central melanocortin-4 receptor antagonism and central neuropeptide-Y infusion in rats produce increased adiposity by divergent pathways. *Diabetes* 51, 152-158.
32. Iqbal, J., Li, X., Chang, B. H. *et al.* (2010) An intrinsic gut leptin-melanocortin pathway modulates intestinal microsomal triglyceride transfer protein and lipid absorption. *J Lipid Res* 51, 1929-1942.
33. Greenfield, J. R., Miller, J. W., Keogh, J. M. *et al.* (2009) Modulation of blood pressure by central melanocortinergic pathways. *N Engl J Med* 360, 44-52.
34. Perez-Tilve, D., Hofmann, S. M., Basford, J. *et al.* (2010) Melanocortin signaling in the CNS directly regulates circulating cholesterol. *Nat Neurosci* 13, 877-882.
35. Hildebrand, R. B., Lammers, B., Meurs, I. *et al.* (2010) Restoration of high-density lipoprotein levels by cholesteryl ester transfer protein expression in scavenger receptor class B type I (SR-BI) knockout mice does not normalize pathologies associated with SR-BI deficiency. *Arterioscler Thromb Vasc Biol* 30, 1439-1445.

Supplementary appendix

2



Supplemental Figure 1 – Effect of SHU9119 on plasma lipid levels. **(A)** In a first experiment, APOE*3-Leiden.CETP mice were treated intracerebroventricularly with vehicle (n=10) or SHU9119 [5 nmol/day] (n=7). After 17 days of treatment, blood was drawn after a 4 h fast (from 8.00 h to 12.00 h) via tail vein bleeding in paraoxon-coated capillary tubes to prevent *ex vivo* lipolysis and assayed for triglycerides (TG), total cholesterol (TC) and phospholipids (PL) using commercially available enzymatic kits for TG (11488872, Roche Diagnostics, Germany), TC (11489232, Roche Diagnostics, Mannheim, Germany) and PL (3009, Instruchemie, Delfzijl, the Netherlands). **(B)** In a second experiment, mice were treated i.c.v. with vehicle (n=21) or SHU9119 (5 nmol/day) while being fed *ad libitum* (n=21) or being pair-fed (pf) to the vehicle-treated group (n=22). Plasma lipids were determined after 4 h of fasting. Values are means \pm SEM. *p<0.05, **p<0.01 compared to control.



Supplemental Figure 2 – Effect of SHU9119 on hepatic SR-BI protein levels. APOE*3-Leiden. CETP mice were treated intracerebroventricularly with vehicle (n=21) or SHU9119 (5 nmol/day) while being fed *ad libitum* (n=21) or being pair-fed (pf) to the vehicle-treated group (n=20). After 17 days of treatment, part of the mouse groups were sacrificed (n=10-11 per group) to collect organs and determine hepatic SR-BI protein levels. Values are means \pm SEM. **p<0.01 compared to control.

3

CENTRAL GLP-1 RECEPTOR SIGNALLING ACCELERATES CLEARANCE OF TRIACYLGLYCEROL AND GLUCOSE BY ACTIVATING BROWN ADIPOSE TISSUE IN MICE

Sander Kooijman*

Yanan Wang *

Edwin T. Parlevliet*

Mariëtte R. Boon

David Edelschaap

Gido Snaterse

Hanno Pijl

Johannes A. Romijn

Patrick C.N. Rensen

*Authors contributed equally

Diabetologia (2015) in press

Abstract

3

Glucagon-like peptide 1 (GLP-1) receptor (GLP-1R) agonism, used in the treatment of type 2 diabetes, has recently been shown to increase thermogenesis via the brain. As brown adipose tissue (BAT) produces heat by burning triacylglycerol (TG) and takes up glucose for de novo lipogenesis, the aim of this study was to evaluate the potential of chronic central GLP-1R activation by exendin-4 to facilitate clearance of lipids and glucose from the circulation by activating BAT. Lean and diet-induced obese (DIO) C57Bl/6J mice were used to explore the effect of a 5 day intracerebroventricular infusion of the GLP-1 analogue exendin-4 or vehicle on lipid and glucose uptake by BAT in both insulin-sensitive and insulin-resistant conditions. Central administration of exendin-4 in lean mice increased sympathetic outflow towards BAT and white adipose tissue (WAT), resulting in increased thermogenesis as evidenced by increased uncoupling protein 1 (UCP-1) protein levels and decreased lipid content, while the uptake of TG-derived fatty acids was increased in both BAT and WAT. Interestingly, in DIO mice, the effects on WAT were blunted, while exendin-4 still increased sympathetic outflow towards BAT and increased the uptake of plasma TG-derived fatty acids and glucose by BAT. These effects were accompanied by increased fat oxidation, lower plasma TG and glucose concentrations, and reduced body weight. Collectively, our results suggest that BAT activation may be a major contributor to the glucose- and TG-lowering effects of GLP-1R agonism.

Introduction

Glucagon-like peptide-1 (GLP-1) receptor (GLP-1R) agonists, such as exendin-4, have been used in the treatment of type 2 diabetes; they increase glucose-dependent insulin secretion, regulate gastric emptying and reduce food intake and body weight (1). At least some of these actions are mediated through neuroendocrine mechanisms, as shown by rodent studies, consistent with the notion that GLP-1R is highly expressed in the hypothalamus. Intracerebroventricular (i.c.v.) administration of GLP-1 reduces food intake and body weight (2,3). Moreover, the central GLP-1R signalling system is linked to the control of peripheral glucose metabolism by inhibiting non-insulin-mediated glucose uptake by muscle and increasing insulin secretion from the pancreas (4,5). Previously, we have shown that subcutaneous GLP-1 treatment reduces hepatic glucose production in mice, partly through central GLP-1R signalling (6). Hence, one of the functions of the central GLP-1R system is the modulation of the metabolic activity in peripheral organs that are crucial for the maintenance of energy homeostasis.

Brown adipose tissue (BAT) is a regulator of overall energy homeostasis by combusting triacylglycerol (TG) and glucose into heat. Enhancement of the thermogenic capacity of BAT induces weight loss through increased energy expenditure (7,8) and lowers the plasma levels of TG and glucose. In fact, BAT activation can correct hyperlipidaemia (9) and hyperglycemia (10) by increased uptake of TG-derived fatty acids (11) and glucose from plasma. Recently, it has been shown that activation of central GLP-1R increases thermogenesis in BAT and induces browning within white adipose tissue (WAT), and that this correlates with increased expression of genes required for thermogenesis, including uncoupling protein-1 (12,13). While these findings suggest an important role of the central GLP-1R system in BAT activation, the effect of central GLP-1R activation on lipid and glucose control by BAT has not yet been investigated. Furthermore, although GLP-1R agonists are implemented to treat type 2 diabetes, the responsiveness of the central GLP-1R system to activate BAT to take up TG-derived fatty acids and glucose under central insulin resistance (14), is unknown.

The aim of this study was to evaluate the potential of activating central GLP-1R by exendin-4 to facilitate clearance of lipids and glucose from the circulation by activating BAT, under both insulin-sensitive and insulin-resistant conditions in diet-induced obese (DIO) C57Bl/6J mice.

Materials & Methods

Animals

For all experiments, 20-week-old male C57Bl/6J mice (Charles River, Saint-Germain-Nuelles, France) were used, housed with a regular 12:12 h light/dark cycle in a temperature- and humidity-controlled environment, with free access to food and water unless noted otherwise. For diet-induced obesity, mice were fed a high-fat diet (44% energy derived from bovine fat; Hope Farms, Woerden, the Netherlands) for 12 weeks, starting at 8 weeks of age. All animal experiments were performed in accordance with the regulations of the Dutch law on animal welfare, and the Institutional Ethics Committee for Animal Procedures, Leiden University Medical Center, Leiden, the Netherlands, approved the protocol.

Intracerebroventricular surgery and treatment

Mice were randomised based on body weight, anaesthetised and cannulas (Brain Infusion Kit 3, ALZET Cupertino, CA, USA) were stereotactically implanted into the left lateral ventricle of the brain (coordinates -0.45 mm anteroposterior, -1.00 mm lateral and 2.50 mm dorsoventral from bregma). Osmotic minipumps (Model 1004, Alzet, CA, USA) attached to the cannula via a catheter were implanted subcutaneously on the back, slightly posterior to the scapulae. The catheter connected to the osmotic minipump was filled with artificial cerebrospinal fluid (aCSF; Harvard Apparatus, Holliston, MA, USA) to delay the start of drug delivery by 2 days. The minipump assured continuous delivery of 0.75 nmol/day exendin-4 (Bachem, Weil am Rhein, Germany) dissolved in aCSF or aCSF only. The dose of exendin-4 was expected to suppress food intake. Therefore, an aCSF-receiving pair-fed control group (restricted to the same amount of food each day as consumed by the i.c.v. exendin-4-infused mice) was also included. Because of the inclusion of a pair-fed group, blinding to group assignment was not feasible. Body weight and food intake were measured daily. One lean mouse (assigned to exendin-4 group) and three obese mice (assigned to control group) were excluded from the study because of complications after surgery. After 5 days of intervention, TG and glucose clearance was determined as described below.

Triacylglycerol and glucose clearance

Triacylglycerol-rich lipoprotein (TRL)-like particles were prepared from 100 mg of total lipid including glycerol trioleate (triolein; 70 mg), egg yolk phosphatidylcholine (22.7 mg), lysophosphatidylcholine (2.3 mg), cholesteryl oleate (3.0 mg) and cholesterol (2.0 mg), with addition of glycerol tri- ^3H oleate (^3H TO) (3.7 MBq). The emulsion was sonicated and fractionated by consecutive density gradient ultracentrifugation steps (15). The emulsion fraction containing TRL-like particles with an average size 80 nm was isolated and mixed with 2-[1- ^{14}C]deoxy-D-glucose (^{14}C DG) in a 3:1 ratio

based on radioactive count. Emulsions were stored at 4°C under argon and used for in vivo kinetic experiments within 5 days following preparation. Animals were fasted for 4 h. At t=0, blood was drawn via the tail vein to determine, via enzymatic assays, basal plasma TG (Roche Molecular Biochemicals, Indianapolis, IN, USA) and glucose (Instruchemie, Delfzijl, the Netherlands). Mice then received an i.v. injection of TRL-like particles (1 mg TG) and [¹⁴C]DG. Blood samples were taken from the tail vein at 2, 5, 10 and 15 min after injection, and plasma 3H and 14C activities were counted. After the last blood sample, the mice were killed, perfused via the heart with ice-cold PBS and various organs were collected. Organs were dissolved overnight at 60°C in Tissue Solubilizer (Amersham Biosciences, Roosendaal, the Netherlands), and 3H and 14C activities were counted. Uptake of [3H]TO- and [14C]DG-derived radioactivity by the organs was calculated from the 3H and 14C activities in each organ and expressed as percentage of injected dose per g wet tissue weight.

Body composition

After the treatment period, body composition (lean and fat mass) was determined in conscious DIO mice using an EchoMRI-100 (EchoMRI, Houston, TX, USA).

Indirect calorimetry

During the treatment period of the DIO mice, oxygen uptake ($\dot{V}O_2$), carbon dioxide production ($\dot{V}CO_2$) and physical activity were measured in metabolic cages (LabMaster System, TSE Systems, Bad Homburg, Germany). The average respiratory exchange ratio (RER), energy expenditure, carbohydrate and fat oxidation rates were calculated from day 1 to day 4 of treatment, as described previously (16).

Histology

Formalin-fixed paraffin-embedded interscapular BAT (iBAT) and subcutaneous WAT (sWAT) tissue sections (5 µm) were stained with haematoxylin and eosin (H&E) using standard protocols. For staining of UCP-1 and tyrosine hydroxylase (TH), sections were dewaxed, rehydrated and treated with peroxidase. Antigen retrieval was accomplished in 10 mmol/l citrate buffer (pH=6.0). Slides were blocked with normal goat serum (UCP-1) or BSA (TH) and incubated overnight at 4°C with anti-UCP-1 antibodies (1:4,000; Ab10983; Abcam, Cambridge, UK) or anti-TH antibodies (1:2,000; Ab112; Abcam). Next, sections were incubated for 30 min with biotinylated goat α-rabbit secondary antibodies (UCP-1; 1:600; Vector Labs, Burlingame, CA, USA) or DAKO EnVision anti-rabbit antibodies (DAKO, Glostrup, Denmark). Immunostaining was amplified and visualised using the Elite ABC Nova Red kit (Vector Labs). Counterstaining was performed with Mayer's haematoxylin (1:4). The areas occupied by intracellular lipid vacuoles, UCP-1 and TH protein were quantified using ImageJ.

Statistical analysis

Differences between groups were determined with the Kruskal–Wallis non-parametric test. When significant differences were found, the Mann–Whitney nonparametric test was used as a post hoc test to determine differences between two independent groups. Serum decay in the clearance experiment was analysed using repeated measurements ANOVA with Tukey's post hoc test. A p value of <0.05 was considered statistically significant. Data are presented as mean \pm SD.

Results

Central GLP-1R activation decreases body weight and induces BAT activation in lean C57Bl/6J mice

Intracerebroventricular infusion of exendin-4 in lean C57Bl/6J mice decreased body weight as compared with controls (**Figure 1A,B**) this was accompanied by a reduced food intake (**Figure 1C**), both of which are well-known effects of activation of the central GLP-1R system (3,17). Reduction of food intake per se, as shown by the control mice that were pair fed with the exendin-4-treated mice (**Figure 1C**), resulted in a reduction in body weight compared with controls that was delayed compared with that evoked by exendin-4 (**Figure 1A**).

As central GLP-1 infusion increases sympathetic outflow towards BAT and WAT and subsequently stimulates thermogenesis (12,13,18), we analysed the expression of TH, a marker for activity of noradrenergic (norepinephrine) nerve fibres (19). Exendin-4 increased the TH content in both iBAT (+103%; $p<0.01$) and sWAT (+331%; $p<0.05$) as compared to controls (**Figure 1D,E**). This increased sympathetic nervous system (SNS) signalling was accompanied by enhanced thermogenic capacity, as exendin-4 increased UCP-1 protein content in iBAT (+44%, $p<0.01$) and sWAT (+142%, $p<0.05$) compared with the control group (**Figure 1F,G**), indicating more active BAT as well as browning of WAT. Reduction of food intake per se evoked similar increases in UCP-1 protein content in both BAT and WAT, but it was apparently independent of sympathetic input, which suggests the involvement of other pathways. The effects of exendin-4 on UCP-1 content were accompanied by a decreased lipid droplet content in iBAT (–67%, $p<0.001$) and sWAT (–53%, $p<0.05$) (**Figure 1H,I**), probably as activation of BAT results in combustion of intracellular lipid stores as well as browning of WAT. The lipid content in iBAT was reduced to a greater extent in exendin-4-treated mice than in food-restricted mice (–46%, $p<0.05$), which coincided with a higher level of TH, reflecting higher SNS activity towards BAT induced by exendin-4.

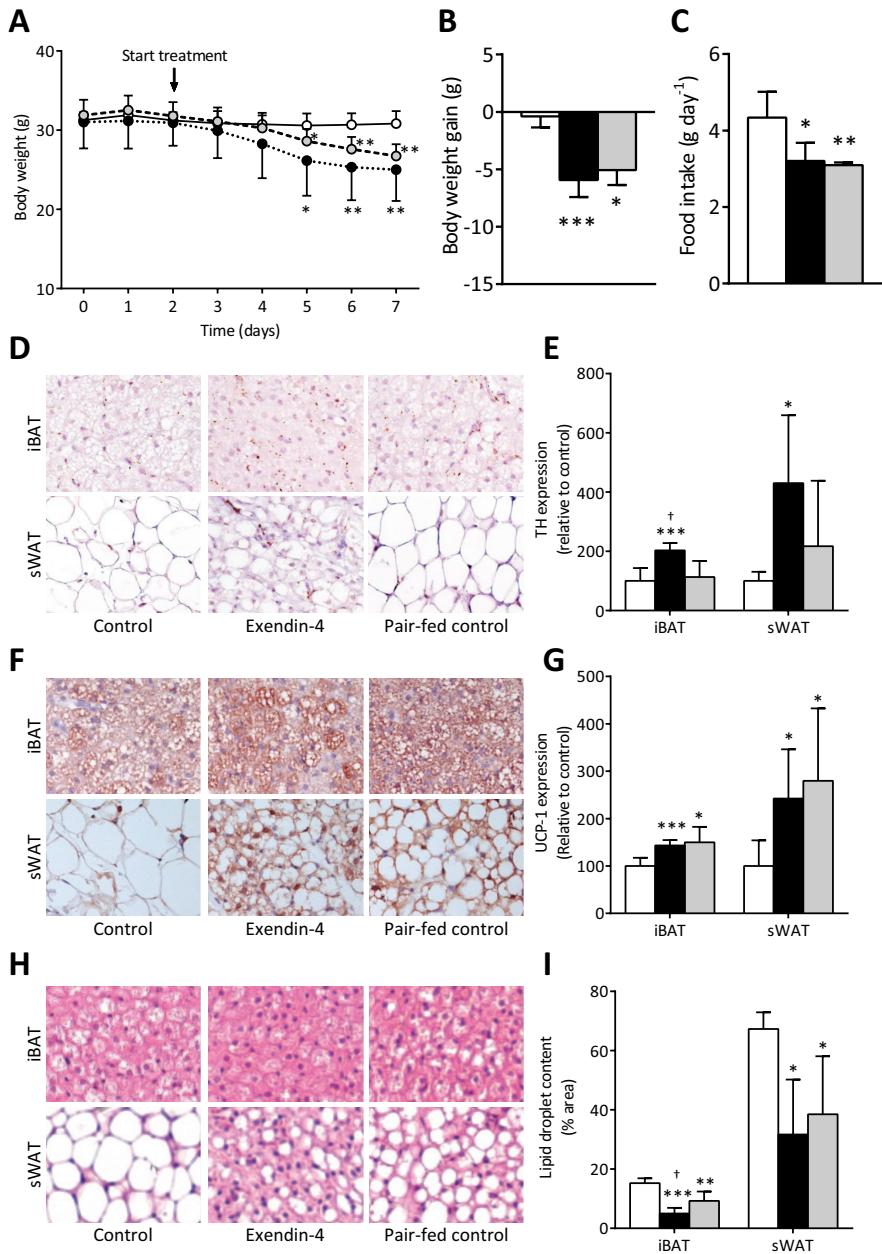


Figure 1 – Central GLP-1R activation decreases body weight and food intake and induces activation of BAT in lean mice. Mice were treated for 5 days with i.c.v. exendin-4 (n=8) or vehicle [control n=9, pair-fed n=6]. On a daily basis, body weight (A,B) and food intake (C) were monitored. Samples of BAT and WAT were collected and stained for TH and UCP-1. Representative pictures and quantification of TH (D,E), UCP-1 (F,G) and lipid droplet content with H&E staining (H,I) are shown. Values are mean ±SD. *p<0.05, **p<0.01 and ***p<0.001 compared with control; †p<0.01 compared with pair-fed control. White bars, control; black bars, exendin-4; grey bars, pair-fed control.

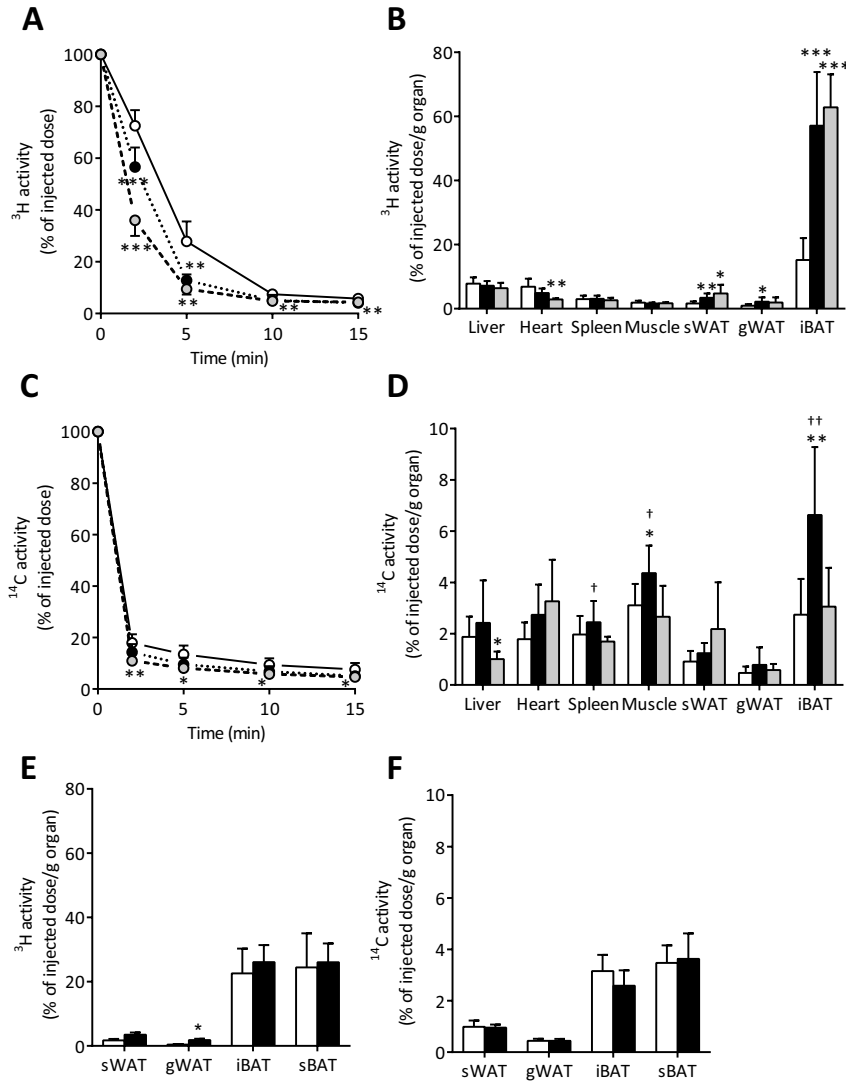


Figure 2 – Central GLP-1R activation increases uptake of plasma TG-derived fatty acids and glucose by BAT in lean mice. Mice were treated for 5 days via i.c.v. [A-D] or i.v. [E-F] routes with exendin-4 (n=8) or vehicle (control n=9, pair-fed n=6). After treatment, mice were injected with [^3H]TJ0-labelled particles and [^{14}C]DG. Plasma 3H activity (A) and 14C activity (C) were plotted relative to the injected dose. At 15 min after injection, organs were isolated and uptake of 3H activity (B,E) and 14C activity (D,F) was determined. Values are mean \pm SD. *p<0.05, **p<0.01 and ***p<0.001 compared with control. †p<0.05 and ††p<0.01 compared with pair-fed control. White bars/circles, control; black bars/circles, exendin-4; grey bars/circles, pair-fed control.

Central GLP-1R activation enhances uptake of plasma TG-derived fatty acids and glucose by BAT and browns WAT in lean C57Bl/6J mice

Subsequently, we tested our hypothesis that BAT activated during chronic GLP-1R activation is a major contributor to the plasma clearance of TG and glucose. To this end, mice were injected i.v. with [^3H]TO-labelled TRL-like emulsion particles and [^{14}C]DG. Indeed, exendin-4 accelerated the clearance of [^3H]TO from plasma (**Figure 2A**). This enhanced clearance was the result of a greatly increased uptake of [^3H]TO-derived activity by iBAT (+276%; $p < 0.001$; **Figure 2B**). In addition, exendin-4 enhanced the uptake of [^3H]TO-derived activity by both sWAT (+111%, $p < 0.01$) and gonadal (g)WAT (+138%, $p < 0.05$) compared with the control group, corresponding to the browning observed in these WAT depots. The pair-fed animals showed similar results for [^3H]TO kinetics as the exendin-4-treated group. Plasma clearance was increased (**Figure 2A**), relating to a marked increase in uptake of ^3H -activity by iBAT as compared with control-infused animals (+314%; $p < 0.001$; **Figure 2B**). In addition, the uptake by sWAT was increased (+194%; $p < 0.05$), whereas there was no significant effect on uptake by gWAT (+109%; $p = 0.20$) in pair fed conditions.

Similar to plasma [^3H]TO clearance, chronic infusion of exendin-4 accelerated the clearance of [^{14}C]DG from plasma (**Figure 2C**). This enhanced clearance from the circulation was the result of an increased uptake of [^{14}C]DG by iBAT (+142%; $p < 0.01$) and skeletal muscle (+40%; $p < 0.05$) compared with controls (**Figure 2D**). Interestingly, while the uptake of [^3H]TO-derived activity by BAT in pair-fed mice was increased to a similar extent as in exendin-4 treated animals, the uptake of [^{14}C]DG by iBAT was not increased in the pair-fed control mice.

To rule out that the effects of i.c.v. administered exendin-4 on the uptake of TG-derived fatty acids and glucose by BAT were caused by leakage of exendin-4 into the circulation, we next administered exendin-4 peripherally at the same dose as administered centrally. Peripheral exendin-4 treatment for 5 days delivered via subcutaneous minipumps did not enhance the uptake of [^3H]TO-derived activity (**Figure 2E**) or [^{14}C]DG (**Figure 2F**) by BAT. Peripheral exendin-4 only slightly increased the uptake of [^3H]TO-derived activity by gWAT, possibly via a direct effect of GLP-1R signalling on white adipocyte formation [20].

Central GLP-1R activation decreases body weight, plasma TG and glucose levels, and shifts combustion from carbohydrates towards fat in DIO C57Bl/6J mice

Whether chronic i.c.v. exendin-4 infusion still leads to an increased uptake of plasma TG-derived fatty acids and glucose via BAT when obesity and insulin resistance have developed, we next explored the effects of central GLP-1R activation after 12 weeks of high-fat feeding. In DIO mice, continuous infusion of exendin-4 for 5 days decreased

body weight compared with control-infused mice (**Figure 3A**), which could only partly be attributed to reduced food intake (**Figure 3B**) as the reduction in body weight was greater than in pair-fed controls. Determination of body composition showed that exendin-4 and pair feeding decreased body weight because of a selective decrease in fat mass compared with controls (**Figure 3C**). Furthermore, plasma TG and glucose levels were both decreased from baseline values in the exendin-4-infused mice at the end of the treatment period (**Table 1**). In the pair-fed mice, plasma glucose levels were reduced from baseline values, but remained significantly higher than in the exendin-4-treated mice.

Indirect calorimetry showed that the decreased fat mass in the exendin-4-infused DIO mice was accompanied by an increased fat oxidation (**Figure 3D**) at the expense of carbohydrate oxidation (**Figure 3E**). This was also reflected by a decreased RER (**Figure 3F**) compared with controls, suggesting a shift in nutrient combustion. Of note, exendin-4 reduced total energy expenditure (**Figure 3G**) and decreased physical activity (**Figure 3H**). Pair feeding also increased fat oxidation and decreased carbohydrate oxidation compared with the controls, but these effects were less pronounced than those of exendin-4. This implies that the effects of exendin-4 on energy metabolism are only partly caused by reduced food intake in DIO mice.

Table 1 – Central GLP-1R activation decreases plasma TG and glucose levels in DIO mice

		Control	Exendin-4	Pair fed Control
TG (mmol/l)	Start	0.7 ± 0.1	0.7 ± 0.1	0.6 ± 0.1
	End	0.7 ± 0.5	0.5 ± 0.2*	0.6 ± 0.4
Glucose (mmol/l)	Start	11.3 ± 0.8	11.6 ± 1.1	11.4 ± 1.1
	End	10.6 ± 0.9	4.5 ± 1.2****	7.4 ± 1.1***

After 12 weeks of high-fat feeding, mice were treated for 5 days with i.c.v. exendin-4 (n=10) or vehicle (control n=6, pair-fed n=9). Blood was collected before and after treatment by tail bleeding after 4 h of fasting and plasma TG and glucose were determined. Values are mean ±SD *p<0.05 and ***p<0.001 compared with baseline; †††p<0.001 compared with pair-fed control.

Central GLP-1R activation increases BAT thermogenesis, but does not induce browning of WAT in DIO C57Bl/6J mice

Under high-fat-fed conditions, i.c.v. exendin-4 treatment still increased SNS output towards BAT compared with controls, reflected by increased TH content (sBAT: +59%; p<0.05 [not shown], iBAT: +107%; p<0.01, **Figure 4A,B**) and increased UCP-1 protein content (sBAT: +62%; p<0.001 [not shown], iBAT: +93%; p<0.01, **Figure 4C,D**), indicative of more active BAT. As a consequence, lipid droplet content was decreased in the exendin-4 treated animals compared with controls (sBAT: -49%; p<0.05, iBAT: -41%; p<0.01, **Figure 4E,F**). Pair fed feeding did not affect TH expression in BAT (**Figure 4A,B**), slightly increased UCP-1 protein content (**Figure 4C,D**) and slightly

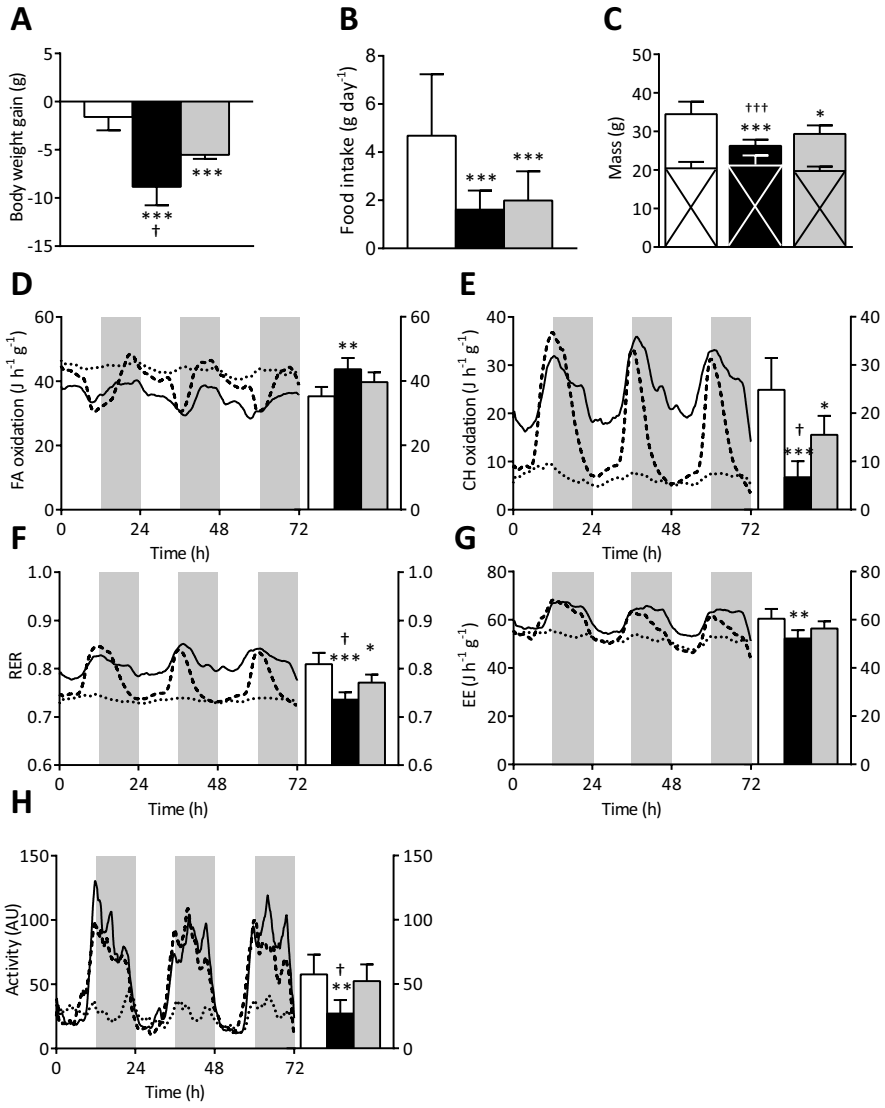


Figure 3 – Central GLP-1R activation decreases body weight and shifts combustion from carbohydrates towards fat in DIO mice. After 12 weeks of high-fat feeding, mice were treated for 5 days with i.c.v. exendin-4 (n=10) or vehicle (control n=6, pair-fed n=9). Body weight gain (A) and food intake (B) were determined. Lean (crossed area) and fat (no cross) mass were measured (C). During the treatment period, mice were housed in metabolic cages. Fatty acid oxidation (D), carbohydrate oxidation (E), RER (F) and energy expenditure (G) were calculated from O2 uptake and CO2 excretion. (H) Magnitude of physical activity in arbitrary units. Values are mean ±SD. *p<0.05, **p<0.01 and ***p<0.001 compared with control. †p<0.05 and †††p<0.001 compared with pair-fed control. White bars/continuous lines, control; black bars/dotted lines, exendin-4; grey bars/dashed lines, pair-fed controls. AU, arbitrary units; CH, carbohydrate; EE, energy expenditure; FA, fatty acid.

decreased lipid content (**Figure 4E,F**) compared with controls. In contrast to the lean mice, infusion of exendin-4 in DIO mice did not induce browning of WAT as evidenced by unaffected TH expression, UCP-1 protein and lipid content.

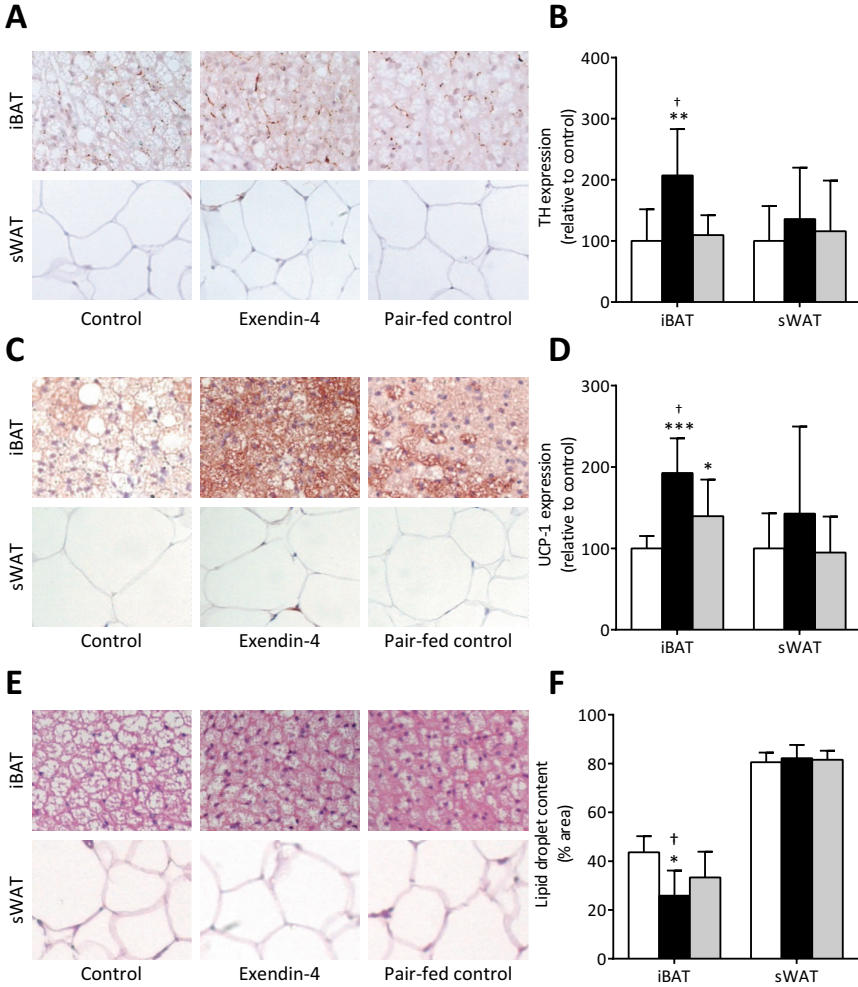


Figure 4 – Central GLP-1R activation increases TH and UCP-1 protein levels and decreases lipid droplet content in BAT in DIO mice. After 12 weeks of high-fat feeding, mice were treated for 5 days with i.c.v. exendin-4 (n=10) or vehicle (control n=6, pair-fed n=9). After treatment, mice were killed and BAT and WAT were collected and stained for TH and UCP-1. Staining with H&E was performed for lipid droplet content. Representative pictures and quantification of TH (**A,B**), UCP-1 (**C,D**) and lipid droplet content (**E,F**) are shown. Values are mean \pm SD. * p <0.05, ** p <0.01 and *** p <0.001 compared with control. † p <0.01 compared with pair-fed control. White bars, control; black bars, exendin-4; grey bars, pair-fed control.

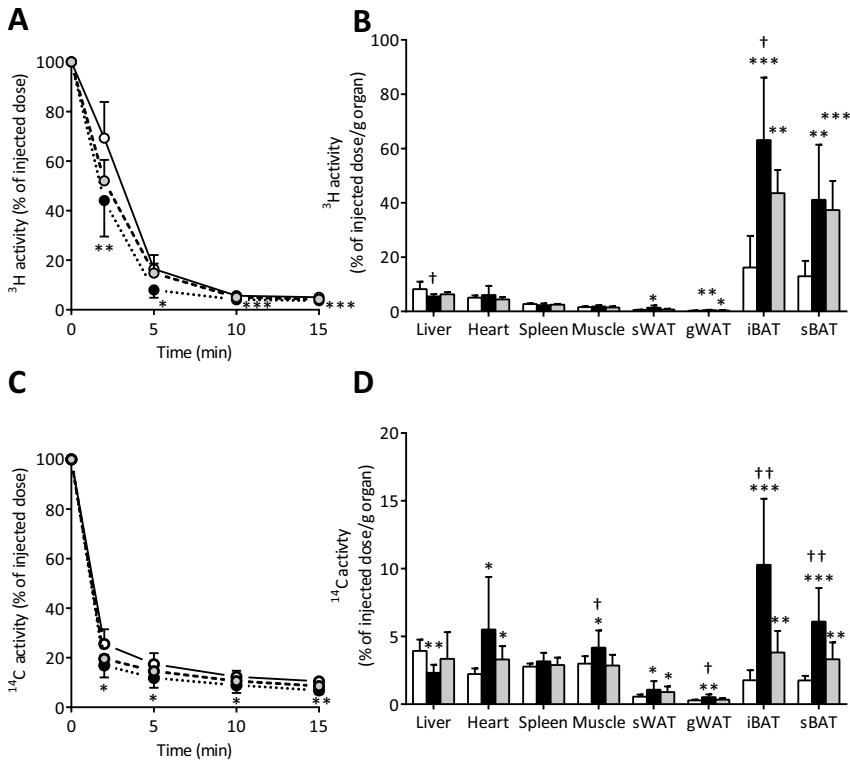


Figure 5 – Central GLP-1R activation increases uptake of plasma TG-derived fatty acids and glucose by BAT in DIO mice. After 12 weeks of high-fat feeding, mice were treated for 5 days with i.c.v. exendin-4 (n=10) or vehicle (control n=6, pair-fed n=9). After treatment, mice were injected with [³H]T0 labelled particles and [¹⁴C]DG. Plasma ³H activity (A) and ¹⁴C activity (C) were plotted relative to the injected dose. At 15 min after injection, organs were isolated and uptake of the ³H activity (B) and ¹⁴C activity (D) was determined. Values are mean ±SD. *p<0.05, **p<0.01 and ***p<0.001 compared with control. †p<0.05 and ††p<0.01 compared with pair-fed control. White bars, control; black bars, exendin-4; grey bars, pair-fed control.

Central GLP-1R activation enhances TG and glucose clearance by BAT in DIO C57Bl/6J mice

Similar to lean mice, chronic i.c.v. infusion of exendin-4 in DIO mice accelerated the plasma clearance of [³H]T0 (Figure 5A) and [¹⁴C]DG (Figure 5C). This was accompanied by a selectively increased uptake of [³H]T0-derived activity and [¹⁴C]DG by iBAT (+291%; p<0.001 and +482%; p<0.001, respectively) and sBAT (+217%; p<0.01 and +247%; p<0.001, respectively) (Fig 5B,D). Despite lack of evidence for browning of WAT, exendin-4 enhanced the uptake of both [³H]T0-derived activity and [¹⁴C]DG by both sWAT (+146%; p<0.05 and +93%; p<0.05) and gWAT (+69%; p<0.01 and +82%; p<0.01). To some extent, the pair fed animals showed similar results on [³H]T0 and

[¹⁴C]DG kinetics as the exendin-4 treated mice. Plasma clearance was increased (**Figure 5A,C**), associated with a marked increase in uptake of [³H]TO-derived activity and [¹⁴C]DG by iBAT (+170%; $p < 0.01$ and +482%; $p < 0.001$, respectively) and sBAT (+188%; $p < 0.001$ and +247%; $p < 0.001$ respectively) compared with control infused animals (**Figure 5B,D**). Interestingly, the uptake of [³H]TO-derived activity by iBAT and the uptake of [¹⁴C]DG by iBAT and sBAT were significantly lower compared with exendin-4 treated mice (-31%; $p < 0.05$, -63%; $p < 0.01$, and -43%; $p < 0.01$ respectively), indicating that exendin-4 exerts its effects partly independent of lowering food intake.

Discussion

In the present study we show that central GLP-1R activation by exendin-4 increases the plasma clearance of TG and glucose in both lean and DIO C57Bl/6J mice via increased uptake of TG-derived fatty acids and glucose by BAT, accompanied by activation of BAT and browning of WAT.

First, we showed that continuous central infusion of the GLP-1R analogue exendin-4 (5 days, 0.75 nmol/day) evokes the well-known effect of reducing food intake and body weight (3,17). In addition, central administration of exendin-4 increased SNS activity towards BAT and WAT, as evidenced by increased TH and UCP-1 protein content and lowered lipid content. This corroborates previous findings demonstrating the essential role of the SNS in BAT and WAT activation by central GLP-1R signalling (12,18). Exendin-4 also caused a robustly accelerated clearance of plasma TG and glucose, which likely contributed to reduced plasma TG and glucose concentrations observed in DIO mice. Strikingly, the uptake of TG-derived activity, presumably [³H]oleate liberated by lipoprotein lipase (LPL) (11), was not only increased by BAT but also by WAT, together with the increase in UCP-1 content indicative of so-called browning. Although activation of BAT and WAT are likely involved in the observed reduction of plasma TG and glucose by central exendin-4, further studies are warranted to investigate the quantitative contribution of GLP-1R signalling towards BAT and WAT to the overall metabolic improvements on GLP-1R agonism.

It has been reported that central GLP-1 infusion reduces the lipid content of WAT in lean mice but not DIO mice (18), suggesting that some resistance to the actions of central GLP-1 is induced in DIO mice. Clearly, this effect is not desirable for a drug to treat obesity. Therefore, we explored the effects of chronic central exendin-4 infusion after 12 weeks of high-fat feeding, sufficient to induce obesity and insulin resistance in this mouse model (21,22). Our results show that under these conditions, chronic central GLP-1R signalling still improves the clearance of plasma TG and glucose via a robustly increased uptake by BAT. However, central GLP-1R agonism did not alter

UCP-1 protein content or lipid droplet content in WAT in DIO mice, consistent with previous findings by Nogueiras et al (18). It is interesting to speculate on why, during obesity, WAT is not susceptible to browning on exendin-4 treatment. Previous studies reported a decreased sensitivity of white adipocytes to adrenergic stimulation in obese individuals (23). However, in our study we also describe the absence of exendin-4-induced TH expression in WAT in DIO mice. It is possible that different brain areas modulate specific BAT and WAT functions. While multiple tissues are simultaneously sympathetically stimulated during cold exposure, there are many examples of treatments that result in differential sympathetic outflow to various types of tissues (e.g. WAT vs BAT) and even within a type of tissue (e.g. different WAT pads) (24). The GLP-1R is widely expressed through the hypothalamus (25), and exerts effects via different nuclei. For example, GLP-1R signalling in the arcuate nucleus regulates glucose metabolism, while it modulates feeding via the paraventricular nucleus (5). Altogether, it is likely that GLP-1R signalling and subsequent sympathetic outflow differ during obesity and lean conditions.

In apparent contrast to the notion that increased BAT activity is generally correlated with an enhanced total energy expenditure (26), central GLP-1R activation in fact reduced total energy expenditure, an effect we have observed before during chronic peripheral exendin-4 treatment (27). Possibly, the reduction in energy intake is compensated by a relative reduction in energy expenditure. In addition, it appears that chronic central GLP-1R activation results in a shift from using carbohydrates to fatty acids as an energy source, which is consistent with previous studies that showed that chronic i.c.v. GLP-1 treatment decreased the respiratory quotient, indicative of a higher level of fat oxidation by BAT (18,28). The exendin-4-induced decrease in physical activity, resulting from a diminished food-seeking behaviour (29), is less likely to contribute to the change in total energy expenditure (30).

From a clinical perspective, the possibility that BAT activity in humans may be amenable to pharmacological manipulation by GLP-1R agonism to control insulin sensitivity and body weight is attractive but, as yet, undemonstrated. Drugs targeting the GLP-1R system are already widely prescribed for their incretin properties to treat type 2 diabetes, but they may be useful in a wider context related to energy balance. The resting energy expenditure of obese individuals with type 2 diabetes increases with 1 year of treatment with a combination of metformin and exenatide or liraglutide (13). It is tempting to speculate that BAT may be activated in these patients. Increasing our knowledge about the mechanism of action of exendin-4 may add to the (further) development of peptidomimetics in our battle against obesity and type 2 diabetes.

In conclusion, our results show that chronic central infusion of exendin-4 increases SNS output to enhance BAT activity in both lean and DIO C57Bl/6J mice. Via highly active BAT, the plasma clearance of TG and glucose is accelerated and body fat

content is decreased, which, together with reduced food intake, leads to a decrease in body weight. Therefore, we suggest that GLP-1R agonists via BAT activation reduce both hyperlipidaemia and hyperglycaemia, and possibly even atherosclerosis (31), in addition to the effects of BAT activation on obesity.

Acknowledgements

We acknowledge the support from the Netherlands CardioVascular Research Initiative: 'the Dutch Heart Foundation, Dutch Federation of University Medical Centers, the Netherlands Organisation for Health Research and Development and the Royal Netherlands Academy of Sciences' for the GENIUS project 'Generating the best evidence-based pharmaceutical targets for atherosclerosis' (CVON2011-19). MR Boon was supported by a grant from the Board of Directors of LUMC and is supported by a Rubicon grant from ZonMW (825.13.021). PCN Rensen is an Established Investigator of the Netherlands Heart Foundation (grant 2009T038).

References

1. Gallwitz, B. (2011) Glucagon-like peptide-1 analogues for Type 2 diabetes mellitus: current and emerging agents. *Drugs* 71, 1675-1688.
2. Hwa, J. J., Ghibaudi, L., Williams, P. *et al.* (1998) Differential effects of intracerebroventricular glucagon-like peptide-1 on feeding and energy expenditure regulation. *Peptides* 19, 869-875.
3. Turton, M. D., O'Shea, D., Gunn, I. *et al.* (1996) A role for glucagon-like peptide-1 in the central regulation of feeding. *Nature* 379, 69-72.
4. Knauf, C., Cani, P. D., Perrin, C. *et al.* (2005) Brain glucagon-like peptide-1 increases insulin secretion and muscle insulin resistance to favor hepatic glycogen storage. *J Clin Invest* 115, 3554-3563.
5. Sandoval, D. A., Bagnol, D., Woods, S. C. *et al.* (2008) Arcuate glucagon-like peptide 1 receptors regulate glucose homeostasis but not food intake. *Diabetes* 57, 2046-2054.
6. Parlevliet, E. T., de Leeuw van Weenen JE, Romijn, J. A. *et al.* (2010) GLP-1 treatment reduces endogenous insulin resistance via activation of central GLP-1 receptors in mice fed a high-fat diet. *Am J Physiol Endocrinol Metab* 299, E318-E324.
7. Boon, M. R., van den Berg, S. A., Wang, Y. *et al.* (2013) BMP7 activates brown adipose tissue and reduces diet-induced obesity only at subthermoneutrality. *PLoS One* 8, e74083.
8. Geerling, J. J., Boon, M. R., van der Zon, G. C. *et al.* (2014) Metformin lowers plasma triglycerides by promoting VLDL-triglyceride clearance by brown adipose tissue in mice. *Diabetes* 63, 880-891.
9. Bartelt, A., Bruns, O. T., Reimer, R. *et al.* (2011) Brown adipose tissue activity controls triglyceride clearance. *Nat Med* 17, 200-205.
10. Emanuelli, B., Vienberg, S. G., Smyth, G. *et al.* (2014) Interplay between FGF21 and insulin action in the liver regulates metabolism. *J Clin Invest* 124, 515-527.
11. Khedoe, P. P., Hoeke, G., Kooijman, S. *et al.* (2015) Brown adipose tissue takes up plasma triglycerides mostly after lipolysis. *J Lipid Res* 56, 51-59.
12. Lockie, S. H., Heppner, K. M., Chaudhary, N. *et al.* (2012) Direct control of brown adipose tissue thermogenesis by central nervous system glucagon-like Peptide-1 receptor signaling. *Diabetes* 61, 2753-2762.
13. Beiroa, D., Imbernon, M., Gallego, R. *et al.* (2014) GLP-1 Agonism Stimulates Brown Adipose Tissue Thermogenesis and Browning Through Hypothalamic AMPK. *Diabetes* 63, 3346-58.
14. Coomans, C. P., Biermasz, N. R., Geerling, J. J. *et al.* (2011) Stimulatory effect of insulin on glucose uptake by muscle involves the central nervous system in insulin-sensitive mice. *Diabetes* 60, 3132-3140.
15. Rensen, P. C., Herijgers, N., Netscher, M. H. *et al.* (1997) Particle size determines the specificity of apolipoprotein E-containing triglyceride-rich emulsions for the LDL receptor versus hepatic remnant receptor in vivo. *J Lipid Res* 38, 1070-1084.
16. Van Klinken, J. B., van den Berg, S. A., Havekes, L. M. *et al.* (2012) Estimation of activity related energy expenditure and resting metabolic rate in freely moving mice from indirect calorimetry data. *PLoS One* 7, e36162.
17. Al-Barazanji, K. A., Arch, J. R., Buckingham, R. E. *et al.* (2000) Central extendin-4 infusion reduces body weight without altering plasma leptin in (fa/fa) Zucker rats. *Obes Res* 8, 317-323.
18. Nogueiras, R., Perez-Tilve, D., Veyrat-Durebex, C. *et al.* (2009) Direct control of peripheral lipid deposition by CNS GLP-1 receptor signaling is mediated by the sympathetic nervous system and blunted in diet-induced obesity. *J Neurosci* 29, 5916-5925.
19. Giordano, A., Frontini, A., & Cinti, S. (2008) Adipose organ nerves revealed by immunohistochemistry. *Methods Mol Biol* 456, 83-95.
20. Challa, T. D., Beaton, N., Arnold, M. *et al.* (2012) Regulation of adipocyte formation by GLP-1/GLP-1R signaling. *J Biol Chem* 287, 6421-6430.
21. Korshennnikova, E., van der Zon, G. C., Voshol, P. J. *et al.* (2006) Sustained activation of the mammalian target of rapamycin nutrient sensing pathway

- is associated with hepatic insulin resistance, but not with steatosis, in mice. *Diabetologia* 49, 3049-3057.
22. Surwit, R. S., Kuhn, C. M., Cochrane, C. *et al.* (1988) Diet-induced type II diabetes in C57BL/6J mice. *Diabetes* 37, 1163-1167.
 23. van Baak, M. A. (2001) The peripheral sympathetic nervous system in human obesity. *Obes Rev* 2, 3-14.
 24. Bartness, T. J. & Song, C. K. (2007) Brain-adipose tissue neural crosstalk. *Physiol Behav* 91, 343-351.
 25. Goke, R., Larsen, P. J., Mikkelsen, J. D. *et al.* (1995) Distribution of GLP-1 binding sites in the rat brain: evidence that exendin-4 is a ligand of brain GLP-1 binding sites. *Eur J Neurosci* 7, 2294-2300.
 26. Cannon, B. & Nedergaard, J. (2004) Brown adipose tissue: function and physiological significance. *Physiol Rev* 84, 277-359.
 27. Parlevliet, E. T., Wang, Y., Geerling, J. J. *et al.* (2012) GLP-1 Receptor Activation Inhibits VLDL Production and Reverses Hepatic Steatosis by Decreasing Hepatic Lipogenesis in High-Fat-Fed APOE*3-Leiden Mice. *PLoS One* 7, e49152.
 28. Tachibana, T., Oikawa, D., Adachi, N. *et al.* (2007) Intracerebroventricular injection of glucagon-like peptide-1 changes lipid metabolism in chicks. *Comp Biochem Physiol A Mol Integr Physiol* 147, 1104-1108.
 29. Dickson, S. L., Shirazi, R. H., Hansson, C. *et al.* (2012) The glucagon-like peptide 1 (GLP-1) analogue, exendin-4, decreases the rewarding value of food: a new role for mesolimbic GLP-1 receptors. *J Neurosci* 32, 4812-4820.
 30. Virtue, S., Even, P., & Vidal-Puig, A. (2012) Below thermoneutrality, changes in activity do not drive changes in total daily energy expenditure between groups of mice. *Cell Metab* 16, 665-671.
 31. Berbee, J. F., Boon, M. R., Khedoe, P. P. *et al.* (2015) Brown fat activation reduces hypercholesterolaemia and protects from atherosclerosis development. *Nat Commun* 6, 6356.

4

PROLONGED DAILY LIGHT EXPOSURE INCREASES BODY FAT MASS THROUGH ATTENUATION OF BROWN ADIPOSE TISSUE ACTIVITY

Sander Kooijman*

Rosa van den Berg*

Ashna Ramkisoensing

Mariëtte R. Boon

Eline N. Kuipers

Marieke Loef

Tom C.M. Zonneveld

Eliane A. Lucassen

Hetty C.M. Sips

Iliana A. Chatzisprou

Riekelt H. Houtkooper

Johanna H. Meijer

Claudia P. Coomans

Nienke R. Biermasz†

Patrick C.N. Rensent

*Authors contributed equally

†Authors share last authorship

Abstract

4

Disruption of circadian rhythmicity is associated with obesity and related disorders including type 2 diabetes and cardiovascular disease. Specifically, prolonged artificial light exposure associates with obesity in humans, although the underlying mechanism is unclear. Here, we report that increasing the daily hours of light exposure increases body adiposity through attenuation of brown adipose tissue (BAT) activity, a major contributor of energy expenditure. Mice exposed to a prolonged day length of 16 h and 24 h light, compared to regular 12 h light, showed increased adiposity without affecting food intake or locomotor activity. Mechanistically, we demonstrated that prolonged day length decreases sympathetic input into BAT and reduces β 3-adrenergic intracellular signalling. Concomitantly, prolonging day length decreased the uptake of fatty acids from triglyceride-rich lipoproteins as well as of glucose from plasma selectively by BAT. We conclude that impaired BAT activity is an important mediator in the association between disturbed circadian rhythm and adiposity and anticipate that activation of BAT may overcome the adverse metabolic consequences of disturbed circadian rhythmicity.

Introduction

Modern world society is subjected to disturbances of circadian rhythms by shift work, sleep deprivation and environmental light pollution. Importantly, increasing prevalence of obesity is associated with disrupted sleep-wake pattern in humans (1) and coincides with the availability of artificial light (2,3). Additionally, a recent study revealed a relationship between exposure to light at night and obesity in a cross-sectional analysis of over 100,000 women (4). Light input is the most important cue for generation of circadian (~24 h) rhythms by the master clock. Both in rodents and humans the master clock is situated in the suprachiasmatic nucleus (SCN) of the hypothalamus. The SCN is responsible for synchronization of peripheral clocks throughout the body, which is mediated by endocrine and neuronal signals (5). A causal role for a disturbed circadian rhythm in the development of obesity has been demonstrated by animal studies. Mice with genetically dysfunctional clock genes develop obesity and insulin resistance (6-9). Moreover, specific ablation of the SCN induces acute weight gain (10). These results indicate a crucial role for the SCN in the regulation of adiposity.

Interestingly, we previously showed that prolonged light exposure only is sufficient to enhance weight gain in mice. Constant light disrupts the central circadian clock, evidenced by an immediate reduction in the circadian amplitude of SCN electrical activity. Moreover, constant light induces body weight gain and insulin resistance, even faster than high-fat diet, which was not due to increased food intake or reduced locomotor activity (11). Therefore, disruption of the central biological clock likely induces weight gain by decreasing energy expenditure.

Recently, it has been recognized that brown adipose tissue (BAT) importantly contributes to energy expenditure. BAT combusts high amounts of triglycerides (TG) into heat, a process called thermogenesis that is mediated by uncoupling protein 1 (UCP1). Interestingly, SCN neurons project onto BAT and injection of glutamate into the SCN increases BAT thermogenesis in rats (12,13). This indicates that BAT may mediate the association between circadian rhythmicity and energy expenditure. Therefore, the aim of this study was to shed light on the association between prolonged light exposure and obesity in humans by investigating the effect of day length on BAT activity in mice in relation to body fat gain, independent of ambient temperature. We demonstrate that daily light exposure negatively associates with the uptake of TG-derived fatty acids and glucose from plasma by BAT, pointing to decreased activity of the tissue. Furthermore, we show that increasing daily light exposure decreases BAT activity through reduced sympathetic stimulation.

Materials & Methods

Animal study

All animal experiments were approved by the institutional ethics committee on animal care and experimentation at Leiden University Medical Center (LUMC), Leiden, The Netherlands. 9-12 week old male C57Bl/6J mice (Charles River) were single housed in clear plastic cages within light-tight cabinets at constant room temperature of 22°C. Stable temperature inside the light-tight cabinets was verified in 12 h vs. 24 h light conditions. The cages were illuminated with white fluorescent light with an intensity of approximately 85 $\mu\text{W}/\text{cm}^2$. Before start of the experiment, mice were kept on a regular 12:12 light-dark cycle. Mice had *ad libitum* access to standard laboratory chow (Special Diets Services, UK) and water throughout experiments. Mice were matched on body weight and light intervention consisted of subjecting mice to either 12, 16 or 24 h light exposure per day (i.e. 24 h) for the duration of five weeks (n= 9).

In a second study, mice were randomized to either bilateral selective sympathetic denervation (n=17) of iBAT or sham surgery (n=6). Mice were anesthetized (isoflurane inhalation) and a midline incision of the skin was made, exposing both iBAT pads. Sympathetic branches were visualized and cut on both sides. Wounds were closed and mice received post-operative analgesia (0.03 mg/kg buprenorphine, Temgesic, Merck). Successful denervation was confirmed retrospectively by absence of TH in iBAT sections (see below). After four days of recovery, mice that underwent denervation were randomized based on body weight and exposed to 12, 16, or 24 h light per day for five weeks while sham operated mice were exposed to 12 h light per day and served as a reference group.

Body composition, food intake and locomotor activity

At the end of the experiment, body weight was measured and body composition (i.e., lean mass and fat mass) was determined in conscious mice using an EchoMRI-100 (EchoMRI, Houston, Texas). Food intake was monitored by weighing food on lids either during last two weeks of light intervention or throughout the five weeks of light exposure (denervation experiment). Behavioural activity of mice was assessed with passive infrared detectors and recorded using Actimetrics software (Wilmette, IL, USA).

TG and glucose clearance

At the end of the experiments, the clearance of TG and glucose was assessed. Glycerol tri[^3H]oleate ([^3H]TO) labeled VLDL-like emulsion particles (80 nm) were prepared as previously described [14] and [^{14}C]deoxyglucose ([^{14}C]DG) was added (ratio $^3\text{H}:^{14}\text{C} = 6:1$). After 5 weeks of light intervention, mice were fasted for 4 h (9AM

to 1PM clock time, corresponding to Zeitgeber time (ZT) 2-6 for 12 h group and ZT 4-8 for 16 h group) and intravenously injected with the radiolabeled emulsion particles (1.0 mg TG in 200 μ L PBS) and glucose via the tail vein. At time points $t=2, 5, 10$ and 15 min after injection, blood was taken from the tail vein to determine the serum decay of both radiolabels. Immediately after the last blood withdrawal, mice were euthanized by cervical dislocation and perfused with ice-cold PBS for 5 min. Organs were harvested, weighed, and the uptake of ^3H and ^{14}C radioactivity was determined.

Histology

Formalin-fixed paraffin-embedded iBAT and gWAT sections were cut ($5 \mu\text{m}$). To determine gWAT cell size, sections were stained with Mayer's haematoxylin and eosin. White adipocyte size was quantified using ImageJ software. To determine sympathetic activation of iBAT a TH staining was performed. Sections were rehydrated and incubated 15 min with 10 mM citrate buffer (pH 6.0) at 120°C for antigen retrieval. Sections were blocked with 5% BSA/PBS followed by overnight incubation with anti-TH antibody (1:2000, AB-112, Abcam) at 4°C . Next, sections were incubated with a secondary antibody (anti-rabbit antibody, DAKO enVision), stained with Nova Red and counterstained with Mayer's haematoxylin. Percentage of area positive for TH staining was quantified using Image J software.

Gene expression analysis and mitochondrial assays

A part of iBAT and sBAT was snap frozen and stored at -80°C for gene expression analysis and protein analysis (see below). Total RNA was isolated using TriPure (Roche) according to the manufacturer's instructions. $1 \mu\text{g}$ of total RNA was reverse-transcribed using M-MLV reverse transcriptase (Promega, Madison, WI, USA). Real-time PCR was carried out on a CFX96 PCR machine (Bio-Rad) using IQ SYBR-Green Supermix (Bio-Rad). Expression levels were normalized to *36B4* as housekeeping gene. Expression of mitochondrial genes was measured with quantitative PCR on a Roche Lightcycler 480 using Roche SYBR-green mastermix, using mitochondrial specific primers (Table S1). Mitochondrial DNA (mtDNA) abundance was quantified as described before (15). In short, total DNA was extracted from sBAT tissue, using the QIAamp DSP DNA Mini Kit (Qiagen). Citrate synthase activity was measured in sBAT tissue as described before (16).

Western blot analysis

The iBAT samples stored at -80°C were homogenized in lysis buffer. Samples were diluted and denatured for 5 min at 95°C after adding Laemmli Sample Buffer (1:1, vol/vol; Serva, Heidelberg, Germany). Proteins within homogenates ($15 \mu\text{g}$) were separated on a 10% SDS-page gel and subsequently transferred onto blotting membranes. The blotting membranes were blocked with 5% milk powder and

incubated overnight at 4°C with the primary antibody β -actin, pCREB, pAMPK or pHS1 S565 (Cell Signaling). Secondary antibody (anti-rabbit IgG HRP conjugate; 1:5000; Promega, Madison, WI, USA) was added and SuperSignal Western Blot Enhancer (Thermo Scientific, Rockford, IL, USA) was used to visualize protein bands. Blots were analysed with Bio-Rad Quantity One and normalized to β -actin.

Statistical analysis

Data are presented as means \pm SEM. Correlations between two dependent variables were made using Pearson's correlation. Associations of variables with day length were assessed by linear regression analysis. Differences between groups were determined using T-tests for normally distributed data. Contribution of light exposure as a covariate to body weight gain was analysed by mixed model analysis using IBM SPSS Statistics version 20. To assess behavioural activity, actograms were analysed using Clock lab and rhythmicity F periodogram analysis was performed on activity bins of 10 minutes of the last 10 consecutively recorded days, based on the algorithm of Dörrscheidt and Beck (17). Differences at P values < 0.05 were considered statistically significant.

Results

Entrainment to light schedules

Male 12 week old C57Bl/6J mice, fed *ad libitum* a regular chow diet, were exposed to daily light exposure of either 12 h, 16 h or to 24 h during 5 weeks at a constant ambient temperature of 22°C. During the last 2 weeks of light intervention, circadian rhythm in behavioural activity was assessed in their home cages. As compared to a day length of 12 h (**Supplemental Figure 1A**), mice exposed to a day length of 16 h showed a retained circadian (24 h) rhythm in behavioural activity, with high activity during night-time (**Supplemental Figure 1B**). In contrast, circadian rhythmicity of behavioural activity was largely reduced in mice exposed to constant light (**Supplemental Figure 1C**).

Prolonged daily light exposure increases adiposity without increasing food intake

After 5 weeks of light intervention, body weight was determined and body composition was assessed by EchoMRI. Prolonged light exposure did not significantly increase total body weight (**Figure 1A**) or lean mass (**Figure 1B**). Interestingly, we observed a daily light exposure-dependent increase in fat mass which reached significance for 24 h *versus* 12 h exposure (+57%; $p=0.01$; **Figure 1C**). In fact, duration of light exposure positively correlated with the body fat mass ($\beta=0.053$; $r^2=0.21$; $p=0.02$) (**Figure 1D**). Mixed model analysis of weekly body weight development showed that light exposure

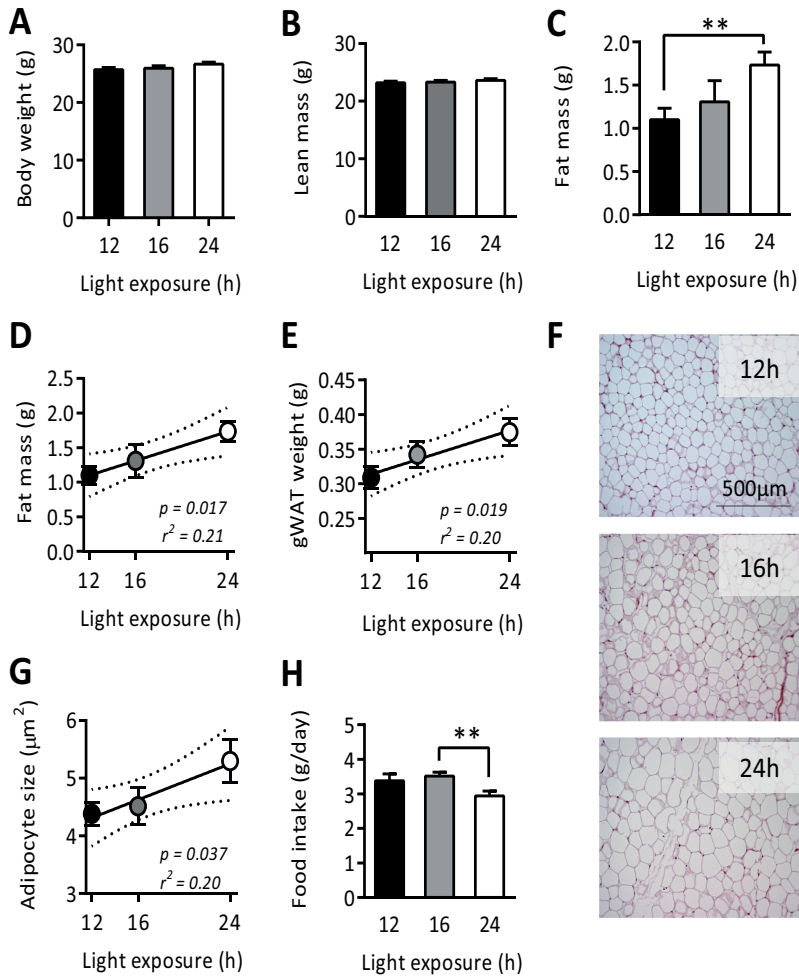


Figure 1 – Mice were exposed to either 12, 16 or 24 h light ($n = 9$) for 5 weeks, and body weight (A), lean mass (B) and fat mass (C) were determined. Correlations are depicted between the light exposure period and total fat mass (D), gWAT weight (E) and adipocyte size in gWAT (G). Representative images of gWAT stained with haematoxylin and eosin are shown (F). Food intake of the last two weeks of light intervention was measured (H). Data are presented as means \pm SEM. Dotted lines represent 95% confidence interval of the regression line. ** $p < 0.01$.

significantly contributed to weight gain ($p = 0.028$). After 5 weeks of light intervention, mice were sacrificed after a kinetic experiment with radioactive tracers (see below), and gonadal white adipose tissue (gWAT) was quantitatively weighed and examined histologically. A positive correlation was found between light exposure duration and gWAT weight ($\beta = 0.005$; $r^2 = 0.20$; $p = 0.02$) (Figure 1E) as well as average adipocyte size ($\beta = 0.08$; $r^2 = 0.20$; $p = 0.04$) (Figure 1F,G). The gWAT weight and adipocyte size

were significantly increased in mice exposed to 24 h light compared to 12 h (+21%; $p=0.02$ and +21%; $p=0.04$, respectively). Notably, food intake was not different in mice exposed to 16 h light, and even tended to be reduced in mice continuously exposed to light (-13%; $p=0.08$) compared to mice exposed to 12 h light per day, (**Figure 1H**). Therefore, the positive correlation between day length and adiposity is not explained by hyperphagia, consistent with our previous observations that exposure of mice to constant light decreases energy expenditure rather than increasing food intake (11).

Prolonged daily light exposure decreases the nutrient uptake by brown adipose tissue

To investigate whether prolonged daily light exposure reduces BAT activity, consistent with decreased energy expenditure, we determined the effect of light exposure duration on the ability of BAT to take up TG-derived free fatty acids and glucose from plasma. Hereto, we assessed the kinetics of intravenously injected glycerol tri^[3H]oleate ([^{3H}]TO)-labeled VLDL-like emulsion particles and [^{14C}]deoxyglucose ([^{14C}]DG) and determined the distribution of radiolabels at 15 min after injection.

Prolonged daily light exposure did not substantially alter the kinetics of plasma clearance of [^{3H}]TO and [^{14C}]DG (**Supplemental Figure 2A,B**). In mice exposed to a 12 h light per day, the uptake of [^{3H}]TO-derived radioactivity was much higher in the various BAT depots (interscapular BAT (iBAT), subscapular BAT (sBAT), and perivascular adipose tissue (pVAT)) as compared to liver (~3.5-fold), heart (~10-fold), muscle (~15-fold) and white adipose tissue (WAT) (~25-650-fold) (**Figure 2A**). Interestingly, the uptake of [^{3H}]TO-derived activity by iBAT, sBAT and pVAT decreased with prolonged light exposure reaching -47% ($p=0.001$), -34% ($p=0.03$) and -48% ($p=0.01$) for 24 h *versus* 12 h light exposure (**Figure 2A**). Accordingly, the day length negatively associated with the uptake of [^{3H}]TO-derived activity by iBAT ($\beta=-0.83$; $r^2=0.32$; $p=0.002$) (**Figure 2B**), sBAT ($\beta=-0.58$; $r^2=0.12$; $p=0.08$) (**Figure 2C**) and pVAT ($\beta=-0.90$; $r^2=0.30$; $p=0.005$) (**Figure 2D**). Prolonged light exposure did not alter the uptake of [^{3H}]TO-derived radioactivity by organs other than BAT. Consistent with reduced TG-derived free fatty acid uptake by BAT, we found that prolonged light exposure associated to increased plasma free fatty acid levels ($\beta=0.03$; $r^2=0.45$; $p<0.001$) (**Supplemental Figure 2C**).

Prolonged daily light exposure also decreased the uptake of [^{14C}]DG by BAT. As compared to 12 h light exposure, 24 h light exposure decreased the uptake of [^{14C}]DG by iBAT (-54%; $p=0.002$), sBAT (-48%; $p=0.02$) and pVAT (-57%; $p=0.001$) (**Figure 2F**). Additionally, 16 h of light a day significantly decreased glucose uptake in pVAT (-32%; $p=0.04$) compared to 12 h (**Figure 2E**). Similar to the uptake of [^{3H}]TO-derived radioactivity, day length negatively associated with the uptake of glucose by iBAT ($\beta=-0.02$; $r^2=0.26$; $p=0.007$) (**Figure 2F**), sBAT ($\beta=-0.13$; $r^2=0.18$; $p=0.03$) (**Figure 2G**) and pVAT ($\beta=-0.03$; $r^2=0.42$; $p=0.0005$) (**Figure 2H**).

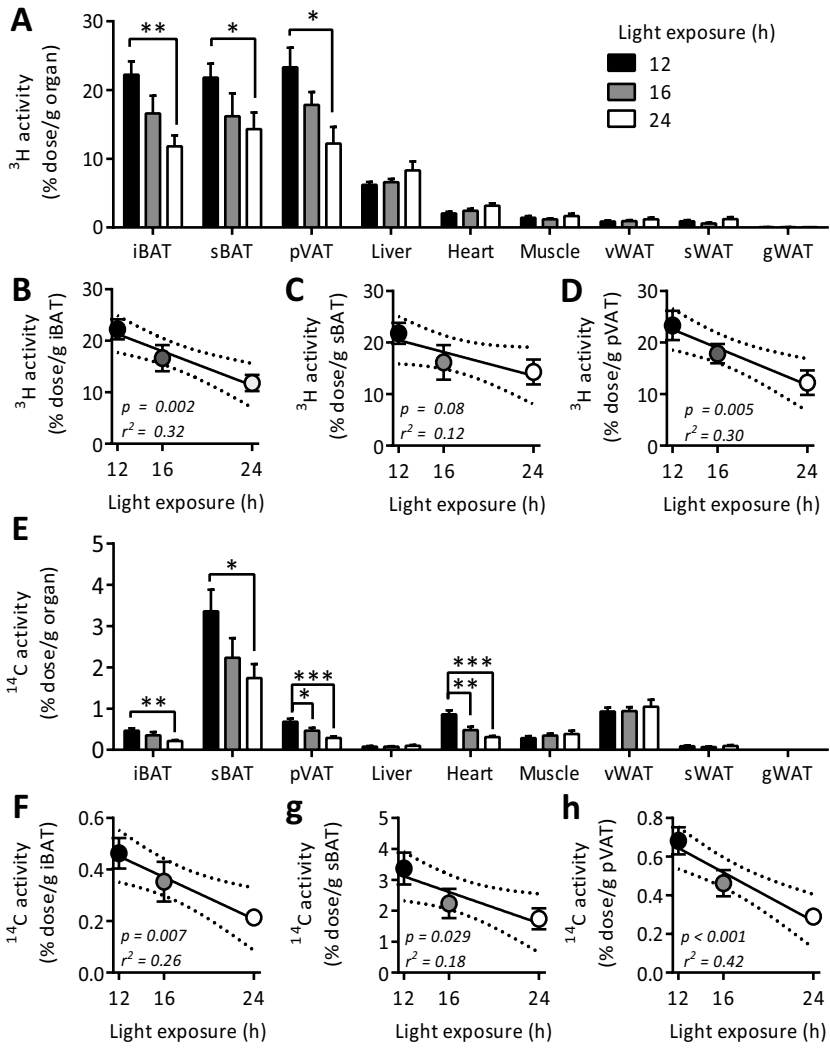


Figure 2 – Mice were exposed to either 12, 16 or 24 h light ($n = 8-9$) for 5 weeks, and the VLDL-TG and glucose kinetics were assessed by injection of glycerol tri[³H]oleate ([³H]TO)-labeled emulsion particles and [¹⁴C]deoxyglucose ([¹⁴C]DG). Uptake of [³H]TO-derived activity by the various organs was determined [A], and correlations were determined between light exposure and [³H]TO-derived activity in iBAT [B], sBAT [C] and pVAT [D]. Concomitantly, the uptake of [¹⁴C]DG by the various organs was determined [E], and correlations were determined between light exposure and the uptake of [¹⁴C]DG by iBAT [F], sBAT [G] and pVAT [H]. Data are presented as means \pm SEM. Dotted lines represent 95% confidence interval of the regression line. * $p < 0.05$, ** $p < 0.01$, *** $p < 0.001$. Abbreviations of organs: iBAT, interscapular BAT; sBAT, subscapular BAT; pVAT, perivascular adipose tissue; vWAT, visceral WAT; sWAT, subcutaneous WAT; gWAT, gonadal WAT.

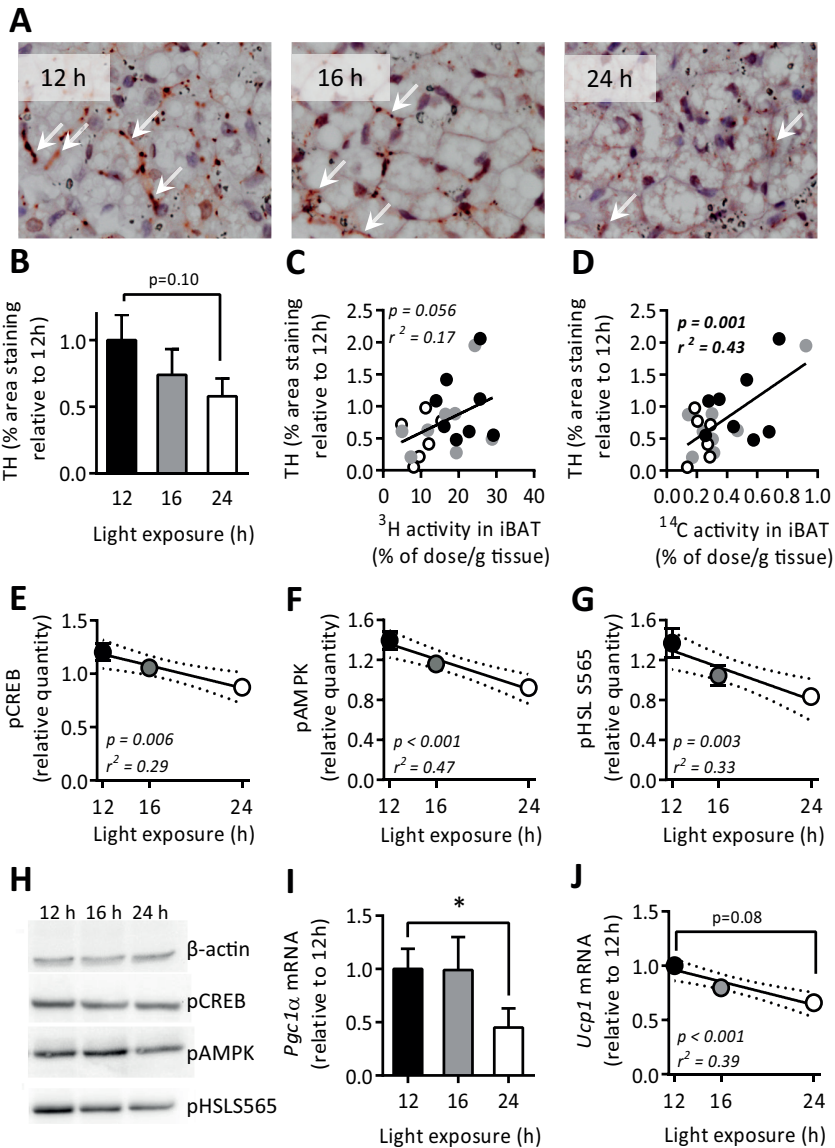


Figure 3 – Mice were exposed to either 12, 16, or 24 h light ($n = 9$) for 5 weeks, and interscapular BAT was isolated. Histological sections were stained for tyrosine hydroxylase (TH), representative images are shown (**A**; arrows indicate TH staining), and quantified (**B**). Correlation was determined between TH staining and uptake of [3 H]TO-derived activity (**C**) and [14 C]DG (**D**). Also, correlations were determined between light exposure and protein levels of pCREB (**E**), pAMPK (**F**), and pHSL S 565 (**G**). Protein levels were normalized to β -actin levels. Representative blots for β -actin, pCREB, pAMPK and pHSL S 565 are shown (**H**). Gene expression of *Pgc1 α* (**I**) and *Ucp1* (**J**) were determined and normalized to *36B4* expression. Data are presented as means \pm SEM. Dotted lines represent 95% confidence interval of the regression line. * $p < 0.05$.

These data imply that prolonged daily light exposure decreases the uptake of nutrients from plasma quite specifically by the various BAT depots, indicating that prolonged daily light exposure decreases the activity of brown adipocytes.

Prolonged daily light exposure decreases intracellular adrenergic signalling in BAT

As the SCN is directly connected to BAT via the sympathetic nervous system, we reasoned that prolonged daily light exposure decreases sympathetic activation of BAT. Indeed, immunohistochemical analysis of iBAT showed that the amount of tyrosine hydroxylase (TH), the rate-limiting enzyme in the synthesis of noradrenalin tended to decrease with increasing day length, up to -42% in 24 h compared to 12 h ($p=0.10$) (**Figure 3A,B**). Additionally, the amount of TH detected in BAT correlated with the uptake of [^3H]TO-derived activity by BAT ($r^2=0.17$; $p=0.056$) (**Figure 3C**) as well as with the uptake of [^{14}C]DG by BAT ($r^2=0.43$; $p=0.001$) (**Figure 3D**).

Since activation of the β_3 -adrenergic receptor by noradrenalin increases intracellular levels of cyclic AMP (cAMP) which activates protein kinase A (PKA), resulting in phosphorylation of cAMP response-binding element (CREB) and activates AMP-activated protein kinase (AMPK), we next determined the phosphorylation status of these proteins involved in thermogenesis in iBAT. Phosphorylated CREB (pCREB) was decreased in 24 h light exposure compared to 12 h (-27%; $p=0.009$) (**Figure 3E**). Phosphorylated AMPK (pAMPK) was decreased in mice on a day length of 16 h (-14%; $p=0.05$) and 24 h (-32%; $p=0.002$) (**Figure 3F,H**) compared to 12 h of light exposure per day, independent of total AMPK levels (**Supplemental Figure 3A,B**). Daily light duration negatively associated with levels of both pCREB ($\beta=-0.03$, $r^2=0.29$, $p=0.006$) (**Figure 3E, H**) and pAMPK ($\beta=-0.04$, $r^2=0.47$, $p=0.0003$) (**Figure 3F,H**). Both pAMPK and pCREB induce phosphorylation of the lipolytic enzyme hormone-sensitive lipase (HSL). While day length did not affect PKA-mediated phosphorylation of HSL on serine 563 position (pHSL S⁵⁶³) (**Supplemental Figure 3A,C**), it reduced AMPK-mediated phosphorylation of HSL on serine 565 (pHSL S⁵⁶⁵). A day length of 24 h decreased pHSL S⁵⁶⁵ compared to a day length of 12 h (-39%; $p=0.009$) and day length negatively correlated with pHSL S⁵⁶⁵ ($\beta=-0.04$, $r^2=0.33$, $p=0.0031$) (**Figure 3G,H**).

Gene targets of pCREB include peroxisome proliferator-activated receptor 1 α (PPARGC1 α or PGC1 α) that drives transcription of genes involved in mitochondrial biogenesis, and UCP1, which is essential for BAT thermogenesis. Prolonged daily light exposure (24 h vs. 12 h) decreased gene expression of *Pgc1 α* (-55%; $p<0.05$) (**Figure 3I**) and tended to decrease gene expression of *Ucp1* (-37%; $p=0.08$) (**Figure 3J**). Increasing day length negatively associated with expression of *Ucp1* ($\beta=-0.03$, $r^2=0.39$, $p=0.0005$) (**Figure 3J**).

Next, we examined the possibility that prolonged light exposure reduces BAT thermogenic capacity by decreasing mitochondrial function. Prolonged light exposure did not affect gene expression of genes involved in mitochondrial biogenesis (*Tfam*, *Cox7a1*, *Cyc1*, *Atp5g1*), fatty acid oxidation enzymes (*Acadvl*, *Acadl*, *Acadm*) or mitochondrial fusion (*Mfn2*) (**Supplemental Figure 4A**). Additionally, the amount of mitochondrial DNA (**Supplemental Figure 4B**) as well as citrate synthase activity (**Supplemental Figure 4C**) was similar between the different light exposure groups. In line with this finding, total BAT amount was not different upon prolonged light exposure (**Supplemental Figure 4D**).

Together, these data indicate that prolonged daily light exposure reduces sympathetic signalling in BAT that is not accompanied by a decrease in mitochondrial capacity, but does result in reduced uptake of TG-derived fatty acids and glucose.

Sympathetic denervation of iBAT largely reduces nutrient uptake and abolishes effects of prolonged light exposure

To confirm that sympathetic outflow is crucial for the observed effects of prolonged daily light exposure, we performed selective, bilateral denervation of the iBAT prior to exposing mice to 12, 16 or 24 h light per day. A reference group of mice underwent sham surgery and were exposed to 12 h light per day. Denervation completely abolished sympathetic input into iBAT, as evidenced by absence of TH (**Figure 4A**). In line with the previous experiment, light exposure did not affect food intake (**Figure 4B**). Additionally, spontaneous locomotor activity was similar between all groups (**Figure 4C**). Interestingly, body weight gain only increased in mice that were subjected to 24 h light exposure (**Figure 4D**). This increase was likely due to increased fat mass gain in these animals (**Figure 4E**).

Next, iBAT and sBAT activity was investigated by determining the ability to take up TG-derived fatty acids and glucose from plasma by injection of radiolabeled particles as described above. While the uptake of [³H]TO and [¹⁴C]DG by non-denervated sBAT remained high (**Figure 4F** and **Figure 4G** resp.), specific iBAT denervation lowered the uptake of [³H]TO-derived activity (**Figure 4H**) and [¹⁴C]DG (**Figure 4I**) by iBAT with approximately 70-80% compared to sham operated animals ($p < 0.001$), indicating the importance of noradrenergic input in BAT activity. Importantly, prolonged daily light exposure did not further decrease the uptake of [³H]TO and [¹⁴C]DG. These data indicate the reduction in adrenergic signalling may be causal in the negative correlations of hours of light exposure and BAT activity.

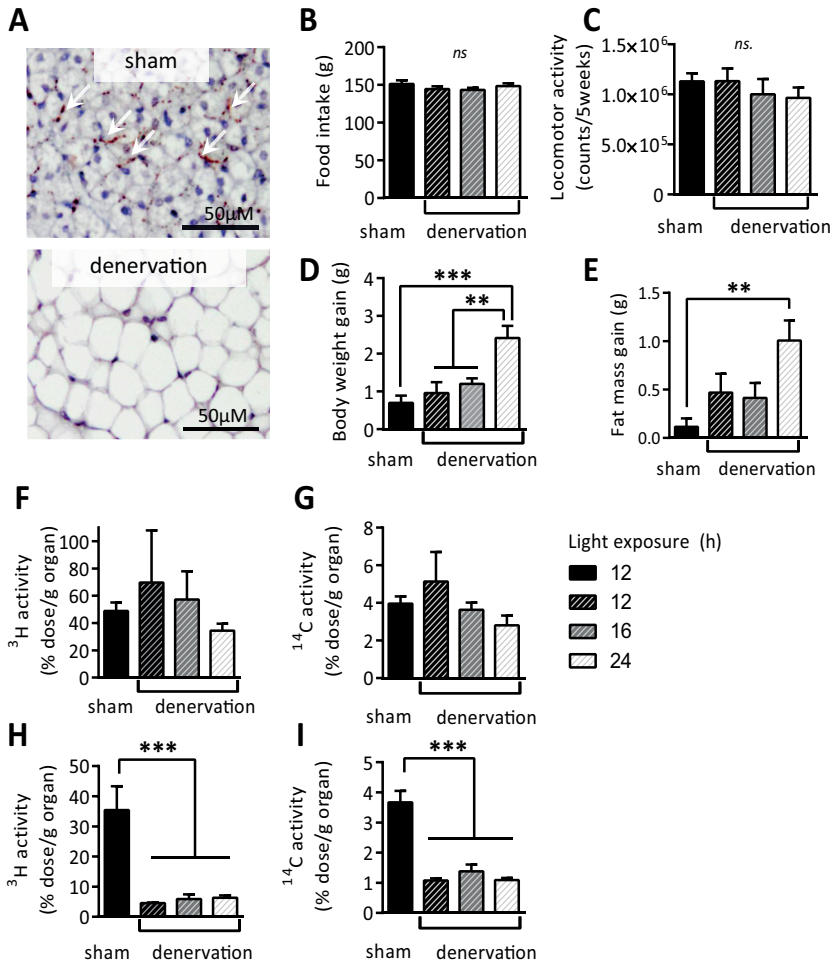


Figure 4 – Mice underwent bilateral sympathetic denervation of iBAT or sham surgery. Denervated mice were exposed to either 12, 16 or 24 h light (n = 5-6) while sham mice were exposed to 12 h light exposure (n=6). After 5 weeks, iBAT was isolated and histologically stained for tyrosine hydroxylase (TH). Representative images are shown (A). Total food intake (B), locomotor activity (C), body weight gain (D) and fat mass gain (E) were determined. VLDL-TG and glucose kinetics were assessed by injection of glycerol tri[³H]oleate ([³H]TO)-labeled emulsion particles and [¹⁴C]deoxyglucose ([¹⁴C]DG). Uptake of [³H]TO-derived and [¹⁴C]DG activity by sBAT (F,G) and by iBAT was determined (H,I). Data are presented as means ±SEM. ns. = not significant, *p<0.05, **p<0.01, *** p<0.001.

Discussion

This study addressed the effect of daily light exposure (12, 16 and 24 h) on energy metabolism in chow-fed C57Bl/6J mice. We show that prolonging the daily light exposure increases adiposity and reduces the uptake of TG-derived fatty acids and glucose specifically by BAT, accompanied by decreased β -adrenergic signalling in BAT and decreased phosphorylation of intracellular proteins involved in thermogenesis.

Daily light exposure duration positively associated with body fat mass and white adipocyte hypertrophy. These data are in line with observations in field voles, switching the day length from 8 h to 16 h increased body weight by 24% in 4 weeks compared to animals that remained on a day length of 8 h (18). Accordingly, we previously showed that prolonging day length from 12 h to 24 h decreases energy expenditure in mice without increasing food intake or locomotor activity (11). Although acute light exposure at night can reduce locomotor activity (19) and prolonged light exposure affects wheel running activity (20,21), our present study confirms previous reports from us (11) and others (22) that prolonged light exposure does not decrease spontaneous locomotor activity. Together, these studies support the idea that prolonged daily light exposure increases body fat mass through a decrease in energy expenditure rather than to an increase in food intake or decrease of locomotor activity.

The present study strongly suggests that prolonged daily light exposure increases adiposity due to attenuation of BAT activity as reflected by the negative association between daily light exposure and the uptake of fatty acids and glucose by several BAT depots. Of note, prolonged daily light exposure did not affect uptake of nutrients by other metabolic organs, such as WAT. These data are consistent with our recent findings that attenuating BAT activity by inhibiting the central melanocortin system also reduces the influx of nutrients into BAT (23). In fact, activation of BAT, e.g. by cold exposure, increases expression of genes involved in fatty acid oxidation, glucose uptake and lipogenesis (24) and strongly increases the uptake of TG-derived fatty acids (25) and glucose (24).

Our data are consistent with the hypothesis that prolonged daily light exposure decreases BAT activity through reduction of the sympathetic outflow towards BAT. Tyrosine hydroxylase (TH), the rate limiting enzyme in noradrenalin production, correlates with nutrient uptake by BAT and we observed a decrease in sympathetic signalling pathways in BAT. Prolonged light exposure decreased phosphorylation of CREB and AMPK, two main targets of β 3-adrenergic signalling in the brown adipocyte. AMPK not only modulates intracellular lipolysis by phosphorylation of HSL, but also regulates uptake of lipids and glucose by inducing translocation of CD36, LPL and GLUT4 to the plasma membrane (26,27), which may explain the reduced nutrient

uptake by BAT. Moreover, we showed that in the absence of sympathetic input, BAT activity is equal among the various light exposure groups.

We propose that the SCN directly mediates the decrease in sympathetic outflow upon prolonging daily light exposure. In previous studies we demonstrated that prolonged light exposure dampens the amplitude of electrical activity in the SCN *in vitro* [28] and *in vivo* [10]. Interestingly, the amplitude of electrical activity in the SCN is linked to sympathetic outflow towards multiple organs [29]. This mechanism also explains previous findings that exposure of mice to dim light (5 lux) during 10 h nights for 4 weeks already results in an increase in body weight, which was accompanied by an attenuated amplitude of circadian gene expression in the hypothalamus [30]. Also, sympathetic outflow towards BAT depots other than interscapular BAT would explain our observations that denervation of iBAT does not increase body weight. Only 24 h light exposure decreases sympathetic outflow to such an extent, that mice increase significantly in body weight. Of note, the effects of light exposure on BAT are independent of melatonin secretion, since C57Bl/6J mice are genetically melatonin deficient [31]. However, we cannot exclude the possibility that in humans melatonin does play a role in the association between light pollution and adiposity as administration of melatonin increases BAT growth [32] and activity [33,34] in hamsters and rats.

Based on our collective data, we thus propose the following mechanism by which prolonging daily light exposure increases adiposity: prolonged day length dampens the SCN amplitude thereby lowering sympathetic outflow towards BAT resulting in decreased β 3-adrenergic signalling and thermogenesis in brown adipocytes. As a consequence, the uptake of VLDL-TG derived fatty acids and glucose by BAT is reduced. The decreased combustion of fatty acids by BAT at equal energy intake thus results in a positive energy balance and therefore storage of lipids in WAT (**Figure 5**).

Recent evidence suggests that BAT activity in humans is physiologically regulated by the biological clock. The detectability of BAT by [18 F]fluorodeoxyglucose (FDG)-PET-CT imaging at room temperature follows a circannual cycle, both in the northern and southern hemisphere [35-37], with low detectability of BAT in summer (i.e., short day) as compared to winter (i.e., long day). Although differences in outside temperature over the year would be a likely explanation for this phenomenon, the detectability of BAT showed a stronger correlation with day length than with outside temperature [35]. Based on our present data, the daily light exposure may thus well explain the circannual cycle of BAT detectability. Likewise, impaired BAT activity may also explain, at least partly, the relationship between obesity and disturbances in circadian rhythmicity in humans by light pollution [2,3,38], and possibly also by shift work [39-41] and sleep curtailment [1,42,43]. Additionally, our data may provide the link in the relationship between exposure to light in the bedroom and obesity [4]. The suggested causal relationship has clear implications for the prevention of

obesity in humans. Although the association between light in the bedroom and BAT activity in humans remains to be investigated, future lifestyle advice could include instructing people to darken their bedroom.

In conclusion, our study provides evidence that prolonged daily light exposure increases body fat mass through reduction of BAT activity. The present findings support the hypothesis that the relationship between disturbed circadian rhythmicity and adiposity in humans is mediated by impaired BAT activity.

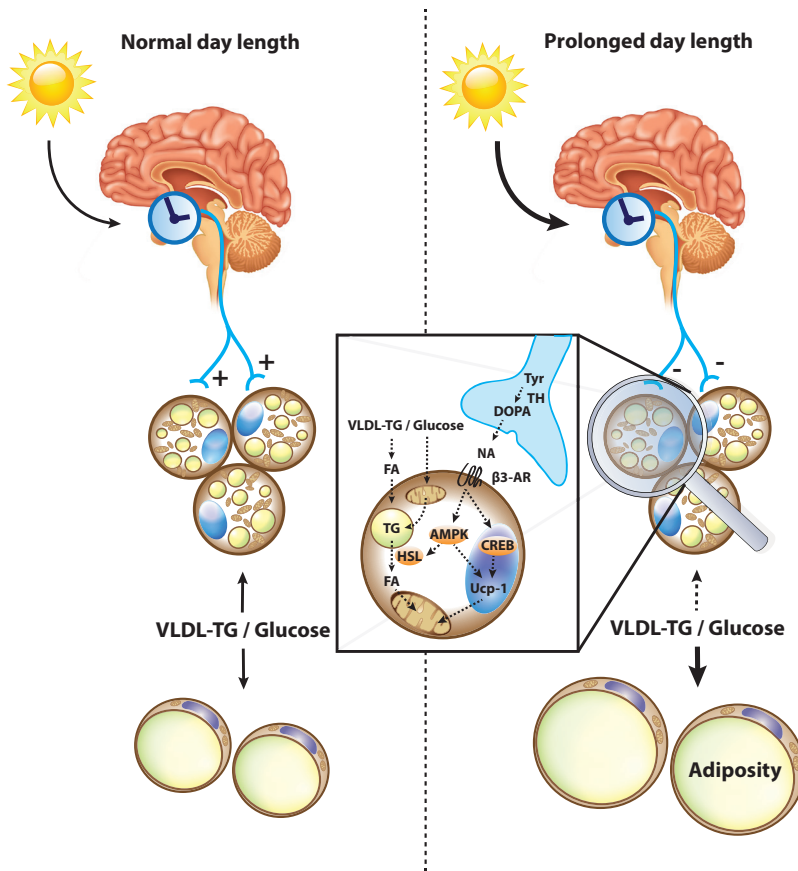


Figure 5 – Proposed model on how light exposure modulates body fat mass through brown adipose tissue activity. Daily light exposure duration is perceived by the suprachiasmatic nucleus, that signals towards BAT via the sympathetic nervous system. At normal day length uptake of nutrients by BAT and WAT is in balance, while increasing daily light exposure result in reduced BAT activation and subsequent storage of excess energy in WAT. The decrease in noradrenaline (NA) availability for stimulation of the β 3-adrenergic receptor (β 3-AR) leads 1) reduced phosphorylation of CREB, which decreases transcription of UCP1; 2) reduced phosphorylation of AMPK resulting in decreased phosphorylation of HSL and thus decreased lipolysis.

Acknowledgements

The authors thank Simone Denis, Julia Melia Aloma and Lianne van der Wee-Pals for excellent technical support. This research was supported by the Netherlands Organisation for Scientific Research (NWO-VENI grants 016.136.125 to NR Biermasz and 91613050 to RH Houtkooper), the European Foundation for the Study of Diabetes and the Programme Partner Novo Nordisk (grant 94802 to CP Coomans, JH Meijer and PCN Rensen), the Dutch Diabetes Research Foundation (grant 2013.81.1663 to CP Coomans), the Rembrandt Institute for Cardiovascular Science (RICS) (Rembrandt Research Award to MR Boon and RH Houtkooper) and an AMC PhD fellowship (to IA Chatzisyrou). PCN Rensen is an Established Investigator of the Netherlands Heart Foundation (grant 2009T038).

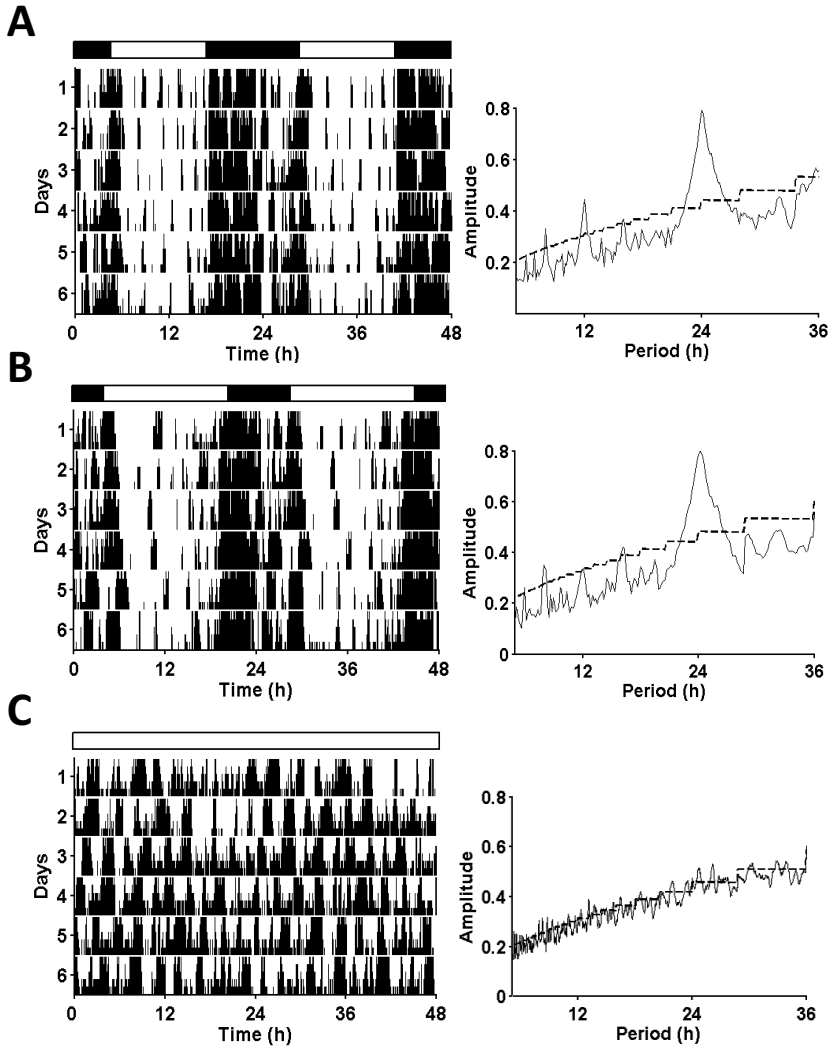
References

1. Killick, R., Banks, S., & Liu, P. Y. (2012) Implications of sleep restriction and recovery on metabolic outcomes. *J Clin Endocrinol Metab* 97, 3876-3890.
2. Obayashi, K., Saeki, K., Iwamoto, J. et al. (2013) Exposure to light at night, nocturnal urinary melatonin excretion, and obesity/dyslipidemia in the elderly: a cross-sectional analysis of the HEIJO-KYO study. *J Clin Endocrinol Metab* 98, 337-344.
3. Wyse, C. A., Selman, C., Page, M. M. et al. (2011) Circadian desynchrony and metabolic dysfunction; did light pollution make us fat? *Med Hypotheses* 77, 1139-1144.
4. McFadden, E., Jones, M. E., Schoemaker, M. J. et al. (2014) The Relationship Between Obesity and Exposure to Light at Night: Cross-Sectional Analyses of Over 100,000 Women in the Breakthrough Generations Study. *Am J Epidemiol*.
5. Perreau-Lenz, S., Pevet, P., Buijs, R. M. et al. (2004) The biological clock: the bodyguard of temporal homeostasis. *Chronobiol Int* 21, 1-25.
6. Cho, H., Zhao, X., Hatori, M. et al. (2012) Regulation of circadian behaviour and metabolism by REV-ERB- α and REV-ERB- β . *Nature* 485, 123-127.
7. Shi, S. Q., Ansari, T. S., McGuinness, O. P. et al. (2013) Circadian disruption leads to insulin resistance and obesity. *Curr Biol* 23, 372-381.
8. Shimba, S., Ishii, N., Ohta, Y. et al. (2005) Brain and muscle Arnt-like protein-1 (BMAL1), a component of the molecular clock, regulates adipogenesis. *Proc Natl Acad Sci USA* 102, 12071-12076.
9. Turek, F. W., Joshi, C., Kohsaka, A. et al. (2005) Obesity and metabolic syndrome in circadian Clock mutant mice. *Science* 308, 1043-1045.
10. Coomans, C. P., van den Berg, S. A., Lucassen, E. A. et al. (2013) The suprachiasmatic nucleus controls circadian energy metabolism and hepatic insulin sensitivity. *Diabetes* 62, 1102-1108.
11. Coomans, C. P., van den Berg, S. A., Houben, T. et al. (2013) Detrimental effects of constant light exposure and high-fat diet on circadian energy metabolism and insulin sensitivity. *FASEB J* 27, 1721-1732.
12. Amir, S. (1989) Retinohypothalamic tract stimulation activates thermogenesis in brown adipose tissue in the rat. *Brain Res* 503, 163-166.
13. Bamshad, M., Song, C. K., & Bartness, T. J. (1999) CNS origins of the sympathetic nervous system outflow to brown adipose tissue. *Am J Physiol* 276, R1569-R1578.
14. Rensen, P. C., Herijgers, N., Netscher, M. H. et al. (1997) Particle size determines the specificity of apolipoprotein E-containing triglyceride-rich emulsions for the LDL receptor versus hepatic remnant receptor in vivo. *J Lipid Res* 38, 1070-1084.
15. Houtkooper, R. H., Argmann, C., Houten, S. M. et al. (2011) The metabolic footprint of aging in mice. *Sci Rep* 1, 134.
16. Ventura, F. V., Ruiter, J., Ijlst, L. et al. (2005) Differential inhibitory effect of long-chain acyl-CoA esters on succinate and glutamate transport into rat liver mitochondria and its possible implications for long-chain fatty acid oxidation defects. *Mol Genet Metab* 86, 344-352.
17. Dörrscheidt GL & Beck L. (1975) Advanced methods for evaluating characteristic parameters of circadian rhythms. *J Mathemat Biol*. 2, 107-121.
18. Krol, E., Redman, P., Thomson, P. J. et al. (2005) Effect of photoperiod on body mass, food intake and body composition in the field vole, *Microtus agrestis*. *J Exp Biol* 208, 571-584.
19. Redlin, U. (2001) Neural basis and biological function of masking by light in mammals: suppression of melatonin and locomotor activity. *Chronobiol Int* 18, 737-758.
20. Morin, L. P., Lituma, P. J., & Studholme, K. M. (2010) Two components of nocturnal locomotor suppression by light. *J Biol Rhythms* 25, 197-207.
21. Mrosovsky, N., Foster, R. G., & Salmon, P. A. (1999) Thresholds for masking responses to light in three strains of retinally degenerate mice. *J Comp Physiol A* 184, 423-428.
22. Fonken, L. K., Workman, J. L., Walton, J. C. et al. (2010) Light at night

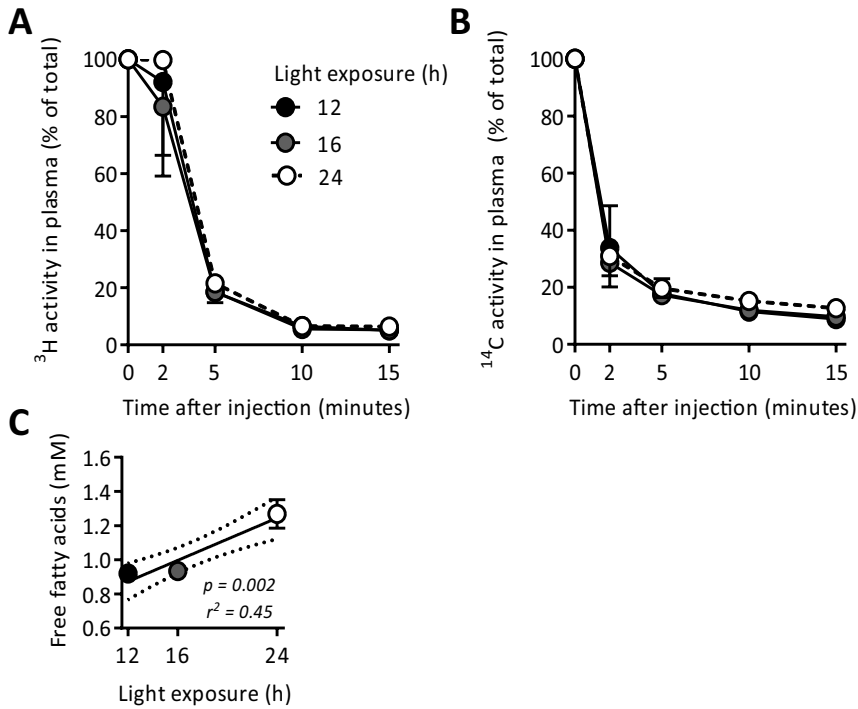
- increases body mass by shifting the time of food intake. *Proc Natl Acad Sci USA* 107, 18664-18669.
23. Kooijman, S., Boon, M. R., Parlevliet, E. T. *et al.* (2014) Inhibition of the central melanocortin system decreases brown adipose tissue activity. *J Lipid Res.*
 24. Yu, X. X., Lewin, D. A., Forrest, W. *et al.* (2002) Cold elicits the simultaneous induction of fatty acid synthesis and beta-oxidation in murine brown adipose tissue: prediction from differential gene expression and confirmation in vivo. *FASEB J* 16, 155-168.
 25. Bartelt, A., Bruns, O. T., Reimer, R. *et al.* (2011) Brown adipose tissue activity controls triglyceride clearance. *Nat Med* 17, 200-205.
 26. Samovski, D., Su, X., Xu, Y. *et al.* (2012) Insulin and AMPK regulate FA translocase/CD36 plasma membrane recruitment in cardiomyocytes via Rab GAP AS160 and Rab8a Rab GTPase. *J Lipid Res* 53, 709-717.
 27. Jeppesen, J., Albers, P. H., Rose, A. J. *et al.* (2011) Contraction-induced skeletal muscle FAT/CD36 trafficking and FA uptake is AMPK independent. *J Lipid Res* 52, 699-711.
 28. VanderLeest, H. T., Houben, T., Michel, S. *et al.* (2007) Seasonal encoding by the circadian pacemaker of the SCN. *Curr Biol* 17, 468-473.
 29. Kalsbeek, A., Palm, I. F., La Fleur, S. E. *et al.* (2006) SCN outputs and the hypothalamic balance of life. *J Biol Rhythms* 21, 458-469.
 30. Fonken, L. K., Aubrecht, T. G., Melendez-Fernandez, O. H. *et al.* (2013) Dim light at night disrupts molecular circadian rhythms and increases body weight. *J Biol Rhythms* 28, 262-271.
 31. Roseboom, P. H., Namboodiri, M. A., Zimonjic, D. B. *et al.* (1998) Natural melatonin 'knockdown' in C57BL/6J mice: rare mechanism truncates serotonin N-acetyltransferase. *Brain Res Mol Brain Res* 63, 189-197.
 32. Heldmaier, G. & Hoffmann, K. (1974) Melatonin stimulates growth of brown adipose tissue. *Nature* 247, 224-225.
 33. Holtorf, A. P., Heldmaier, G., Thiele, G. *et al.* (1985) Diurnal changes in sensitivity to melatonin in intact and pinealectomized Djungarian hamsters: effects on thermogenesis, cold tolerance, and gonads. *J Pineal Res* 2, 393-403.
 34. Hagelstein, K. A. & Folk, G. E., Jr. (1979) Effects of photoperiod, cold acclimation and melatonin on the white rat. *Comp Biochem Physiol C* 62C, 225-229.
 35. Au-Yong, I. T., Thorn, N., Ganatra, R. *et al.* (2009) Brown adipose tissue and seasonal variation in humans. *Diabetes* 58, 2583-2587.
 36. Perkins, A. C., Mshelia, D. S., Symonds, M. E. *et al.* (2013) Prevalence and pattern of brown adipose tissue distribution of 18F-FDG in patients undergoing PET-CT in a subtropical climatic zone. *Nucl Med Commun* 34, 168-174.
 37. Persichetti, A., Sciuto, R., Rea, S. *et al.* (2013) Prevalence, mass, and glucose-uptake activity of (11)8F-FDG-detected brown adipose tissue in humans living in a temperate zone of Italy. *PLoS One* 8, e63391.
 38. Reid, K. J., Santostasi, G., Baron, K. G. *et al.* (2014) Timing and intensity of light correlate with body weight in adults. *PLoS One* 9, e92251.
 39. Karlsson, B. H., Knutsson, A. K., Lindahl, B. O. *et al.* (2003) Metabolic disturbances in male workers with rotating three-shift work. Results of the WOLF study. *Int Arch Occup Environ Health* 76, 424-430.
 40. Di Lorenzo L., De, P. G., Zocchetti, C. *et al.* (2003) Effect of shift work on body mass index: results of a study performed in 319 glucose-tolerant men working in a Southern Italian industry. *Int J Obes Relat Metab Disord* 27, 1353-1358.
 41. Barbadoro, P., Santarelli, L., Croce, N. *et al.* (2013) Rotating shift-work as an independent risk factor for overweight Italian workers: a cross-sectional study. *PLoS One* 8, e63289.
 42. Watanabe, M., Kikuchi, H., Tanaka, K. *et al.* (2010) Association of short sleep duration with weight gain and obesity at 1-year follow-up: a large-scale prospective study. *Sleep* 33, 161-167.
 43. Hairston, K. G., Bryer-Ash, M., Norris, J. M. *et al.* (2010) Sleep duration and five-year abdominal fat accumulation in a minority cohort: The IRAS family study. *Sleep* 33, 289-295.

Supplementary appendix

4

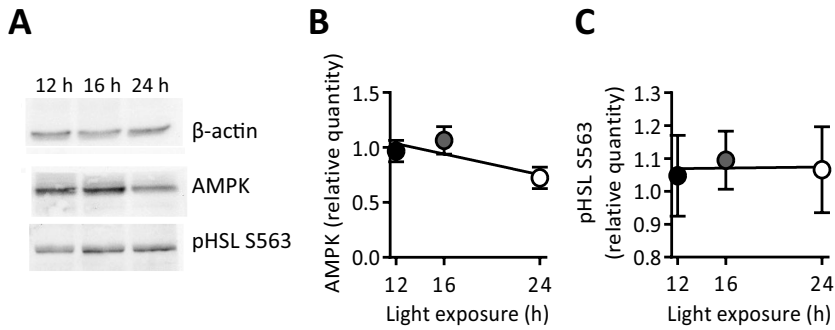


Supplemental Figure 1 – Prolonged daily light exposure affects behavioural rhythms in mice. Mice were exposed to either 12, 16 or 24 h light ($n = 9$) for 5 weeks, and behavioural activity was monitored by passive infrared detectors. Representative actograms (left panels) and the pertaining F periodogram (right panels) are shown of a mouse exposed to 12 (A), 16 (B) and 24 h (C) of light. The double-plotted actograms show consecutive days on successive lines and the vertical black upticks indicate behavioural activity measured by passive infrared detectors. The light regimes are plotted on top of the actograms; white areas represent light and black areas represent darkness. Periodogram analysis visualizes the strength of behavioural rhythmicity. The dotted lines in the periodograms indicate the 0.05 level of significance.

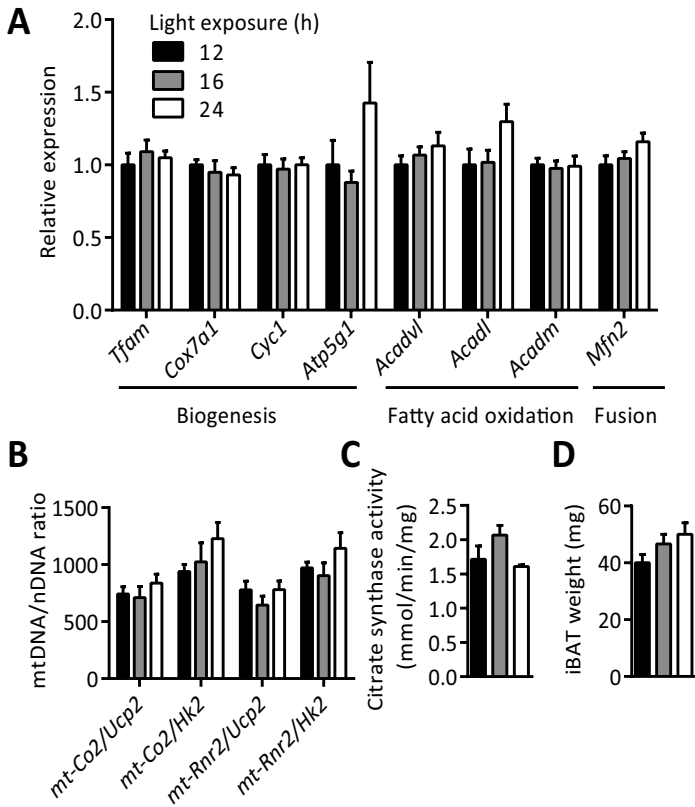


Supplemental Figure 2 – Effect of light exposure on TG and glucose plasma clearance.

Prolonged daily light exposure does not affect TG and glucose plasma clearance. Mice were exposed to either 12, 16 or 24 h light for 5 weeks, and the VLDL-TG and glucose kinetics were assessed by injection of glycerol tri[³H]oleate ([³H]TO)-labeled emulsion particles and [¹⁴C] deoxyglucose ([¹⁴C]DG). Blood was drawn 2, 5, 10 and 15 min after injection. [³H]TO (n=8-9) (**A**) and [¹⁴C]DG (n=6-7) (**B**) derived activity was assessed in plasma samples by liquid oscillation counting. Data are represented as means ±SEM. Statistical significance was determined by unpaired two-tailed Student's t-test.



Supplemental Figure 3 – Prolonged daily light exposure does not affect AMPK and pHSLS⁵⁶³ in BAT. Prolonged daily light exposure does not affect AMPK and pHSLS⁵⁶³ in BAT. Mice exposed to either 12, 16, or 24 h light (n= 9) for 5 weeks, and interscapular BAT was isolated for protein quantification. Representative western blots are shown for β -actin, total AMPK and pHSLS⁵⁶³ (A). Correlation was determined between hours of light exposure and protein levels of AMPK (B) and pHSLS⁵⁶³ (C). Protein levels were normalized to β -actin levels. Data are represented as means \pm SEM. Statistical significance between groups was determined by unpaired two-tailed Student's t-test, linear regression analysis was performed to analyse the association of gene expression with light exposure.



Supplemental Figure 4 – Effects of prolonged light exposure on mitochondrial function.

Prolonged daily light exposure does not decrease structural mitochondrial function in BAT and quantity of BAT. Mice were exposed to either 12, 16, or 24 h light ($n=9$) for 5 weeks, and interscapular and subscapular BAT was isolated for gene expression and mitochondrial function analysis. Expression of genes involved in mitochondrial biogenesis, fatty acid oxidation and fusion genes did not change upon prolonged light exposure (A). The same is true for relative mitochondrial DNA quantity (B) and mitochondrial citrate synthase activity (C). iBAT was removed quantitatively and weighed (D). Gene expression levels were normalized to *36B4* levels. Mitochondrial DNA quantity is expressed as ratio of mitochondrial gene expression relative to nuclear gene expression (genes indicated below) Data are represented as means \pm SEM. Abbreviations: *Tfam*, transcription factor A, mitochondrial; *Cox7a1*, cytochrome c oxidase subunit VIIa 1; *Cyc1*, cytochrome C-1; *Atp5g1*, ATP synthase, H⁺ transporting, mitochondrial F0 complex, subunit C1; *Acadvl*, acyl-Coenzyme A dehydrogenase, very long chain; *Acadl*, acyl-Coenzyme A dehydrogenase, long-chain; *Acadm*, acyl-Coenzyme A dehydrogenase, medium chain; *Mfn2*, mitofusin 2; *mtCo2*, cytochrome c oxidase II, mitochondrial; *mt-Rnr2*, 16S rRNA, mitochondrial; *Ucp2*, uncoupling protein 2; *Hk2*, hexokinase 2.

5

DAILY AND SEASONAL ENCODING OF RHYTHMS IN BROWN ADIPOSE TISSUE ACTIVITY

Sander Kooijman*

Rosa van den Berg*

Ashna Ramkisoensing

Laura Sardon Puig

Claudia P. Coomans

Johanna H. Meijer

Nienke R. Biermasz†

Patrick C.N. Rensent

*Authors contributed equally

†Authors share last authorship

In preparation

Abstract

Brown adipose tissue (BAT) contributes importantly to non-shivering thermogenesis by its ability to combust large amount of triglycerides (TG) into heat. Interestingly, BAT is not only connected through the sympathetic nervous system to the hypothalamic temperature center but also to the suprachiasmatic nucleus (SCN). The SCN drives circadian (i.e. 24h) rhythms and activity of the SCN is known to adapt to seasonal changes in photoperiod. However, the effects of SCN on circadian and seasonal rhythms of BAT activity are largely unknown. Therefore, the aim of this study was to identify circadian and seasonal rhythms in BAT activity. Hereto, C57Bl/6J male mice were subjected to a short photoperiod of 8h (reflecting winter), a regular photoperiod of 12h or a long photoperiod of 16h (reflecting summer) per day. After 5 weeks, we assessed the uptake of TG-derived fatty acids from the circulation by BAT and other metabolically active tissues along the day. Under regular photoperiod, the various BAT depots showed a strong circadian rhythm in the uptake of fatty acids with a peak at ZT (Zeitgeber time) 12, just before the onset of the dark period. Strikingly, exposure to short photoperiod advanced the peak to ZT8 and increased the average diurnal fatty acid uptake, compared to long photoperiod that both delayed the peak and reduced the average fatty acid uptake. Similarly, short photoperiod resulted in an advanced onset of sympathetic outflow and expression of key thermogenic genes. Interestingly, this strong diurnal rhythm in fatty acid uptake as well as the adaptation to long and short photoperiod did not occur in other metabolically active tissues, including white adipose tissue, muscle and heart. In dyslipidemic APOE*3-Leiden. CETP mice exposed to a 10h photoperiod, at ZT10 compared to ZT0, the plasma half-life of TG-derived fatty acids was 1.6-fold lower, while the uptake of fatty acids by BAT was 4-fold higher, and plasma TG levels were 2.4-fold lower. In conclusion, our findings show that BAT activity is strongly regulated by the biological clock, incorporating both seasonal (i.e. photoperiod) and circadian information, which may contribute to circadian rhythms in plasma lipid levels.

Introduction

While the main function of white adipose tissue (WAT) is the storage of surplus energy in the form of triglycerides (TG), brown adipose tissue (BAT) combusts large amounts of TG into heat, a process called non-shivering thermogenesis. The thermogenic capacity of BAT arises from uncoupled respiration through expression of uncoupling protein-1 (UCP-1) and is initiated by sympathetic nervous system activity upon exposure to cold. Interestingly, retrograde tracing has not only identified direct neuronal connections between the hypothalamic temperature center and BAT, but also direct connections between the suprachiasmatic nucleus (SCN) and BAT (1).

The SCN is the central biological clock, responsible for the regulation of daily (*i.e.* circadian) rhythms in *e.g.* sleep-wake activity, endocrine function and body temperature. Administration of the excitatory neurotransmitter glutamate directly into the SCN increases BAT temperature (2), suggesting that an increased neuronal activity in the SCN may directly increase BAT activity. Accordingly, the expression of several nuclear receptors as well as the key thermogenic protein UCP-1 follows a circadian rhythm in BAT (3), and mice have a lower cold tolerance in the light phase than during the dark phase (4). Collectively, these data indicate functional differences in BAT reactivity throughout the circadian cycle.

The SCN also functions as a seasonal clock through adaptation to seasonal changes in daily photoperiod (5). This sophisticated timing system evolved in order to anticipate cyclic challenges, such as changes in food availability and temperature. Interestingly, detectability of human BAT by [¹⁸F]fluorodeoxyglucose (FDG) PET-CT scans at room temperature follows a circannual cycle, with low detectability of BAT in summer as compared to winter (6). Although differences in outside temperature over the year would be a likely explanation for this phenomenon, the detectability of BAT showed a stronger correlation with photoperiod than with outside temperature (6).

We recently demonstrated in mice that prolonged daily light exposure (*i.e.* 16h and 24h of light per day compared to 12h of light per day) decreases sympathetic outflow towards BAT and reduces BAT activity (7). Since the effects of the SCN on more refined rhythms in BAT function are largely unknown, the aim of this study was to identify daily and seasonal rhythms in BAT activity. Thereto, we examined the daily rhythms in BAT with respect to changes in histology, gene expression and fatty acid uptake, and identified the effects of short photoperiod (reflecting winter) and long photoperiod (reflecting summer) on rhythmicity of BAT activity.

Materials & Methods

Animal studies

All animal experiments were approved by the institutional ethics committee on animal care and experimentation at Leiden University Medical Centre (LUMC), Leiden, The Netherlands. 12 week old male C57Bl/6J mice (Charles River) were single housed in clear plastic cages within light-tight cabinets at constant room temperature of 22°C. The cages were illuminated with white fluorescent light with an intensity of approximately 85 $\mu\text{W}/\text{cm}^2$. Before start of the experiment, mice were kept on a regular 12h:12h light-dark cycle. Mice were matched on body weight. Light intervention consisted of subjecting mice to a photoperiod of either 8, 12 or 16h of light per day (*i.e.* 24h) for the duration of five weeks ($n=24$ per group). Mice had *ad libitum* access to standard laboratory chow (Special Diets Services, UK) and water throughout the experiment. After being exposed to a specific photoperiod for five weeks, a TG-derived fatty acid uptake experiment (see below) was performed at time points ZT (Zeitgeber Time, time after lights on) 0, 4, 6, 8, 12 and 18 ($n=4$ per specific photoperiod per time point). At the end of this experiment, mice were sacrificed via cervical dislocation and organs were collected for further gene expression and histological analysis (see below).

Homozygous human cholesteryl ester transfer protein (*CETP*) transgenic mice were crossbred with hemizygous *APOE*3-Leiden* mice at our Institutional Animal Facility to obtain female *APOE*3-Leiden.CETP* mice on a C57Bl/6J background (8). Before start of the experiment, mice were kept on a regular 12h:12h light-dark cycle and matched on body weight and plasma TG. Mice were single housed on a photoperiod of 10h per day and had *ad libitum* access to Western-type diet (containing 16% fat and 0.1% cholesterol; AB diet, Woerden, the Netherlands) and water throughout the experiment. After 4 weeks, a TG-derived fatty acid uptake experiment (see below) was performed both at the onset of light (ZT0) and the onset of darkness (ZT10).

TG-derived fatty acid uptake

After 5 weeks of exposure to a specific photoperiod, the uptake of TG-derived fatty acids was assessed. Glycerol tri[^3H]oleate-labeled lipoprotein-like emulsion particles (80 nm) were prepared as previously described (9). Mice were fasted for 4h and intravenously injected with the radiolabeled emulsion particles (1.0 mg TG in 200 μL PBS) via the tail vein. Two mice could not be injected (12h ZT6 and ZT18). Blood was collected after 2, 5, 10 and 15 min to determine plasma decay of the radiolabel. After 15 minutes, mice were euthanized by cervical dislocation and perfused with ice-cold PBS for 5 min. Organs were harvested, weighed, and the uptake of ^3H -derived activity was determined.

Histology

Formalin-fixed paraffin-embedded iBAT sections were cut (5 μ m). To determine sympathetic activation of iBAT a TH staining was performed. Sections were rehydrated and incubated 15 min with 10 mM citrate buffer (pH 6.0) at 120°C for antigen retrieval. Sections were blocked with 5% BSA/PBS followed by overnight incubation with anti-TH antibody (1:2000, AB-112, Abcam) at 4°C. Next, sections were incubated with a secondary antibody (anti-rabbit antibody, DAKO enVision), stained with Nova Red and counterstained with Mayer's haematoxylin. Percentage of area positive for TH staining was quantified using Image J software.

Gene expression analysis

A part of iBAT was snap frozen and stored at -80°C for gene expression analysis. Total RNA was isolated using TriPure (Roche) according to the manufacturer's instructions. 1 μ g of total RNA was reverse-transcribed using M-MLV reverse transcriptase (Promega, Madison, WI, USA). Real-time PCR was carried out on a CFX96 PCR machine (Bio-Rad) using IQ SYBR-Green Supermix (Bio-Rad). Melt curve analysis was included to assure a single PCR product was formed. Expression levels were normalized to *36B4* and *Hprt* housekeeping gene expression. Data were plotted as relative expression to expression in 12h light group at ZT0. Primer sequences are shown in Table S1.

Plasma TG concentration

After 5 weeks, blood was collected from the tail vein of 4h fasted mice. Plasma was assayed for TG using a commercially available enzymatic kit (Roche, Mannheim, Germany).

Statistical analysis

Data are presented as means \pm SEM. Contribution of Zeitgeber time and photoperiod to TG-derived FA uptake was analysed by two-way ANOVA. Differences between groups were determined by T-tests (for two groups) or using one-way ANOVA (more than two groups). Graph Pad Prism v6.0 was used for all calculations. Associations of variables with day length exposure as independent variable were assessed by linear regression analysis. Differences at p values < 0.05 were considered statistically significant.

Results

TG-derived fatty acid uptake shows circadian rhythm in metabolic organs, most pronounced in BAT

To study the daily and seasonal rhythms in BAT activity, C57Bl/6J male mice were exposed to a photoperiod of 8h (short), 12h (regular) or 16h (long) per day. After 5 weeks, we determined the ability of BAT and other metabolic organs to take up TG-derived fatty acids at 6 different Zeitgeber time (ZT) points (0, 4, 6, 8, 12 and 18).

First, we identified daily rhythms in the uptake of [³H]oleate from glycerol tri[³H]oleate-labeled lipoprotein-like emulsion particles under the standard laboratory photoperiod of 12h. Zeitgeber time determined the uptake of [³H]oleate in liver, subcutaneous WAT (sWAT), gonadal WAT (gWAT), heart, muscle, interscapular BAT (iBAT), subscapular BAT (sBAT) and perivascular adipose tissue (PVAT) (all *p*-values for ZT, $p_{ZT} \leq 0.01$; **Figure 1A-H**). The peak in uptake of ³H-activity was found at ZT18 for liver (**Figure 1A**), sWAT (**Figure 1B**) and gWAT (**Figure 1C**), corresponding with the active phase of the animals, when energy intake is usually high and available for storage. The peak in uptake of ³H-activity for heart (**Figure 1D**) and muscle (**Figure 1E**) was found at ZT4, corresponding to the period of low energy intake and a required shift towards fat oxidation. For the BAT depots the [³H]oleate uptake peaked just before onset of the active dark phase at ZT12, and was 17 ± 4 % dose/g for iBAT (**Figure 1F**) and 28 ± 19 % dose/g sBAT (**Figure 1G**), respectively. The uptake at this peak was 1.7-15 fold higher than the maximum uptake by other organs, indicating that BAT is highly metabolically active. Additionally, the difference between the minimum and maximum [³H]oleate uptake by iBAT (4.3-fold) and sBAT (12.0-fold) was higher than the difference observed in liver (1.7-fold), sWAT (2.0-fold), gWAT (3.3-fold), heart (1.9-fold) and muscle (2.3-fold). The maximum uptake of [³H]oleate by PVAT was 15.3-fold higher than its minimum and, therefore, comparable to other BAT depots, albeit that the peak in uptake (i.e. ZT18) was similar to WAT depots (**Figure 1H**). Most likely this discrepancy is explained by the fact that PVAT is a composed of a mixture of brown and white adipocytes.

Circadian rhythm of TG-derived fatty acid uptake adapts to photoperiod, only in BAT

Next, we assessed the ability of the various tissues to adapt the circadian rhythm of [³H]oleate uptake to either a short (8h) or long (16h) photoperiod. Interestingly, the photoperiod changed the circadian [³H]oleate uptake pattern only by brown adipocyte depots. Light exposure (LE) duration significantly determined [³H]oleate uptake by iBAT (*p*-value for LE, $p_{LE} = 0.0034$; **Figure 1F**), sBAT ($p_{LE} = 0.0085$; **Figure 1G**) and PVAT ($p_{LE} = 0.014$; **Figure 1H**), but not by liver ($p_{LE} = 0.141$; **Figure 1A**), sWAT ($p_{LE} = 0.75$; **Figure 1B**), gWAT ($p_{LE} = 0.3040$; **Figure 1C**), heart ($p_{LE} = 0.1765$; **Figure 1D**) and muscle

($p_{LE} = 0.3232$; **Figure 1E**). Short photoperiod increased the amplitude (*i.e.* difference between maximum and minimum uptake) of [^3H]oleate uptake by iBAT (264%) and sBAT (226%) compared to a photoperiod of 12h. Notably, photoperiod did not only determine amplitude, but also the timing of the maximum [^3H]oleate uptake by BAT. Long photoperiod delayed maximum [^3H]oleate uptake by iBAT from ZT12 to ZT18. Likewise, short photoperiod advanced and increased the maximum [^3H]oleate uptake by both iBAT and sBAT depots from ZT12 to ZT8. Strikingly, short photoperiod resulted in an increased area under the curve for [^3H]oleate uptake (**Figure 2A**) and increased the average [^3H]oleate uptake of all time points by iBAT (+190%; $p < 0.05$), sBAT (+207%; $p < 0.05$) and pVAT (+230%; $p < 0.05$) compared to long photoperiod (**Figure 2B**). The light exposure period (h) negatively correlated with [^3H]oleate uptake by iBAT ($R^2 = 0.107$, $p = 0.006$; **Figure 2C**), sBAT ($R^2 = 0.099$, $p = 0.010$; **Figure 2D**) and PVAT ($R^2 = 0.096$, $p = 0.011$; **Figure 2E**) and not by other metabolic organs (not shown).

Because changes in photoperiod specifically affected the circadian pattern of fatty acid uptake by the various brown adipocyte depots, we further investigated on the effect of photoperiod on BAT function. Since BAT activation decreases the lipid content of BAT (10) whereas BAT inactivation increases its lipid content (11), we histologically determined the daily rhythm of lipid content in BAT, and the effect of photoperiod thereon. A short photoperiod resulted in a maximum intracellular lipid depletion at time point ZT8 (**Figure 2F**) corresponding with the period of maximum uptake of [^3H]oleate by iBAT (**Figure 1F**). A long photoperiod delayed maximum lipid depletion to ZT18 (**Figure 2F**) at which a maximum uptake of [^3H]oleate by iBAT was observed (**Figure 1F**). Previously, we proposed that the SCN regulates BAT activity via the sympathetic nervous system (7). Since tyrosine hydroxylase (TH) is the rate-limiting enzyme in norepinephrine production and, therefore, a measure of sympathetic activity we next quantified TH content in BAT. The dip in lipid content at ZT8 during short photoperiod coincided with a peak in TH content in BAT (**Figure 2G**). Long photoperiod shifted the peak in TH to ZT18, corresponding to the maximum lipid depletion of BAT (**Figure 2F**) and maximum uptake of [^3H]oleate by iBAT (**Figure 1F**). These data indicate that the daily and seasonal rhythms in BAT activity indeed may depend on sympathetic outflow.

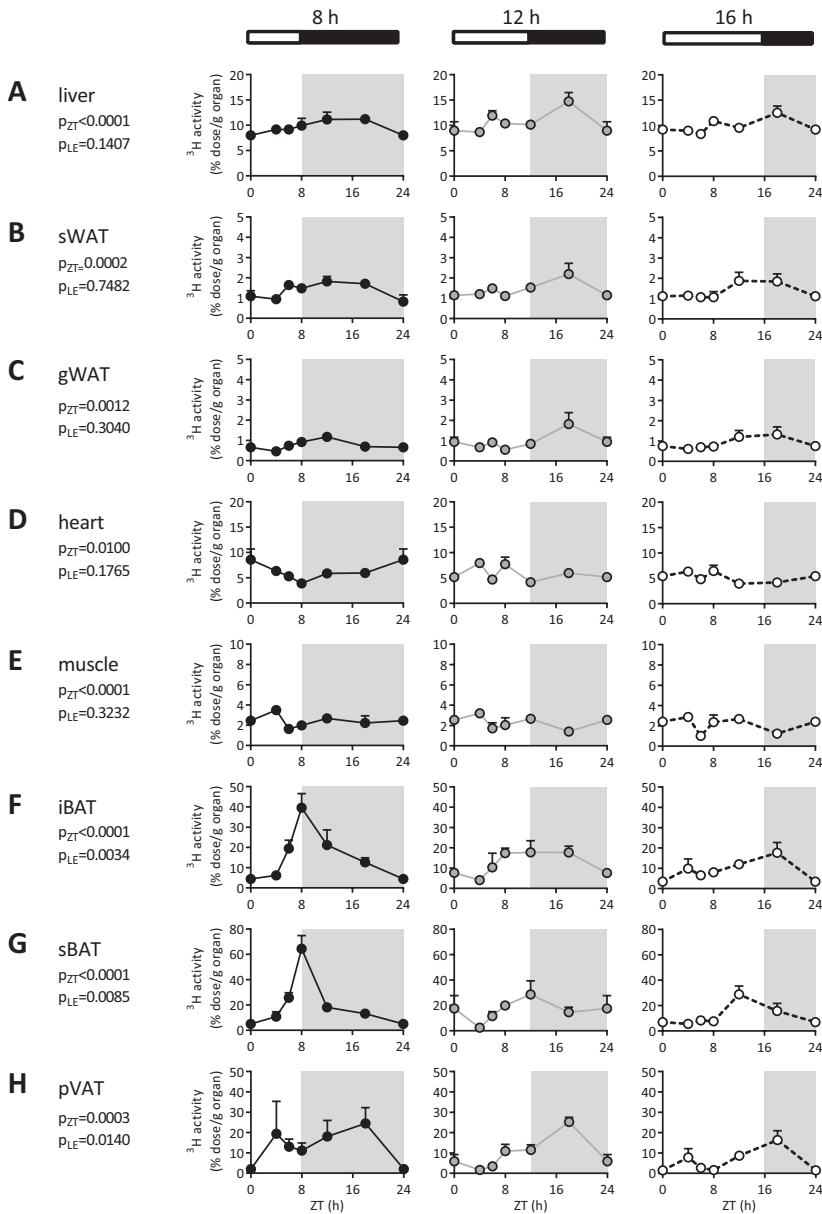


Figure 1 – Daily and seasonal rhythms in TG-derived fatty acid uptake in wild-type mice. Wild-type mice were exposed to photoperiods of 8, 12 or 16h of light per day for five weeks and injected with glycerol tri[^3H]oleate-labeled lipoprotein-like particles at six time points ($n=3-4$ /group). Mice were sacrificed and uptake of [^3H]oleate was determined for liver (**A**), sWAT (**B**), gWAT (**C**), heart (**D**), muscle (**E**), iBAT (**F**), sBAT (**G**) and PVAT (**H**). Data are presented as means \pm SEM and ZT0/ZT4 was double plotted for visualization purposes. P_{ZT} and P_{LE} represent p-values for the factors Zeitgeber Time (*i.e.* time point) and light exposure, respectively (two-way ANOVA). Abbreviations: iBAT, interscapular BAT; sBAT, subscapular BAT; pVAT, perivascular adipose tissue; sWAT, subcutaneous white adipose tissue; gWAT, gonadal white adipose tissue.

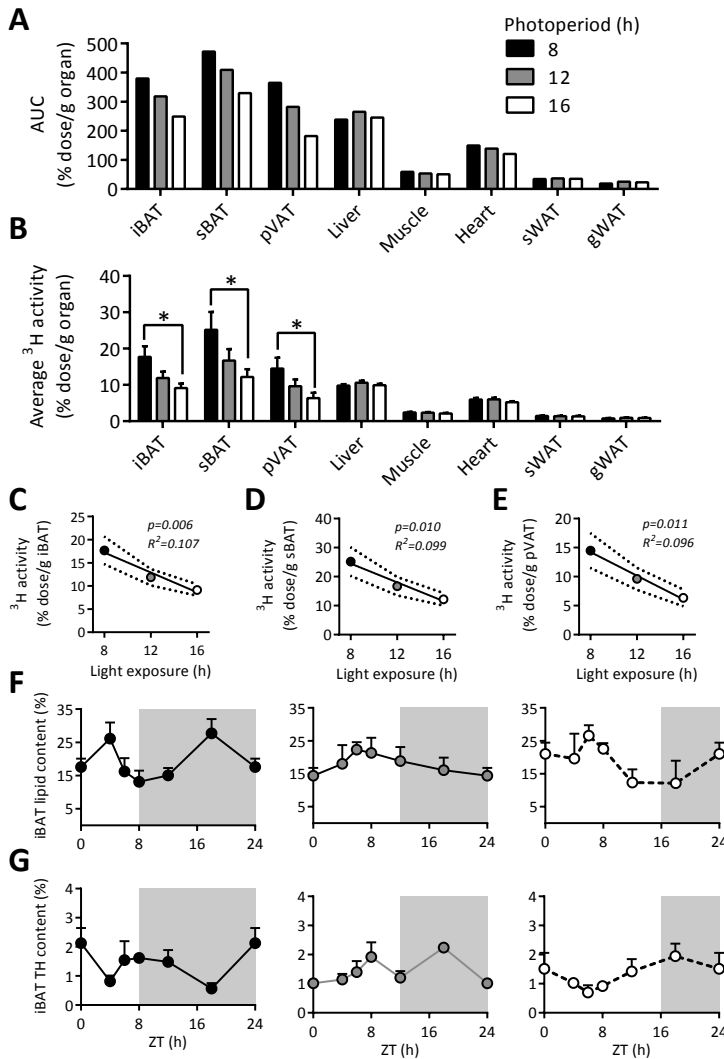


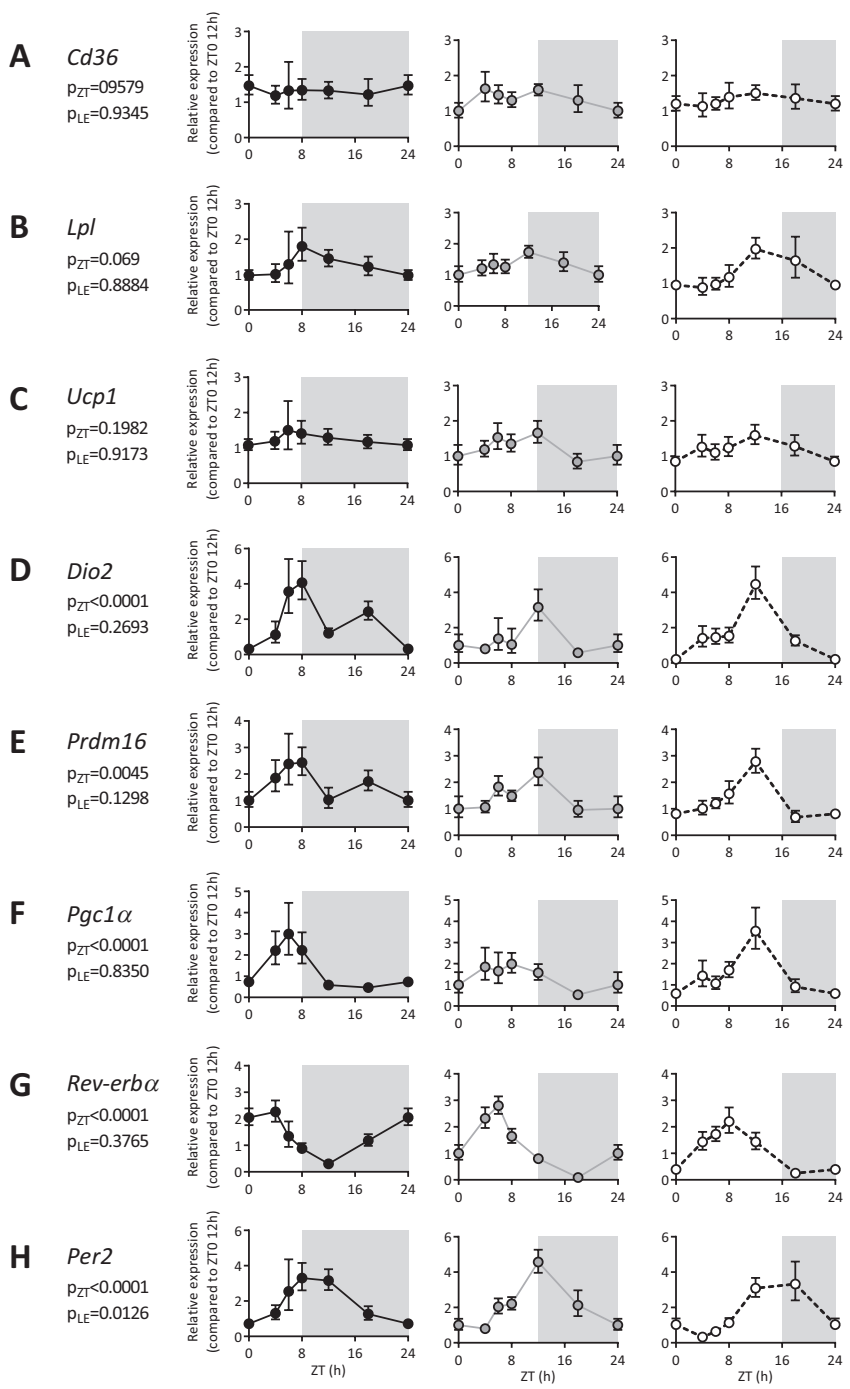
Figure 2 – Photoperiodic regulation of TG-derived fatty acid uptake by BAT of wild-type mice. Wild-type mice were exposed to photoperiods of 8, 12 or 16h of light per day for five weeks and injected with glycerol tri[³H]oleate-labeled lipoprotein-like particles (n=24/group). Mice were sacrificed at six time points [ZT 0, 4, 6, 8, 12, 18] and the area under the curve (A) and average daily uptake of [³H]oleate derived activity was determined (B). Interscapular BAT (iBAT) was collected for histological purposes. Intracellular lipid content was quantified from H&E stained sections (A) and tyrosine hydroxylase (TH) content was determined by immunohistochemistry (B). Data are presented as means ±SEM and ZT0/ZT24 was double plotted for visualization purposes. Correlations were made between photoperiod and uptake of [³H]oleate by iBAT (C), sBAT (D) and pVAT (E). Interscapular BAT (iBAT) was collected for histological purposes. Intracellular lipid content was quantified from H&E stained sections (F) and tyrosine hydroxylase (TH) content was determined by immunohistochemistry (G). * p<0.05 [one-way ANOVA, Tukey’s post-hoc test]. Correlations were analyzed by linear regression. Abbreviations: iBAT, interscapular BAT; sBAT, subscapular BAT; pVAT, perivascular adipose tissue; SWAT, subcutaneous white adipose tissue; gWAT, gonadal white adipose tissue.

The daily and seasonal rhythms of BAT activity coincide with expression of thermogenic genes.

Next, we determined expression patterns of key genes involved in BAT thermogenesis (Figure 3). Zeitgeber Time did not significantly determine expression of *Cd36* (Figure 3A), lipoprotein lipase (*Lpl*; Figure 3B) and uncoupling protein 1 (*Ucp1*; Figure 3C), but did determine gene expression of deiodinase type II (*Dio2*; Figure 3D), *Prdm16* (Figure 3E), peroxisome proliferator-activated receptor gamma coactivator 1-alpha (*Pgc1a*; Figure 3F) and clock genes *Rev-erba* (Figure 3G) and period 2 (*Per2*; Figure 3H) in iBAT. When mice were exposed to a regular photoperiod of 12h, gene expression of *Ucp1*, *Dio2*, *Prdm16* and *Pgc1a* were highest at ZT12 and lowest at ZT18 (1.9-fold, 5.1-fold, 2.4-fold and 4.6-fold difference, respectively). Gene expression of *Rev-erba* was highest at ZT6 and lowest at ZT18 (4.6-fold difference), while expression of *Per2* was highest at ZT12 and lowest at ZT4 (5.7-fold difference).

Light exposure duration significantly determined expression of *Per2* ($p_{LE}=0.0126$), as both long and short photoperiod shifted the rhythmic pattern. Long photoperiod only shifted the peak of *Pgc1a* expression from ZT8 to ZT12, and that of the clock genes *Rev-erba* from ZT6 to ZT8 and *Per2* from ZT12 to ZT18, while the maximum gene expression of the other genes remained at ZT12. Interestingly, short photoperiod resulted in a phase advance of the peaks in gene expression to ZT8 for *Lpl*, *Dio2* and *Prdm16*, and to ZT6 for *Ucp1* and *Pgc1a*, indicating adaptation the circadian expression of all these genes to the photoperiod.

► **Figure 3 – Daily and seasonal rhythms in gene expression in BAT of wild-type mice.** Wild-type mice were exposed to photoperiods of 8, 12 or 16h of light per day for five weeks and sacrificed at six time points ($n=4$ /group). Interscapular BAT (iBAT) was collected for gene expression analysis. Normalized gene expression was calculated for *Cd36* (A), *Lpl* (B), *Ucp1* (C), *Dio2* (D), *Prdm16* (E), *Pgc1a* (F) and clock genes *Rev-erba* (G) and *Per2* (H). Data are presented as means \pm SEM and ZT0/ZT24 was double plotted for visualization purposes.



Circadian rhythm in BAT activity determines diurnal variation in plasma TG levels

Since activation of BAT importantly contributes to lowering of plasma TG levels in hyperlipidemic mice (12), we next investigated the consequences of the circadian rhythm in BAT activity on plasma TG levels in hyperlipidemic *APOE*3-Leiden.CETP* mice. Mice were exposed to a photoperiod of 10h and after 5 weeks we determined the uptake of TG-derived fatty acids by BAT and other metabolic organs at the onset of light- and dark phase. The uptake of glycerol tri^[3H]oleate-derived ^[3H]oleate was higher at ZT10 compared to ZT0 for iBAT (4.2-fold; $p < 0.01$), sBAT (3.8-fold; $p < 0.05$) and sWAT (2.2-fold; $p < 0.01$), and lower for heart (1.6-fold; $p < 0.01$) (**Figure 4A**). The increase in ^[3H]oleate uptake at ZT10 compared to ZT0 by iBAT (up to 34 ± 6 % of injected dose/g organ) and sBAT (up to 33 ± 10 % of injected dose/g organ) resulted in an enhanced clearance of the radiolabel from the circulation (**Figure 4B**) reflected by a 1.6-fold shorter half-life (2.8 ± 0.2 min vs 4.5 ± 1.0 min; $p < 0.01$; **Figure 4C**), and was accompanied by lower plasma TG levels (7.2 ± 1.6 mM vs 3.0 ± 0.6 mM; $p < 0.05$; **Figure 4D**). These data indicate that the endogenous high activity of BAT at the start of the dark phase leads to increased TG clearance and lowering of plasma TG in hyperlipidemic mice.

Discussion

In the present study we investigated daily and seasonal rhythms in BAT. We show that circadian timing as well as photoperiodic seasonal information are important for BAT activity, as demonstrated by studies evaluating TG-derived fatty acid uptake from plasma, lipid content and expression of thermogenic genes. We found that BAT activity is the highest at the onset of the active, dark period. Strikingly, short photoperiod advanced the peak in BAT activity and resulted in an increased total capacity to take up circulating lipids, while long photoperiod reduced the uptake of fatty acids by BAT. Metabolic organs other than BAT, including liver, WAT, muscle and heart, also displayed a circadian pattern in their metabolic activity but did not adapt to photoperiodic changes.

While the daily peaks in TG-derived fatty acid uptake by WAT and liver corresponded with periods of excessive energy availability (*i.e.* active period at dark phase) and the uptake by heart and muscle with the period of low carbohydrates (*i.e.* inactive period during light phase), the uptake of BAT depots reached its maximum at the onset of the dark phase. In addition, we observed high TH content, lipid depletion and high expression of key thermogenic genes at the same time, overall indicating increased BAT activity just before waking. These patterns are in line with a previous report on circadian rhythm in glucose uptake by BAT using [¹⁸F]FDG-PET-CT scanning (6) and correspond with the known rhythm in core temperature for mice, which declines

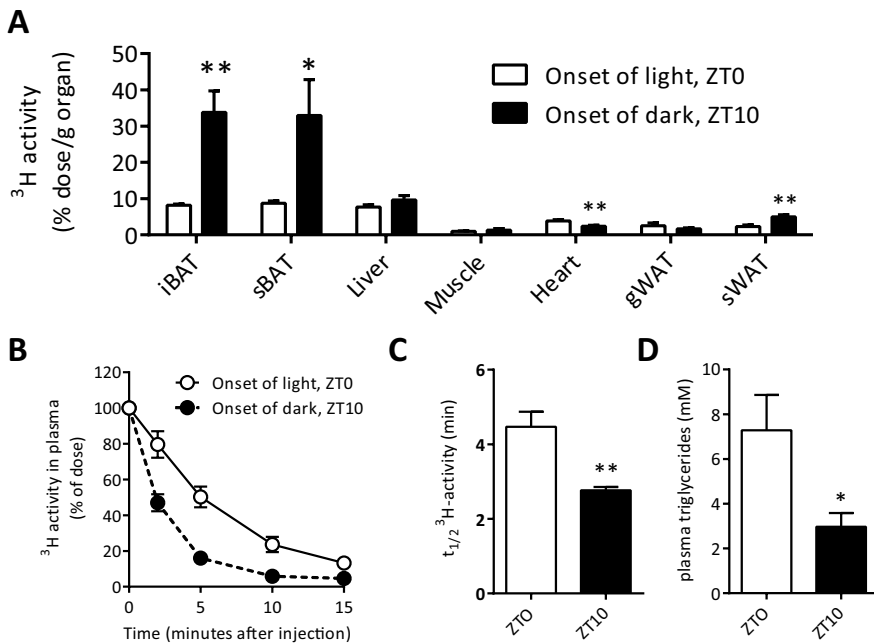


Figure 4 – Daily rhythms in TG metabolism in hyperlipidemic *APOE*3-Leiden.CETP* mice. *APOE*3-Leiden.CETP* mice were exposed to a photoperiod of 10h of light per day. After 5 weeks, mice were injected with glycerol tri[³H]oleate-labeled lipoprotein-like particles at ZT0 and ZT10 (n=6/ time point). Uptake of [³H]oleate by various metabolic organs was determined (A). [³H]oleate was quantified in plasma at several time points after injection and expressed as percentage of the injected dose (B), and the plasma half-life of [³H]oleate was calculated (C). Triglycerides were measured in plasma at the onset and light phase [ZT0] and dark phase [ZT10] (D). Data are presented as means ±SEM. *p<0.05, **p<0.01 (T-test). Abbreviations: iBAT, interscapular BAT; sBAT, subscapular BAT; pWAT, perivascular adipose tissue; sWAT, subcutaneous white adipose tissue; gWAT, gonadal white adipose tissue.

during sleep and rises before wake (13). The pronounced gene in *Pgc1a*, *Ucp1*, *Prdm16* and *Dio2* are in line with previous reports of gene expression under normal photoperiod regimes (3,14,15). The rhythmicity of *Ucp1* seems less consistent as one study found a high amplitude (3) while others reported weaker rhythmicity (15) similar to the present data. A possible explanation for this discordance is that *Ucp1* expression may be more influenced by fasting or feeding of the mice, since the feeding state varies across the different studies.

We found large differences in uptake of TG-derived fatty acids and expression of genes involved in thermogenesis, including *Prdm16* and *Pgc1a*, by BAT along the day, indicating that disturbed circadian rhythmicity may have considerable effects on BAT function and adiposity. Indeed, genetic mouse models of circadian dysfunction,

among others *Clock^{mt/mt}* mice (16) and *Per2^{-/-}* mice (17), are prone to develop obesity. In addition lesioning of the SCN and continuous light exposure result in disturbed circadian behavior and acute weight gain (7,18,19). However, these severe models for disturbed circadian rhythmicity can be considered as a pathophysiological condition. In the current study, exposure to a photoperiod of 16h was sufficient to severely diminish the uptake of TG-derived fatty acids by BAT when compared to short photoperiod, which most likely corresponded with lower energy expenditure. Comparable, hibernating animals typically increase their food intake and decrease energy expenditure during summer, resulting in lipid deposition in WAT (20). Conversely, during winter hibernating animals almost exclusively rely on lipid oxidation. These changes in energy expenditure can partly be mimicked by exposing animals to different photoperiods under laboratory conditions (20). Interestingly, this regulation of energy balance by photoperiod is not limited to hibernating animals. Switching photoperiod in field voles to a length of 16h increases body weight by 24% in 4 weeks compared to animals that remained on a photoperiod of 8h (21). Further, it has been reported that overweight and obese children experience accelerated weight gain during the summer (22), suggesting that photoperiodic regulation of energy expenditure may apply to humans as well.

It is tempting to speculate why especially BAT is sensitive to changes in photoperiod, reflecting seasonal regulation, with respect to TG uptake, compared to other metabolic organs such as white adipose tissue, liver, muscle and heart. Heat production by BAT is activated whenever the animal is in need of extra heat, e.g. during arousal from hibernation or upon wakening, so a possible explanation is the adaptation to photoperiodic changes in sleep-wake pattern (23). However, this does probably not explain the change in overall daily capacity of BAT to take up TG-derived fatty acids as observed within our study. As noted before, detectability of human BAT by [¹⁸F]FDG PET-CET scans at room temperature displays a stronger correlation with photoperiod than ambient temperature (6), and changes in photoperiod and BAT detectability seem to occur before changes in outside temperature. Therefore, a change in photoperiod likely signals to BAT to be prepared for upcoming seasonal changes, as in general, changes in photoperiod precede changes in ambient temperature.

Despite the increasing interest in circadian clock research, the exact mechanism how light information is perceived by the eye and transmitted to the periphery is not fully understood. Lesioning of the SCN does not lead to loss of cyclic activity in metabolic organs, but does prevent synchronization of peripheral clocks to the environment (24). As synchronization of peripheral clocks occurs during seasonal adaptation, the SCN is likely crucial for the regulation of seasonal adaptation. Studies reported that the SCN communicates to the periphery via the autonomic nervous system, via hormonal cues such as corticosterone and melatonin, and via rhythmic

behavior (25). Considering the importance of the sympathetic activity for cold-induced thermogenesis (1,26) and the direct neuronal connection between the SCN and BAT (1), it is likely that the autonomic nervous system regulates circadian and seasonal rhythmicity in BAT. Compatible with this hypothesis, in this study we found peaks in TH content of BAT occurring simultaneously with lipid depletion in BAT, uptake of TG-derived fatty acids by BAT and expression of thermogenic genes in BAT. In addition, we recently demonstrated that prolonged daily light exposure diminishes BAT activity, an effect that was abolished by surgical sympathetic denervation of the tissue (7).

In summary, we identified circadian and seasonal rhythms in BAT activity, contributing to diurnal rhythmicity in TG plasma levels in dyslipidemic mice. Future studies should reveal to what extent these data can be extrapolated to humans. At least in light of pre-clinical research on BAT activity, but potentially also in clinical research, timing of experiments clearly is a crucial factor that should be carefully considered.

Acknowledgements

This work was supported by the Netherlands Organization for Scientific Research (NWO-VENI grant 016.136.125 to NR Biermasz), the European Foundation for the Study of Diabetes and the Programme Partner Novo Nordisk (grant 94802 to CP Coomans, JH Meijer and PCN Rensen) and the Dutch Diabetes Research Foundation (grant 2013.81.1663 to CP Coomans). PCN Rensen is an Established Investigator of the Netherlands Heart Foundation (grant 2009T038). The authors declare no conflict of interest.

References

- Bamshad, M., Song, C. K., & Bartness, T. J. (1999) CNS origins of the sympathetic nervous system outflow to brown adipose tissue. *Am J Physiol* 276, R1569-R1578.
- Amir, S., Shizgal, P., & Rompre, P. P. (1989) Glutamate injection into the suprachiasmatic nucleus stimulates brown fat thermogenesis in the rat. *Brain Res* 498, 140-144.
- Yang, X., Downes, M., Yu, R. T. *et al.* (2006) Nuclear receptor expression links the circadian clock to metabolism. *Cell* 126, 801-810.
- Gerhart-Hines, Z., Feng, D., Emmett, M. J. *et al.* (2013) The nuclear receptor Rev-erb α controls circadian thermogenic plasticity. *Nature* 503, 410-413.
- VanderLeest, H. T., Houben, T., Michel, S. *et al.* (2007) Seasonal encoding by the circadian pacemaker of the SCN. *Curr Biol* 17, 468-473.
- van der Veen, D. R., Shao, J., Chapman, S. *et al.* (2012) A diurnal rhythm in glucose uptake in brown adipose tissue revealed by in vivo PET-FDG imaging. *Obesity (Silver Spring)* 20, 1527-1529.
- Kooijman, S., van den Berg, R., Ramkisoensing, A. *et al.* (2015) Prolonged daily light exposure increases body fat mass through attenuation of brown adipose tissue activity. *Proc Natl Acad Sci USA*.
- Westerterp, M., van der Hoogt, C. C., de, H. W. *et al.* (2006) Cholesteryl ester transfer protein decreases high-density lipoprotein and severely aggravates atherosclerosis in APOE*3-Leiden mice. *Arterioscler Thromb Vasc Biol* 26, 2552-2559.
- Rensen, P. C., Herijgers, N., Netscher, M. H. *et al.* (1997) Particle size determines the specificity of apolipoprotein E-containing triglyceride-rich emulsions for the LDL receptor versus hepatic remnant receptor in vivo. *J Lipid Res* 38, 1070-1084.
- Berbee, J. F., Boon, M. R., Khedoe, P. P. *et al.* (2015) Brown fat activation reduces hypercholesterolaemia and protects from atherosclerosis development. *Nat Commun* 6, 6356.
- Kooijman, S., Boon, M. R., Parlevliet, E. T. *et al.* (2014) Inhibition of the central melanocortin system decreases brown adipose tissue activity. *J Lipid Res* 55, 2022-2032.
- Bartelt, A., Bruns, O. T., Reimer, R. *et al.* (2011) Brown adipose tissue activity controls triglyceride clearance. *Nat Med* 17, 200-205.
- Refinetti, R. (2012) Integration of biological clocks and rhythms. *Compr Physiol* 2, 1213-1239.
- Hatori, M., Vollmers, C., Zarrinpar, A. *et al.* (2012) Time-restricted feeding without reducing caloric intake prevents metabolic diseases in mice fed a high-fat diet. *Cell Metab* 15, 848-860.
- Paschos, G. K., Ibrahim, S., Song, W. L. *et al.* (2012) Obesity in mice with adipocyte-specific deletion of clock component Arntl. *Nat Med* 18, 1768-1777.
- Turek, F. W., Joshu, C., Kohsaka, A. *et al.* (2005) Obesity and metabolic syndrome in circadian Clock mutant mice. *Science* 308, 1043-1045.
- Yang, S., Liu, A., Weidenhammer, A. *et al.* (2009) The role of mPer2 clock gene in glucocorticoid and feeding rhythms. *Endocrinology* 150, 2153-2160.
- Coomans, C. P., van den Berg, S. A., Houben, T. *et al.* (2013) Detrimental effects of constant light exposure and high-fat diet on circadian energy metabolism and insulin sensitivity. *FASEB J* 27, 1721-1732.
- Coomans, C. P., van den Berg, S. A., Lucassen, E. A. *et al.* (2013) The suprachiasmatic nucleus controls circadian energy metabolism and hepatic insulin sensitivity. *Diabetes* 62, 1102-1108.
- Dark, J. (2005) Annual lipid cycles in hibernators: integration of physiology and behavior. *Annu Rev Nutr* 25, 469-497.
- Krol, E., Redman, P., Thomson, P. J. *et al.* (2005) Effect of photoperiod on body mass, food intake and body composition in the field vole, *Microtus agrestis*. *J Exp Biol* 208, 571-584.
- Baranowski, T., O'Connor, T., Johnston, C. *et al.* (2014) School year versus summer differences in child

- weight gain: a narrative review. *Child Obes* 10, 18-24.
23. Deboer, T. & Tobler, I. (1996) Shortening of the photoperiod affects sleep distribution, EEG and cortical temperature in the Djungarian hamster. *J Comp Physiol A* 179, 483-492.
24. Cailotto, C., La Fleur, S. E., Van, H. C. et al. (2005) The suprachiasmatic nucleus controls the daily variation of plasma glucose via the autonomic output to the liver: are the clock genes involved? *Eur J Neurosci* 22, 2531-2540.
25. Buijs, R. M. & Kalsbeek, A. (2001) Hypothalamic integration of central and peripheral clocks. *Nat Rev Neurosci* 2, 521-526.
26. Tupone, D., Madden, C. J., & Morrison, S. F. (2014) Autonomic regulation of brown adipose tissue thermogenesis in health and disease: potential clinical applications for altering BAT thermogenesis. *Front Neurosci* 8, 14.

6

PERIPHERAL CANNABINOID 1 RECEPTOR BLOCKADE ACTIVATES BROWN ADIPOSE TISSUE AND DIMINISHES DYSLIPIDEMIA AND OBESITY

Sander Kooijman*

Mariëtte R. Boon*

Andrea D. van Dam

Leonard R. Pelgrom

Jimmy F.P. Berbée

Cheryl A.R. Visseren

Robin C. van Aggele

Anita M. van den Hoek

Hetty C.M. Sips

Marc Lombès

Louis M. Havekes

Jouke T. Tamsma

Bruno Guigas

Onno C. Meijer

J. Wouter Jukema

Patrick C.N. Rensen

*Authors contributed equally

Abstract

The endocannabinoid system is an important player in energy metabolism by regulating appetite, lipolysis and energy expenditure. Chronic blockade of the cannabinoid 1 receptor (CB1R) leads to long-term maintained weight loss and reduction of dyslipidemia in experimental and human obesity. The molecular mechanism by which CB1R blockade reverses dyslipidemia in obesity has not been clarified yet. In this study, we showed that CB1R blockade with the systemic CB1R blocker rimonabant enhanced whole-body energy expenditure and activated brown adipose tissue (BAT) indicated by increased expression of genes involved in BAT thermogenesis and decreased lipid droplet size in BAT. This was accompanied by selectively increased triglyceride (TG) uptake by BAT and lower plasma TG levels. Interestingly, the effects on BAT activation were still present at thermoneutrality and could be recapitulated by using the strictly peripheral CB1R antagonist AM6545, indicating direct peripheral activation of BAT. Indeed, CB1R blockade directly activated T37i brown adipocytes resulting in enhanced uncoupled respiration, most likely via enhancing cAMP/PKA signalling via the adrenergic receptor pathway. Our data indicate that selective targeting of the peripheral CB1R in BAT has therapeutic potential in attenuating dyslipidemia and obesity.

Introduction

The endocannabinoid system regulates a broad range of physiological functions (1) and consists of G-protein coupled cannabinoid receptors, its endogenous lipid ligands (endocannabinoids) and the enzymes involved in the biosynthesis and degradation of endocannabinoids (2,3). The cannabinoid type 1 receptor (CB1R) is expressed at high levels in the brain but also at functionally relevant concentrations in various peripheral tissues (1). In contrast, the cannabinoid type 2 receptor is mainly expressed on immune cells (4). CB1R knockout mice display reduced adiposity and are resistant to diet-induced obesity (5). Moreover, overweight and obese humans exhibit an overactive endocannabinoid system (6,7), suggesting a role of the endocannabinoid system in energy metabolism.

Chronic systemic blockade of the CB1R with the inverse agonist rimonabant leads to long-term maintained weight loss and reduction of dyslipidemia in obese rodents (8,9) and humans (10-13). Rimonabant was considered one of the most promising therapeutic drugs to treat obesity, until the appearance of central psychiatric side effects resulted in its removal from the market in 2008. Nevertheless, several lines of evidence indicate that the effect of CB1R blockade is not restricted to a central mode of action, especially since the CB1R has been shown to be present in peripheral tissues including the liver (14), skeletal muscle (15) and adipocytes (16). More specifically, Tam *et al.* (17) recently showed that the strictly peripheral CB1R antagonist AM6545 induced weight loss and diminished hepatic steatosis in a mouse model. Thus, it seems plausible that psychiatric side effects can be avoided by strict peripheral blockade of the CB1R, while retaining the beneficial anti-obesity and lipid-lowering effects.

Despite clear evidence that pharmacological CB1R antagonism improves dyslipidemia, the exact mechanisms and the peripheral tissues involved have not yet been elucidated. Recently, brown adipose tissue (BAT) emerged as an important player in triglyceride (TG) clearance (18). In contrast to white adipose tissue (WAT), which stores excess TG as fat, BAT dissipates energy into heat, a process mediated by the mitochondrial uncoupling protein-1 (UCP-1) (19). The best known trigger for activation of BAT is cold, which increases sympathetic outflow from the hypothalamic temperature centre towards BAT, leading to release of noradrenalin and increased thermogenesis (19). Metabolically active BAT stores exist in adult humans (20-22), and BAT volume and activity are lower in obese subjects (21). In addition, BAT volume and activity are lower in South Asians, a population prone to develop type 2 diabetes mellitus and cardiovascular disease (23). Together, these findings have increased interest in the therapeutic potential of BAT to combat obesity and related disorders, such as dyslipidemia.

In this study, we aimed at elucidating the molecular mechanism by which CB1R blockade attenuates dyslipidemia in diet-induced obesity by using a mouse model for human-like lipoprotein metabolism.

MATERIALS & METHODS

Animals and diet

6

Homozygous human cholesteryl ester transfer protein (CETP) transgenic mice were crossbred with hemizygous APOE*3-Leiden (E3L) mice at our Institutional Animal Facility to obtain E3L.CETP mice, as previously described (24). We chose to perform our studies in this specific mouse model, since these mice are a well-established model for human-like lipoprotein metabolism and respond to lipid-lowering pharmacological interventions (24-26). In all the studies described below, 10 week-old E3L.CETP male mice were housed under standard conditions in conventional cages in a 12:12 h light: dark cycle with *ad libitum* access to food and water, and were fed a high-fat diet (HFD; Research diets, New Brunswick, USA, 60% lard fat) for 12 weeks to induce obesity. From the 7th week onwards, the drinking water was supplied with 10% fructose. All mouse experiments were performed in accordance with the Institute for Laboratory Animal Research Guide for the Care and Use of Laboratory Animals and have received approval from the Departmental Ethical Review Board (Leiden University Medical Center, Leiden, The Netherlands).

Pharmacological intervention

After 12 weeks of HFD, diet-induced obese (DIO) mice were randomised according to their body weight and plasma total cholesterol (TC) and triglyceride (TG) levels into four groups. Subsequently, mice were housed at either 21°C (subthermoneutral) or 28°C (thermoneutral), and received 60% HFD with or without 10 mg/kg body weight/day (0.00885%, w/w) rimonabant (Axon Medchem, Groningen, the Netherlands) or AM6545 (Sigma-Aldrich, St. Louis, USA) for 4 weeks.

Body weight and food intake

In all experiments, mice were housed individually during the 4 week treatment period. Food intake was recorded daily by weighing the food that was left in the cage or was recorded automatically in metabolic cages (see below). Body weight was measured twice a week.

Indirect calorimetry and physical activity

Indirect calorimetry was performed in fully automatic metabolic cages (LabMaster System, TSE Systems, Bad Homburg, Germany) during the fourth week of treatment. After 20 h acclimatization, oxygen uptake ($\dot{V} \text{ O}_2$), carbon dioxide production ($\dot{V} \text{ CO}_2$)

and caloric intake were measured for 5 consecutive days. Carbohydrate (CHO) and fat oxidation rates were calculated from $\dot{V} \text{ O}_2$ and $\dot{V} \text{ CO}_2$ as described previously (27). Total energy expenditure (EE) was calculated from $\dot{V} \text{ O}_2$ and $\dot{V} \text{ CO}_2$ using the Weir equation (28). Physical activity was measured using infrared sensor frames.

Dual-energy X-ray absorptiometry (DEXA) scan

After 4 weeks treatment, body composition was measured by DEXA using the Norland pDEXA Sabre X-ray Bone Densitometer. Mice were anaesthetized intraperitoneally with a combination of 6.25 mg/kg acepromazine (Alfasan), 6.25 mg/kg midazolam (Roche) and 0.31 mg/kg fentanyl (Janssen-Cilag). The total body of the mice was scanned, yet the heads were excluded from the analyses.

Plasma parameters

Blood was collected from the tail vein of 4-6 hour fasted mice into chilled capillaries that were coated with paraoxon (Sigma, St. Louis, MO) to prevent ongoing lipolysis (29). Capillaries were placed on ice and centrifuged, and plasma was assayed for TG, TC, and phospholipids (PL) using commercially available enzymatic kits from Roche Diagnostics (Mannheim, Germany for TG and TC) and Instruchemie (Delfzijl, the Netherlands for PL). Free fatty acids (FFA) were measured using NEFA C kit from Wako Diagnostics (Instruchemie, Delfzijl, The Netherlands).

Lipoprotein profiles

To determine lipid distribution over plasma lipoproteins, pooled plasma was used for fast performance liquid chromatography (FPLC). Plasma was injected onto a Superose 6 column (ÄKTA System, Amersham Pharmacia Biotech, Piscataway, NJ) and eluted at a constant flow rate of 50 $\mu\text{L}/\text{min}$ with PBS pH 7.4. TG and TC were measured as described above in collected fractions of 50 μL .

In vivo clearance of labeled VLDL-like emulsion particles

VLDL-like TG-rich emulsion particles (80 nm) labeled with glycerol tri[^3H]oleate (triolein, TO) were prepared and characterized as described previously (30). To study the *in vivo* clearance of the VLDL-like particles, mice were fasted for 4 h and injected ($t = 0$) via the tail vein with 200 μL of emulsion particles (1.0 mg TG per mouse). Blood samples were taken from the tail vein at 2, 10, 20 and 30 min after injection to determine the serum decay of [^3H]TO. Plasma volumes were calculated as $0.04706 \times \text{body weight (g)}$ as determined from ^{125}I -BSA clearance studies as described previously (31). After taking the last blood sample, mice were cervically dislocated and perfused with ice-cold PBS via the heart to remove blood from the organs. Subsequently, the liver, heart, spleen, hindlimb muscle, gonadal WAT (gWAT), subcutaneous WAT (sWAT) and brown adipose tissue (BAT) were collected. Organs

were dissolved overnight at 60°C in Tissue Solubilizer (Amersham Biosciences, Rosendaal, The Netherlands), and ^3H activity was quantified. Uptake of [^3H]TO-derived radioactivity by the organs was expressed per gram wet tissue weight.

In vivo hepatic VLDL-TG and VLDL-apoB production

To measure VLDL production *in vivo*, mice were fasted for 4 h and anesthetized by intraperitoneal injection of 6.25 mg/kg acepromazine (Alfasan), 6.25 mg/kg midazolam (Roche) and 0.31 mg/kg fentanyl (Janssen-Cilag). Mice were injected intravenously with Tran [^{35}S] label (150 $\mu\text{Ci}/\text{mouse}$) (MP Biomedicals, Eindhoven, The Netherlands) to label newly produced apolipoprotein B (apoB). After 30 min, at $t=0$ min, Triton WR-1339 (Sigma-Aldrich) was injected intravenously (0.5 mg/g body weight, 10% solution in PBS) to block serum VLDL-TG clearance. Blood samples were drawn before ($t = 0$) and at 15, 30, 60, and 90 min after injection of Triton WR-1339 and used for determination of plasma TG concentration as described above. After 90 min, mice were exsanguinated via the retro-orbital plexus. VLDL was isolated from serum after density gradient ultracentrifugation at $d < 1.006$ g/mL by aspiration [32] and examined for incorporated ^{35}S -activity.

RNA isolation and qRT-PCR analysis

Total RNA was isolated with the Nucleospin® RNA II Kit (Macherey-Nagel) according to the manufacturer's instructions. 1 μg of total RNA was reverse-transcribed with iScript cDNA synthesis kit (Bio-Rad), and the obtained cDNA was purified with Nucleospin Extract II kit (Macherey-Nagel). Real-time PCR was carried out on the IQ5 PCR machine (Bio-Rad) using the Sensimix SYBR Green RT-PCR mix (Quantace). Melt curve analysis was included to assure a single PCR product was formed. Expression levels were normalized using glyceraldehyde-3-phosphate dehydrogenase (*Gapdh*), *$\beta 2$ -microglobulin* and *36b4* as housekeeping genes. Primer sequences are listed in **Table 1**.

Histology

Interscapular BAT, liver and sWAT were removed and fixed directly in 4% paraformaldehyde, dehydrated and embedded in paraffin. For UCP-1 staining in BAT, sections (5 μm) were dewaxed in xylene, rehydrated in ethanol and treated with 3% H_2O_2 (Sigma) in absolute methanol for 30 min. Next, sections were immersed in 10 mmol/L citrate buffer (pH 6.0), boiled for 10 min and cooled down at room temperature. Slides were blocked during 60 min with normal goat serum (1:75 in PBS) and incubated overnight at 4°C with rabbit monoclonal anti-UCP-1 antibodies (Abcam) diluted 1:400 in normal goat serum (1:75). Next, sections were incubated for 60 min with biotinylated goat α -rabbit secondary antibodies (Vector Labs) diluted 1:600 in normal goat serum (1:75). Immunostaining was amplified using Vector

Table 1 – List of primer sequences for RT-PCR

Gene	Forward primer	Reverse primer
<i>36b4</i>	GGACCCGAGAAGACCTCCTT	GCACATCACTCAGAATTTCAATGG
<i>Acc2</i>	AGATGGCCGATCAGTACGTC	GGGGACCTAGGAAAGCAATC
<i>Acs1l</i>	TGCCAGAGCTGATTGACATTC	GGCATAACCAGAAGGTGGTGAG
<i>Atgl</i>	ACAGTGTCCCCATTCTCAGG	TTGGTTCAGTAGGCCATTCC
<i>β2-microglobulin</i>	TGACCGGCTTGATGCTATC	CAGTGTGAGCCAGGATATAG
<i>Cd36</i>	GCAAAGAACAGCAGCAAAATC	CAGTGAAGGCTCAAAGATGG
<i>Fasn</i>	GCGCTCCTCGCTTGTCGTCT	TAGAGCCCAGCCTTCCATCTCCTG
<i>Hsl</i>	AGACACCAGCCAACGGATAC	ATCACCTCGAAGAAGAGCA
<i>Lpl</i>	CCCTAAGGACCCCTGAAGAC	GGCCCCGATACAACCAAGTCTA
<i>Pgc1a</i>	TGCTAGCGGTTCTCACAGAG	AGTGCTAAGACCGCTGCATT
<i>Prdm16</i>	ACTTTGGATGGGAGCAGATG	CTCCAGGCTCGATGTCCTTA
<i>Scd1</i>	GCGATACACTCTGGTGCTCA	CCCAGGAAAACCAGGATATT
<i>Ucp1</i>	TCAGGATTGGCCTCTACGAC	TGCATTCTGACCTTACGAC

Laboratories Elite ABC kit (Vector Labs) and the immunoperoxidase complex was visualized with Nova Red (Vector Labs). Counterstaining was performed with Mayer's hematoxylin (1:4). Haematoxylin and Eosin stainings of liver and sWAT sections were done using standard protocols. Intracellular lipid content in BAT was quantified by use of ImageJ (version 1.47).

Liver lipid extraction

Lipids were extracted from livers consistent with a modified protocol from Bligh and Dyer (33). Small liver samples (approx. 50 mg) were homogenized in 10 µL of ice-cold methanol per mg tissue. Lipids were extracted into an organic phase by adding 1800 µL of CH₃OH: CHCl₃ (3:1, vol/vol) to 45 µL of homogenate and subsequent centrifugation. The lower, organic phase was dried and suspended in 2% Triton X-100. Hepatic TG and TC concentrations were measured using commercial kits, as explained (see: *Plasma parameters*). Liver lipids were expressed per milligram of protein, which was determined using the BCA protein assay kit (Thermo Scientific, Rockford, IL, USA).

In vitro experiments with brown adipocytes

The murine brown preadipocyte cell line T37i (34) was cultured in HAM'S-F12 medium (Gibco-Invitrogen) supplemented with 10% fetal calf serum, 2 mM HEPES, 100 U/mL penicillin and 100 µg/mL streptomycin (Gibco-Invitrogen). For experiments, T37i cells were seeded in 6-wells plates and grown towards confluence. Two days after reaching confluence, cells were differentiated using normal culture medium supplemented with 2 nM triiodothyronine (T3) (Sigma) and 112 ng/mL bovine insulin (Sigma). The differentiation medium was replaced every 2 or 3 days. After 9 days of

differentiation, cells were stimulated for 8 h with rimonabant (Axon Medchem) at 0.1 μM or 1 μM or with vehicle (DMSO) in absence or presence of noradrenalin (1 μM). Subsequent experiments were performed after pre-incubation for 1 h with and in the presence of PKA inhibitor H89 (25 μM). Then, 500 μL of supernatant was collected and snap-frozen in liquid nitrogen. Cells were washed twice with ice-cold PBS and cells were harvested in ice-cold lysis buffer as described below.

Oxygen consumption measurements

A Seahorse Bioscience XF24 extracellular flux analyzer (Seahorse Biosciences, North Billerica, MA, USA) was used to measure oxygen consumption rate (OCR) in differentiated T37i cells. T37i cells were differentiated in T75 flasks. On day 9 of differentiation, the cells were trypsinized and seeded in poly-D-lysine (Sigma Aldrich) coated 24-well-Seahorse-assay plates. The next day, the cells were treated with DMSO vehicle or rimonabant (1 μM). After 4 h, the cells were placed in freshly prepared seahorse medium comprising DMEM with 5 mM glucose and 1 mM pyruvate with pH 7 and incubated for 1 h in a 37°C incubator without supplemental CO_2 . The ATP synthetase inhibitor oligomycin and the β_3 -specific agonist CL316,243 (Tocris) were preloaded in the reagent delivery chambers of the Seahorse sensor cartridge and then pneumatically injected into the wells to reach final working concentrations. Three baseline OCR measurements were performed, followed by injection with CL316,243 to a final concentration of 1 μM or oligomycin to a final concentration of 0.5 μM . Post exposure OCR was measured three times after 2 min of mixing. The averages of three baseline measurements and three post-exposure OCRs were used for data analyses.

In vitro experiments with white adipocytes

3T3-L1 cells (mouse embryonic fibroblast cells, ATCC CCL 92.1) were cultured at 37 °C under 5% CO_2 in DMEM containing GlutaMAX (4.5 g/L L-D-Glucose and sodium pyruvate) (GIBCO) supplemented with 10% fetal calf serum (FCS, GIBCO), 100 U/mL penicillin and 100 $\mu\text{g}/\text{mL}$ streptomycin (Gibco-Invitrogen). Confluent 3T3-L1 cells were induced to differentiate by treatment with a combination of 1.5 μM insulin, 0.5 mM 3-isobutyl-1-methylxanthine (IBMX, Sigma) and 1 μM dexamethasone (Sigma). After 48 h of treatment the differentiation was maintained by addition of culture medium that contained 10 μM insulin. After 15 days of differentiation, cells were stimulated for 8 h with rimonabant (Axon Medchem) at 0.1 μM or 1 μM or with vehicle (DMSO). Then, 500 μL of supernatant was collected and snap-frozen in liquid nitrogen.

Protein isolation and Western blot

T37i cells or snap-frozen tissue samples were lysed in ice-cold buffer containing 50 mM Hepes (pH 7.6), 50 mM NaF, 50 mM KCl, 5 mM NaPPi, 1 mM EDTA, 1 mM EGTA, 1 mM DTT, 5 mM β -glycerophosphate, 1 mM sodium vanadate, 1% NP40 and protease inhibitors using cocktail tablets (Roche). Homogenates were centrifuged at 13,000 rpm for 15 min at 4°C and the protein content of the supernatant was determined using the BCA Protein Assay Kit from Thermo Scientific. Proteins (20 μ g) were separated by 10% SDS-PAGE followed by transfer to a polyvinylidene fluoride transfer membrane (Merck, Amsterdam, The Netherlands). Membranes were blocked for 1 h at room temperature in Tris-buffered saline tween-20 buffer with 5% non-fat dry milk followed by an overnight incubation with specific primary antibodies. Primary antibodies specific for cannabinoid type 1 receptor (CB1R), E2-F, AMPK, P-AMPK, ACC, P-ACC, P-HSL (ser563), P-HSL (ser565) and tubulin were purchased from Cell Signaling (Leiden, The Netherlands). A primary antibody specific for uncoupling protein 1 (UCP1) was purchased from Sigma-Aldrich. All antibodies were diluted 1:1000. Blots were incubated with horseradish peroxidase-conjugated secondary antibodies for 1 h at room temperature. Bands were visualized with SuperSignal West Pico Chemiluminescent Substrate (Pierce) and quantified using ImageJ (version 1.47).

Statistical analysis

All data are expressed as mean \pm SEM. Statistical analysis using the unpaired two-tailed Student's test was performed with the SPSS 20.0 software package for Windows (SPSS, Chicago, United States) to determine differences between vehicle- and compound-treated groups. A P-value < 0.05 was considered statistically significant.

RESULTS

Systemic CB1R blockade by rimonabant in DIO mice reduces obesity and dyslipidemia and increases energy expenditure

To investigate the effect of systemic CB1R blockade on body composition and energy balance, E3L.CETP transgenic mice were fed a HFD for 12 weeks to render them obese (mean body weight: 53.2 \pm 0.9 g) and treated with rimonabant or vehicle for 4 weeks. Rimonabant elicited a profound decrease in body mass (-25%, $p < 0.001$; **Figure 1A**) which was not due to a decrease in lean mass but rather to a massive decrease in fat mass (-32%, $p < 0.001$; **Figure 1B**). Rimonabant decreased caloric intake transiently (i.e. until day 6) (**Figure 1C**), in accordance with previous observations (35,36), while it persistently induced weight loss throughout the treatment period (i.e. 4 weeks). Furthermore, rimonabant markedly diminished plasma TG levels (-59%, $p < 0.05$) and

TC levels (-40%, $p < 0.01$) (**Figure 1D**), which is in line with previous human studies (10-12). Rimonabant tended to reduce plasma phospholipid (PL) levels (-31%, $p = 0.05$) and had no effect on plasma free fatty acid (FFA) levels. Lipoprotein profiling showed that the marked decrease in plasma TG mostly resulted from a reduction in VLDL-TG (AUC -62%) (**Figure 1E**). The persistent reduction in body weight despite the transient decrease in food intake following rimonabant treatment suggests increased energy expenditure. Indeed, rimonabant increased substrate utilization reflected by increased fat oxidation (+18%, $p < 0.05$; **Figure 1F**), carbohydrate (CHO) oxidation (+18%, $p < 0.05$; **Figure 1G**), and consequently total energy expenditure (+17%, $p < 0.05$; **Figure 1H**), as measured via indirect calorimetry, without increasing locomotor activity (**Figure 1I**) or RQ values (data not shown).

Systemic CB1R blockade by rimonabant attenuates dyslipidemia by activating brown adipose tissue

Plasma VLDL-TG levels are determined by the balance between hepatic VLDL-TG production and VLDL-TG clearance by lipoprotein lipase (LPL)-expressing peripheral organs. Therefore, to gain insight into the mechanism by which systemic CB1R antagonism reduces plasma VLDL-TG, we first assessed the effect of rimonabant on VLDL production. DIO mice were treated with rimonabant or vehicle for 4 weeks and then sequentially injected with Trans³⁵S and Triton WR1339 resulting in linear accumulation of VLDL in which newly synthesized apolipoproteins are radiolabeled. Rimonabant did not affect the time-dependent accumulation of plasma TG following Triton injection (**Figure 2A**). Therefore, the VLDL-TG production rate, as determined from the slope of the curve, was not significantly different. In addition, the rate of VLDL-apoB production did not change (**Figure 2B**). In line with these observations, hepatic expression of lipogenic genes such as fatty acid synthase (*Fasn*) and stearoyl-CoA desaturase (*Scd1*) was unchanged (**Figure 2C**). All together, these data demonstrate that global CB1R antagonism does not diminish dyslipidemia by lowering hepatic VLDL-TG production.

To investigate whether rimonabant increases VLDL-TG clearance, we determined the kinetics of i.v. injected [³H]TO-labeled TG-rich VLDL-like emulsion particles, which have been previously shown to mimic the metabolic behavior of TG-rich lipoproteins (30), and studied the plasma clearance and organ distribution of [³H]TO-derived fatty acids (FA) in mice treated with rimonabant or vehicle for 4 weeks. Rimonabant accelerated clearance of [³H]TO from plasma ($t_{1/2} = 3.9 \pm 0.6$ vs. 6.4 ± 0.4 min, $p < 0.05$) (**Figure 2D**), as explained by increased uptake of [³H]TO-derived activity by energy-dissipating BAT (+53%, $p < 0.05$; **Figure 2E**). Of note, rimonabant decreased the uptake of [³H]TO by the energy-storing sWAT depot (-42%, $p < 0.05$).

To further investigate the mechanism by which systemic CB1R blockade increased FA uptake by BAT, we determined the mRNA expression of genes involved

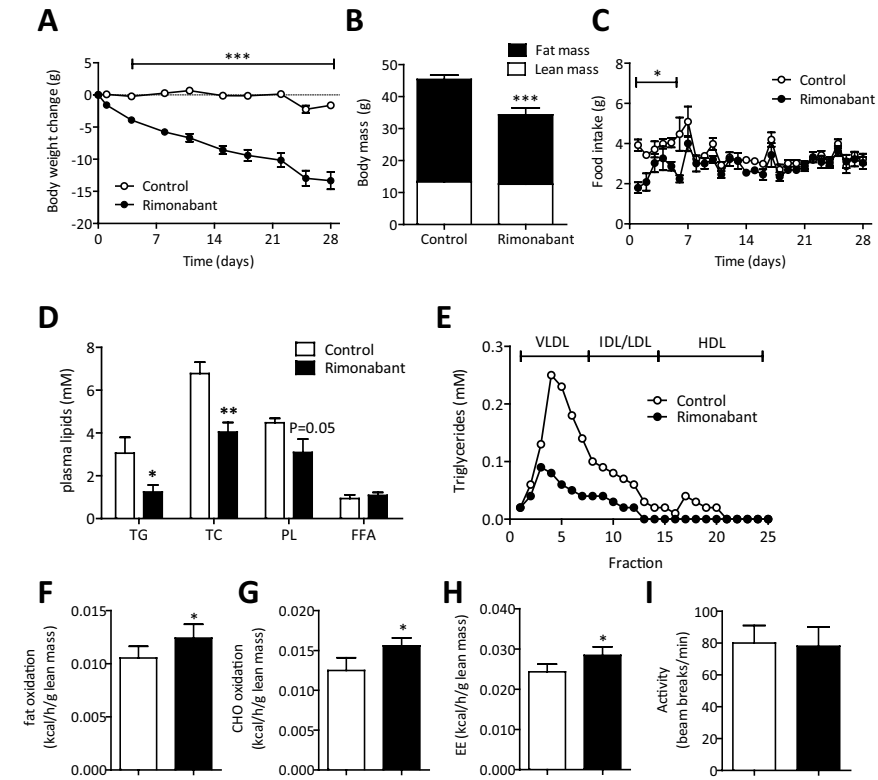


Figure 1 – Systemic CB1R blockade by rimonabant in DIO mice reduces obesity and dyslipidemia and increases energy expenditure. Male E3L.CETP mice were fed a HFD for 12 weeks to induce DIO and were then treated with rimonabant or vehicle for 4 weeks while housed at 21°C. **(A)** Body weight change (g) during the treatment period. **(B)** Lean and fat mass (g) as measured via DEXA-scan after 4 weeks of treatment. **(C)** Mean daily food intake (g) during the treatment period. **(D)** Plasma triglyceride (TG), total cholesterol (TC), phospholipid (PL), and free fatty acid (FFA) levels in 4-hour fasted mice after 4 weeks of treatment. **(E)** TG distribution over lipoproteins after separation from pooled plasma (n=9) by FPLC. **(F)** Fat oxidation, **(G)** carbohydrate (CHO) oxidation, **(H)** energy expenditure (EE), and **(I)** activity levels as measured during 5 consecutive days in the fourth week of treatment via fully automatic metabolic cages. **(F-H)** Measurements were corrected for lean mass. Values are means ± SEM (n=9) *p<0.05, **p<0.01, ***p<0.001 compared to the control group.

in both BAT differentiation, BAT activity, TG lipolysis and FA uptake. Rimonabant did not affect expression of genes involved in BAT differentiation (*Pgc1a*, *Prdm16*) and intracellular lipolysis (*Hsl*, *Atgl*) (data not shown). However, as shown in **Figure 2F**, rimonabant increased expression of *Lpl* (+30%, p<0.05) and *Cd36* (+24%, p<0.05) that drive extracellular VLDL-TG lipolysis and subsequent uptake of FA by BAT (18). In addition, rimonabant increased expression of *Ucp1*, which encodes the uncoupling

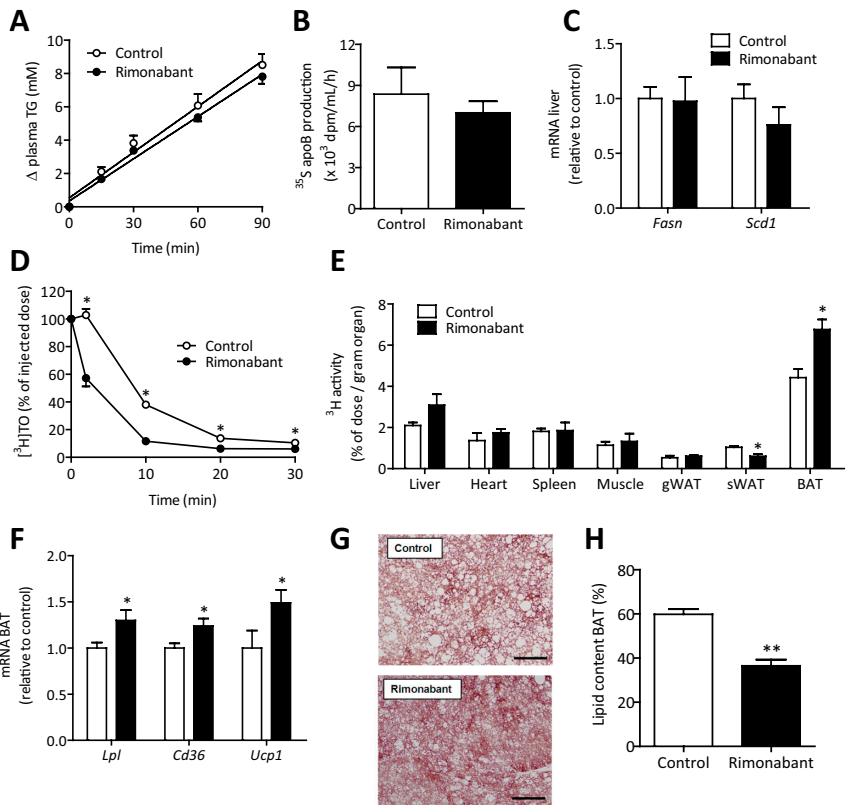


Figure 2 – Systemic CB1R blockade by rimonabant in DIO mice attenuates dyslipidemia by activating brown adipose tissue. Male E3L.CETP mice were fed a HFD for 12 weeks to induce DIO and were then treated with rimonabant or vehicle for 4 weeks while housed at 21°C (A) After 4 weeks of treatment, 4-hour fasted mice were injected intravenously with Tran^[35S] and TritonWR1339 and blood samples were drawn at the indicated time points. TG concentrations were determined and plotted as the increase in plasma TG relative to t=0. (B) ApoB production rate, as measured by counting ^{35S}-activity in the VLDL fraction isolated after 90 min. (C) Expression of *Fasn* and *Scd1* in liver as measured by qRT-PCR. (D) After 4 weeks of treatment, 4-hour fasted mice were injected intravenously with [³H]TO-labeled VLDL-like emulsion particles, blood was collected at the indicated time points and radioactivity was measured in plasma. (E) Uptake of [³H]TO-derived radioactivity by various organs was determined, and expressed as percentage of the injected dose per gram wet tissue weight. (F) Noradrenalin (NA) content in BAT was measured and expressed as pg/mg BAT (G) Expression of *Lpl*, *Cd36*, and *Ucp1* in BAT as measured by qRT-PCR. (H) Representative pictures of immunohistochemical UCP-1 stainings of BAT in vehicle (top) and rimonabant (bottom) treated mice. Pictures were taken at 100x magnification (scale bar 100 µm). (I) Percentual lipid content in BAT tissue sections as quantified by use of ImageJ. Values are means ± SEM (n=9) and expression of genes was corrected for the housekeeping genes *β2-microglobulin* and *36b4*. *p<0.05, ***p<0.001 compared to the control group. gWAT, gonadal white adipose tissue; sWAT, subcutaneous white adipose tissue.

protein that mediates thermogenesis (+49%, $p < 0.05$). Furthermore, histology showed a more intense immunohistochemical staining of UCP-1 in BAT (**Figure 2G**) as well as a decrease in intracellular lipid droplet size, reflected by a decrease in relative lipid area (-39%, $p < 0.001$; **Figure 2H**), both pointing to more active BAT (37). Thus, these data provide strong evidence that systemic CB1R antagonism diminishes dyslipidemia and increases energy expenditure, by promoting VLDL-TG uptake and subsequent combustion by BAT.

Systemic CB1R blockade by rimonabant diminishes TG storage in WAT and liver

To investigate whether the increased flux of TG towards BAT reduces (ectopic) TG accumulation, we analyzed WAT and the liver in more detail. Indeed, from the VLDL-TG clearance experiment it appeared that retention of [^3H]TO-derived activity by the energy storing sWAT depot was diminished after rimonabant treatment (-42%, $p < 0.05$; **Figure 2E**). In line with this, the cell size of white adipocytes was decreased in this depot as evident after H&E staining (**Supplemental Figure 1A**). In addition, rimonabant diminished expression of the lipogenic genes *Fasn* (-58%, $p < 0.05$) and *Scd1* (-54%, $p < 0.05$), while it increased expression of the lipolytic enzyme hormone sensitive lipase (*Hsl*) (+126%, $p < 0.05$) in WAT (**Supplemental Figure 1B**), suggesting net FA efflux from WAT. To investigate whether rimonabant may directly enhance intracellular lipolysis in WAT, we assessed its effect on glycerol release in 3T3-L1 cells, an *in vitro* model of differentiated (white) adipocytes. Rimonabant did not affect glycerol release (**Supplemental Figure 1C**), suggesting that the enhanced FA efflux from WAT may occur secondary to the enhanced BAT activation.

In liver, rimonabant markedly decreased liver weight (**Supplemental Figure 2A**), which was accompanied by a reduction in liver TG content (-45%, $p < 0.01$) (**Supplemental Figure 2B**) and smaller intracellular lipid vacuoles (**Supplemental Figure 2C**). Furthermore, rimonabant caused a (likely compensatory) downregulation of hepatic expression of genes involved in lipid oxidation, such as acyl-CoA synthetase long-chain family member 1 (*Acs1l*) and acetyl-CoA carboxylase 2 (*Acc2*) (**Supplemental Figure 2D**), while genes involved in lipogenesis were not affected (**Figure 2C**). Thus, these data suggest that systemic CB1R blockade reduces storage of TG in WAT and liver, which may, at least in part, be a consequence of increased FA demand and flux towards BAT.

The anti-obesity and lipid-lowering effects of systemic CB1R blockade by rimonabant are not abrogated at thermoneutrality

BAT is densely innervated by the sympathetic nervous system (SNS) (19). Therefore, one of the mechanisms by which systemic CB1R blockade may lead to BAT activation could involve central CB1R blockade resulting in increased sympathetic outflow

towards BAT. To investigate whether rimonabant acts centrally by increasing sympathetic nervous system (SNS) activation towards BAT, we next evaluated the effects of rimonabant in DIO mice that were housed at thermoneutral temperature (28°C). At thermoneutrality, rimonabant still markedly reduced obesity (**Figure 3A,B**) without affecting lean mass. This was accompanied by a transient decrease in food intake (i.e. until day 6) (**Figure 3C**). Importantly, at thermoneutrality rimonabant still lowered plasma TG (-70%, $p < 0.05$; **Figure 3D**), which was mainly due to a reduction in VLDL-TG (AUC -52%; **Figure 3E**). Furthermore, rimonabant still increased whole-body fat and carbohydrate oxidation (**Supplemental Figure 3A,B**), resulting in increased total energy expenditure (+21%, $p < 0.05$; **Figure 3F**), accompanied by increased markers of BAT activation both on mRNA (**Figure 3G**) and histological levels (**Figure 3H**). Thus, these data suggest that the reduction in dyslipidemia, increase in energy expenditure and activation of BAT by systemic CB1R blockade occurs at least in part independent of SNS activation of BAT.

***In vitro* CB1R blockade by rimonabant induces activation of brown adipocytes which is at least in part mediated by PKA signaling**

To explore the possibility that direct blockade of a CB1R in BAT may be responsible for the anti-obesity and lipid-lowering effect induced by systemic CB1R blockade, we first investigated whether the CB1R is expressed on BAT. Indeed, western blots on protein from tissues derived from untreated mice showed that the CB1R is highly expressed in BAT (**Figure 4A**), even when compared to the expression in hypothalamus and liver. *In vitro* treatment of T37i brown adipocytes with rimonabant (1 μ M) enhanced UCP-1 protein content (**Figure 4B**). In line with this, we found a significantly elevated oxygen consumption rate in the cells upon 5 h of treatment with rimonabant (+23%, $p < 0.05$; **Figure 4C**). Furthermore, under these conditions oligomycin was less capable to suppress oxygen consumption rate (OCR) (**Figure 4D**), pointing to enhanced uncoupling of oxidative phosphorylation. Enhanced uncoupling may be the result of enhanced intracellular lipolysis resulting in allosteric activation of UCP-1 (19). Indeed, we found that rimonabant dose-dependently increased glycerol release (**Figure 4E**), pointing to increased intracellular lipolysis.

AMP-activated protein kinase (AMPK) serves as an intracellular energy sensor and activation of AMPK by means of phosphorylation results in enhanced fatty acid and glucose oxidation in a variety of tissues as well as controls lipolysis in white adipocytes (38). Of note, CB1R blockade has been shown to increase AMPK phosphorylation in both liver cells (39) and white adipocytes (40). In line with this, we found that *in vitro* treatment of cultured T37i brown adipocytes with rimonabant for 8 h induced AMPK phosphorylation (**Figure 4F**) as well as phosphorylation of ACC (**Figure 4G**), the downstream effector of AMPK. Of note, the induction of AMPK phosphorylation was not yet present after 30 min of incubation with rimonabant (data

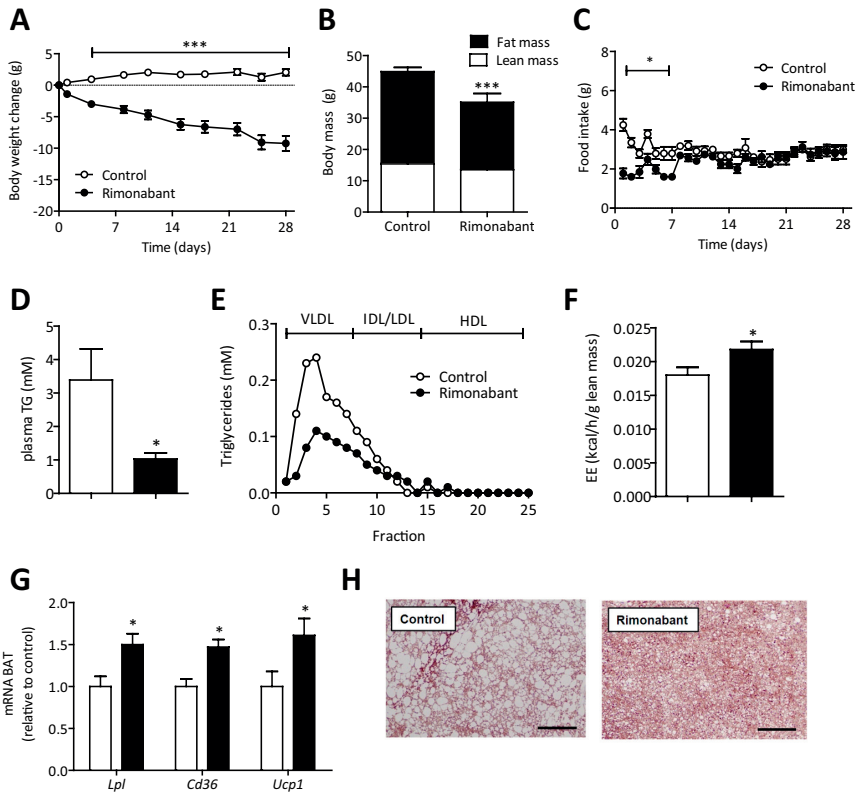
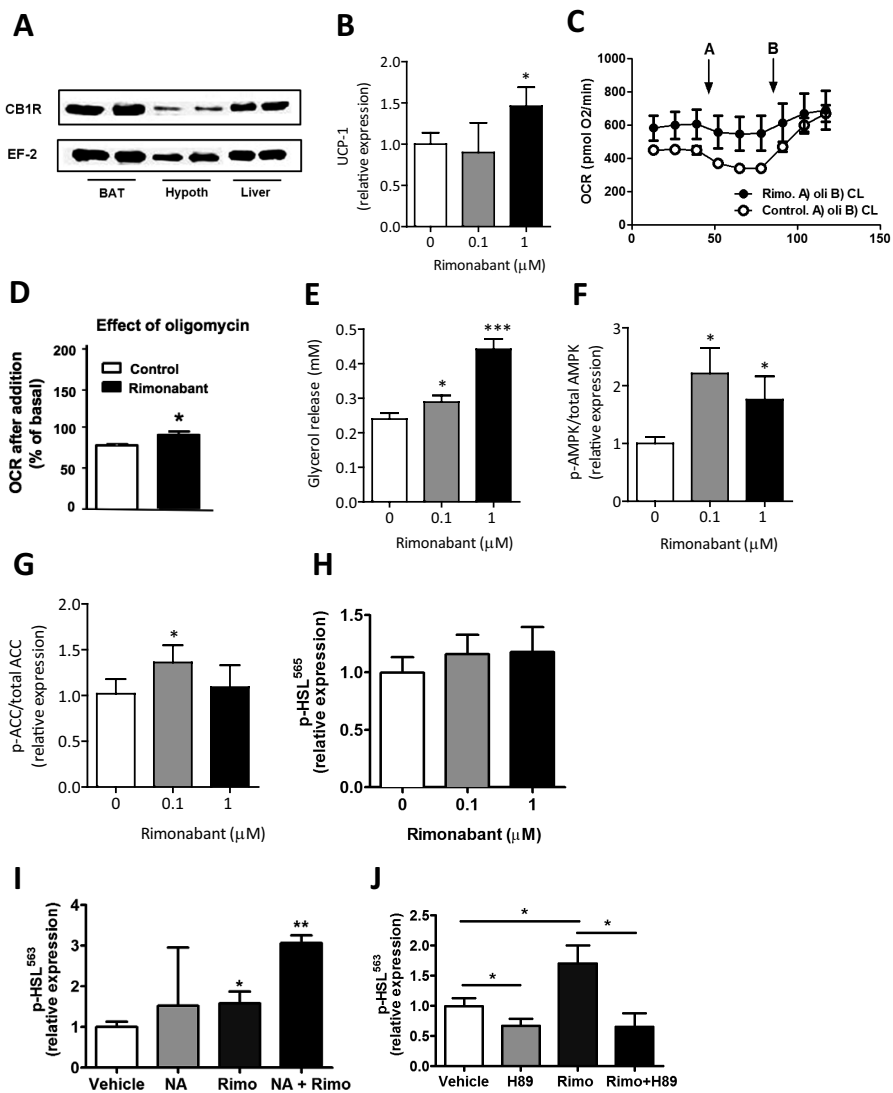


Figure 3 – The anti-obesity and lipid-lowering effects of systemic CB1R blockade by rimonabant in DIO mice are not abrogated at thermoneutrality. Male E3L.CETP mice were fed a HFD for 12 weeks to induce DIO and were then treated with rimonabant or vehicle for 4 weeks while housed at 28°C **(A)** Body weight change (g) during the treatment period. **(B)** Lean and fat mass (g) as measured via DEXA-scan after 4 weeks of treatment. **(C)** Mean daily food intake (g) during the treatment period. **(D)** Plasma triglyceride (TG) levels in 4-hour fasted mice after 4 weeks of treatment. **(E)** TG distribution over lipoproteins after separation from pooled plasma (n=9 per group) by FPLC. **(F)** Energy expenditure (EE) as measured during 5 consecutive days in the fourth week of treatment via fully automatic metabolic cages, corrected for lean mass. **(G)** Expression of *Lpl*, *Cd36*, and *Ucp1* in BAT as measured by qRT-PCR **(H)** Representative pictures of immunohistochemical UCP-1 stainings of BAT in vehicle (left) and rimonabant (right) treated animals. Pictures were taken at 100x magnification [scale bar 100 μ m]. Values are means \pm SEM (n=9) *p<0.05, **p<0.01, ***p<0.001 compared to the control group.



6

not shown). Furthermore, rimonabant did not affect phosphorylation of Ser565-HSL (**Figure 4H**), which is presumably the regulatory site by which the kinase controls HSL activity.

In contrast, rimonabant increased the phosphorylation of the PKA target residue on HSL (Ser563) (**Figure 4I**). As the Ser563 residue is phosphorylated by protein kinase A (PKA), which is itself activated by cAMP, this suggests that the cAMP/PKA pathway at least in part mediates the enhanced intracellular lipolysis in brown adipocytes upon CB1R blockade. Indeed, as shown in **Figure 4I**, the combination of noradrenalin (which also signals through the cAMP/PKA pathway in brown adipocytes) and rimonabant even further enhanced p-HSL⁵⁶³ content (+200%, $p < 0.01$). Moreover, in the presence of the PKA inhibitor H89 the enhanced p-HSL⁵⁶³ content induced upon rimonabant was blunted (**Figure 4J**).

Altogether, these data indicate that direct blockade of the CB1R on brown adipocytes directly stimulates intracellular lipolysis, UCP-1 protein content as well as uncoupling, which may at least in part be mediated by cAMP-PKA signaling.

◀ **Figure 4 – Rimonabant directly stimulates BAT activity in T37i brown adipocytes in vitro.**

(A) CB1R protein content was measured via Western blot in BAT, hypothalamus, and liver derived from DIO E3L.CETP transgenic mice with elongation factor 2 (EF-2) as housekeeping protein. (B) T37i cells were treated with rimonabant (0, 0.1, or 1 μM) for 8 h, and UCP-1 was measured via Western blot. (C) T37i cells were treated with rimonabant (1 μM) for 5 h, and OCR was measured via Seahorse in the basal state, as well as after addition of oligomycin (arrow A) and the 3-adrenergic agonist CL316243 (arrow B). (D) Percentage inhibition of OCR after addition of oligomycin. (E) T37i cells were treated with rimonabant (0, 0.1, or 1 μM) for 8 h, and glycerol release was measured in the supernatant. (F) T37i cells were treated with rimonabant (0, 0.1, or 1 μM) for 8 h, and p-AMPK/AMPK was measured via Western blot. (G) T37i cells were treated with rimonabant (0, 0.1, or 1 μM) for 8 h, and p-ACC/ACC was measured via Western blot. (H) T37i cells were treated with rimonabant (0, 0.1, or 1 μM) for 8 h and p-HSL⁵⁶⁵ was measured via Western blot. (I) T37i cells were treated with rimonabant (1 μM) with or without noradrenalin (NA; 1 μM), and protein content of p-HSL⁵⁶³ was measured via Western blot. (J) T37i brown adipocytes were treated with rimonabant (1 μM), H89 (25 μM) or a combination. Protein content of p-HSL⁵⁶³ was measured via Western blot. Values are means \pm SD (n=3–4). * $p < 0.05$, ** $p < 0.01$, *** $p < 0.001$ vs. control group.

Strictly peripheral CB1R blockade by AM6545 reduces obesity and dyslipidemia and increases energy expenditure in DIO mice

To investigate whether peripheral CB1R blockade is sufficient to induce weight loss and reverse dyslipidemia *in vivo*, we treated DIO mice for four weeks with vehicle or AM6545, a peripherally restricted CB1R antagonist that has been previously shown not to elicit central side effects (17). AM6545 markedly reduced body weight (-19%, $p < 0.001$; **Figure 5A**) and fat mass (-23%, $p < 0.01$; **Figure 5B**), without altering lean mass. AM6545 did not induce the initial transient decrease in food intake as seen with rimonabant, although a slight decrease was evident later during the treatment period (**Figure 5C**). However, total caloric intake was not affected. Furthermore, AM6545 substantially decreased plasma TG levels (-49%, $p < 0.05$; **Figure 5D**), which mostly resulted from a reduction in VLDL-TG (AUC -73%; **Figure 5E**). In addition, AM6545 increased total energy expenditure (**Figure 5F**), which was due to an increase in both fat and carbohydrate oxidation (**Figure 5G,H**). Thus, these data demonstrate that peripheral CB1R blockade is sufficient to diminish obesity and dyslipidemia in DIO.

Strictly peripheral CB1R blockade by AM6545 attenuates dyslipidemia by activating brown adipose tissue

To investigate whether peripheral CB1R blockade also diminished dyslipidemia by increasing FA uptake by BAT, we again assessed VLDL-TG production and clearance. Just like rimonabant, AM6545 did not affect the production rates of VLDL-TG and VLDL-apoB (**Figure 6A,B**) or hepatic expression of lipogenic genes (**Figure 6C**). Instead, AM6545 also accelerated clearance of [³H]TO-labeled VLDL-like emulsion particles from plasma (**Figure 6D**), accompanied by a marked increase of ³H retention by BAT (+235%, $p < 0.01$; **Figure 6E**), and a decrease in ³H uptake by sWAT (-51%, $p < 0.01$). In BAT, AM6545 increased expression of *Lpl* (+67%, $p < 0.05$), *Cd36* (+59%, $p < 0.05$) and *Ucp1* (+32%, $p < 0.05$; **Figure 6F**) and decreased lipid content (**Figure 6G**), all pointing to increased BAT activity. AM6545 also decreased white adipocyte size (**Supplemental Figure 4A**) and liver weight (-24%, $p < 0.001$; **Supplemental Figure 4B**) accompanied by a reduction in liver TG content (-17%, $p < 0.05$) (**Supplemental Figure 4C**) and lipid vacuole size (**Supplemental Figure 4D**). Thus, peripheral CB1R blockade is sufficient to diminish dyslipidemia, and probably also obesity, by promoting VLDL-TG uptake and subsequent combustion of engulfed FA by BAT.

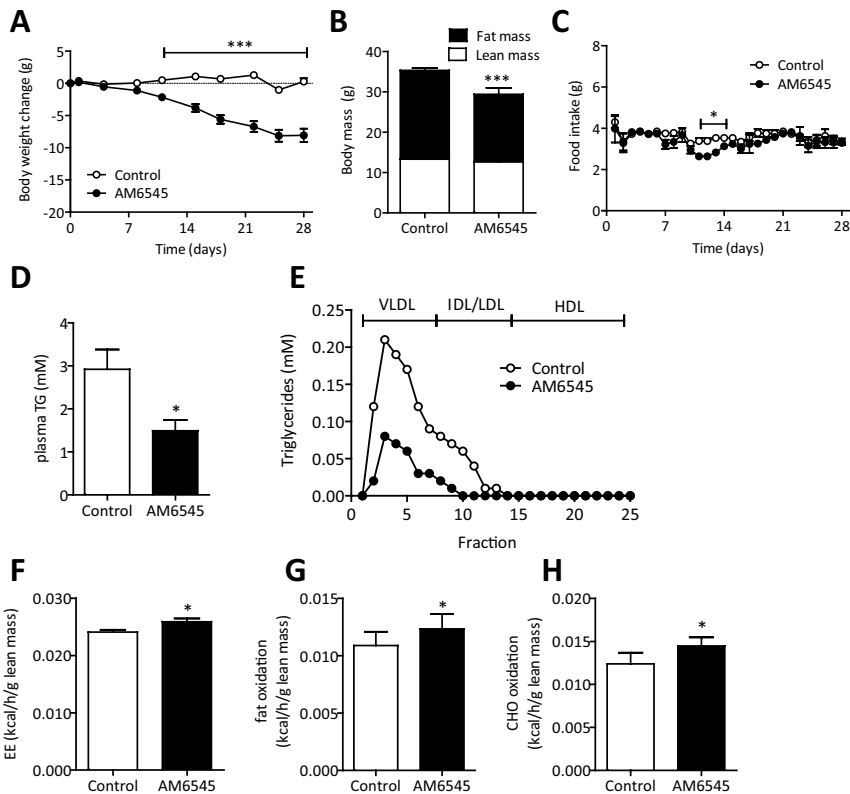


Figure 5 – Strictly peripheral CB1R blockade by AM6545 reduces obesity and dyslipidemia and increases energy expenditure in DIO mice. Male E3L.CETP mice were fed a HFD for 12 weeks to induce DIO and were then treated with AM6545 or vehicle for 4 weeks while housed at 21°C. **(A)** Body weight change (g) during the treatment period. **(B)** Lean and fat mass (g) as measured via DEXA-scan after 4 weeks of treatment. **(C)** Mean daily food intake (g) during the treatment period. **(D)** Plasma triglyceride (TG) levels in 4-hour fasted mice after 4 weeks of treatment. **(E)** TG distribution over lipoproteins after separation from pooled plasma (n=9 per group) by FPLC. **(F-H)** energy expenditure, fat oxidation and carbohydrate (CHO) oxidation as measured during 5 consecutive days in the fourth week of treatment via fully automatic metabolic cages, corrected for lean mass. Values are means \pm SD (n=9) *p<0.05, ***p<0.001 compared to the control group.

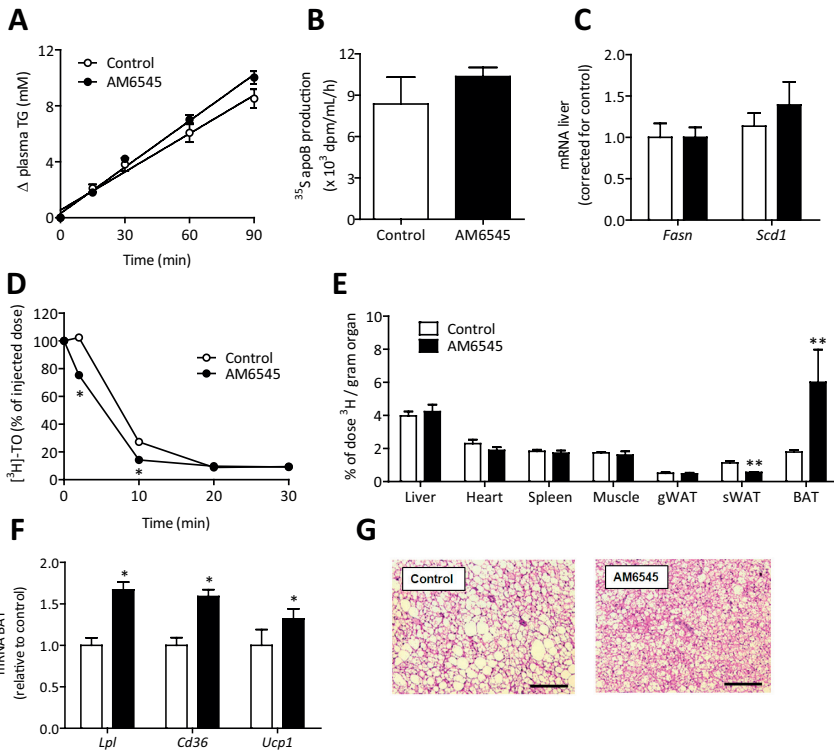


Figure 6 – Strictly peripheral CB1R blockade by AM6545 attenuates dyslipidemia in DIO mice by activating brown adipose tissue. Male E3L.CETP mice were fed a HFD for 12 weeks to induce DIO and were then treated with AM6545 or vehicle for 4 weeks while housed at 21°C. **(A)** After 4 weeks of treatment, 4-hour fasted mice were injected intravenously with Tran ^{35}S and TritonWR1339 and blood samples were drawn at the indicated time points. TG concentrations were determined and plotted as the increase in plasma TG relative to t=0. **(B)** ApoB production rate, as measured by counting ^{35}S -activity in the VLDL fraction after 90 min. **(C)** Expression of *Fasn* and *Scd1* in liver as measured by qRT-PCR. **(D)** After 4 weeks of treatment, 4-hour fasted mice were injected intravenously with ^3H TO-labeled VLDL-like emulsion particles. Blood was collected at the indicated time points and radioactivity was measured in plasma. **(E)** Uptake of ^3H TO-derived radioactivity by various organs, and expression per gram wet tissue weight. **(F)** Expression of *Lpl*, *Cd36*, and *Ucp1* in BAT as measured by qRT-PCR. **(G)** Representative pictures of immunohistochemical UCP-1 stainings of BAT in vehicle (left) and rimonabant (right) treated animals. Pictures were taken at 100x magnification (scale bar 100 μm). **(H)** Noradrenalin (NA) content in BAT was measured and expressed as pg/mg BAT. Values are means \pm SEM (n=9) and expression of genes was corrected for the housekeeping genes $\beta 2$ -microglobulin and *36b4*. *p<0.05, **p<0.01, ***p<0.001 compared to the control group.

DISCUSSION

Systemic CB1R blockade by the inverse CB1R agonist rimonabant alleviates the excess body weight and dyslipidemia that are associated with obesity, both in mice and in humans (8,9,11-13). In this study, we demonstrate that systemic CB1R blockade reverses DIO and reduces plasma VLDL-TG by selectively increasing VLDL-TG clearance by metabolically active BAT followed by combustion. Of note, the mechanism involves peripheral activation of BAT since the effects were still present at thermoneutrality and could be recapitulated by using the strictly peripheral (17) CB1R antagonist AM6545. Accordingly, cultured brown adipocytes could be activated by blockade of the CB1R with rimonabant.

Systemic CB1R blockade by rimonabant resulted in massive activation of BAT, as evidenced by reduced lipid content and increased UCP-1 expression, accompanied by increased energy expenditure, which is in accordance with previous studies (35,41). Of note, by performing kinetic studies with radioactively labeled VLDL-TG we provided clear evidence that the TG-lowering effect of rimonabant is due to increased uptake of TG-derived FAs by BAT. Since metabolically active BAT has been shown to be present and active in human adults (20-23), it is tempting to speculate that the body weight-reducing and TG-lowering effects of rimonabant previously found in obese subjects might be due to activation of BAT, although the precise role of BAT in TG metabolism in humans remains to be established.

Previous studies suggested central CB1R blockade as the main mechanism by which rimonabant induces BAT activation, resulting in increased sympathetic outflow towards BAT and increased energy expenditure (35,41). For instance, Bajzer and colleagues (36) reported that denervation of BAT in mice blunted the effect of rimonabant on insulin-mediated glucose uptake. However, in their study, the increase in energy expenditure and the reduction in body weight and fat mass were not blunted by BAT denervation, suggesting that a peripheral mechanism is at least in part involved in these beneficial effects. Indeed, we found that treatment of DIO mice with the strictly peripheral CB1R antagonist AM6545 still resulted in increased energy expenditure accompanied by increased uptake of TG-derived FAs by BAT as well as significant weight loss and reduction in dyslipidemia. Furthermore, we showed that the CB1R is highly expressed in BAT. It is important to realize that this does not exclude the possibility that presynaptic CB1R on peripheral sympathetic nerve terminals innervating BAT may be the peripheral target whose blockade enhances BAT activation through enhanced noradrenalin release. However, the fact that we found that noradrenalin content in BAT was only increased upon treatment with rimonabant at 21°C and not at thermoneutrality or upon AM6545 treatment (data not shown), makes this mechanism less likely. In line with this, we found that

rimonabant directly activated brown adipocytes *in vitro*, further supporting the possibility of a peripheral mode of action of CB1R blockade in BAT.

We found that systemic blockade of the CB1R by rimonabant did not affect VLDL-TG production following either systemic or selective peripheral CB1R blockade. In contrast, a study by Tam and colleagues (17) reported that blocking the peripheral CB1R by AM6545 treatment resulted in a marked increase in the production of VLDL-TG in both DIO C57Bl/6 and leptin-deficient *ob/ob* mice. This might be explained by differences in study set-up, since Tam and colleagues measured VLDL-TG production after 1 week of treatment while in the present study VLDL-TG production was measured after 4 weeks. Likely, CB1R blockade transiently increases VLDL-TG production, leading to a fast initial reduction in hepatic steatosis as was also observed in their study. The subsequent normalization in VLDL production that we found in our study after 4 weeks of treatment may then be the consequence of a lower supply of FFAs towards the liver for incorporation into VLDL-TG, since these are efficiently cleared by BAT.

While we provide clear evidence that the TG-lowering effect of CB1R blockade is due to peripheral activation of BAT, the mechanism by which CB1R blockade lowers body weight and fat mass is less clear and no consistent mechanism has been reported up to date. Although BAT activation has been repeatedly shown to decrease body weight and fat mass (18,42,43), we cannot exclude that CB1R blockade on peripheral tissues other than BAT may contribute to the weight-reducing effect. For instance, the CB1R has been shown to be present on white adipocytes (16) and treatment of mice with rimonabant and AM6545 increased lipolysis (17,44,45). Accordingly, we also found that rimonabant increased mRNA expression of *Hsl* in subcutaneous WAT. The question remains whether the effect of rimonabant on WAT lipolysis is a primary effect or occurs as a consequence of enhanced BAT activation. As we did not observe a direct effect of rimonabant on glycerol release in 3T3L1 white adipocytes it is more likely that the enhanced WAT lipolysis occurs secondary to BAT activation. Furthermore, the weight-reducing effect of global CB1R blockade is also at least in part due to an initial transient decrease in food intake induced by rimonabant. The greater efficacy of rimonabant over AM6545 in reducing body weight is then likely explained by the fact that AM6545 did not affect total caloric intake over the treatment period, as has been shown before (17). Thus, future studies are needed to elucidate the specific contribution of BAT in the weight-reducing effect of (peripheral) CB1R blockade.

It is interesting to speculate on the possible intracellular mechanisms by which CB1R blockade enhances BAT activity. One of the hallmarks of brown adipocyte activation is enhanced intracellular lipolysis, resulting in release of FA that can subsequently allosterically activate UCP-1 (19). In search for the pathway that is connected to induction of intracellular lipolysis by CB1R blockade, we measured the phosphorylation state of HSL on various regulatory residues in T37i cells

upon treatment with rimonabant. We found that rimonabant selectively enhanced p-HSL^{ser563}, the residue that is phosphorylated by PKA, and that this effect could be blocked by addition of the PKA inhibitor H89. As PKA is itself activated by enhanced intracellular cAMP levels, this suggests that rimonabant enhances the cAMP/PKA pathway in brown adipocytes. This mechanism is not surprising as the major mediators in CB1R signaling are in fact G-proteins of the G(i/o) family that inhibit adenylyl cyclases [46]. Moreover, CB1R agonism in a variety of cell types inhibits adenylyl cyclase activity and thus cAMP levels [46]. In addition, we found that CB1R blockade resulted in increased AMPK phosphorylation in brown adipocytes, which is in accordance with previous studies performed in hepatocytes [39] and white adipocytes [40]. However, as AMPK may be activated in case of low intracellular ATP levels, the effect of rimonabant on the kinase might be secondary to enhanced uncoupling of oxidative phosphorylation induced by rimonabant. Indeed, we found that p-AMPK was only enhanced in brown adipocytes after chronic and not acute stimulation with rimonabant. Thus, we propose a mechanism (**Figure 7**) by which CB1R blockade on the brown adipocyte membrane results in enhanced cAMP/PKA signalling and phosphorylation of HSL^{ser563}. This results in enhanced intracellular lipolysis and release of FA that subsequently activate UCP1 resulting in enhanced uncoupling. As a secondary mechanism, uptake of VLDL-TG derived FA is enhanced through an increase of expression of *Lpl* and *Cd36*.

Together, our study shows that CB1R blockade diminishes dyslipidemia by inducing BAT-mediated VLDL-TG uptake and BAT thermogenesis via a peripheral mode of action. Our data suggest that blockade of the peripheral CB1R in BAT may be a promising therapy to combat obesity and to lower cardiovascular risk without inducing centrally mediated side effects.

Acknowledgements

Mariëtte R. Boon is supported by a grant from the Board of Directors of LUMC. Patrick C.N. Rensen is Established Investigator of the Netherlands Heart Foundation (grant 2009T038). Furthermore, we acknowledge the support from the "Netherlands CardioVascular Research Initiative: the Dutch Heart Foundation, Dutch Federation of University Medical Centers, the Netherlands Organisation for Health Research and Development and the Royal Netherlands Academy of Sciences" for the GENIUS project "Generating the best evidence-based pharmaceutical targets for atherosclerosis" (CVON2011-19).

The authors also thank Lianne van der Wee and Trea Streefland (LUMC, dept. of Endocrinology) for their excellent technical assistance. The excellent help and valuable scientific input from Johanna C. van den Beukel, Gardi J. Voortman, Edith C.H. Friesema and Aldo Grefhorst (all from Dept. Internal Medicine, Erasmus MC, The Netherlands) is highly appreciated.

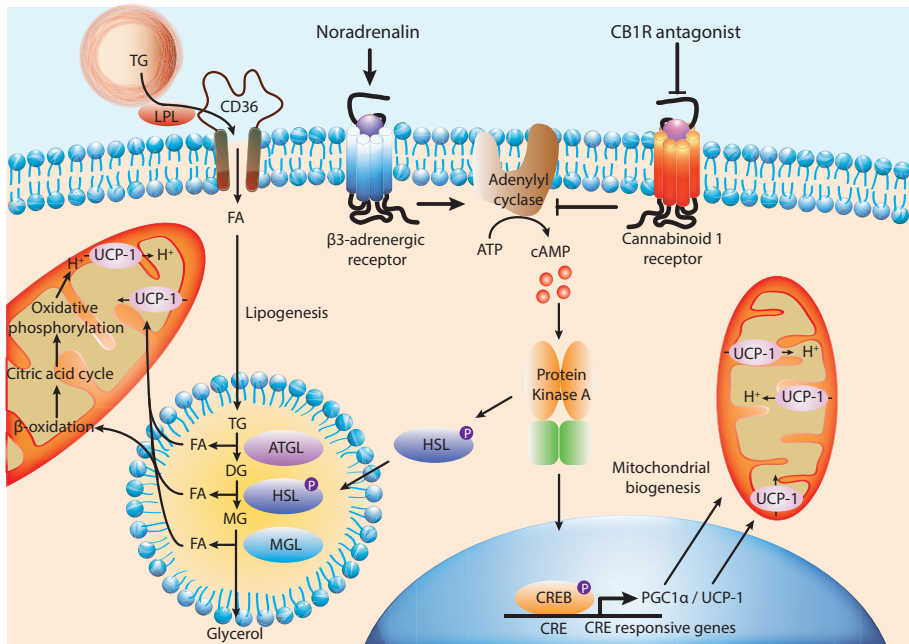


Figure 7 – Proposed mechanism by which CB1R antagonism enhances activation of BAT.

CB1R antagonism abrogates the inhibition of β_3 adrenergic signaling, and thereby enhances adenylyl cyclase activity, resulting in enhanced cAMP levels and activation of protein kinase A (PKA). PKA phosphorylates HSL on Ser⁵⁶³, leading to enhanced intracellular lipolysis and release of FA. FA can either undergo β oxidation or can allosterically activate UCP-1, resulting in enhanced uncoupling. In addition, PKA phosphorylates CREB, enhancing *Ucp1* transcription. The consequently decreasing triglyceride (TG) pool within the intracellular lipid droplets is replenished by enhanced uptake of TG-derived fatty acids (FA) from TG-rich lipoproteins through lipolysis by LPL followed by uptake of FA from the plasma through CD36 eventually resulting in lowering of plasma TG levels. ATGL, adipose triglyceride; CB1R, cannabinoid 1 receptor; DG, di-glyceride; FA, fatty acid; HSL, hormone sensitive lipase; LPL, lipoprotein lipase; MGL, monoacylglycerol lipase; MG, monoglyceride; TAG, triacylglycerol lipase; UCP-1, uncoupling protein-1.

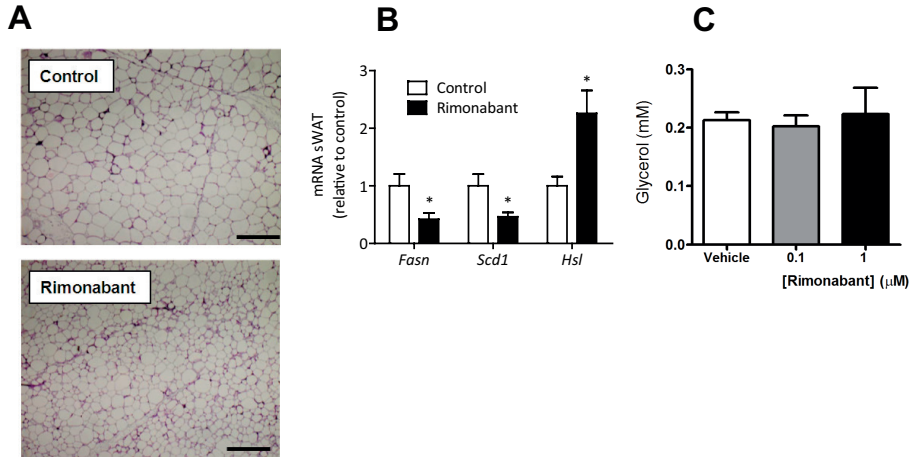
References

1. Pagotto, U., Marsicano, G., Cota, D. *et al.* (2006) The emerging role of the endocannabinoid system in endocrine regulation and energy balance. *Endocr Rev* 27, 73-100.
2. De, P. L., Cascio, M. G., & Di, M., V (2004) The endocannabinoid system: a general view and latest additions. *Br J Pharmacol* 141, 765-774.
3. Piomelli, D. (2003) The molecular logic of endocannabinoid signalling. *Nat Rev Neurosci* 4, 873-884.
4. Howlett, A. C., Barth, F., Bonner, T. I. *et al.* (2002) International Union of Pharmacology. XXVII. Classification of cannabinoid receptors. *Pharmacol Rev* 54, 161-202.
5. Ravinet, T. C., Delgorge, C., Menet, C. *et al.* (2004) CB1 cannabinoid receptor knockout in mice leads to leanness, resistance to diet-induced obesity and enhanced leptin sensitivity. *Int J Obes Relat Metab Disord* 28, 640-648.
6. Bluher, M., Engeli, S., Kloting, N. *et al.* (2006) Dysregulation of the peripheral and adipose tissue endocannabinoid system in human abdominal obesity. *Diabetes* 55, 3053-3060.
7. Engeli, S., Bohnke, J., Feldpausch, M. *et al.* (2005) Activation of the peripheral endocannabinoid system in human obesity. *Diabetes* 54, 2838-2843.
8. Gary-Bobo, M., Elachouri, G., Gallas, J. F. *et al.* (2007) Rimonabant reduces obesity-associated hepatic steatosis and features of metabolic syndrome in obese Zucker fa/fa rats. *Hepatology* 46, 122-129.
9. Ravinet, T. C., Arnone, M., Delgorge, C. *et al.* (2003) Anti-obesity effect of SR141716, a CB1 receptor antagonist, in diet-induced obese mice. *Am J Physiol Regul Integr Comp Physiol* 284, R345-R353.
10. Addy, C., Wright, H., Van, L. K. *et al.* (2008) The acyclic CB1R inverse agonist taranabant mediates weight loss by increasing energy expenditure and decreasing caloric intake. *Cell Metab* 7, 68-78.
11. Despres, J. P., Golay, A., & Sjostrom, L. (2005) Effects of rimonabant on metabolic risk factors in overweight patients with dyslipidemia. *N Engl J Med* 353, 2121-2134.
12. Pi-Sunyer, F. X., Aronne, L. J., Heshmati, H. M. *et al.* (2006) Effect of rimonabant, a cannabinoid-1 receptor blocker, on weight and cardiometabolic risk factors in overweight or obese patients: RIO-North America: a randomized controlled trial. *JAMA* 295, 761-775.
13. Van Gaal, L. F., Rissanen, A. M., Scheen, A. J. *et al.* (2005) Effects of the cannabinoid-1 receptor blocker rimonabant on weight reduction and cardiovascular risk factors in overweight patients: 1-year experience from the RIO-Europe study. *Lancet* 365, 1389-1397.
14. Osei-Hyiaman, D., DePetrillo, M., Pacher, P. *et al.* (2005) Endocannabinoid activation at hepatic CB1 receptors stimulates fatty acid synthesis and contributes to diet-induced obesity. *J Clin Invest* 115, 1298-1305.
15. Eckardt, K., Sell, H., Taube, A. *et al.* (2009) Cannabinoid type 1 receptors in human skeletal muscle cells participate in the negative crosstalk between fat and muscle. *Diabetologia* 52, 664-674.
16. Cota, D., Marsicano, G., Tschop, M. *et al.* (2003) The endogenous cannabinoid system affects energy balance via central orexigenic drive and peripheral lipogenesis. *J Clin Invest* 112, 423-431.
17. Tam, J., Vemuri, V. K., Liu, J. *et al.* (2010) Peripheral CB1 cannabinoid receptor blockade improves cardiometabolic risk in mouse models of obesity. *J Clin Invest* 120, 2953-2966.
18. Bartelt, A., Bruns, O. T., Reimer, R. *et al.* (2011) Brown adipose tissue activity controls triglyceride clearance. *Nat Med* 17, 200-205.
19. Cannon, B. & Nedergaard, J. (2004) Brown adipose tissue: function and physiological significance. *Physiol Rev* 84, 277-359.
20. Cypess, A. M., Lehman, S., Williams, G. *et al.* (2009) Identification and importance of brown adipose tissue in adult humans. *N Engl J Med* 360, 1509-1517.
21. van Marken Lichtenbelt, W. D., Vanhomerig, J. W., Smulders, N. M. *et al.* (2009) Cold-activated brown adipose tissue in healthy men. *N Engl J Med* 360, 1500-1508.

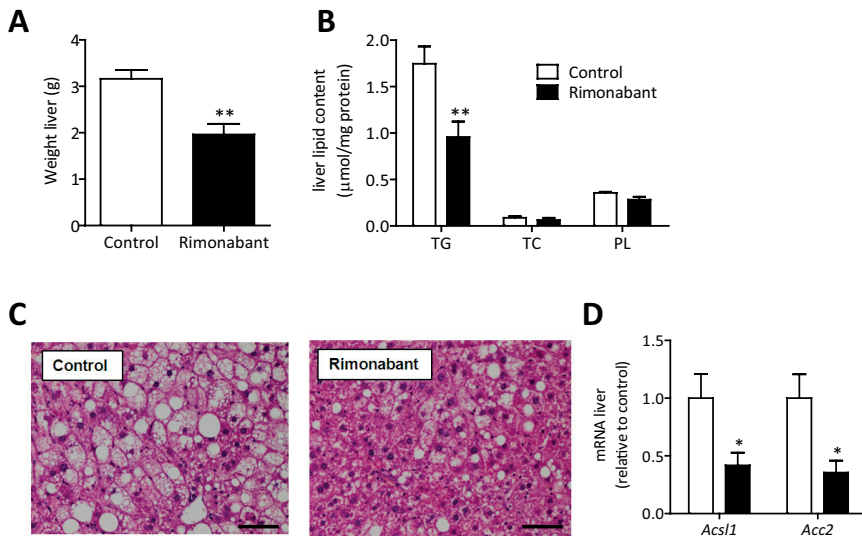
22. Virtanen, K. A., Lidell, M. E., Orava, J. *et al.* (2009) Functional brown adipose tissue in healthy adults. *N Engl J Med* 360, 1518-1525.
23. Bakker, L. E., Boon, M. R., van der Linden, R. A. *et al.* (2014) Brown adipose tissue volume in healthy lean south Asian adults compared with white Caucasians: a prospective, case-controlled observational study. *Lancet Diabetes Endocrinol* 2, 210-217.
24. Westerterp, M., van der Hoogt, C. C., de, H. W. *et al.* (2006) Cholesteryl ester transfer protein decreases high-density lipoprotein and severely aggravates atherosclerosis in APOE*3-Leiden mice. *Arterioscler Thromb Vasc Biol* 26, 2552-2559.
25. de, H. W., van der Hoogt, C. C., Westerterp, M. *et al.* (2008) Atorvastatin increases HDL cholesterol by reducing CETP expression in cholesterol-fed APOE*3-Leiden.CETP mice. *Atherosclerosis* 197, 57-63.
26. van der Hoogt, C. C., de, H. W., Westerterp, M. *et al.* (2007) Fenofibrate increases HDL-cholesterol by reducing cholesteryl ester transfer protein expression. *J Lipid Res* 48, 1763-1771.
27. van Klinken, J. B., van den Berg, S. A., Havekes, L. M. *et al.* (2012) Estimation of activity related energy expenditure and resting metabolic rate in freely moving mice from indirect calorimetry data. *PLoS One* 7, e36162.
28. Feurer I & Mullen JL (1986) Beside measurement of resting energy expenditure and respiratory quotient via indirect calorimetry. *Nutr Clin Prac* 1, 43-49.
29. Zambon, A., Hashimoto, S. I., & Brunzell, J. D. (1993) Analysis of techniques to obtain plasma for measurement of levels of free fatty acids. *J Lipid Res* 34, 1021-1028.
30. Rensen, P. C., van Dijk, M. C., Havenaar, E. C. *et al.* (1995) Selective liver targeting of antivirals by recombinant chylomicrons--a new therapeutic approach to hepatitis B. *Nat Med* 1, 221-225.
31. Jong, M. C., Rensen, P. C., Dahlmans, V. E. *et al.* (2001) Apolipoprotein C-III deficiency accelerates triglyceride hydrolysis by lipoprotein lipase in wild-type and apoE knockout mice. *J Lipid Res* 42, 1578-1585.
32. Redgrave, T. G., Roberts, D. C., & West, C. E. (1975) Separation of plasma lipoproteins by density-gradient ultracentrifugation. *Anal Biochem* 65, 42-49.
33. Bligh, E. G. & Dyer, W. J. (1959) A rapid method of total lipid extraction and purification. *Can J Biochem Physiol* 37, 911-917.
34. Zennaro, M. C., Le, M. D., Viengchareun, S. *et al.* (1998) Hibernoma development in transgenic mice identifies brown adipose tissue as a novel target of aldosterone action. *J Clin Invest* 101, 1254-1260.
35. Bajzer, M., Olivieri, M., Haas, M. K. *et al.* (2011) Cannabinoid receptor 1 (CB1) antagonism enhances glucose utilisation and activates brown adipose tissue in diet-induced obese mice. *Diabetologia* 54, 3121-3131.
36. Hu, C., Wei, H., van den Hoek, A. M. *et al.* (2011) Plasma and liver lipidomics response to an intervention of rimonabant in ApoE*3Leiden.CETP transgenic mice. *PLoS One* 6, e19423.
37. Hardie, D. G., Ross, F. A., & Hawley, S. A. (2012) AMPK: a nutrient and energy sensor that maintains energy homeostasis. *Nat Rev Mol Cell Biol* 13, 251-262.
38. Wu, H. M., Yang, Y. M., & Kim, S. G. (2011) Rimonabant, a cannabinoid receptor type 1 inverse agonist, inhibits hepatocyte lipogenesis by activating liver kinase B1 and AMP-activated protein kinase axis downstream of Galpha i/o inhibition. *Mol Pharmacol* 80, 859-869.
39. Tedesco, L., Valerio, A., Cervino, C. *et al.* (2008) Cannabinoid type 1 receptor blockade promotes mitochondrial biogenesis through endothelial nitric oxide synthase expression in white adipocytes. *Diabetes* 57, 2028-2036.
40. Ortega-Molina, A., Efeyan, A., Lopez-Guadamillas, E. *et al.* (2012) Pten positively regulates brown adipose function, energy expenditure, and longevity. *Cell Metab* 15, 382-394.
41. Verty, A. N., Allen, A. M., & Oldfield, B. J. (2009) The effects of rimonabant on brown adipose tissue in rat: implications for energy expenditure. *Obesity (Silver Spring)* 17, 254-261.

42. Tseng, Y. H., Kokkotou, E., Schulz, T. J. *et al.* (2008) New role of bone morphogenetic protein 7 in brown adipogenesis and energy expenditure. *Nature* 454, 1000-1004.
43. Whittle, A. J., Carobbio, S., Martins, L. *et al.* (2012) BMP8B increases brown adipose tissue thermogenesis through both central and peripheral actions. *Cell* 149, 871-885.
44. Jbilo, O., Ravinet-Trillou, C., Arnone, M. *et al.* (2005) The CB1 receptor antagonist rimonabant reverses the diet-induced obesity phenotype through the regulation of lipolysis and energy balance. *FASEB J* 19, 1567-1569.
45. Molhoj, S., Hansen, H. S., Schweiger, M. *et al.* (2010) Effect of the cannabinoid receptor-1 antagonist rimonabant on lipolysis in rats. *Eur J Pharmacol* 646, 38-45.
46. Turu, G. & Hunyady, L. (2010) Signal transduction of the CB1 cannabinoid receptor. *J Mol Endocrinol* 44, 75-85.

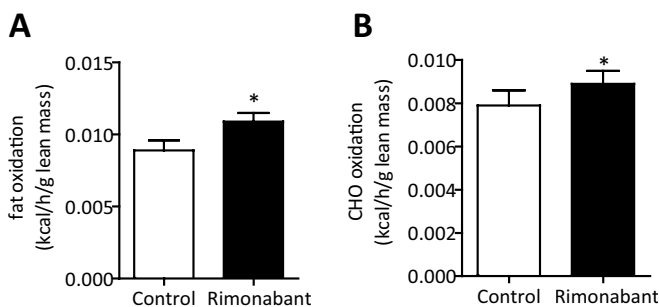
Supplementary appendix



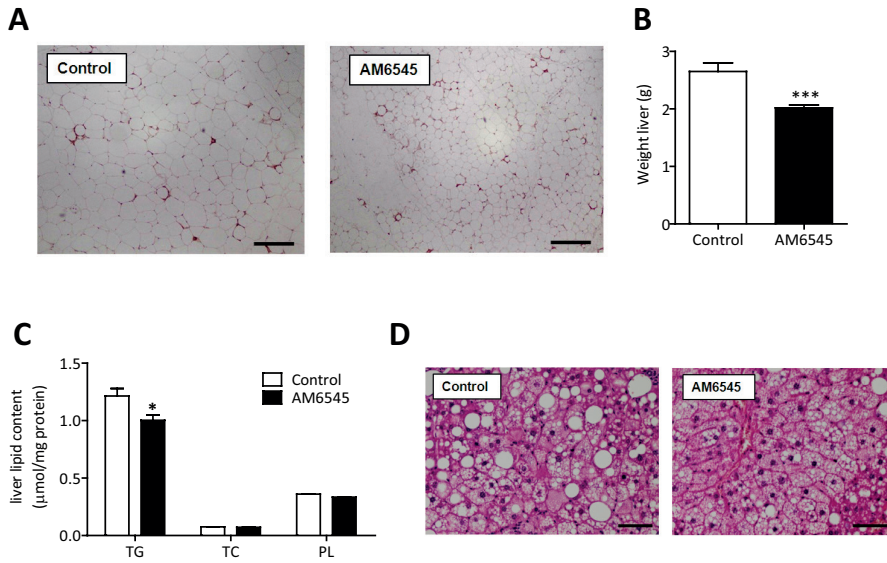
Supplemental Figure 1 – Effect of systemic CB1R blockade by rimonabant on subcutaneous WAT. Male E3L.CETP mice were fed a HFD for 12 weeks to induce diet-induced obesity and were then treated with rimonabant or vehicle for 4 weeks while being housed at an environmental temperature of 21°C. **(A)** Representative pictures of H&E stainings of sWAT in vehicle (left) and rimonabant (right) treated animals. Sections were enlarged 100x (scale bar 100 μm). **(B)** Expression of *Fasn*, *Scd1*, and *Hsl* in sWAT as measured by qRT-PCR. **(C)** 3T3L1 white adipocytes were treated with rimonabant (0, 0.1 or 1 μM) for 8 hours and glycerol release was measured in the supernatant. Values are means ± SEM (n=9 for *in vivo* study and n=4 for *in vitro* study) and expression of genes was corrected for the housekeeping genes $\beta 2$ -microglobulin and *36b4*. *p<0.05 compared to the control group.



Supplemental Figure 2 – Effect of systemic CB1R blockade by rimonabant on hepatic steatosis. Male E3L.CETP mice were fed a HFD for 12 weeks to induce diet-induced obesity and were then treated with rimonabant or vehicle for 4 weeks while being housed at an environmental temperature of 21°C. **(A)** Liver weight (g). **(B)** Liver content of triglycerides (TG), total cholesterol (TC) and phospholipids (PL). **(c)** Representative pictures of H&E stainings of livers from vehicle (left) and rimonabant (right) treated animals. Pictures were taken at 100x magnification (scale bar 100 μm). **(D)** Expression of *Acsl1* and *Acc2* in liver as measured by qRT-PCR. Values are means ± SEM (n=9) and expression of genes was corrected for the housekeeping genes *β2-microglobulin* and *36b4*. *p<0.05, **p<0.01 compared to the control group.



Supplemental Figure 3 – Systemic CB1R blockade increases fat and carbohydrate oxidation at thermoneutrality. Male E3L.CETP mice were fed a HFD for 12 weeks to induce diet-induced obesity and were then treated with rimonabant or vehicle for 4 weeks while being housed at an environmental temperature of 28°C. **(A,B)** Fat and carbohydrate (CH) oxidation as measured during 5 consecutive days in the fourth week of treatment via fully automatic metabolic cages, corrected for lean body mass. Values are means ± SEM (n=9). *p<0.05 compared to the control group.



Supplemental Figure 4 – Effect of strictly peripheral CB1R blockade by AM6545 on lipid storage in sWAT and liver. Male E3L.CETP mice were fed a HFD for 12 weeks to induce diet-induced obesity and were then treated with AM6545 or vehicle for 4 weeks while being housed at an environmental temperature of 21°C. **(A)** Representative pictures of H&E stainings of sWAT in vehicle (left) and AM6545 (right) treated animals. Pictures were taken at 100x magnification (scale bar 100 µm). **(B)** Liver weight (g). **(C)** Liver content of triglycerides (TG), total cholesterol (TC) and phospholipids (PL). **(D)** Representative pictures of H&E stainings of liver in vehicle (left) and AM6545 (right) treated animals. Pictures were taken at 100x magnification (scale bar 100 µm). Sections were enlarged 100x (scale bar 100 µm). Values are means ± SEM (n=9). *p<0.05, ***p<0.001 compared to the control group.

7

HEMATOPOIETIC $\alpha 7$ NICOTINIC ACETYLCHOLINE RECEPTOR DEFICIENCY INCREASES INFLAMMATION AND PLATELET ACTIVATION STATUS, BUT DOES NOT AGGRAVATE ATHEROSCLEROSIS

Sander Kooijman

Illiana Meurs

Marco van der Stoep

Kim L. Habets

Bart Lammers

Jimmy F.P. Berbée

Louis M. Havekes

Miranda van Eck

Johannes A. Romijn

Suzanne J.A. Korporaal

Patrick C.N. Rensen

Abstract

The autonomic nervous system attenuates inflammation through activation of the $\alpha 7$ nicotinic acetylcholine receptor ($\alpha 7$ nAChR), a pathway termed the cholinergic anti-inflammatory reflex. Interestingly, $\alpha 7$ nAChR is expressed on immune cells and platelets, both of which play a crucial role in the development of atherosclerosis. To investigate the role of hematopoietic $\alpha 7$ nAChR in inflammation and platelet function in atherosclerotic *ldlr*^{-/-} mice and to identify its consequences for atherosclerotic lesion development. Bone marrow from *$\alpha 7$ nAChR*^{-/-} mice or wild-type littermates was transplanted into irradiated *ldlr*^{-/-} mice. After a recovery period of 8 weeks, the mice were fed an atherogenic Western-type diet for 7 weeks. Hematopoietic $\alpha 7$ nAChR deficiency clearly increased the number of leukocytes in the peritoneum (2.6-fold, $p < 0.001$), blood (2.9-fold; $p < 0.01$), mesenteric lymph nodes (2.0-fold; $p < 0.001$) and spleen (2.2-fold; $p < 0.01$), indicative of an increased inflammatory status. Additionally, expression of inflammatory mediators was increased in peritoneal leukocytes (TNF α , 1.6-fold, $p < 0.01$; CRP, 1.8-fold; $p < 0.01$) as well as in the spleen (TNF α , 1.6-fold, $p < 0.01$). The lack of $\alpha 7$ nAChR on platelets from these mice increased the expression of active integrin $\alpha_{IIb}\beta_3$ upon stimulation by ADP (1.9-fold, $p < 0.01$), indicating increased activation status, while incubation of human platelets with an $\alpha 7$ nAChR agonist decreased aggregation (-35%, $p < 0.05$). Despite the large effects of hematopoietic $\alpha 7$ nAChR deficiency on inflammatory status and platelet function, it did not affect atherosclerosis development or composition of lesions. Hematopoietic $\alpha 7$ nAChR is important for attenuation of inflammatory responses and maintaining normal platelet reactivity, but loss of hematopoietic $\alpha 7$ nAChR does not aggravate atherosclerosis development.

Introduction

Accumulating evidence indicates a prominent role of the autonomic nervous system in the regulation of inflammation via the so-called 'cholinergic anti-inflammatory pathway'. This pathway relies upon direct activation of the afferent vagus nerve by pro-inflammatory cytokines and subsequent activation of efferent nerve fibers resulting in the release of acetylcholine in peripheral organs (1-4). Acetylcholine stimulates $\alpha 7$ nicotinic acetylcholine receptors ($\alpha 7$ nAChR) which is highly expressed on immune cells, resulting in decreased NF- κ B-mediated gene expression of pro-inflammatory cytokines (5,6). In addition to immune cells, $\alpha 7$ nAChR is expressed on a variety of cells including neuronal cells (7), endothelial cells (8) and platelets (9).

Despite its widespread expression, mice deficient for $\alpha 7$ nAChR are viable, develop normally and show no physical or neurological defects (10). However, upon endotoxin administration, $\alpha 7$ nAChR^{-/-} mice have significantly increased TNF α levels in the serum and spleen compared with wild-type mice (4). Serum IL-6 and C-reactive protein (CRP) are increased in $\alpha 7$ nAChR^{-/-} mice compared to control mice on an atherosclerosis-prone background (11). Accordingly, *in vitro* studies show that acetylcholine attenuates the release of pro-inflammatory cytokines (i.e. TNF α , IL-1 β , and IL-6) by macrophages conditioned by exposure to endotoxin (1). Additionally, cholinergic stimulation of $\alpha 7$ nAChR inhibits endothelial cell activation and leukocyte recruitment during inflammation (8) and modulates platelet function (9). Together, these data suggest an attenuating effect for $\alpha 7$ nAChR signaling on inflammation.

Atherosclerosis is a chronic inflammatory disease and the main cause of cardiovascular events. Atherosclerotic plaque development is initiated by trapping of lipids in the intima of the arterial wall, which stimulates vascular cells to produce inflammatory molecules and recruit monocytes and T cells to the vessel wall (12). Interestingly, the spleen is the most important source of acetylcholine (13) and splenic monocytes contribute largely to atherosclerotic lesion development (14). Additionally, circulating inflammatory markers that are under control of the cholinergic anti-inflammatory pathway, such as CRP and IL-6, have been implicated in the pathogenesis of atherosclerosis (15,16). Furthermore, recruitment, transmigration and activation of leukocytes, as well as platelet function contribute to atherogenesis (15-17).

We thus hypothesized that $\alpha 7$ nAChR activity exhibits an inhibitory effect on atherosclerotic lesion development. As the cholinergic anti-inflammatory pathway exerts its function through hematopoietic $\alpha 7$ nAChR, the aim of this study was to assess the stimulatory effect of hematopoietic $\alpha 7$ nAChR deficiency on inflammation and platelet function, and their consequences for atherosclerotic lesion development. Because wild-type (WT) mice do not develop atherosclerosis due to rapid hepatic (V)LDL clearance resulting in low (V)LDL-cholesterol levels (~2 mM), we used LDL

receptor deficient mice as recipients of $\alpha 7nAChR$ -deficient or WT bone marrow. LDL receptor deficient mice have increased cholesterol levels on a chow diet that are further increased upon Western-type diet feeding, which allows the development of diet-induced atherosclerosis.

Material & Methods

Animals

$\alpha 7nAChR^{+/+}$ and $\alpha 7nAChR^{-/-}$ mice obtained from Charles River Laboratories (L'Arbresle, France) were used to generate $\alpha 7nAChR^{-/-}$ and $\alpha 7nAChR^{+/+}$ (wild-type, WT) mice (both C57Bl/6J background). Homozygous LDL receptor knockout ($ldlr^{-/-}$) mice (C57Bl/6J background) were obtained from The Jackson Laboratory (Bar Harbor, USA) as mating pairs and bred at the Gorlaeus Laboratories (Leiden, The Netherlands). Mice were housed in sterilized filter-top cages in a temperature-controlled room with a 12-h light/dark cycle and food and water were provided *ad libitum*. Mice were maintained on sterilized regular chow, containing 4.3% (w/w) fat and no cholesterol (RM3, Special Diet Services, Witham, UK). To induce atherosclerosis, they were fed a Western-type diet (WTD), containing 15% (w/w) cacao butter, 1% (w/w) corn oil and 0.25% (w/w) cholesterol (Diet W, Abdiets, Woerden, The Netherlands). Drinking water was supplied with antibiotics (83 mg/L ciprofloxacin and 67 mg/L polymyxin B sulfate) and 6.5 g/L sucrose. Animal experiments were performed at the Gorlaeus Laboratories of the Leiden Academic Centre for Drug Research in accordance with the National Laws (ID 10161.1). All animal experiments were approved by the Ethics Committee for Animal Experiments of Leiden University and carried out in compliance with the Dutch government guidelines.

Bone marrow transplantation (BMT)

To induce bone marrow aplasia, female $ldlr^{-/-}$ recipient mice (10-12 weeks old), which represent an established model for the development of atherosclerosis, were exposed to a single dose of 9 Gy (0.19 Gy/min, 200 kV, 4 mA) total body irradiation using an Andrex Smart 225 Röntgen source (YXLON International, Hamburg, Germany) with a 6-mm aluminum filter 1 day before the transplantation. At the day of transplantation, bone marrow from female donor WT and $\alpha 7nAChR^{-/-}$ mice was isolated by flushing the femurs and tibiae with phosphate-buffered saline (PBS) (n=3 per group). Single-cell suspensions were obtained by passing the cells through a 70 μ m cell strainer (Falcon, The Netherlands). Irradiated $ldlr^{-/-}$ recipients received 5×10^6 bone marrow cells by intravenous injection into the tail vein. After a recovery period of 8 weeks mice were fed the WTD for 7 weeks, after which animals were sacrificed. Body mass was recorded weekly throughout the study.

Assessment of successful bone marrow reconstitution

At the end of the study, bone marrow was isolated from the transplanted *ldlr*^{-/-} mice, and hematologic chimerism was determined using genomic DNA by PCR at 15 weeks after BMT. The relative presence of the $\alpha 7nAChR$ in bonemarrow was assessed using primers for murine $\alpha 7nAChR$ (forward: 5'-CCTGGTCCTGCTGTGTTAAACTGCTTC-3'; reverse: 5'-CTGCTGGGAAATCCTAGGCACACTTGAG-3') and for the neomycin gene neocassette (forward: 5'-TGCTCCTGCCGAGAAAGTAT-3'; reverse: 5'-AATATCACGG GTAGCCAACG-3').

Plasma lipid and lipoprotein analysis

Blood was drawn after a 4 h fast at the start of WTD feeding and after 4 weeks of diet via tail-bleeding. At the end of the study, mice were anesthetized by subcutaneous injection of a mixture of xylazine (5 mg/mL), ketamine (40 mg/L) and atropine (0.05 mg/mL) before blood was collected by bleeding via the eye. Plasma was isolated by centrifugation and stored frozen at -80°C until further analyses. The concentrations of total cholesterol (TC) and triglycerides (TG) in plasma were determined using commercially available enzymatic colorimetric kits according to the manufacturer's protocols (236691 and 1488872; Roche Molecular Biochemicals, Indianapolis, IN, USA). The plasma concentration of phospholipids (PL) was determined using another enzymatic colorimetric kit (3009; Instruchemie, Delfzijl, The Netherlands). The distribution of lipids over the various lipoproteins in plasma was determined by fractionation of 50 μ L of pooled plasma using a Superose 6 HR 10/30 column (Äkta System; Amersham Pharmacia Biotech, Piscataway, NJ, USA).

Analysis of leukocytes

For analysis of leukocytes, at the end of the study, mice were anesthetized by subcutaneous injection of a mixture of xylazine (5 mg/mL), ketamine (40 mg/L) and atropine (0.05 mg/mL) before blood was collected by bleeding via the eye. The peritoneal cavities of the transplanted mice were lavaged with 10 mL ice-cold PBS to collect peritoneal leukocytes. Spleen and mesenteric lymphnodes were take out for quantification of cell composition, using an automated Sysmex XT-2000iV analyzer (Sysmex Europe GMBH, Norderstedt, Germany), and for gene expression analysis.

Gene expression analysis

Total RNA was isolated using the Nucleospin RNA II kit (Macherey-Nagel, Düren, Germany) according to manufacturer's instructions. One microgram of total RNA was converted to cDNA with iScript cDNA Synthesis kit (Biorad) and purified with Nucleospin Extract II kit (Macherey-Nagel). RT-PCR was conducted on a IQ5 PCR

machine (Biorad) using Sensimix SYBR Green RT-PCR mix (Quantace, London, UK). mRNA levels were normalized to mRNA levels of *Hprt*, *Gapdh* and *Cyclo*.

Analysis of murine platelet function

For analysis of murine platelet function, blood was collected into 0.1 volume 130 mmol/L trisodium citrate via cardiac puncture. Platelet count and mean platelet volume (MPV) were analyzed in whole blood using a Sysmex XT-2000iV Hematology Analyzer. The platelet count was corrected for the volume of anti-coagulant present.

To investigate platelet activation, we measured the ability of platelets to convert integrin $\alpha_{\text{IIb}}\beta_3$ to its active high-affinity open conformation ($\alpha_{\text{IIb}}\beta_3^*$) upon stimulation by different agonists. For this purpose, 25 μL diluted whole blood (1:20 (v/v) in HEPES-Tyrode buffer (145 mM NaCl, 5 mM KCl, 0.5 mM Na_2HPO_4 , 1 mM MgSO_4 , 10 mM HEPES, 5 mM D-glucose, pH 7.2)) was recalcified (1 mM CaCl_2) and stimulated by ADP (0.5 and 5 μM ; Sigma, St. Louis, MO, USA), PAR-4 peptide (0.1 and 1.0 mM; Bachem, Weil am Rhein, Germany) or the Ca^{2+} ionophore A23187 (1 μM ; Sigma) for 15 min at 20°C in the presence of 5 μL RPE-conjugated anti-active integrin $\alpha_{\text{IIb}}\beta_3$ (clone JON/A; Emfret Analytics, Eibelstadt, Germany). Samples were fixed in 1% formaldehyde in PBS, and integrin $\alpha_{\text{IIb}}\beta_3$ in its active high affinity open confirmation was determined by flow cytometry. The total expression level of integrin $\alpha_{\text{IIb}}\beta_3$ (both active and inactive integrin $\alpha_{\text{IIb}}\beta_3$) was also assessed by flow cytometry in whole blood. Whole blood (25 μL) was diluted (1:20 (v/v) in HEPES-Tyrode buffer (pH 7.2)), recalcified (1 mM CaCl_2), incubated with 5 μL RPE-conjugated anti-integrin $\alpha_{\text{IIb}}\beta_3$ (clone Leo.F2; Emfret Analytics) for 15 min at 20°C and analyzed by flow cytometry after fixation. The ratio of active integrin $\alpha_{\text{IIb}}\beta_3^*$ / total integrin $\alpha_{\text{IIb}}\beta_3$ protein was appointed as a marker for platelet activation.

Analysis of human platelet activation

For human platelet activation studies, platelets were isolated from freshly drawn venous blood from healthy volunteers, who claimed not to have taken any medication 10 days prior to blood collection. These studies were approved by the Medical Ethics Committee of University Medical Center Utrecht and informed consent was obtained for blood sampling from all donors. Blood was collected into 3.2% tri-sodium citrate and was centrifuged (156 $\times g$, 15 min, 20°C) to prepare platelet-rich plasma. Tri-sodium citrate was used instead of EDTA to ensure presence of sufficient calcium for platelet activation. After addition of 0.1 volume ACD (2.5% (w/v) trisodium citrate, 1.5% (w/v) citric acid, 2% (w/v) D-glucose) to lower the pH of the plasma to pH 6.5, platelets were further purified by centrifugation (400 $\times g$, 15 min, 20°C). After resuspension of the platelet pellet in HEPES-Tyrode buffer (pH 6.5), prostacyclin (PGI_2 ; Cayman Chemical, Ann Arbor, MI, USA) was added to a final concentration of 10 ng/mL and the washing procedure was repeated once. The platelet pellet was

resuspended in HEPES-Tyrode buffer (pH 7.2) and the platelet count was adjusted to 2.0×10^{11} platelets/L. Platelets were left for 30 min at 37°C to ensure a resting state.

For aggregation experiments, platelets were pre-incubated for 30 minutes at room temperature with the α_7 nAChR agonist PNU282987 (10 μ M) or vehicle (DMSO). Platelet aggregation was initiated by addition of ADP (10 μ M) in the presence of fibrinogen (0.5 mg/mL; Kordia Life Sciences, Leiden, The Netherlands) and was monitored in a Chrono-Log lumiaggregometer (Chrono-Log Corporation, Haverford, PA, USA) at 37°C and a stirring speed of 1000 rpm. Additionally, surface expression of P-selectin was determined as another marker of platelet reactivity and was measured by flow cytometry in citrated whole blood, treated with PNU282987 (10 μ M) or vehicle prior to stimulation with ADP (serial dilutions ranging from 0-125 μ M) for 20 min in the presence of RPE-conjugated anti-CD62P (BD Pharmingen, Franklin Lakes, NJ, USA).

Atherosclerosis quantification

Atherosclerotic mean lesion area (in μm^2) was quantified in cross-sections (5 μm) throughout the aortic root area starting from the appearance of open aortic valve leaflets. Per mouse, four sections with 50- μm intervals were used for atherosclerosis measurements. Sections were stained with hematoxylin-phloxine-saffron for histological analysis. Lesions were categorized for severity according to the guidelines of the American Heart Association adapted for mice(18,19). Various types of lesions were discerned: no lesions, mild lesions (types 1–3) and severe lesions (types 4–5). Immunohistochemistry for determination of lesion composition was performed as described previously(20). Rat anti-mouse antibody MAC3 (1:1000; BD Pharmingen, The Netherlands) was used to quantify macrophage area. Monoclonal mouse antibody M0851 (1:800; Dako, Heverlee, the Netherlands) against smooth muscle cell (SMC) actin was used to quantify SMC area. Sirius Red staining was used to quantify collagen area. Lesion area and composition were determined using ImageJ.

Statistical analysis

Data are presented as means \pm SEM unless indicated otherwise. To compare differences among groups T-tests were performed. A P-value <0.05 was considered statistically significant.

Results

Hematopoietic $\alpha 7nAChR$ deficiency does not affect body weight and plasma lipid levels

Ldlr^{-/-} mice were transplanted with bone marrow from *$\alpha 7nAChR$* ^{-/-} mice or WT littermates. After a recovery period of 8 weeks on regular murine chow diet, the transplanted mice were challenged with an atherogenic Western-type diet (WTD) for 7 weeks. Mice transplanted with *$\alpha 7nAChR$* ^{-/-} bone marrow showed a modest temporary drop in body weight compared to mice transplanted with WT bone marrow at week 3 and 4 after BMT, but the weight curves were not different while feeding the WTD (**Figure 1A**). Reconstitution of the recipient *Ldlr*^{-/-} mice with bone marrow of donor mice was successful as assessed by $\alpha 7nAChR$ transcript analysis in bone marrow (>90% chimerism; **Supplemental Figure 1**).

To evaluate whether hematopoietic $\alpha 7nAChR$ deficiency affects lipid metabolism, plasma total cholesterol (TC), phospholipids (PL) and triglycerides (TG) were assessed at the start of WTD feeding and after 4 and 7 weeks of diet intervention. No differences in plasma lipid concentrations were found between *$\alpha 7nAChR$* ^{-/-} and WT transplanted mice at the start of the diet (not shown), after 4 weeks (not shown), nor after 7 weeks (**Figure 1B**). In addition, the distribution of cholesterol over lipoproteins of the *$\alpha 7nAChR$* ^{-/-} transplanted mice did not differ from that of the WT transplanted mice (**Figure 1C**).

Hematopoietic $\alpha 7nAChR$ deficiency increases inflammatory status

As a measure of inflammatory status, the leukocyte count within the peritoneal cavity was quantified after lavage. Remarkably, disruption of hematopoietic $\alpha 7nAChR$ significantly increased peritoneal leukocyte count by 2.6-fold ($12.3 \pm 3.4 \times 10^9/L$ vs. $4.8 \pm 0.9 \times 10^9/L$; $p < 0.05$) (**Figure 2A**). This was due to a significant increase in multiple leukocyte cell types within the *$\alpha 7nAChR$* ^{-/-} vs. control transplanted mice, i.e. monocytes ($6.3 \pm 1.6 \times 10^9/L$ vs. $2.9 \pm 0.5 \times 10^9/L$; $p < 0.05$) (**Figure 2B**), lymphocytes ($3.9 \pm 1.3 \times 10^9/L$ vs. $1.7 \pm 0.4 \times 10^9/L$; $p < 0.05$) (**Figure 2C**), and neutrophils ($0.41 \pm 0.14 \times 10^9/L$ vs. $0.16 \pm 0.04 \times 10^9/L$; $p < 0.05$) (**Figure 2D**), suggesting an increased pro-inflammatory status of the body. In line with these observations, in peritoneal leukocytes of *$\alpha 7nAChR$* ^{-/-} vs. control transplanted mice, mRNA expression of the pro-inflammatory cytokines TNF α (1.6-fold; $p < 0.01$) and CRP (1.8-fold; $p < 0.01$) was increased, while mRNA expression of IL-1 β (1.6-fold; $p = 0.26$) and IL-6 (1.2-fold; $p = 0.45$) was not affected (**Figure 2E**). Interestingly, not only the number of leukocytes in the peritoneum was increased upon hematopoietic $\alpha 7nAChR$ deficiency, but also in the blood (2.9-fold; $p < 0.01$), mesenteric lymph nodes (2.0-fold; $p < 0.001$) and spleen (2.2-fold; $p < 0.01$) (**Figure 2F**). Analysis of subsets by flow cytometry revealed, comparable to the sysmex analysis on peritoneal leukocytes, an increase in all leukocyte subpopulations (not shown).

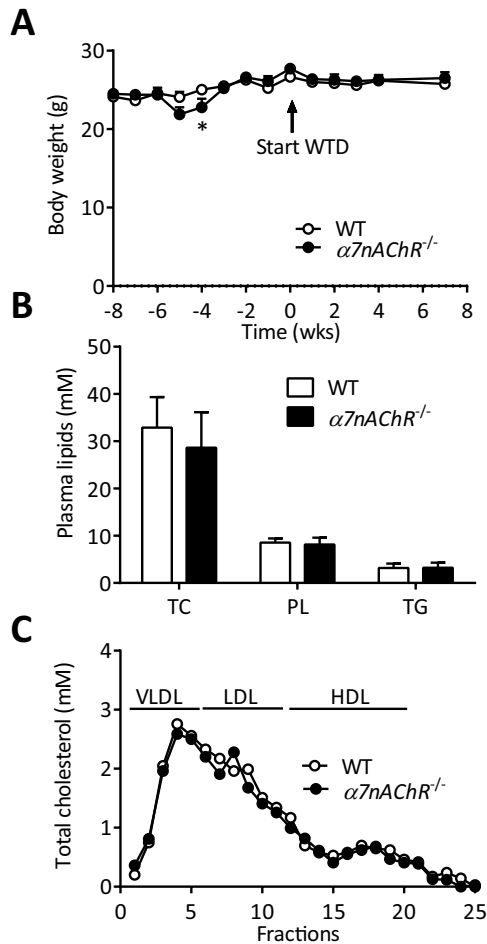


Figure 1 – Effect of hematopoietic $\alpha 7nAChR$ deficiency on body weight, plasma lipid levels and cholesterol distribution over lipoproteins. *ldlr*^{-/-} mice were transplanted with bone marrow of $\alpha 7nAChR^{-/-}$ (n=11) or WT mice (n=20) (t=-8 wks), allowed to recover for 8 weeks and subsequently (t=0 wks) fed a Western-type diet (WTD) during 7 weeks. Body weight was monitored during the whole experiment (A). After 7 wks of WTD feeding, blood samples were drawn and the concentrations of cholesterol, phospholipid and triglycerides in plasma were determined (B). The distribution of cholesterol over the different lipoproteins was determined by fractionation of pooled plasma by FPLC. VLDL, LDL and HDL were collected in fractions 1-6, 7-14, and 15-24, respectively (C). Values represent means \pm SEM.

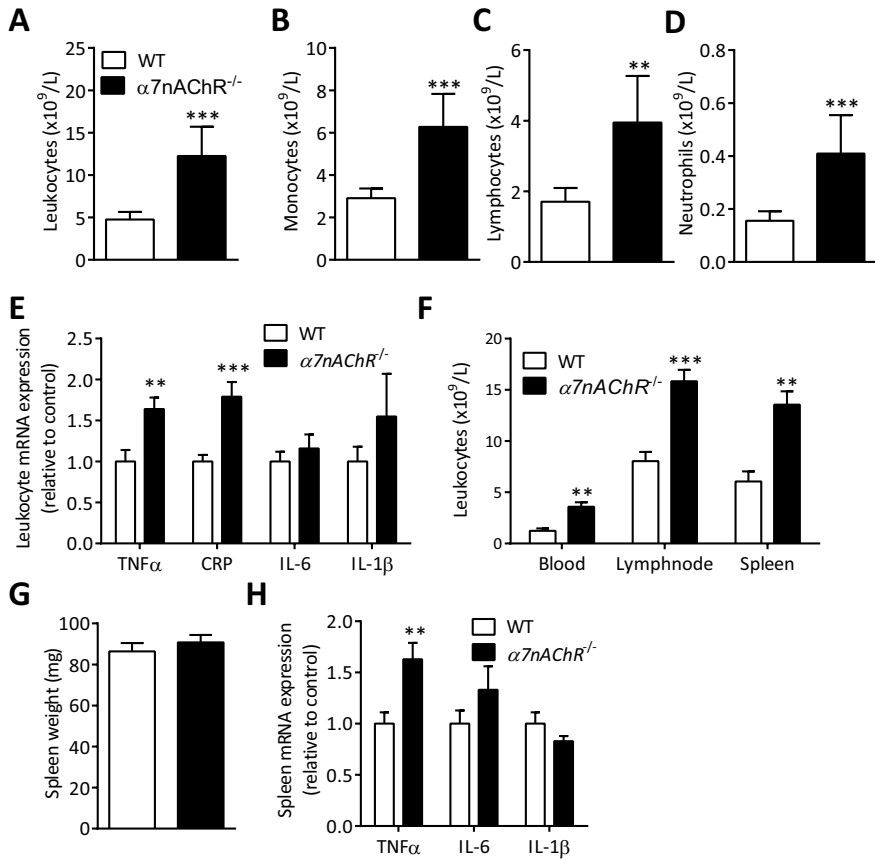


Figure 2 – Effect of hematopoietic $\alpha 7nAChR$ deficiency on inflammation. After 7 weeks of WTD, the number of peritoneal leukocytes was determined (**A**) and their composition was analyzed, i.e. monocytes (**B**), lymphocytes (**C**) and neutrophils (**D**) in hematopoietic $\alpha 7nAChR^{-/-}$ (n=11) or WT mice (n=20). Total RNA was extracted from peritoneal leukocytes and mRNA expression of the pro-inflammatory cytokines TNF α , CRP, IL-6, and IL-1 β was determined (**E**). Leukocytes in blood, lymph nodes and spleen were counted (**F**). The spleen was isolated and weighed (**G**), after which mRNA expression of the pro-inflammatory cytokines TNF α , IL-6, and IL-1 β was determined (**H**). Values represent means \pm SEM. **p<0.01 and ***p<0.001 denote statistical difference vs. controls.

As the cholinergic anti-inflammatory pathway is known to act via the spleen [13], the spleen was further analysed. The spleen of *a7nAChR^{-/-}* and WT transplanted mice did not differ in weight (90±4 mg vs. 86±4 mg; $p=0.47$) (**Figure 2G**), but mRNA expression of TNF α was increased in the spleen of *a7nAChR^{-/-}* transplanted mice compared to controls (1.6-fold; $p<0.01$) (**Figure 2H**), similar as observed for peritoneal leukocytes.

Overall, these findings show an increased inflammatory status of *a7nAChR^{-/-}* transplanted mice compared to control transplanted mice.

Hematopoietic *a7nAChR* deficiency increases platelet reactive status

Functional *a7nAChR* is expressed on platelets and modulates activation of platelets [9], which may represent an important linkage between inflammation, thrombosis and atherosclerosis [17]. Integrin $\alpha_{IIb}\beta_3$ is an integrin complex found on the surface of platelets, and is essential for platelet aggregation upon binding of fibrinogen. Upon platelet activation, integrin $\alpha_{IIb}\beta_3$ changes its conformation to an active high affinity state in which it is able to bind its ligands, including fibrinogen. Using flow cytometry, the expression of active integrin $\alpha_{IIb}\beta_3$ was measured after platelet activation by the agonists ADP and PAR-4 peptide. The lack of *a7nAChR* on platelets did not affect baseline expression of active integrin $\alpha_{IIb}\beta_3$ (not shown), but increased its expression upon stimulation by ADP compared to control platelets (2.0-fold for 0.5 μM , $p<0.05$ and 1.9-fold for 5 μM , $p<0.01$), and induced a non-significant increase of integrin $\alpha_{IIb}\beta_3$ after stimulation by PAR-4 peptide (1.5-fold for 0.1 mM, $p=0.12$ and 1.3-fold for 1 mM, $p=0.19$) (**Figure 3A**). The expression of total integrin $\alpha_{IIb}\beta_3$ (both active and inactive integrin $\alpha_{IIb}\beta_3$) on platelets did not differ between both groups (**Figure 3B,C**). These data indicate that *a7nAChR* signaling is not only involved in diminishing pro-inflammatory cytokine production by immune cells, but also in reducing the reactive state of circulating platelets.

For platelet activation, an increased intracellular Ca^{2+} concentration is essential. To study the contribution of platelet receptor signaling in activation of integrin $\alpha_{IIb}\beta_3$ in the absence of functional *a7nAChR*, the Ca^{2+} ionophore A23187 was used to directly induce Ca^{2+} entry without the activation of platelet receptors. After stimulation with A23187, no differences were observed in the expression of active integrin $\alpha_{IIb}\beta_3$ between both groups (**Figure 3D**). These results indicate that the differences in reactive state of the platelets are likely due to interactions between *a7nAChR* signaling and signaling upstream of Ca^{2+} mobilization. However, it should be noted that A23187 is a potent activator of platelets, which may have blunted the effects of *a7nAChR* deficiency.

As aggregation experiments were unfeasible to perform on platelets of these mice, human platelets from healthy individuals were incubated with the *a7nAChR*-selective agonist PNU-282987 to investigate the effects of *a7nAChR* signaling on platelet aggregation. Incubation with 10 μM PNU-282987, prior to stimulation with

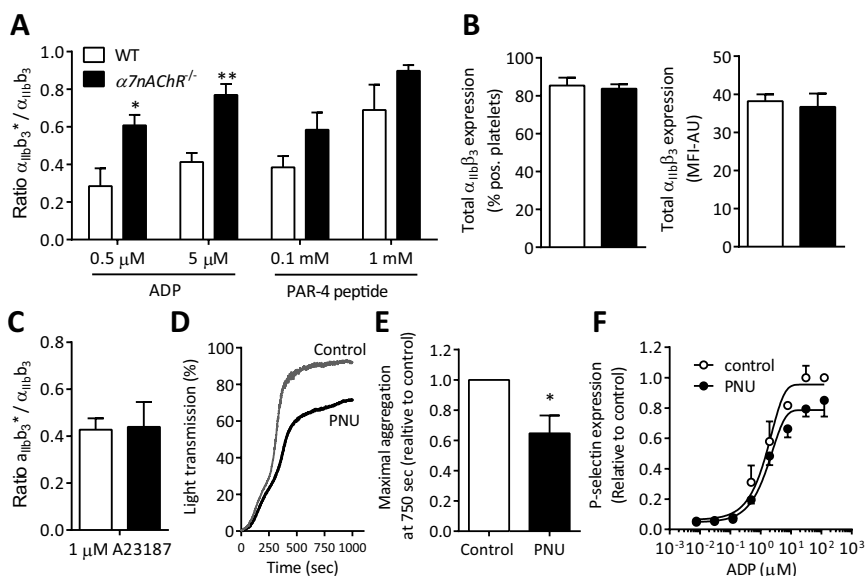


Figure 3 – Effect of hematopoietic $\alpha 7nAChR$ deficiency on platelet reactivity. After 7 weeks of WTD, platelets were isolated from whole blood from hematopoietic $\alpha 7nAChR^{-/-}$ ($n=4$) or WT mice ($n=4$), stimulated with the platelet agonists ADP and PAR-4 peptide, and the ratio of the active form of integrin $\alpha_{IIb}\beta_3^*$ relative to total integrin $\alpha_{IIb}\beta_3$ protein was analyzed by flow cytometry (**A**). The expression of total integrin $\alpha_{IIb}\beta_3$ protein (both active and inactive form) was determined by flow cytometry (**B**). Integrin $\alpha_{IIb}\beta_3$ activation [$\alpha_{IIb}\beta_3^*$ = active form of integrin] without activation of platelet receptors was determined by using the Ca^{2+} ionophore A23187 (**C**). In human platelets ($n=3$), aggregation was assessed upon ADP activation after pre-incubation with the $\alpha 7nAChR$ agonist PNU-282987 (**D**) and maximal aggregation after 750 sec was determined (**E**). P-selectin expression, a marker for human platelet activation, was measured after activation by ADP (**F**). Values represent means \pm SEM. * $p<0.05$ denotes statistical difference vs. controls.

ADP, inhibited platelet aggregation (**Figure 3E**), and reduced the maximal aggregation response by 35% ($p<0.05$) (**Figure 3F**). Additionally, the expression of P-selectin, another marker for platelet reactivity, tended to decrease after treatment with PNU-282987 prior to stimulation with increasing concentrations of ADP (**Figure 3G**). Pre-incubation with a physiological concentration of PNU-282987 (100 nM; **Supplemental Figure 2**) or shorter pre-incubation of 5 min instead of 30 min (**Supplemental Figure 3**) did not reduce P-selectin expression nor decrease platelet-bound fibrinogen, which is another marker for platelet aggregation. Together, these data indicate that stimulation of the $\alpha 7nAChR$ reduces platelet activation and aggregation, while $\alpha 7nAChR$ deficiency results in an increased platelet reactive state.

Hematopoietic $\alpha 7nAChR$ deficiency does not affect atherosclerotic lesion development

An increased inflammatory status and increased platelet activation status, observed in hematopoietic $\alpha 7nAChR$ deficient mice, may be expected to accelerate the development of atherosclerosis. To study the role of hematopoietic $\alpha 7nAChR$ in atherosclerosis development, $\alpha 7nAChR^{-/-}$ and WT transplanted mice were sacrificed after 7 weeks of WTD feeding, and atherosclerotic lesion size and lesion severity were

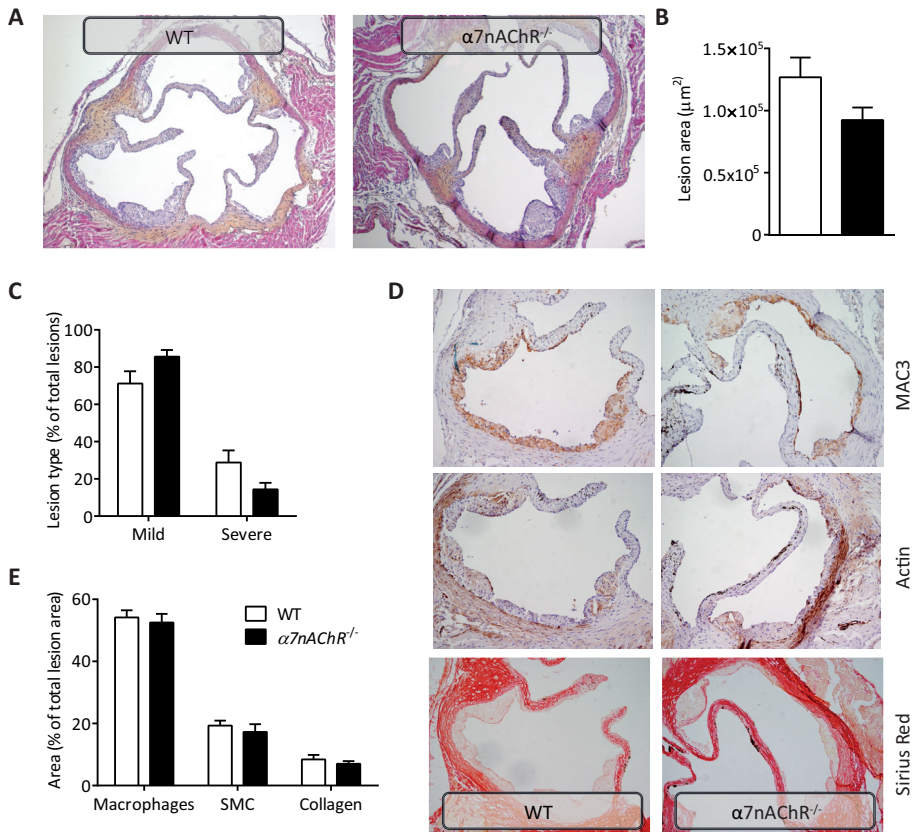


Figure 4 – Effect of hematopoietic $\alpha 7nAChR$ deficiency on atherosclerotic lesion development. After 7 weeks of WTD, hearts were isolated of hematopoietic $\alpha 7nAChR^{-/-}$ (n=11) or WT mice (n=20), and cross-sections (5 μm) with 50- μm intervals throughout the aortic root area starting from the appearance of open aortic valve leaflets were used for atherosclerosis measurements. Sections were stained with hematoxylin-phloxine-saffron (HPS) for histological analysis. Representative images of HPS staining (**A**). Atherosclerotic mean lesion area (in μm^2) was quantified in four subsequent cross-sections (**B**). The same four sections per mouse were categorized according to lesion severity (**C**). Immunohistochemistry for determination of lesion composition; MAC3 for macrophages and actin for smooth muscle cells (SMC) or Sirius Red staining for collagen content (**D**). Comparable to lesion size, the composition of the lesions was determined in four subsequent cross-sections (**E**). Values represent means \pm SEM per group.

determined in the valve area of the aortic root. However, $\alpha 7nAChR$ deficiency in mice did not affect atherosclerotic lesion size (**Figure 4A,B**) and lesion severity, classified as mild (type 1-3) and severe (type 4-5) lesions (**Figure 4C**). In addition, no significant differences could be observed between the lesion composition of $\alpha 7nAChR^{-/-}$ and WT transplanted mice, with respect to the relative area of macrophages (MAC3 staining), smooth muscle cells (SMC; actin staining) and collagen (Sirius Red staining) (**Figure 4D,E**).

Discussion

In the present study, we determined the effect of the absence of hematopoietic $\alpha 7nAChR$ on the inflammatory status and platelet function, and the consequences for atherosclerotic lesion development in hyperlipidemic $ldlr^{-/-}$ mice. We showed that hematopoietic disruption of $\alpha 7nAChR$ clearly increased inflammatory status as indicated by an increased number of peritoneal leukocytes and an increased expression of inflammatory mediators by both peritoneal leukocytes (TNF α , CRP) and the spleen (TNF α). Apparently, hematopoietic $\alpha 7nAChR$ deficiency recapitulates the pro-inflammatory phenotype of total body $\alpha 7nAChR$ -deficient mice (4). Of note, in our study hematopoietic $\alpha 7nAChR^{-/-}$ mice were subjected to a WTD containing 16% fat and 0.25% cholesterol, a diet known to evoke only mild inflammation (21). Still the number of leukocytes in the blood, lymph nodes, spleen and peritoneum all increased by at least 2-fold, consistent with a role for the cholinergic anti-inflammatory pathway in prevention of inflammation during diet-induced hyperlipidemia. The increased number of leukocytes was explained by an increase in various leukocyte cell types (i.e., monocytes, lymphocytes and neutrophils).

In addition to leukocytes, the $\alpha 7nAChR$ is also expressed on platelets (9). Therefore, we evaluated the effect of $\alpha 7nAChR$ deficiency as well as specific $\alpha 7nAChR$ activation on platelet reactivity by determining active integrin $\alpha_{IIb}\beta_3$ expression and platelet aggregation, respectively. Murine $\alpha 7nAChR$ deficiency in platelets increased active integrin $\alpha_{IIb}\beta_3$ expression induced by classical platelet agonists. Accordingly, in human platelets, ADP-induced platelet aggregation was inhibited by the $\alpha 7nAChR$ -selective agonist PNU-282987. As activation of platelets induces inflammation (17), these data are in line with the immunosuppressive function of the cholinergic anti-inflammatory pathway. Furthermore, these results indicate that activation of $\alpha 7nAChR$ signaling is involved in normal platelet function as $\alpha 7nAChR$ deficiency resulted in increased platelet reactivity in response to agonists. In seeming contrast to our findings, Schedel *et al.* (9) reported that stimulation of the $\alpha 7nAChR$ with increasing concentrations of PNU-282987 (100 nM up to 10 μ M) results in increased ADP-induced Ca²⁺ entry into human platelets, suggesting increased platelet activation. However, as platelet aggregation was not affected in these studies, the functional

relevance of those observations is unclear. Of note, PNU-282987 at a concentration of 1 μM also acts as an antagonist for 5-HT(3) receptors (22) that are expressed on platelets (23), which may thus have contributed to the observed effects in human platelets. Evaluation of the amount of platelet-leukocyte complexes *in vivo*, as well as direct platelet aggregation measurements, would have given valuable information on the enhanced platelet activation in response to ADP in the $\alpha 7\text{nAChR}$ deficient mice and the diminished platelet response after $\alpha 7\text{nAChR}$ activation on human platelets. Unfortunately, aggregation experiments were unfeasible to perform on platelets of these mice and therefore remain to be addressed.

In the present study the enhanced inflammation in hematopoietic $\alpha 7\text{nAChR}^{-/-}$ mice did not increase plasma lipids, although previous studies have shown that pro-inflammatory signaling in pre-clinical models does affect lipid metabolism (24). Furthermore, it has been shown that serum CRP and IL-6, which are markers in the pathogenesis of atherosclerosis (15,16), were increased in $\alpha 7\text{nAChR}$ deficient mice on an apoE-deficient background, a highly inflammatory and oxidative stress mouse model (25), but not on a WT background (11). Together, these data indicate that the contribution of $\alpha 7\text{nAChR}$ signaling to lipid metabolism may become apparent only under higher inflammatory conditions.

Hematopoietic $\alpha 7\text{nAChR}$ deficiency increased the inflammatory status and caused increased platelet reactivity, both considered as important risk factors in atherosclerotic lesion development (16,17,26). Nonetheless, hematopoietic $\alpha 7\text{nAChR}$ deficiency did not aggravate WTD-induced atherosclerotic lesion development in $\textit{ldlr}^{-/-}$ mice. As the impact of the of circulating pro-inflammatory cells on plaque infiltration is best observed during early lesion development, we assessed atherosclerotic lesion development already at 7 weeks of Western-type diet feeding, which resulted in early lesions as reflected by the relatively small lesion area ($\sim 1 \times 10^5 \mu\text{m}^2$) and low lesion severity ($\sim 80\%$ mild lesions), comparable to previous studies (27). The macrophage content of the plaque was not affected by hematopoietic $\alpha 7\text{nAChR}$ deficiency, even in these early lesions, suggesting comparable leukocyte infiltration. It should be noted that the $\alpha 7\text{nAChR}$ is also present on endothelial cells and that stimulation of the endothelial $\alpha 7\text{nAChR}$ inhibits leukocyte recruitment during inflammation (8), which is a crucial step in atherosclerotic lesion development (12). Possibly, a potential aggravating effect of hematopoietic $\alpha 7\text{nAChR}$ deficiency on inflammation and platelet activation may thus become apparent only when $\alpha 7\text{nAChR}$ is also absent in endothelial cells. However, the contribution of endothelial cells to the cholinergic anti-inflammatory pathway is unknown, as well as the effects of whole-body $\alpha 7\text{nAChR}$ deficiency on the development of atherosclerosis. Alternatively, it is possible that the diet used was too mild to evoke sufficient inflammation as addition of 0.25% cholesterol to the WTD only slightly increases liver inflammation in APOE*3-Leiden.CETP mice (21).

In conclusion, hematopoietic $\alpha 7nAChR$ deficiency increases inflammatory status and platelet activation status, but does not affect atherosclerotic lesion development in *ldlr*^{-/-} mice.

Acknowledgements

We acknowledge the support from 'the Netherlands CardioVascular Research Initiative: the Dutch Heart Foundation, Dutch Federation of University Medical Centers, the Netherlands Organisation for Health Research and Development and the Royal Netherlands Academy of Sciences' for the GENIUS project 'Generating the best evidence-based pharmaceutical targets for atherosclerosis' (CVON2011-19). P.C.N. Rensen is an Established Investigator of the Netherlands Heart Foundation (grant 2009T038). S.J.A. Korporaal and M. van der Stoep are supported by the Landsteiner Foundation for Blood Transfusion Research (grant 0912F).

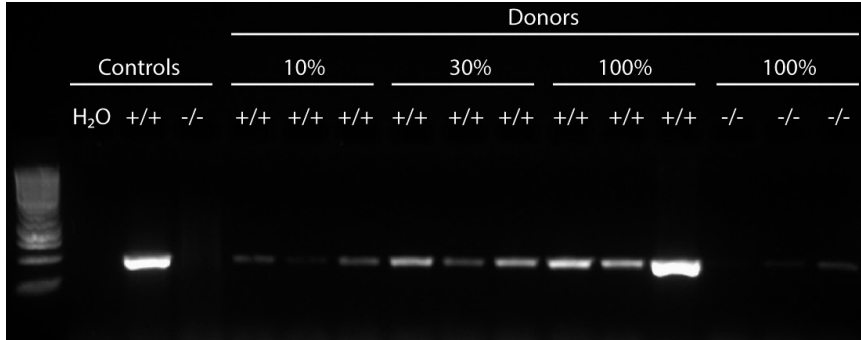
References

1. Borovikova, L. V., Ivanova, S., Zhang, M. *et al.* (2000) Vagus nerve stimulation attenuates the systemic inflammatory response to endotoxin. *Nature* 405, 458-462.
2. Pavlov, V. A., Wang, H., Czura, C. J. *et al.* (2003) The cholinergic anti-inflammatory pathway: a missing link in neuroimmunomodulation. *Mol Med* 9, 125-134.
3. Tracey, K. J. (2002) The inflammatory reflex. *Nature* 420, 853-859.
4. Wang, H., Yu, M., Ochani, M. *et al.* (2003) Nicotinic acetylcholine receptor alpha7 subunit is an essential regulator of inflammation. *Nature* 421, 384-388.
5. Blanchet, M. R., Langlois, A., Israel-Assayag, E. *et al.* (2007) Modulation of eosinophil activation in vitro by a nicotinic receptor agonist. *J Leukoc Biol* 81, 1245-1251.
6. Yoshikawa, H., Kurokawa, M., Ozaki, N. *et al.* (2006) Nicotine inhibits the production of proinflammatory mediators in human monocytes by suppression of I-kappaB phosphorylation and nuclear factor-kappaB transcriptional activity through nicotinic acetylcholine receptor alpha7. *Clin Exp Immunol* 146, 116-123.
7. Steinlein, O. (1998) New functions for nicotinic acetylcholine receptors? *Behav Brain Res* 95, 31-35.
8. Saeed, R. W., Varma, S., Peng-Nemeroff, T. *et al.* (2005) Cholinergic stimulation blocks endothelial cell activation and leukocyte recruitment during inflammation. *J Exp Med* 201, 1113-1123.
9. Schedel, A., Thornton, S., Schloss, P. *et al.* (2011) Human platelets express functional alpha7-nicotinic acetylcholine receptors. *Arterioscler Thromb Vasc Biol* 31, 928-934.
10. Orr-Urtreger, A., Goldner, F. M., Saeki, M. *et al.* (1997) Mice deficient in the alpha7 neuronal nicotinic acetylcholine receptor lack alpha-bungarotoxin binding sites and hippocampal fast nicotinic currents. *J Neurosci* 17, 9165-9171.
11. Wilund, K. R., Rosenblat, M., Chung, H. R. *et al.* (2009) Macrophages from alpha 7 nicotinic acetylcholine receptor knockout mice demonstrate increased cholesterol accumulation and decreased cellular paraoxonase expression: a possible link between the nervous system and atherosclerosis development. *Biochem Biophys Res Commun* 390, 148-154.
12. Libby, P., Ridker, P. M., & Hansson, G. K. (2011) Progress and challenges in translating the biology of atherosclerosis. *Nature* 473, 317-325.
13. Huston, J. M. (2012) The vagus nerve and the inflammatory reflex: wandering on a new treatment paradigm for systemic inflammation and sepsis. *Surg Infect (Larchmt)* 13, 187-193.
14. Robbins, C. S., Chudnovskiy, A., Rauch, P. J. *et al.* (2012) Extramedullary hematopoiesis generates Ly-6C(high) monocytes that infiltrate atherosclerotic lesions. *Circulation* 125, 364-374.
15. Libby, P. (2002) Inflammation in atherosclerosis. *Nature* 420, 868-874.
16. Ross, R. (1999) Atherosclerosis--an inflammatory disease. *N Engl J Med* 340, 115-126.
17. Gawaz, M., Langer, H., & May, A. E. (2005) Platelets in inflammation and atherogenesis. *J Clin Invest* 115, 3378-3384.
18. Gijbels, M. J., van der Cammen, M., van der Laan, L. J. *et al.* (1999) Progression and regression of atherosclerosis in APOE3-Leiden transgenic mice: an immunohistochemical study. *Atherosclerosis* 143, 15-25.
19. Volger, O. L., Mensink, R. P., Plat, J. *et al.* (2001) Dietary vegetable oil and wood derived plant stanol esters reduce atherosclerotic lesion size and severity in apoE*3-Leiden transgenic mice. *Atherosclerosis* 157, 375-381.
20. Hu, L., Boesten, L. S., May, P. *et al.* (2006) Macrophage low-density lipoprotein receptor-related protein deficiency enhances atherosclerosis in ApoE/LDLR double knockout mice. *Arterioscler Thromb Vasc Biol* 26, 2710-2715.
21. Kleemann, R., Verschuren, L., van Erk, M. J. *et al.* (2007) Atherosclerosis and liver inflammation induced by increased dietary cholesterol intake: a combined transcriptomics and metabolomics analysis. *Genome Biol* 8, R200.

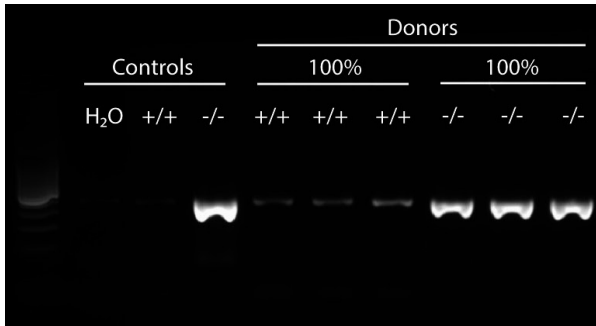
22. Bodnar, A. L., Cortes-Burgos, L. A., Cook, K. K. *et al.* (2005) Discovery and structure-activity relationship of quinuclidine benzamides as agonists of alpha7 nicotinic acetylcholine receptors. *J Med Chem* 48, 905-908.
23. Stratz, C., Trenk, D., Bhatia, H. S. *et al.* (2008) Identification of 5-HT3 receptors on human platelets: increased surface immunoreactivity after activation with adenosine diphosphate (ADP) and thrombin receptor-activating peptide (TRAP). *Thromb Haemost* 99, 784-786.
24. van Diepen, J. A., Berbee, J. F., Havekes, L. M. *et al.* (2013) Interactions between inflammation and lipid metabolism: relevance for efficacy of anti-inflammatory drugs in the treatment of atherosclerosis. *Atherosclerosis* 228, 306-315.
25. Palinski, W., Ord, V. A., Plump, A. S. *et al.* (1994) ApoE-deficient mice are a model of lipoprotein oxidation in atherogenesis. Demonstration of oxidation-specific epitopes in lesions and high titers of autoantibodies to malondialdehyde-lysine in serum. *Arterioscler Thromb* 14, 605-616.
26. Reinhart, W. H. (2013) Platelets in vascular disease. *Clin Hemorheol Microcirc* 53, 71-79.
27. Meurs, I., Lammers, B., Zhao, Y. *et al.* (2012) The effect of ABCG1 deficiency on atherosclerotic lesion development in LDL receptor knockout mice depends on the stage of atherogenesis. *Atherosclerosis* 221, 41-47.

Supplementary appendix

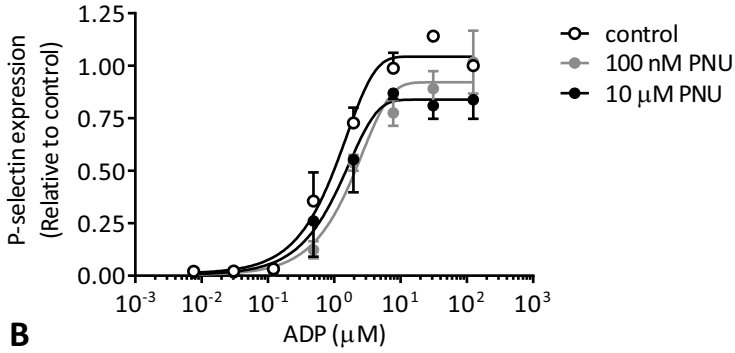
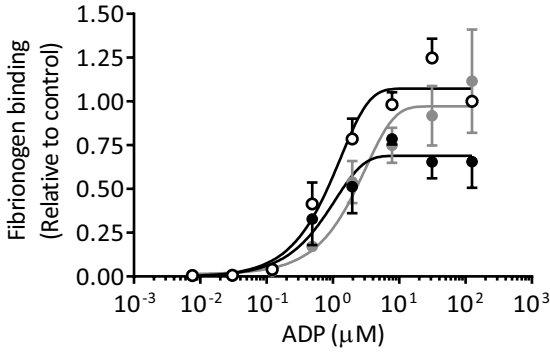
A



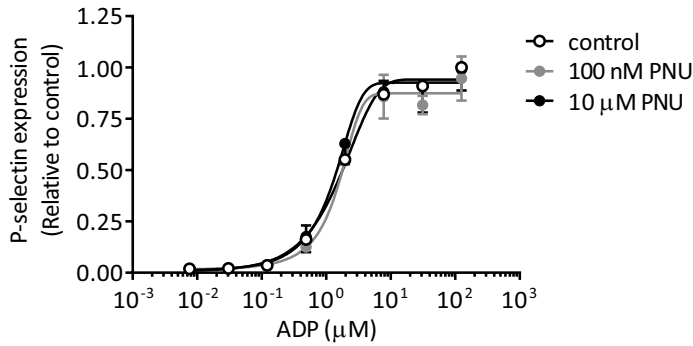
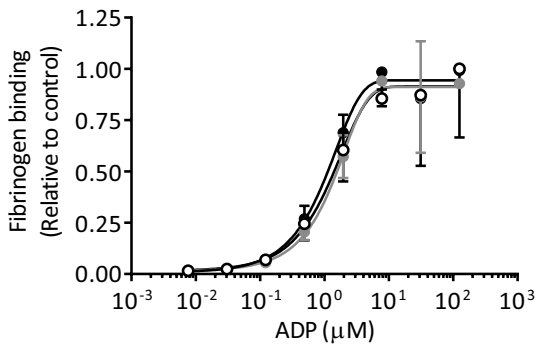
B



Supplemental Figure 1 – Hematologic chimerism of $\alpha 7nAChR^{-/-}$ mice. At the end of the study, bone marrow was isolated from the transplanted *ldlr*^{-/-} mice, and hematologic chimerism was determined using genomic DNA by PCR at 15 weeks after BMT. The relative presence of the $\alpha 7nAChR$ was assessed for murine $\alpha 7nAChR$, diluted up to 10% for hematopoietic $\alpha 7nAChR^{+/+}$ to determine chimerism (**A**), and for the neomycin gene neocassette (**B**). Figure include three representative hematopoietic $\alpha 7nAChR^{+/+}$ and $\alpha 7nAChR^{-/-}$ mice. Controls include DNA from $\alpha 7nAChR^{+/+}$ and $\alpha 7nAChR^{-/-}$ mice.

A**B**

Supplemental Figure 2 - Effects of low dose $\alpha 7$ nAChR agonist PNU282987 on human platelets. Human platelets were isolated from freshly drawn venous blood from healthy volunteers. Surface expression of P-selectin (**A**) and fibrinogen-binding (**B**) were determined by flow cytometry in citrated whole blood, treated with $\alpha 7$ nAChR agonist PNU282987 (100 nM or 10 μ M) or vehicle for 30 min prior to stimulation with ADP (serial dilutions ranging from 0-125 μ M) for 20 min. Values represent means \pm SEM.

A**B**

Supplemental Figure 3 – Effects of short incubation with $\alpha 7$ nAChR agonist PNU282987 on human platelets. Human platelets were isolated from freshly drawn venous blood from healthy volunteers. Surface expression of P-selectin (**A**) and fibrinogen-binding (**B**) were determined by flow cytometry in citrated whole blood, treated with $\alpha 7$ nAChR agonist PNU282987 (100 nM or 10 μ M) or vehicle for 5 min prior to stimulation with ADP (serial dilutions ranging from 0-125 μ M) for 20 min. Values represent means \pm SEM.

SPLENIC DENERVATION DOES NOT
AGGRAVATE ATHEROSCLEROTIC
LESION DEVELOPMENT IN
APOE*3-LEIDEN.CETP TRANSGENIC MICE

Sander Kooijman

Illiana Meurs

Lianne van Beek

P. Padmini S.J. Khedoe

Annabel Giezekamp

Karin Pike-Overzet

Catthy Cailotto

Jan van der Vliet

Vannesa van Harmelen

Guy Boeckxstaens

Jimmy F.P. Berbée

Patrick C.N. Rensen

Abstract

The brain plays a prominent role in the regulation of inflammation. Immune cells are under control of the so-called cholinergic anti-inflammatory reflex, mainly acting via autonomic innervation of the spleen. Activation of this reflex inhibits the secretion of pro-inflammatory cytokines and may reduce the development of atherosclerosis. Therefore, the aim of this study was to evaluate the effects of selective parasympathetic (Px) and sympathetic (Sx) denervation of the spleen on inflammatory status and atherosclerotic lesion development. Female APOE*3-Leiden.CETP mice, a well-established model for human-like lipid metabolism and atherosclerosis, were fed a cholesterol-containing Western-type diet for 4 weeks after which they were sub-divided into three groups receiving either splenic Px, splenic Sx or sham surgery. The mice were subsequently challenged with the same diet for an additional 15 weeks. Selective Px increased leukocyte counts (i.e. dendritic cells, B cells and T cells) in the spleen and increased gene expression of pro-inflammatory cytokines in the liver and peritoneal leukocytes as compared to Sx and sham surgery. Both Px and Sx increased circulating pro-inflammatory cytokines IL-1 β and IL-6. However, the increased pro-inflammatory status in denervated mice did not affect atherosclerotic lesion size or lesion composition. Predominantly selective Px of the spleen enhances the inflammatory status, which however does not aggravate diet-induced atherosclerotic lesion development.

Introduction

Atherosclerosis is a chronic inflammatory disease initiated by innate and adaptive immune responses to endogenously modified structures, in particular oxidized lipoproteins, within the arterial wall (1). The autonomic nervous system may enhance innate immune responses by sympathetic activity (2), while it suppresses inflammation via the vagus nerve, a mechanism termed the cholinergic anti-inflammatory pathway (3,4). In response to circulating pro-inflammatory cytokines afferent vagal nerves are directly activated. Subsequent efferent vagal activity results in the release of acetylcholine which activates the $\alpha 7$ nicotinic acetylcholine receptor ($\alpha 7$ nAChR) on resident tissue macrophages and other immune cells, thereby inhibiting the production and release of pro-inflammatory cytokines (e.g. TNF α , IL-6, IL-18) (5). $\alpha 7$ nAChR is integral to the cholinergic anti-inflammatory pathway, as vagus nerve stimulation fails to inhibit TNF α production in pharmacologically $\alpha 7$ nAChR inhibited or $\alpha 7$ nAChR-deficient mice (5,6). Recently, we demonstrated that hematopoietic $\alpha 7$ nAChR deficiency in dyslipidemic mice enhances systemic inflammation as evidenced by increased leukocytes in the blood, lymph nodes, spleen and peritoneum (all by at least 2-fold) and increased gene expression of TNF α in peritoneal leukocytes and spleen (7).

As the spleen contains half of the body's monocyte population, it is not surprising that the cholinergic anti-inflammatory pathway acts mainly via the spleen. Indeed, Huston *et al.* (8) reported that vagus nerve stimulation fails to inhibit TNF α production in splenectomised animals during endotoxemia, indicating an essential role for the spleen in the cholinergic anti-inflammatory pathway. Furthermore, splenectomy reduces the production of antibodies directed against oxidized LDL in apoE-deficient mice and was associated with increased atherosclerotic lesion development (9). Trauma patients who undergo splenic removal are more prone to develop coronary heart disease, in which enhanced atherosclerotic lesion development may be causal (10).

Taken together, these findings suggests that autonomic innervation of the spleen and the development of atherosclerosis may be closely interrelated. Therefore, the aim of this study was to determine the effect of selective parasympathetic denervation (Px), as compared to sympathetic denervation (Sx) of the spleen and sham surgery, on systemic inflammation and atherosclerotic lesion development in female APOE*3-Leiden.CETP mice, a well-established mouse model for human-like lipoprotein metabolism.

Material and Methods

Animals

APOE*3-Leiden mice were crossbred with mice expressing human cholesteryl ester transfer protein (CETP) under control of its natural flanking regions to generate heterozygous APOE*3-Leiden.CETP mice (11). Mice were housed under standard conditions with a 12:12h light:dark cycle and had free access to food and water. At the age of 10-12 weeks, female APOE*3-Leiden.CETP mice received a Western-type diet (WTD) containing 0.1% cholesterol (w/w), 1% (w/) corn oil and 15% (w/w) cacao butter (AB diets, Woerden, the Netherlands). After a run-in period of 4 weeks, mice (n=45) were randomized based on plasma lipid levels and body weight into three groups (n=15 each) receiving either splenic parasympathetic denervation (Px), splenic sympathetic denervation (Sx) or sham surgery. A schematic representation of the innervation of the spleen and the sites of denervation can be found in **Figure 1A**. For all surgeries, mice were anesthetized by an intraperitoneal (i.p.) injection of a mixture of fentanyl/citrate/fluanisone (Hypnorm; Janssen, Beerse, Belgium), midazolam (Dormicum; Roche, Mijdrecht, The Netherlands), and H₂O (1: 1: 2, v/v). All animal experiments had been approved by the Institutional Ethics Committee on Animal Care and Experimentation.

8

Selective parasympathetic denervation of the spleen

Since parasympathetic nerves enter the spleen at both tips, these tips were sequentially exposed during surgery to allow cutting of the nerves. After a midline abdominal incision the spleen was pulled gently towards the site of the incision, and the nerve at the tip of the spleen was cut. The connective tissue between the tip and the first hilus was also removed, as some parasympathetic input reaches the spleen via this connective tissue. Subsequently, the spleen was further pulled towards the midline to reach the lower tip of the spleen. After following back the nerve to the plexus, the connective tissue from this plexus back to the spleen was removed. The wound was closed with novosyn suture (B. Braun Medical, Oss, The Netherlands) (12).

Selective sympathetic denervation of the spleen

A midline abdominal incision was performed along the linea alba and the stomach was pushed up and to the right to reveal the blood vessels to and from the spleen. After the arterial branch to the stomach a bifurcation indicates the first branching point of the arterial supply to the spleen. From this bifurcation on the arteries will split many times and end at the hili of the spleen. Sympathetic nerves run along and around these arteries to reach the spleen. The area just before and after the bifurcation was chosen to remove the sympathetic nerves. The wound was closed

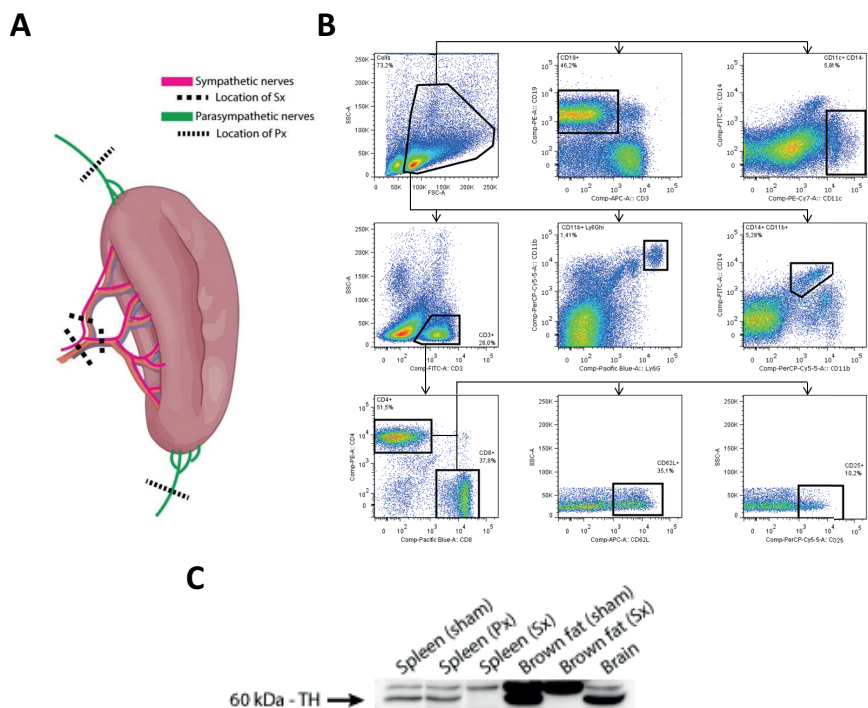


Figure 1 – Confirmation of splenic denervations and gating strategy. Schematic representation of the innervation of the spleen (A). The sympathetic input (pink) reaches the spleen via the arteries, the parasympathetic input (green) reaches the spleen via both tips of the spleen. The location at which denervations were performed are shown by the dashed lines. Gating strategy for flow cytometry analysis (B). Confirmation of sympathetic denervation (C) by measurement of tyrosine hydroxylase protein content of the spleen. As controls, TH content for the brain and (denervated) brown fat are included.

with novosyn suture (B. Braun Medical, Oss, The Netherlands) (12). Sympathetic denervation was confirmed 15 weeks after surgery by measurement of Tyrosine hydroxylase (TH) content Western blotting (anti-TH antibody; AB-112; Abcam).

Gene expression analysis in spleen, liver and peritoneal leukocytes

After surgery, the mice were fed the WTD for another 15 weeks. Subsequently, mice were sacrificed and organs were collected and peritoneal leukocytes isolated by lavage of the peritoneum with ice-cold PBS. Total RNA from spleen, liver and peritoneal leukocytes was isolated using the Nucleospin RNA II kit (Macherey-Nagel, Düren, Germany) according to manufacturer's instructions. One microgram of total RNA was converted to cDNA with iScript cDNA Synthesis kit (Biorad) and purified with Nucleospin Extract II kit (Macherey-Nagel). Real-time polymerase chain reaction

(RT-PCR) was conducted on the IQ5 PCR machine (Biorad) using the Sensimix SYBR Green RT-PCR mix (Quantace, London, UK). mRNA levels were normalized to mRNA levels of $\beta 2$ microglobulin, cyclophilin, and acidic ribosomal phosphoprotein P0 [36B4].

Flow cytometry analysis

From five randomly selected animals per group, peripheral blood and spleens were processed for flow cytometry. Thereto, single cell suspensions were obtained by mashing the cells through a 70 μm cell strainer (Falcon, The Netherlands). Subsequently, cells were counted and 2×10^6 cells were stained with appropriate antibodies (**Table 1**) to determine immune cell subsets: Live immune cells were selected from the forward and sideward scatter, and populations of B-cells (CD19+), dendritic cells (CD11c+CD14-), T-cells (CD3+), neutrophils (CD11b+Ly6Ghigh), and macrophages (CD14+CD11b+) were identified. Specific T cell subsets were determined within the CD3+ fraction as T helper cells (CD4+), cytotoxic T cells (CD8+), activated T cells (CD25+), naïve T cells (CD62L+). Data were acquired on a FACSAria or a FACSCanto II (BD Biosciences). Analyses were performed using FlowJo software (Treestar, Ashland, OR, USA). Gating strategy is shown in **Figure 1B**.

Table 1 – Detailed information of antibodies used for flow cytometry analysis

Antibody	Conjugate	Clone	Source	Dilution
CD19	PE	ID3	BD	1,600
CD14	FITC	Sa14-2	eBioscience	500
CD11c	Biotin	HL3	BD	200
CD3	APC	145-2C11	BD	300
CD3	FITC	145-2C11	BD	400
CD11b	PerCP	M1/70	BD	800
Ly6G	Ef450	RB6-8C5	eBioscience	800
CD4	PE	L3T4 GK1.5	BD	1,000
CD8	biotin	53-6.7	BD	400
CD62L	APC	MEL-14	Biologend	1,600
CD25	PerCP	PC61	BD	500
Second step: Sav-PE-Cy7			BD	500

Serum measurements

Serum was isolated and stored frozen at -80°C until further analyses. The cytokines TNF α , IL-1 β and IL-6 were determined using V-PLEX Proinflammatory Panel1 (mouse) Kit (Meso Scale Discovery, Rockville, MD, USA) according to the manufacturer's instructions. In 50x diluted serum samples, E-selectin concentrations were measured according to the manufacturer's instructions (DY575, R&D systems, Minneapolis, MN, USA).

Plasma lipid and lipoprotein analyses

Blood was collected after a 4-h fast into EDTA-containing cups by tail bleeding, and plasma was isolated by centrifugation and stored frozen at -80°C until further analyses. The concentrations of total cholesterol (TC) and triglycerides (TG) in plasma were determined using commercially available enzymatic colorimetric kits according to the manufacturer's protocols (236691 and 1488872; Roche Molecular Biochemicals, Indianapolis, IN, USA). The concentrations of phospholipids (PL) in plasma were determined using a commercially available enzymatic colorimetric kit (3009; Instruchemie, Delfzijl, The Netherlands). The distribution of lipids over the different lipoproteins in plasma was determined after fractionation of pooled plasma (14-15 mice per pool) by FPLC using a Superose 6 HR 10/30 column (Äkta System; Amersham Pharmacia Biotech, Piscataway, NJ).

Atherosclerosis quantification

From all mice, hearts were isolated and fixed in phosphate-buffered 4% formaldehyde, dehydrated and embedded in paraffin. Cross-sections ($5\ \mu\text{m}$) were made throughout the aortic root area and stained with hematoxylin-phloxine-saffron for histological analysis. Lesions were categorized for severity according to the guidelines of the American Heart Association adapted for mice (13). Various types of lesions were discerned: no lesions, mild lesions (types 1-3) and severe lesions (types 4-5). Immunohistochemistry for determination of lesion composition was performed as described previously (14). Rat anti-mouse antibody MAC3 (1:1000; BD Pharmingen, Breda, The Netherlands) was used to quantify macrophage area. Monoclonal mouse antibody M0851 (1:800; Dako, Heverlee, the Netherlands) against smooth muscle cell (SMC) α -actin was used to quantify SMC area. Sirius Red was used to quantify collagen area. Lesion area was quantified in the aortic root starting from the appearance of open aortic valve leaflets in four subsequent sections with $50\ \mu\text{m}$ intervals. In ImageJ the lesions were delineated to determine mean lesion area (in μm^2) and a color threshold was set to determine the area percentage of MAC3, SMC or collagen staining in a consistent manner across the different slides.

Statistical analysis

Data are presented as means \pm SEM unless indicated otherwise. To compare differences among groups one-way ANOVA with Turkey's post-test was performed using GraphPad Prism version 4.00 for Windows (GraphPad Software, San Diego, CA, USA, www.graphpad.com). Differences at a P-value <0.05 were considered statistically significant.

Results

Female APOE*3-Leiden.CETP mice were fed a WTD during 4 weeks, and were randomized into three groups receiving either parasympathetic denervation (Px) of the spleen, sympathetic denervation (Sx) of the spleen (**Figure 1A**), or sham surgery. After surgery, the mice received WTD feeding for 15 additional weeks to induce atherosclerotic lesion development. To confirm that Sx was successful and that sympathetic nerves did not regenerate, tyrosine hydroxylase (TH) content of the spleen was determined (**Figure 1C**), showing the absence of TH still 15 weeks after Sx. Upon sacrifice of the mice, the tips of the spleen were gently exposed to confirm that the re-innervation of the parasympathetic nerves was not the case.

Splenic parasympathetic denervation increases immune cell count in spleen

The spleen plays an important role in the immune system and, therefore, contains a wide range of immune cell types, including monocytes, macrophages, dendritic cells, neutrophils, T cells and B cells. To define the effect of the selective denervations on immune cell composition, flow cytometry analyses were performed. Total splenic immune cell count was increased (+49%, $p < 0.01$) in Px mice ($200 \pm 10 \times 10^6$ cells) compared to sham operated mice ($134 \pm 10 \times 10^6$ cells), while Sx denervation did not affect immune cell count ($156 \pm 25 \times 10^6$ cells) (**Figure 2A**). In a fraction of immune cells (i.e. 2.0×10^6 cells), percentages of each cell type were analyzed using flow cytometry and multiplied with total immune cell counts (see **Figure 1B** for the gating strategy). This revealed an increase in the number of various immune cell subtypes, including B cells ($98 \pm 7 \times 10^6$ cells vs. $61 \pm 5 \times 10^6$ cells, $p < 0.01$) (**Figure 2B**), T cells ($63 \pm 4 \times 10^6$ cells vs. $41 \pm 4 \times 10^6$ cells, $p < 0.01$) (**Figure 2C**) and dendritic cells (DCs; $10 \pm 1 \times 10^6$ cells vs. $7 \pm 1 \times 10^6$ cells, $p < 0.05$) (**Figure 2D**). Neutrophils (**Figure 2E**) and monocytes/macrophages (**Figure 2F**) only showed a non-significant increase upon Px.

As T cells are integral to the cholinergic anti-inflammatory pathway [15], the phenotype of the T cells (i.e. naivity or activation status of the T helper or cytotoxic T cells) was further studied. In accordance to the general increase in various immune cells, Px increased both T-helper (T_H ; +60%, $p < 0.01$) (**Figure 2G**) and cytotoxic T cells (T_{cyt} ; +49%, $p < 0.01$) (**Figure 2H**). Further subdivision revealed that Px increased naïve (**Figure 2I**) as well as activated (**Figure 2J**) T_H cells, and increased naïve T_{cyt} cells (**Figure 2K**) without increasing activated T_{cyt} cells (**Figure 2L**). Thus, splenic Px resulted in an overall increase in immune cells in the spleen, while Sx did not affect immune cell count compared to sham surgery, indicating the importance of the parasympathetic nerve in regulation of the immune system.

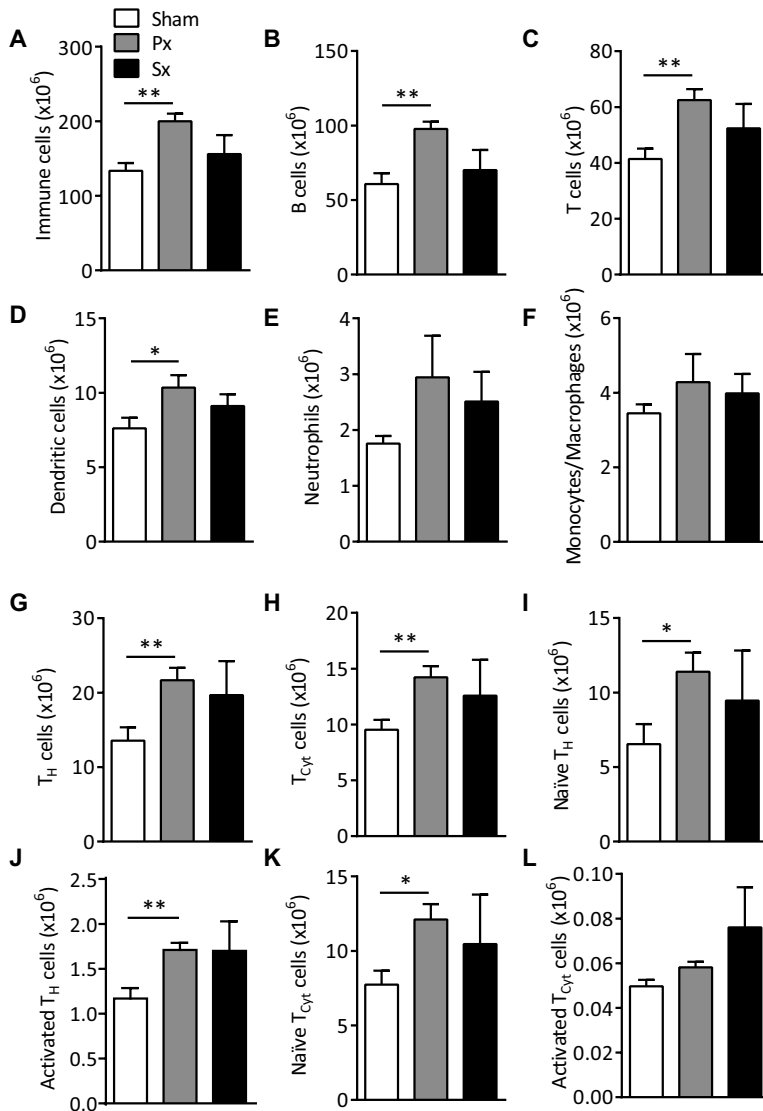


Figure 2 – Effect of splenic denervation on immune cell composition of the spleen. APOE*3-Leiden.CETP mice were fed a WTD during 4 weeks, were randomized into three groups receiving either splenic parasympathetic denervation (Px), sympathetic denervation (Sx), or sham surgery (t=0). Mice were fed a WTD during 15 additional weeks before spleens were isolated and cellular composition was analyzed by flow cytometry. Immune cells were counted based on FSC (**A**) and further subdivided into B-cells (CD19⁺) (**B**), T-cells (CD3⁺) (**C**), dendritic cells (CD11c⁺CD14⁻) (**D**), neutrophils (CD11b⁺Ly6G^{high}) (**E**) and monocytes/macrophages (CD14⁺CD11b⁺) (**F**). Specific T cells subsets were identified as T_H (CD4⁺) (**G**), T_{Cyt} (CD8⁺) (**H**), naïve T_H (CD4⁺CD62L⁺) (**I**), activated T_H (CD4⁺CD25⁺) (**J**), naïve T_{Cyt} (CD8⁺CD62L⁺) (**K**) and activated T_{Cyt} (CD8⁺CD25⁺) (**L**). Values represent means ± SEM of 5 mice per group. *p<0.05, **p<0.01 compared to sham surgery.

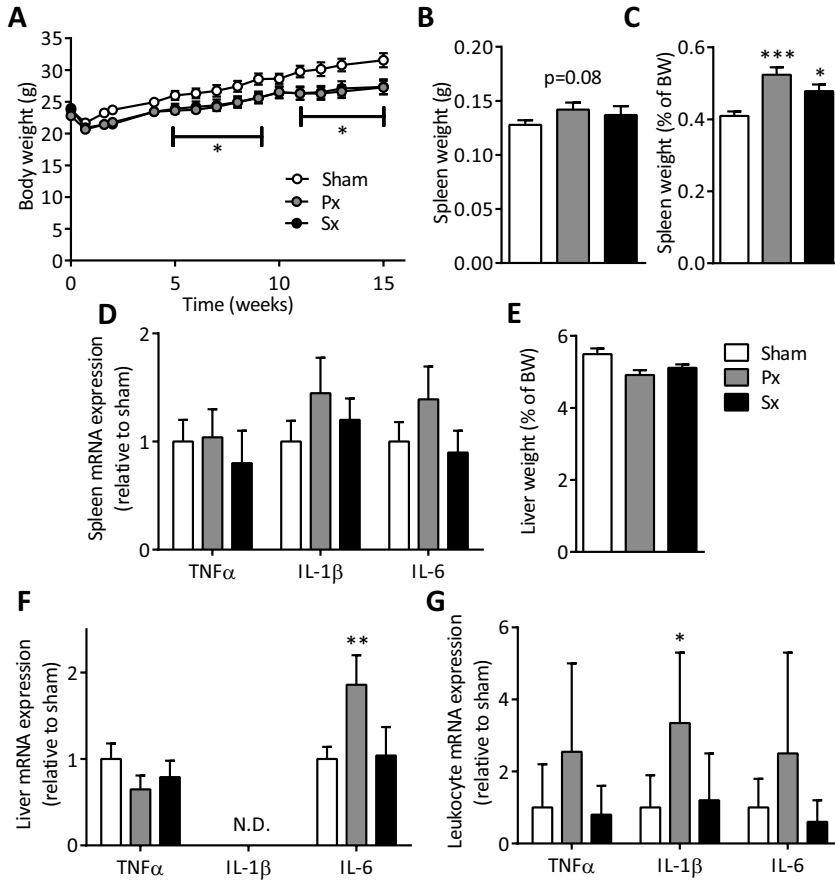


Figure 3 - Effect of splenic denervation on the gene expression of inflammatory genes. During the course of the experiment body weight was monitored (A). At 15 weeks after Px, Sx or sham surgery, spleens were weighed (B) and spleen weight was expressed as percentage of body weight (C), total RNA was extracted and expression levels of TNF α , IL-1 β and IL-6 were determined by real-time PCR (D). Similarly, livers were weighed (E) and hepatic expression of these genes was determined (F). Peritoneal leukocytes were isolated and gene expression was quantified (G). Values represent means \pm SEM of 15 mice per group * p <0.05, ** p <0.01, *** p <0.001 compared to sham surgery.

Splenic parasympathetic denervation increases expression of inflammatory cytokines

During the course of the experiment, body weight gain was slightly lower in both Px and Sx mice. At the end of the experiment, body weight of sham operated mice was 31.6 ± 1.1 g, compared to 27.3 ± 1.1 g ($p < 0.05$) and 27.4 ± 1.2 g ($p < 0.05$) for Px and Sx mice, respectively (**Figure 3A**). Splenic weight tended to be increased in Px (**Figure 3B**) and was different when expressed as percentage of the body weight for Px (0.52 ± 0.02 %; $p < 0.001$) and Sx (0.47 ± 0.02 %; $p < 0.05$) compared to sham (0.41 ± 0.01 %) (**Figure 3C**). Gene expression analyses revealed that Px only caused a trend towards an increase of the inflammatory cytokines IL-1 β and IL-6 within the spleen (**Figure 3D**). Further analysis of other organs showed no difference in liver weight when expressed as percentage of the body weight (**Figure 3E**). Interestingly, Px increased gene expression of IL-6 in the liver (+80%; $p < 0.01$) (**Figure 3F**) and increased gene expression of TNF α , IL-1 β and IL-6 in isolated peritoneal leukocytes, which reached significance for IL-1 β (3.3-fold; $p < 0.05$) (**Figure 3G**). Next we determined the effect of Px on white blood cell count in peripheral blood and further analysed subsets by flow cytometry. Px tended to increase total immune cell count albeit significance was not reached (+41%; $p = 0.18$) (**Figure 4A**). Subdivision of leukocytes into B cells (**Figure 4B**), T cells (**Figure 4C**), dendritic cells (**Figure 4D**), neutrophils (**Figure 4E**) or monocytes (**Figure 4F**) did not reveal differences. However, as the number of immune cells per se does not reflect activity of these cells, we measured serum levels of TNF α (**Figure 4G**), IL-1 β (**Figure 4H**) and IL-6 (**Figure 4I**) in serum. While TNF α levels remained unaffected, both IL-1 β and IL-6 serum concentrations were increased by Px. Interestingly, in contrast to our gene expression in liver, spleen and peritoneal leukocytes, also Sx increased inflammatory status as IL-1 β and IL-6 levels compared to sham operated mice.

Splenic parasympathetic denervation does not affect atherosclerotic lesion development

Since inflammation can influence lipid metabolism [16], we next evaluated whether selective splenic denervations had an effect on lipid metabolism. Plasma total cholesterol (TC), phospholipids (PL) and triglycerides (TG) were assessed at 2, 4, 6 and 15 weeks after surgery. No differences in plasma lipid concentrations were found between the Px, Sx and sham operated mice at weeks 2, 4, 6 (not shown) and 15 weeks (**Figure 4J**). Likewise, the distribution of cholesterol over the various lipoproteins did not differ between Px, Sx or sham control mice (**Figure 4K**). Serum E-selectin as marker for vascular inflammation, was increased in Px as well as in Sx compared to sham, suggesting that immune cell infiltration into atherosclerotic lesions might be enhanced by the selective denervations (**Figure 4L**).

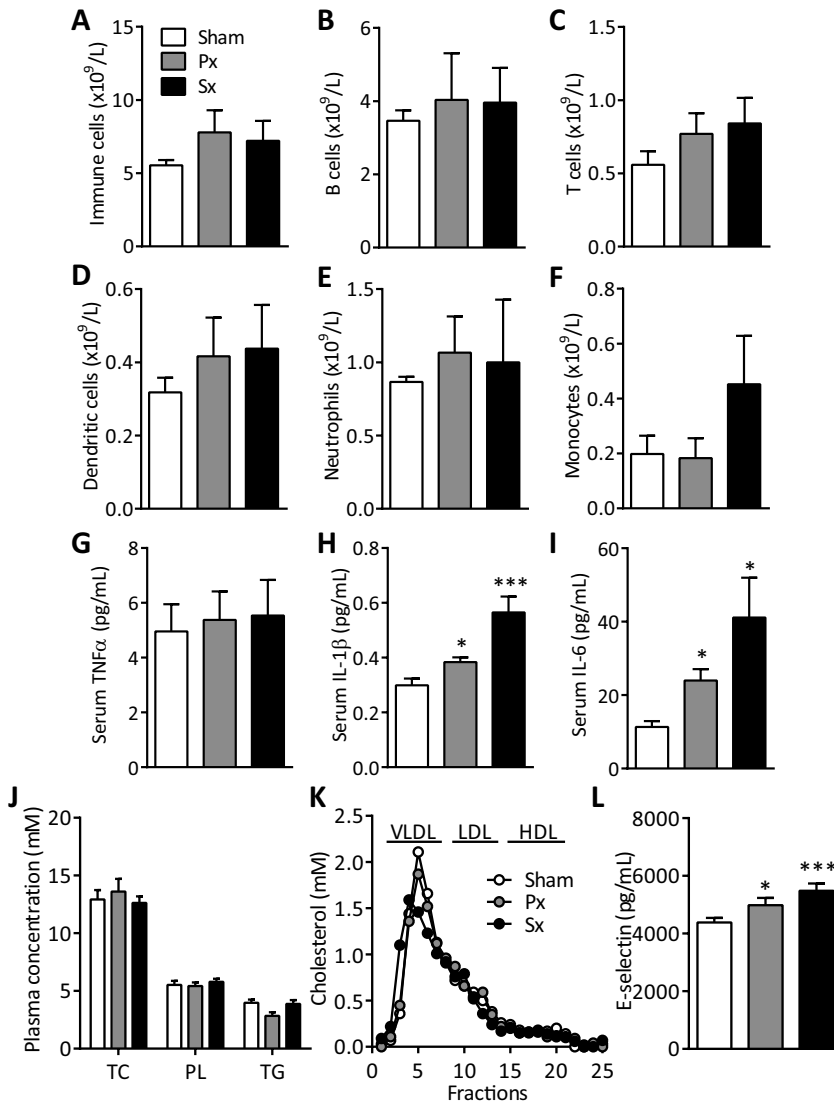


Figure 4 – Effect of splenic denervation on white blood cell composition, serum cytokines and plasma lipids. At 15 weeks after Px, Sx or sham surgery, blood was drawn and analyzed by flow cytometry. Immune cells were counted (**A**) and further subdivided into B-cells (CD19⁺) (**B**), T-cells (CD3⁺) (**C**), dendritic cells (CD11c⁺CD14⁻) (**D**), neutrophils (CD11b⁺Ly6G^{high}) (**E**) and monocytes (CD14⁺CD11b⁺) (**F**). Serum cytokine levels of TNF α (**G**), IL-1 β (**H**) and IL-6 (**I**) were measured. Plasma concentrations of total cholesterol (TC), phospholipids (PL) and triglycerides (TG) were determined (**J**). The distribution of cholesterol over the different lipoproteins was determined by fractionation of pooled plasma by FPLC (**K**). Serum E-selectin (**L**). Values represent means \pm SEM of 5 (**A-F**) or 15 (**G-L**) mice per group.

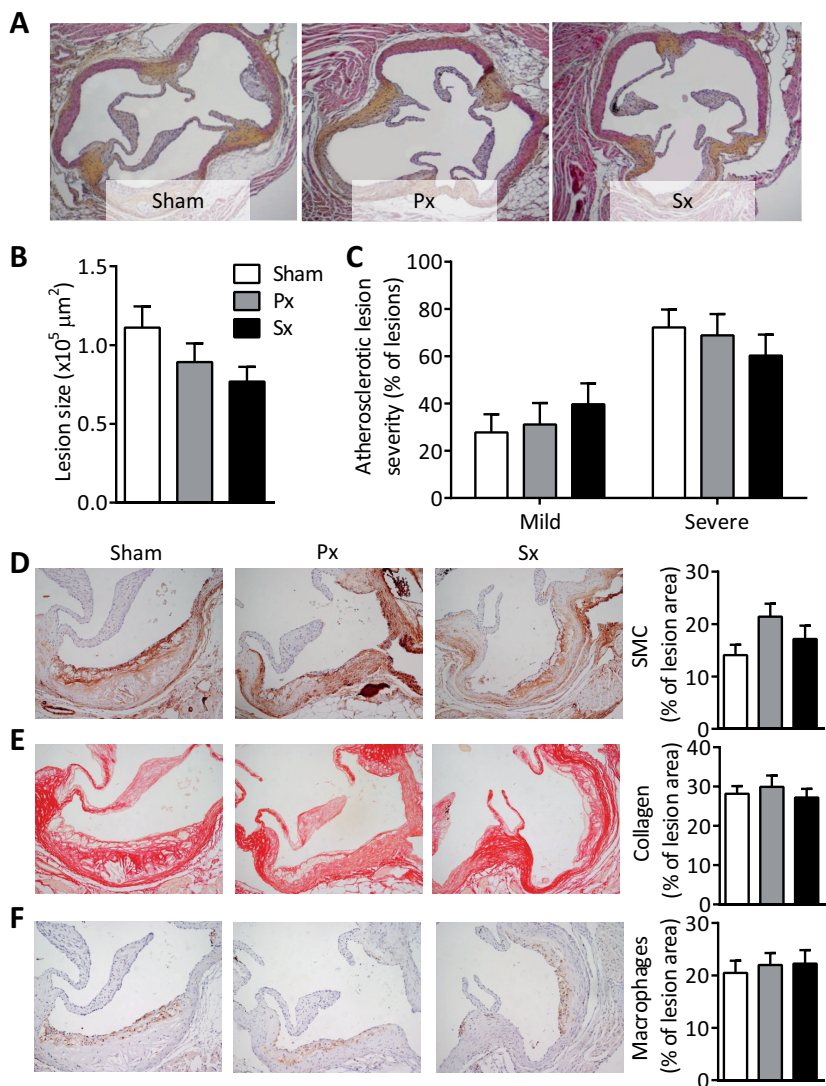


Figure 5 – Effect of splenic denervation on atherosclerotic lesion size and composition. At 15 weeks after Px, Sx or sham surgery, hearts were isolated and cross-sections (5 μm) with 50 μm intervals throughout the aortic root area starting from the appearance of open aortic valve leaflets were used for atherosclerosis measurements. Sections were stained with hematoxylin-phloxine-saffron for histological analysis and representative images are shown (A). Atherosclerotic mean lesion area (in μm^2) was quantified in four subsequent cross-sections (B). The same four sections per mouse were categorized according to lesion severity (C). Lesion composition was determined by immunohistochemistry in four subsequent cross-sections using α -actin for smooth muscle cells (SMC) (D), Sirius Red staining for collagen content (E) and MAC3 for macrophages (F). Values represent means \pm SEM of 15 mice per group.

To study the effect of splenic denervation on atherosclerosis development, mice were sacrificed after 15 weeks after surgery, and atherosclerotic lesion size and lesion severity were determined in the valve area of the aortic root. Both Px and Sx did neither affect atherosclerotic lesion size (**Figure 5A,B**) nor lesion severity, when classified as mild (type 1-3) and severe (type 4-5) lesions (**Figure 5C**). However, also no significant differences were observed in lesion composition between Px, Sx and sham operated mice, with respect to the relative area of smooth muscle cells (SMC; α -actin staining; **Figure 5D**), collagen (Sirius Red staining; **Figure 5E**) and macrophages (MAC3 staining; **Figure 5F**).

Discussion

In the current study, we tested the hypothesis that the brain plays a prominent role in modulating the activity of immune cells and may therefore affect atherosclerosis development. We determined the effect of selective splenic parasympathetic denervation (Px), sympathetic denervation (Sx) on the inflammatory status and examined the potential consequences for plasma lipids and the development of atherosclerosis in APOE*3-Leiden.CETP mice. We showed that predominantly splenic Px increased the inflammatory state of the body as indicated by increased leukocyte counts within the spleen and increased pro-inflammatory cytokine expression. However, splenic Px as well as Sx did not affect atherosclerotic lesion development.

Interestingly, we found increased circulating levels of the pro-inflammatory cytokines IL-1 β and IL-6 upon both Px and Sx. Classically, the parasympathetic and sympathetic nerves system act in opposite direction to facilitate control over physiological responses to maintain homeostasis. However, for the spleen, it has been suggested that both systems in fact act together to restrain inflammation by projection of the vagus nerve also onto the sympathetic splenic nerve (6,17). Previous studies even suggested absence of direct parasympathetic innervation of the spleen as neither choline acetyltransferase nor vesicular acetylcholine transporter producing nerve endings could be detected within the spleen (6,18). However the absence of the classical vagus transmitter acetylcholine is not sufficient proof for the absence of direct input from the vagus. In previous studies we identified neuronal connections between the spleen and both the intermedio lateral column of the spinal cord (IML) and the dorsal motor nucleus of the vagus nerve (DMV) by retrograde tracing using pseudorabies virus (PRV) and cholera toxin-b (CTB) (12,19), suggesting sympathetic as well as parasympathetic neuronal connectivity. Surgical ablation of the nerves along the splenic arteries (similar to Sx) resulted in undetectable retrograde tracer in the IML and absence of TH in the spleen. In contrast, surgical ablation of the nerve branches at the splenic ends (similar to Px) resulted in a loss

of detectability of the tracers in the DMV and can therefore most likely be allocated to the parasympathetic nerves system. In addition, Px severely diminished (~70%) LPS-induced antibody production, clearly indicating functional involvement of these nerve branches in the control of the immune response (12). In contrast, Sx did not affect the production of specific antibodies. While absence of sympathetic input 15 wk after Sx was confirmed by measuring TH content, confirmation of Px was limited to visual inspection due to the lack of specific markers for these neurons. However, consistent with the notion that vagal activation suppresses the immune response (5), we found that Px enhances the number of leukocytes and increases expression of proinflammatory cytokines. It may seem contradictory that Px results in diminished LPS-induced antibody production (12), while here we report enhanced inflammatory responses. However, one should consider the dual challenge for the brain during inflammation, namely to contain the inflammation by for example reducing cytokine production and subsequently to induce memory within the immune system to prevent new infections by inducing antibody production.

Despite that Px increased the number of immune cells in the spleen in the current study, no differences in splenic TNF α gene expression or circulating TNF α were found. Possibly stronger inflammatory stimuli are required to attenuate TNF α production by spleen macrophages via stimulation of the vagus nerve, as has been shown for LPS-induced endotoxemia (6). Compatible with the notion that TNF α is crucially involved in the pathogenesis and progression of atherosclerosis (20,21), Px and Sx did not aggravate WTD-induced atherosclerotic lesion development and did not affect lesion composition in APOE*3-Leiden.CETP mice. Similarly, we previously showed that hematopoietic $\alpha 7$ nAChR deficiency in ApoE $^{-/-}$ mice does increase inflammatory status of the body and enhances platelet reactivity, but does not aggravate atherosclerosis as lesion size and plaque composition remained unaffected (7). In contrast, Johansson *et al.* (22) recently reported an increase in atherosclerotic lesion development upon hematopoietic $\alpha 7$ nAChR deficiency in Ldlr $^{-/-}$ mice, indicating that the genetic and environmental context are important to determine the outcome of disrupted anti-inflammatory reflexes. Despite conflicting outcomes, interfering with inflammatory reflexes might be an interesting target in the prevention of atherosclerosis. Several animal studies report beneficial effects of low dose β -blockers on atherogenesis (23,24), mainly via reducing of inflammatory responses rather than changes in lipid metabolism. Also in humans, the use of metoprolol slows progression of intima-media thickness (25,26).

While the role of the autonomic splenic nerves in human physiology is unclear, splenectomy in trauma patients has been associated with frequency of ischemic coronary diseases, probably explained by increased plasma lipids (10). Rodent studies confirmed the role of the spleen in lipid metabolism as splenectomized rats showed reduced HDL-cholesterol and increased plasma triglycerides. Complete

removal of the spleen in ApoE-deficient mice increased plaque development, although the underlying mechanism remained elusive (9). In the current study, no differences in plasma lipids were found upon splenic denervations, suggesting that regulation of lipid metabolism via the spleen is probably not mediated via innervation of the splenic nerves, which may explain why atherosclerosis development was not aggravated in this study. Interestingly, splenectomized trauma patients do display increased infection rates and have increased leukocyte counts (27), corresponding with the data presented in the current study, however the exact contribution of an isolated increased inflammatory status without effects on plasma lipid levels to atherosclerosis development is unclear.

In conclusion, selective disruption of mainly the splenic parasympathetic nerve increases splenic immune cell counts and the systemic inflammatory status, but does not contribute to atherosclerotic lesion development.

Acknowledgements

P.C.N. Rensen is an Established Investigator of the Netherlands Heart Foundation (grant 2009T038).

References

1. Hansson, G. K. & Libby, P. (2006) The immune response in atherosclerosis: a double-edged sword. *Nat Rev Immunol* 6, 508-519.
2. Janig, W. (2014) Sympathetic nervous system and inflammation: a conceptual view. *Auton Neurosci* 182, 4-14.
3. Borovikova, L. V., Ivanova, S., Zhang, M. *et al.* (2000) Vagus nerve stimulation attenuates the systemic inflammatory response to endotoxin. *Nature* 405, 458-462.
4. Gallowitsch-Puerta, M. & Pavlov, V. A. (2007) Neuro-immune interactions via the cholinergic anti-inflammatory pathway. *Life Sci* 80, 2325-2329.
5. Wang, H., Yu, M., Ochani, M. *et al.* (2003) Nicotinic acetylcholine receptor alpha7 subunit is an essential regulator of inflammation. *Nature* 421, 384-388.
6. Rosas-Ballina, M., Ochani, M., Parrish, W. R. *et al.* (2008) Splenic nerve is required for cholinergic antiinflammatory pathway control of TNF in endotoxemia. *Proc Natl Acad Sci USA* 105, 11008-11013.
7. Kooijman, S., Meurs, I., van der Stoep, M. *et al.* (2014) Hematopoietic alpha7 nicotinic acetylcholine receptor deficiency increases inflammation and platelet activation status, but does not aggravate atherosclerosis. *J Thromb Haemost*
8. Huston, J. M., Ochani, M., Rosas-Ballina, M. *et al.* (2006) Splenectomy inactivates the cholinergic antiinflammatory pathway during lethal endotoxemia and polymicrobial sepsis. *J Exp Med* 203, 1623-1628.
9. Rezende, A. B., Neto, N. N., Fernandes, L. R. *et al.* (2011) Splenectomy increases atherosclerotic lesions in apolipoprotein E deficient mice. *J Surg Res* 171, e231-e236.
10. Robinette, C. D. & Fraumeni, J. F., Jr. (1977) Splenectomy and subsequent mortality in veterans of the 1939-45 war. *Lancet* 2, 127-129.
11. Westerterp, M., van der Hoogt, C. C., de, H. W. *et al.* (2006) Cholesteryl ester transfer protein decreases high-density lipoprotein and severely aggravates atherosclerosis in APOE*3-Leiden mice. *Arterioscler Thromb Vasc Biol* 26, 2552-2559.
12. Buijs, R. M., van, d., V, Garidou, M. L. *et al.* (2008) Spleen vagal denervation inhibits the production of antibodies to circulating antigens. *PLoS One* 3, e3152.
13. Wong, M. C., van Diepen, J. A., Hu, L. *et al.* (2012) Hepatocyte-specific IKKbeta expression aggravates atherosclerosis development in APOE*3-Leiden mice. *Atherosclerosis* 220, 362-368.
14. Hu, L., Boesten, L. S., May, P. *et al.* (2006) Macrophage low-density lipoprotein receptor-related protein deficiency enhances atherosclerosis in ApoE/ LDLR double knockout mice. *Arterioscler Thromb Vasc Biol* 26, 2710-2715.
15. Rosas-Ballina, M., Olofsson, P. S., Ochani, M. *et al.* (2011) Acetylcholine-synthesizing T cells relay neural signals in a vagus nerve circuit. *Science* 334, 98-101.
16. van Diepen, J. A., Berbee, J. F., Havekes, L. M. *et al.* (2013) Interactions between inflammation and lipid metabolism: relevance for efficacy of anti-inflammatory drugs in the treatment of atherosclerosis. *Atherosclerosis* 228, 306-315.
17. Vida, G., Pena, G., Deitch, E. A. *et al.* (2011) alpha7-cholinergic receptor mediates vagal induction of splenic norepinephrine. *J Immunol* 186, 4340-4346.
18. Berthoud, H. R. & Powley, T. L. (1996) Interaction between parasympathetic and sympathetic nerves in prevertebral ganglia: morphological evidence for vagal efferent innervation of ganglion cells in the rat. *Microsc Res Tech* 35, 80-86.
19. Cailotto, C., Costes, L. M., van, d., V *et al.* (2012) Neuroanatomical evidence demonstrating the existence of the vagal anti-inflammatory reflex in the intestine. *Neurogastroenterol Motil* 24, 191-200, e93.
20. Branen, L., Hovgaard, L., Nitulescu, M. *et al.* (2004) Inhibition of tumor necrosis factor-alpha reduces atherosclerosis in apolipoprotein E knockout mice. *Arterioscler Thromb Vasc Biol* 24, 2137-2142.
21. Kleinbongard, P., Heusch, G., & Schulz, R. (2010) TNFalpha in atherosclerosis, myocardial ischemia/ reperfusion and heart failure. *Pharmacol Ther* 127, 295-314.

22. Johansson, M. E., Ulleryd, M. A., Bernardi, A. *et al.* (2014) alpha7 Nicotinic acetylcholine receptor is expressed in human atherosclerosis and inhibits disease in mice--brief report. *Arterioscler Thromb Vasc Biol* 34, 2632-2636.
23. Shimada, K., Hirano, E., Kimura, T. *et al.* (2012) Carvedilol reduces the severity of atherosclerosis in apolipoprotein E-deficient mice via reducing superoxide production. *Exp Biol Med (Maywood)* 237, 1039-1044.
24. Ulleryd, M. A., Bernberg, E., Yang, L. J. *et al.* (2014) Metoprolol reduces proinflammatory cytokines and atherosclerosis in ApoE^{-/-} mice. *Biomed Res Int* 2014, 548783.
25. Hedblad, B., Wikstrand, J., Janzon, L. *et al.* (2001) Low-dose metoprolol CR/XL and fluvastatin slow progression of carotid intima-media thickness: Main results from the Beta-Blocker Cholesterol-Lowering Asymptomatic Plaque Study (BCAPS). *Circulation* 103, 1721-1726.
26. Wiklund, O., Hulthe, J., Wikstrand, J. *et al.* (2002) Effect of controlled release/extended release metoprolol on carotid intima-media thickness in patients with hypercholesterolemia: a 3-year randomized study. *Stroke* 33, 572-577.
27. (1996) Guidelines for the prevention and treatment of infection in patients with an absent or dysfunctional spleen. *BMJ* 312, 430-434.

9

GENERAL DISCUSSION AND FUTURE PERSPECTIVES

Adapted from:

- Sympathetic nervous system control of triglyceride metabolism: novel concepts derived from recent studies. *J Lipid Res.* 2014, 55:180-9
- Brown fat as a novel target to attenuate hyperlipidemia and atherosclerosis. *Circ Res.* 2015, *in press*
- Regulation of brown fat by AMP-activated protein kinase. *Trends Mol Med* 2015, *in press*
- Hypothalamic regulation of brown fat activity. *Trends Endocrinol Metab* (2015) *in press*

One of the first studies confirming a crucial role of the nervous system in homeostasis dates back to 1942 when Hetherington and Ranson described that hypothalamic lesioning of rats frequently causes obesity by increasing food intake and decreasing energy expenditure (1). In following fascinating experiments, Hervey surgically connected the circulatory system of hypothalamic lesioned rats via subcutaneous tissues to normal rats. In these parabiotic experiments, the normal rats that were connected to the obese rats decreased their food intake and lost weight (2). About 35 years later, leptin was isolated and identified as the satiety signal (3) that was overproduced in obesity but to which hypothalamic lesioned rats could not respond.

Today, the hypothalamus and autonomic nervous system (ANS) are increasingly recognized as the regulators of body homeostasis and as possible treatment target in obesity and related disorders including type II diabetes (T2D) and cardiovascular disease (CVD). This thesis further revealed the role of the ANS in the control of lipid metabolism and inflammation, and identified pathological consequences of disturbed regulation. We found that mainly the parasympathetic nervous system (PNS) is required for maintaining anti-inflammatory reflexes, while the sympathetic nervous system (SNS) is highly important for energy expenditure and lipid metabolism, largely via regulating brown adipose tissue (BAT) activity.

Hypothalamic multi-tasking to maintain energy balance

Leptin was initially discovered as the satiety signal lacking in genetically obese *ob/ob* mice (3). More recent studies specified the central melanocortin system as main target of leptin (4). Leptin and other anorexigenic peptides including insulin, glucagon-like peptide-1 (GLP-1), peptide YY (PYY) and cholecystokinin (CCK) act by activation of cocaine- and amphetamine-regulated transcript (CART)/pro-opiomelanocortin (POMC)-expressing neurons and suppression of neuropeptide Y (NPY)/Agouti-related protein (AgRP)-expressing neurons, resulting in activation of melanocortin 4 receptor (MC4R) signalling (**Figure 1**). Probably because of MC4R's integral role, MC4R deficiency is the most common form of monogenic obesity (5) and associated with increased risk of cardiovascular disease. In addition to increased food intake in MC4R deficient individuals, energy expenditure is lower and nutrient usage shifts from fatty acid oxidation towards carbohydrate oxidation (6). Similarly, we (**Chapter 2**) and others (6) have shown that inhibition of MC4R signalling in mice by intracerebroventricular (ICV) administration of the synthetic antagonist SHU9119 increases food intake and weight gain, and also reduces fat oxidation. Interestingly, we observed that the increase in adiposity was also present in mice receiving ICV SHU9119 that were limited in food intake to the amount consumed by the control group, indicating that the reduction in fat oxidation contributes to the increase in fat mass. Apparently, the central melanocortin system exerts a dual-role in maintaining energy balance, namely by regulating energy intake as well as by regulating energy

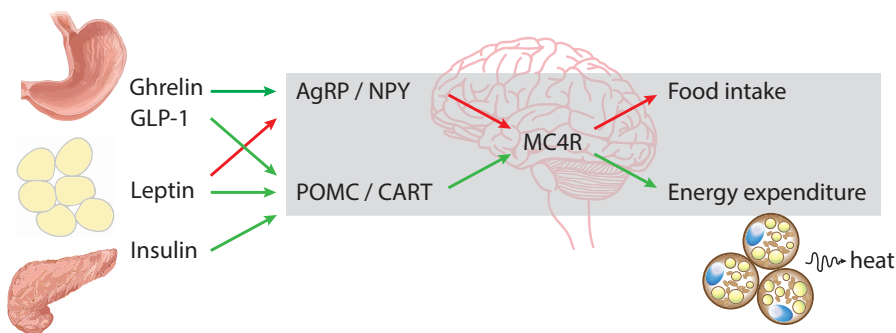


Figure 1 – The melanocortin system as central regulator of food intake and energy expenditure. See text for details. AgRP, agouti-related protein; CART, cocaine- and amphetamine-regulated transcript; GLP-1, glucagon-like peptide-1; MC4R, melanocortin 4 receptor; NPY, neuropeptide Y; POMC, pro-opiomelanocortin. Red arrow, inhibition; green arrow, stimulation.

expenditure. Indeed, ICV administration of leptin (7), insulin (8) and GLP-1 (**Chapter 3**) result in both reduced food intake and an increase in energy expenditure, while ghrelin that is produced by the stomach upon fasting exerts opposing effects (9). By performing dedicated mechanistic experiments as described in this thesis, we now identified regulation of BAT activity as mechanism underlying the changes in energy expenditure (**Chapters 2 and 3**).

9

Considering the importance of energy balance for survival, in addition to the response to satiety hormones, the brain also directly monitors energy status of the body. High energy availability drives *de novo* lipogenesis not only in metabolic organs but also in the hypothalamus, yielding increased levels of malonyl coenzyme A (CoA) and long-chain fatty acyl-CoAs that signal the need to reduce food intake. Correspondingly, ICV administration of long-chain fatty acids, *e.g.* oleic acid, reduces food intake (10). Conversely, ICV administration of inhibitors of fatty acid synthase (FAS) has a profound orexigenic effect (11). Interestingly, fatty acid synthesis is tightly regulated/inhibited by 5' adenosine monophosphate-activated protein kinase (AMPK), that is a cellular energy sensor by itself being active upon low energy availability (high AMP/ATP). This mechanism also mediates at least part of the GLP-1-mediated reduction in food intake. GLP-1 signalling lowers hypothalamic AMPK activity thereby increasing neuronal fatty acid synthesis resulting in decreased expression of orexigenic peptides and increased expression of anorexigenic peptides and finally reduced food intake. Consistent with this pathway, both ICV administration of AICAR [potent AMPK activator] and an adenoviral vector overexpressing constitutively active AMPK diminish weight loss induced by the GLP-1 analogue liraglutide (12).

So far, we have discussed that the hypothalamus monitors the body's energy status directly (e.g. by fatty acid synthesis and AMPK activity) and indirectly (e.g. signaling induced by anorexigenic and orexigenic peptides) and responds by regulating both food intake and energy expenditure. This dual mode of action makes the hypothalamus and more specifically the melanocortin system an attractive target in the treatment of obesity and related disorders. In fact, GLP-1 analogues (e.g. exenatide, liraglutide and dulaglutide) and DPP-4 inhibitors (e.g. sitagliptin, saxagliptin and alogliptin) that prevent the breakdown of GLP-1, are already implemented in the treatment of T2D. The potential of these drugs to prevent CVD remains to be determined and future studies may focus on combinations of drugs targeting multiple aspects of the central melanocortin system thereby enhancing efficacy.

Hypothalamic (dys)regulation of circadian rhythms

Via several pathways, feeding provides negative feedback to the hypothalamus in order to enhance satiety thereby reducing food intake. In addition, feeding behavior is a so-called Zeitgeber for the central clock, located in the suprachiasmatic nucleus (SCN) of the hypothalamus, and for peripheral clocks that drive circadian rhythms. In general, disturbed circadian rhythmicity leads to adiposity. For example, dim light at night [13] shifts circadian rhythmicity and increases body fat mass. When we exposed mice to more hours of light per day (*i.e.* 16 h or 24 h compared to regular 12 h), we observed increased adiposity (**Chapter 4**). Genetic mouse models of circadian dysfunction, among others *Clock^{mt/mt}* mice [14] and *Per2^{-/-}* mice [15], are also prone to develop obesity. Lesioning of the central circadian clock in the SCN in mice results in disturbed rhythmicity and an acute induction of weight gain [16]. The underlying mechanism may include timing of feeding that is disturbed in these animal models. This is reflected by mouse studies showing that feeding restricted to the light phase (*i.e.* the inactive period) leads to increased body weight gain compared to dark phase restricted feeding [17,18]. Conversely, restricting food intake to the active period of mice was shown to prevent diet-induced obesity [19,20].

In humans, plasma levels of lipids display diurnal variations independent of food intake [21], suggesting that the circadian clock is an important determinant of lipid levels. Consequently, disturbed rhythmicity may lead to dyslipidemia and eventually CVD. In fact, already in 1949 a Scandinavian observational study among factory workers reported an association between shift-work and cardiovascular mortality [22]. The underlying mechanism remained elusive. Meanwhile, the behavioral patterns of human activity, especially in industrialized countries, have undergone dramatic changes with respect to adherence to day and night rhythms. For example, 1) electrical light has uncoupled behavioral active period from the natural occurring day, 2) aircraft travel has resulted in jet-lag phenomenon, and 3) the 24-hour economy necessitates working at night and social activities are

shifted, simultaneously affecting sleep duration. Notably, the increasing prevalence of obesity is associated with disrupted sleep-wake pattern (23) and coincides with the availability of artificial light (24,25). However, for these association studies, it is rather difficult to identify causality. For example, shift-work leads to changes in locomotor activity, food intake and light exposure that all potentially affect circadian rhythmicity, adiposity and the development of CVD. Randomized clinical trials and animal studies are needed to determine the contribution of the different factors to metabolic health and to design specific intervention strategies.

Circadian rhythms are not limited to energy metabolism but are also present in other factors involved in the development of CVD, including blood pressure (26), thrombotic factors (27) and the immune system (28). Maintenance of circadian rhythmicity may be an additional strategy to prevent and treat human dyslipidemia and CVD. This could be achieved by for example providing advice on life style changes regarding sleep and food intake behavior. Currently, the feasibility of extending sleep duration by giving sleep advice is being explored in randomized controlled trials. Pilot data show that sleep duration of obese individuals may be extended by from less than 6 hours to more than 7 hours for more than 20 nights out of 28 nights, resulting in body weight loss, appetite loss and improvement of sleep quality (29).

Sympathetic activation of brown fat to protect against dyslipidemia and CVD

Retrograde tracing in Syberian hamsters identified neuroanatomical connections between the SCN and BAT (30), indicating possible involvement of BAT in the associations between disturbed circadian rhythm and obesity. Indeed, we now showed that prolonging day light exposure not only changes circadian rhythmicity but also reduces sympathetic outflow towards BAT accompanied by decreased BAT activity and increased body fat mass in mice (**Chapter 4**). Recent evidence suggests that in humans, BAT activity is also physiologically regulated by the circadian clock. The detectability of BAT by [¹⁸F]fluorodeoxyglucose (FDG)-PET-CT imaging at room temperature follows a circannual cycle (31,32), with low detectability of BAT in summer (*i.e.* short day) as compared to winter (*i.e.* long day). Although differences in outside temperature over the year would be a likely explanation for this phenomenon, the detectability of BAT showed a stronger correlation with day length than with outside temperature (31). Likewise, we demonstrated that exposure of mice to short day length of 8 h enhances BAT activity reflected by the total daily uptake of lipids from the circulation when compared to 12 and 16 h of light (**Chapter 5**). It is tempting to speculate that this seasonal adaptation of BAT activity to day length precedes changes in temperature and thereby prepares the body for upcoming changes in ambient temperature. Future studies should reveal the contribution of prolonged

light exposure, shift-work and other circadian disturbances on human BAT function and metabolism.

The importance of the SNS for BAT function is reflected by the number of nerve endings in the tissue. Each brown adipocyte is in close proximity to a nerve ending that releases norepinephrine upon sympathetic activity initiated by for example cold exposure. In addition to its crucial role in non-shivering thermogenesis, BAT is probably required for maintaining energy balance and is activated upon overeating, a process called diet-induced thermogenesis (DIT). Although the existence of DIT is under debate (33), we and others have identified the central melanocortin system, crucial in the regulation of food intake and energy expenditure as described above, as an important determinant of BAT activity. Inhibition of MC4R receptor signaling reduces BAT activity (**Chapter 2**), while activation of the melanocortin system by ICV administration of GLP-1 (**Chapter 3**), insulin (34) and leptin (35) results in enhanced sympathetic outflow and activation of BAT. These studies suggest that reduced BAT activity may underlie at least part of the obese phenotype in MC4R deficient individuals, and underscore the potency of targeting the melanocortin system as therapeutic target for obesity and related disorders.

In humans, BAT activity, as quantified by [¹⁸F]FDG PET-CT scan, inversely correlates with body mass index and body fat mass (36-39). BAT activation by cold exposure alleviates hypertriglyceridemia through its large potential to take up and combust TG-derived fatty acids, at least in mice (40,41) and likely also in humans (37). Other potent BAT activators that act via the SNS are thyroid hormone (42), estradiol (43), nicotine (44) and bone morphogenetic protein-8 (45). Alternatively, BAT can be activated directly by for example metformin (46), irisin (47), salsalate (48) or CB1R inhibitors (**Chapter 6**), the latter being dependent on sympathetic signaling. Central and peripheral contributors to BAT activity as described within this thesis are summarized in **Figure 2**. SNS-mediated activation of BAT and subsequent lowering of plasma TG can be pharmacologically mimicked by β 3-adrenergic receptor (β 3-AR) agonists in mice (49,50). Interestingly, a recent study showed that the β 3-AR agonist mirabregon acutely increases BAT activity in human volunteers. Future chronic studies are evidently needed to illuminate the role of β 3-AR agonism in human obesity and hyperlipidemia.

The primacy of BAT activation on hypertriglyceridemia is clear, however, the effect on hypercholesterolemia, which especially underlies development of atherosclerosis, is less well known. Experimental studies report either reduced (46,51) or increased (52) levels of plasma cholesterol after BAT activation. Dong *et al.* (52) were the first to document an effect BAT activation on atherosclerosis development, and unexpectedly found that cold BAT activation via exposure aggravates atherosclerosis development in *Ldlr*^{-/-} and *ApoE*^{-/-} mice. However, it should be noted that BAT activation increases lipolytic processing of (V)LDL particles (41),

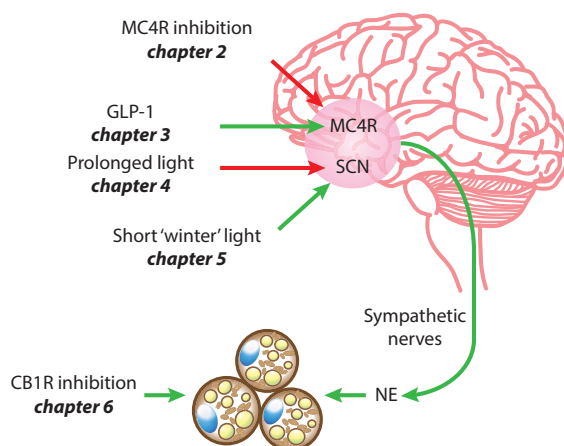


Figure 2 – Regulation of brown adipose tissue by central systems and peripheral pharmaceutical compounds. See text for details. CB1R, cannabinoid 1 receptor; GLP-1, glucagon-like peptide-1; MC4R, melanocortin 4 receptor; NE, norepinephrine; SCN, suprachiasmatic nucleus.

leading to enhanced formation of cholesterol-rich remnants that are normally taken up by the liver, mainly through ApoE-LDLR interactions, both of which obviously do not occur in *Ldlr*^{-/-} and *ApoE*^{-/-} mice. Strikingly, we recently showed that B3-AR agonism in *APOE*3-Leiden.CETP* mice, with functional ApoE-LDLR interactions, not only alleviates hypercholesterolemia but also reduces atherosclerotic lesion area and lesion severity [49].

The effect of BAT activation on hypercholesterolemia and atherosclerosis development in humans is still largely unknown as only few studies investigated the effect of BAT activation on plasma cholesterol levels. One study reported that subjects with detectable BAT have lower plasma total cholesterol and LDL-cholesterol levels as compared to subjects without detectable BAT [53]. De Lorenzo *et al.* [54] showed that daily cold exposure of 20 min for 90 days reduced total cholesterol, LDL-cholesterol and body mass in hypercholesterolemic patients. These data show that SNS-mediated BAT activation may also improve hypercholesterolemia in humans and underscore its potential as anti-atherogenic treatment as well.

Modulation of the immune response by the autonomic nervous system

Metabolic regulation and inflammatory responses are highly integrated. Salicylate and its derivative salicylate not only activate BAT, but also reduce NF- κ B activity thereby lowering inflammation [48] and atherosclerosis [55]. Anti-inflammatory processes

allow skewing of macrophages from M1 macrophages to norepinephrine-producing M2 macrophages in BAT, thereby inducing similar responses as via SNS-mediated BAT activation (56). The ANS itself exerts a complex control on inflammation, which depends on bidirectional communication between the brain and the immune system. Lymphoid organs such as bone marrow and the spleen are mainly innervated by sympathetic noradrenergic neurons. Primary afferent visceral neurons are often not labelled parasympathetic or sympathetic but do form reflex circuits with the autonomic pathways. Neuroanatomical evidence is limited for the involvement of the parasympathetic nerves in immune organs and its functional existence is highly under debate (57). However, electrical stimulation of the vagus nerve does inhibit pro-inflammatory responses (58) and recent studies indicate evidence for presence and functional activity of parasympathetic branches in the spleen (59,60). We now observed that surgical dissection of these splenic parasympathetic nerves enhanced inflammation in mice (**Chapter 8**), consistent with disruption of the cholinergic anti-inflammatory reflex as proposed by Tracey *et al.* (61) and the pro-inflammatory effects of hematopoietic $\alpha 7$ nAChR deficiency (**Chapter 7**). In addition, hematopoietic $\alpha 7$ nAChR deficiency resulted in a higher activation status of platelets. Regulation of the immune response by autonomic reflexes as described within this thesis are summarized in **Figure 3**.

As the ANS mainly responds to pro-inflammatory cytokines, pharmaceutical targeting of these systems to reduce inflammation does not seem feasible. Surprisingly, training of the ANS by meditation, breathing techniques, and exposure to cold (*i.e.* immersions in ice cold water) results in increased plasma epinephrine levels and reduced inflammation upon endotoxemia (62). However, it remains to be determined whether such an intervention can be used to prevent or treat chronic inflammation as is often the case in obesity or during atherosclerosis development. At least, one may question the autonomy of the ANS.

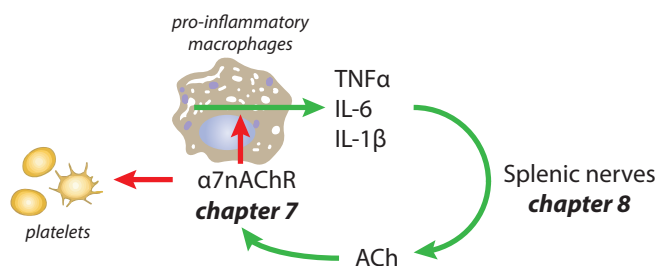


Figure 3 – Regulation of the immune response by autonomic reflexes and pharmaceutical compounds. See text for details. $\alpha 7$ nAChR, $\alpha 7$ nicotinic acetylcholine receptor; ACh, acetylcholine; IL-1 β , interleukin-1 β ; IL-6, interleukin-6; TNF α , tumor necrosis factor α .

Currently large-scale phase III trials with cardiovascular events as end-point are underway for drug agents that reduce IL-6 and C-reactive protein (*e.g.* canakinumab and low dose methotrexate). Pre-clinical studies suggest that at least part of the anti-inflammatory and atheroprotective effects of methotrexate in mouse models result from increased adenosine release and subsequent activation of the A_{2A} -receptor leading to enhanced reverse-cholesterol transport and reduced foam-cell formation (63). Combined with the observation that A_{2A} -receptor agonists activate BAT (64), these studies indicate that A_{2A} -receptor agonism is a potential treatment target for CVD. Unfortunately, many A_{2A} -receptor ligands are known to alter cardiac function.

Concluding remarks

The central nervous system is an important regulator of lipid metabolism and inflammation. The fact that many of the systems involved, including the melanocortin system, exert multiple modes of action, makes these systems attractive and powerful targets for obesity and related disorders. Although pharmaceutical targeting of the brain appears to be difficult in humans, one may circumvent this by improving circadian rhythmicity, training the ANS by cold exposure, or the use of sympathomimetic compounds. Additionally, several unique approaches have been developed including combinatorial compounds (65) and nanoparticles (66) to specifically target hypothalamic sites.

Since its (re-)discovery in 2009, BAT became a hot research topic in the field of metabolism. Pre-clinical studies, including those described in this thesis, have shown that BAT activation protects against obesity, dyslipidemia and even atherosclerosis. So far only a couple of studies explored the metabolic benefits of BAT activation in humans. Future studies should elucidate to what extent the promising results obtained in animal studies can be extrapolated to the treatment of human obesity and related disorders.

References

1. Hetherington, A. W. & Ranson, S. W. (1942) The spontaneous activity and food intake of rats with hypothalamic lesions. *American Journal of Physiology* 136, 609-617.
2. HERVEY, G. R. (1959) The effects of lesions in the hypothalamus in parabiotic rats. *J Physiol* 145, 336-352.
3. Zhang, Y., Proenca, R., Maffei, M. *et al.* (1994) Positional cloning of the mouse obese gene and its human homologue. *Nature* 372, 425-432.
4. van de Wall, E., Leshan, R., Xu, A. W. *et al.* (2008) Collective and individual functions of leptin receptor modulated neurons controlling metabolism and ingestion. *Endocrinology* 149, 1773-1785.
5. Farooqi, I. S., Keogh, J. M., Yeo, G. S. *et al.* (2003) Clinical spectrum of obesity and mutations in the melanocortin 4 receptor gene. *N Engl J Med* 348, 1085-1095.
6. Nogueiras, R., Wiedmer, P., Perez-Tilve, D. *et al.* (2007) The central melanocortin system directly controls peripheral lipid metabolism. *J Clin Invest* 117, 3475-3488.
7. Wang, T., Hartzell, D. L., Rose, B. S. *et al.* (1999) Metabolic responses to intracerebroventricular leptin and restricted feeding. *Physiol Behav* 65, 839-848.
8. McGowan, M. K., Andrews, K. M., Fenner, D. *et al.* (1993) Chronic intrahypothalamic insulin infusion in the rat: behavioral specificity. *Physiol Behav* 54, 1031-1034.
9. Tschop, M., Smiley, D. L., & Heiman, M. L. (2000) Ghrelin induces adiposity in rodents. *Nature* 407, 908-913.
10. Obici, S., Feng, Z., Morgan, K. *et al.* (2002) Central administration of oleic acid inhibits glucose production and food intake. *Diabetes* 51, 271-275.
11. Kumar, M. V., Shimokawa, T., Nagy, T. R. *et al.* (2002) Differential effects of a centrally acting fatty acid synthase inhibitor in lean and obese mice. *Proc Natl Acad Sci USA* 99, 1921-1925.
12. Beiroa, D., Imbernon, M., Gallego, R. *et al.* (2014) GLP-1 agonism stimulates brown adipose tissue thermogenesis and browning through hypothalamic AMPK. *Diabetes* 63, 3346-3358.
13. Borniger, J. C., Maurya, S. K., Periasamy, M. *et al.* (2014) Acute dim light at night increases body mass, alters metabolism, and shifts core body temperature circadian rhythms. *Chronobiol Int* 31, 917-925.
14. Turek, F. W., Joshu, C., Kohsaka, A. *et al.* (2005) Obesity and metabolic syndrome in circadian Clock mutant mice. *Science* 308, 1043-1045.
15. Yang, S., Liu, A., Weidenhammer, A. *et al.* (2009) The role of mPer2 clock gene in glucocorticoid and feeding rhythms. *Endocrinology* 150, 2153-2160.
16. Coomans, C. P., van den Berg, S. A., Lucassen, E. A. *et al.* (2013) The suprachiasmatic nucleus controls circadian energy metabolism and hepatic insulin sensitivity. *Diabetes* 62, 1102-1108.
17. Arble, D. M., Bass, J., Laposky, A. D. *et al.* (2009) Circadian timing of food intake contributes to weight gain. *Obesity (Silver Spring)* 17, 2100-2102.
18. Bray, M. S., Tsai, J. Y., Villegas-Montoya, C. *et al.* (2010) Time-of-day-dependent dietary fat consumption influences multiple cardiometabolic syndrome parameters in mice. *Int J Obes (Lond)*.
19. Hatori, M., Vollmers, C., Zarrinpar, A. *et al.* (2012) Time-restricted feeding without reducing caloric intake prevents metabolic diseases in mice fed a high-fat diet. *Cell Metab* 15, 848-860.
20. Sherman, H., Genzer, Y., Cohen, R. *et al.* (2012) Timed high-fat diet resets circadian metabolism and prevents obesity. *FASEB J* 26, 3493-3502.
21. Rivera-Coll, A., Fuentes-Arderiu, X., & Diez-Noguera, A. (1994) Circadian rhythmic variations in serum concentrations of clinically important lipids. *Clin Chem* 40, 1549-1553.
22. Thijs-Evensen Eyv (1949) Skiftarbeid og helse [Shift work and health]: en undersøkelse av mortalitet og morbiditet hos arbeidere i en kjemisk fabrikk [Porsgrunn; Jacobsen].
23. Killick, R., Banks, S., & Liu, P. Y. (2012) Implications of sleep restriction and recovery on metabolic outcomes. *J Clin Endocrinol Metab* 97, 3876-3890.

24. Obayashi, K., Saeki, K., Iwamoto, J. et al. (2013) Exposure to light at night, nocturnal urinary melatonin excretion, and obesity/dyslipidemia in the elderly: a cross-sectional analysis of the HEIJO-KYO study. *J Clin Endocrinol Metab* 98, 337-344.
25. Wyse, C. A., Selman, C., Page, M. M. et al. (2011) Circadian desynchrony and metabolic dysfunction; did light pollution make us fat? *Med Hypotheses* 77, 1139-1144.
26. Fabbian, F., Smolensky, M. H., Tiseo, R. et al. (2013) Dipper and non-dipper blood pressure 24-hour patterns: circadian rhythm-dependent physiologic and pathophysiologic mechanisms. *Chronobiol Int* 30, 17-30.
27. Scheer, F. A. & Shea, S. A. (2014) Human circadian system causes a morning peak in prothrombotic plasminogen activator inhibitor-1 (PAI-1) independent of the sleep/wake cycle. *Blood* 123, 590-593.
28. Logan, R. W. & Sarkar, D. K. (2012) Circadian nature of immune function. *Mol Cell Endocrinol* 349, 82-90.
29. Arora, T., Thomas, G., & Taheri, S. (2012) A Pilot Intervention to Investigate the Feasibility of Extending Sleep Duration to Reduce Body Weight in Short Sleeping Obese Individuals. *Sleep* 35, A445.
30. Bamshad, M., Song, C. K., & Bartness, T. J. (1999) CNS origins of the sympathetic nervous system outflow to brown adipose tissue. *Am J Physiol* 276, R1569-R1578.
31. Au-Yong, I. T., Thorn, N., Ganatra, R. et al. (2009) Brown adipose tissue and seasonal variation in humans. *Diabetes* 58, 2583-2587.
32. Perkins, A. C., Mshelia, D. S., Symonds, M. E. et al. (2013) Prevalence and pattern of brown adipose tissue distribution of 18F-FDG in patients undergoing PET-CT in a subtropical climatic zone. *Nucl Med Commun* 34, 168-174.
33. Kozak, L. P. (2010) Brown fat and the myth of diet-induced thermogenesis. *Cell Metab* 11, 263-267.
34. Muller, C., Voirol, M. J., Stefanoni, N. et al. (1997) Effect of chronic intracerebroventricular infusion of insulin on brown adipose tissue activity in fed and fasted rats. *Int J Obes Relat Metab Disord* 21, 562-566.
35. Enriori, P. J., Sinnayah, P., Simonds, S. E. et al. (2011) Leptin action in the dorsomedial hypothalamus increases sympathetic tone to brown adipose tissue in spite of systemic leptin resistance. *J Neurosci* 31, 12189-12197.
36. Cypess, A. M., Lehman, S., Williams, G. et al. (2009) Identification and importance of brown adipose tissue in adult humans. *N Engl J Med* 360, 1509-1517.
37. Ouellet, V., Labbe, S. M., Blondin, D. P. et al. (2012) Brown adipose tissue oxidative metabolism contributes to energy expenditure during acute cold exposure in humans. *J Clin Invest* 122, 545-552.
38. van Marken Lichtenbelt, W. D., Vanhommel, J. W., Smulders, N. M. et al. (2009) Cold-activated brown adipose tissue in healthy men. *N Engl J Med* 360, 1500-1508.
39. Vijgen, G. H., Bouvy, N. D., Teule, G. J. et al. (2011) Brown adipose tissue in morbidly obese subjects. *PLoS One* 6, e17247.
40. Bartelt, A., Bruns, O. T., Reimer, R. et al. (2011) Brown adipose tissue activity controls triglyceride clearance. *Nat Med* 17, 200-205.
41. Khedoe, P. P., Hoeke, G., Kooijman, S. et al. (2015) Brown adipose tissue takes up plasma triglycerides mostly after lipolysis. *J Lipid Res* 56, 51-59.
42. Lopez, M., Varela, L., Vazquez, M. J. et al. (2010) Hypothalamic AMPK and fatty acid metabolism mediate thyroid regulation of energy balance. *Nat Med* 16, 1001-1008.
43. Martinez de Morentin, P. B., Gonzalez-Garcia, I., Martins, L. et al. (2014) Estradiol regulates brown adipose tissue thermogenesis via hypothalamic AMPK. *Cell Metab* 20, 41-53.
44. Martinez de Morentin, P. B., Whittle, A. J., Ferno, J. et al. (2012) Nicotine induces negative energy balance through hypothalamic AMP-activated protein kinase. *Diabetes* 61, 807-817.
45. Whittle, A. J., Carobbio, S., Martins, L. et al. (2012) BMP8B increases brown adipose tissue thermogenesis through both central and peripheral actions. *Cell* 149, 871-885.

46. Geerling, J. J., Boon, M. R., van der Zon, G. C. *et al.* (2014) Metformin lowers plasma triglycerides by promoting VLDL-triglyceride clearance by brown adipose tissue in mice. *Diabetes* 63, 880-891.
47. Lee, P., Linderman, J. D., Smith, S. *et al.* (2014) Irisin and FGF21 are cold-induced endocrine activators of brown fat function in humans. *Cell Metab* 19, 302-309.
48. van Dam, A. D., Nahon, K. J., Kooijman, S. *et al.* (2015) Salsalate activates brown adipose tissue in mice. *Diabetes* 64, 1544-1554.
49. Berbee, J. F., Boon, M. R., Khedoe, P. P. *et al.* (2015) Brown fat activation reduces hypercholesterolaemia and protects from atherosclerosis development. *Nat Commun* 6, 6356.
50. Yoshida, T., Sakane, N., Wakabayashi, Y. *et al.* (1994) Anti-obesity and anti-diabetic effects of CL 316,243, a highly specific beta 3-adrenoceptor agonist, in yellow KK mice. *Life Sci* 54, 491-498.
51. Ohyama, K., Nogusa, Y., Suzuki, K. *et al.* (2015) A combination of exercise and capsinoid supplementation additively suppresses diet-induced obesity by increasing energy expenditure in mice. *Am J Physiol Endocrinol Metab* 308, E315-E323.
52. Dong, M., Yang, X., Lim, S. *et al.* (2013) Cold exposure promotes atherosclerotic plaque growth and instability via UCP1-dependent lipolysis. *Cell Metab* 18, 118-129.
53. Matsushita, M., Yoneshiro, T., Aita, S. *et al.* (2014) Impact of brown adipose tissue on body fatness and glucose metabolism in healthy humans. *Int J Obes (Lond)* 38, 812-817.
54. De, L. F., Mukherjee, M., Kadziola, Z. *et al.* (1998) Central cooling effects in patients with hypercholesterolaemia. *Clin Sci (Lond)* 95, 213-217.
55. de Vries-van der Weij, Toet, K., Zadelaar, S. *et al.* (2010) Anti-inflammatory salicylate beneficially modulates pre-existing atherosclerosis through quenching of NF-kappaB activity and lowering of cholesterol. *Atherosclerosis* 213, 241-246.
56. Nguyen, K. D., Qiu, Y., Cui, X. *et al.* (2011) Alternatively activated macrophages produce catecholamines to sustain adaptive thermogenesis. *Nature* 480, 104-108.
57. Bellingier, D. L. & Lorton, D. (2014) Autonomic regulation of cellular immune function. *Auton Neurosci* 182, 15-41.
58. Wang, H., Yu, M., Ochani, M. *et al.* (2003) Nicotinic acetylcholine receptor alpha7 subunit is an essential regulator of inflammation. *Nature* 421, 384-388.
59. Buijs, R. M., van, d., V, Garidou, M. L. *et al.* (2008) Spleen vagal denervation inhibits the production of antibodies to circulating antigens. *PLoS One* 3, e3152.
60. Cailotto, C., Costes, L. M., van, d., V *et al.* (2012) Neuroanatomical evidence demonstrating the existence of the vagal anti-inflammatory reflex in the intestine. *Neurogastroenterol Motil* 24, 191-200, e93.
61. Tracey, K. J. (2002) The inflammatory reflex. *Nature* 420, 853-859.
62. Kox, M., van Eijk, L. T., Zwaag, J. *et al.* (2014) Voluntary activation of the sympathetic nervous system and attenuation of the innate immune response in humans. *Proc Natl Acad Sci USA* 111, 7379-7384.
63. Reiss, A. B., Rahman, M. M., Chan, E. S. *et al.* (2004) Adenosine A2A receptor occupancy stimulates expression of proteins involved in reverse cholesterol transport and inhibits foam cell formation in macrophages. *J Leukoc Biol* 76, 727-734.
64. Gnad, T., Scheibler, S., von, K., I *et al.* (2014) Adenosine activates brown adipose tissue and recruits beige adipocytes via A2A receptors. *Nature* 516, 395-399.
65. Finan, B., Yang, B., Ottaway, N. *et al.* (2012) Targeted estrogen delivery reverses the metabolic syndrome. *Nat Med* 18, 1847-1856.
66. Peluffo, H., Unzueta, U., Negro-Demontel, M. L. *et al.* (2015) BBB-targeting, protein-based nanomedicines for drug and nucleic acid delivery to the CNS. *Biotechnol Adv* 33, 277-287.

10

SUMMARY

NEDERLANDSE SAMENVATTING

LIST OF PUBLICATIONS

CURRICULUM VITAE

SUMMARY

Cardiovascular disease (CVD) is currently the leading cause of morbidity and mortality in our Western society. The main cause of CVD is atherosclerosis, for which dyslipidemia and inflammation are major risk factors. The autonomic nervous system (ANS) is known to innervate key organs involved in lipid metabolism and immune responses, and is therefore a potential target to prevent or treat CVD. In **Chapter 1** we provide an overview of the autonomic control of energy homeostasis, inflammatory reflexes and the potential interactions.

The hypothalamus, particularly the melanocortin system, integrates nutritional information originating from peripheral organs mediated through circulating hormones and metabolites. It responds by regulating food intake and energy expenditure. In **Chapter 2** we set out to investigate the underlying mechanism of the association between melanocortin 4 receptor (MC4R) deficiency and reduction in energy expenditure. We continuously infused the MC4R antagonist SHU9119 or vehicle into the lateral ventricle of mice for two weeks. We found that SHU9119 increased food intake and body weight, and markedly diminished fat oxidation and the uptake of [³H]oleate from glycerol tri[³H]oleate-labeled lipoprotein-like emulsion particles by brown adipose tissue (BAT). In BAT, SHU9119 decreased uncoupling protein-1 (UCP1) protein levels resulting in a lower core body temperature. All of these effects were independent of the increased food intake as mice that received SHU9119 while being pair-fed to the vehicle treated group still exhibited these effects. We concluded that inhibition of the MC4R signalling impairs BAT function accompanied by reduced energy expenditure thereby promoting adiposity.

Next, in **Chapter 3**, we determined the potential beneficial metabolic effects of activation of the melanocortin system by the glucagon-like peptide-1 (GLP-1) analogue exendin-4. Chronic central infusion of exendin-4 enhanced sympathetic outflow towards BAT and increased the UCP1 content in BAT in both lean and diet-induced obese mice. This activation of BAT was accompanied by enhanced uptake of fatty acids from glycerol tri[³H]oleate-labeled lipoprotein-like emulsion particles and [¹⁴C]deoxyglucose by BAT, resulting in lower plasma TG and glucose concentrations, and reduced body weight. Pair-fed animals were included during all experiments to confirm that regulation of BAT by the central melanocortin system was independent of food intake. Collectively, these data suggest that BAT is a major contributor in the regulation of energy expenditure by the central melanocortin system and we anticipate that activation of this system, *e.g.* by GLP1 receptor activation, is a promising strategy to combat obesity and related disorders by increasing BAT activity.

Another brain region that is highly involved in regulation of lipid metabolism is the suprachiasmatic nucleus (SCN) that drives circadian rhythms. In general, disturbed

circadian rhythmicity is associated with obesity and related disorders such as CVD. Specifically, prolonged artificial light exposure associates with obesity in humans. In **Chapter 4** we aimed to investigate the underlying mechanism in an experimental mouse study. Mice were exposed to prolonged 16 h or 24 h of light per day and effects were compared to exposure to 12 h of light per day. Increasing the daily light exposure for 5 weeks increased body fat mass without affecting food intake or locomotor activity. Mechanistically, we demonstrated that prolonged light exposure decreases sympathetic input into BAT, reduces β 3-adrenergic intracellular signalling as well as the uptake of fatty acids from glycerol tri ^3H oleate-labeled lipoprotein-like emulsion particles and [^{14}C]deoxyglucose by BAT. Surgical sympathetic denervation of BAT completely abolished effects of light exposure on the uptake of ^3H oleate by BAT, indicating a crucial role for the sympathetic nervous system (SNS). We concluded that impaired BAT activity is an important mediator in the association between disturbed circadian rhythm and adiposity and anticipate that activation of BAT may overcome the adverse metabolic consequences of disturbed circadian rhythmicity.

Activity of the SCN adapts to seasonal changes in light exposure. Interestingly, detectability of human BAT by [^{18}F]fluorodeoxyglucose (FDG) PET-CET scans at room temperature follows a circannual cycle, with low detectability of BAT in summer as compared to winter. Although differences in outside temperature over the year would be a likely explanation for this phenomenon, the detectability of BAT showed a stronger correlation with daily light exposure than with outside temperature. In **Chapter 5**, we evaluated this relationship in mice that were exposed to 8 h, 12 h or 16 h of light per day. The uptake of ^3H oleate by BAT from glycerol tri ^3H oleate-labeled lipoprotein-like emulsion particles showed a strong daily rhythm. Additionally, expression of genes involved in thermogenesis revealed comparable patterns, mostly the expression being highest at the end of the resting phase. Strikingly, compared to 12 h, the rhythmicity of BAT was highest in mice exposed to 8 h of light per day, accompanied by an increased overall uptake of ^3H oleate by BAT while 16 h of light per day markedly flattened the rhythm and lowered overall uptake of ^3H oleate by BAT.

Rimonabant is a systemic cannabinoid 1 receptor (CB1R) blocker that induces sustained weight loss and lowering of plasma TG levels in obese patients. In **Chapter 6**, we determined whether the beneficial metabolic effects of rimonabant were due to activation of BAT. Diet-induced obese mice were treated with rimonabant, resulting in lowered body weight and enhanced energy expenditure accompanied by increased uptake of ^3H oleate from glycerol tri ^3H oleate-labeled lipoprotein-like emulsion particles by BAT. Of note, these results could be fully recapitulated at thermoneutral temperature, which reduces sympathetic outflow to BAT, suggesting that the mechanism involves direct rather than SNS-mediated activation of BAT. Indeed, we demonstrated that the CB1R is expressed in BAT and that blockade of the

CB1R in cultured brown adipocytes *in vitro* increases UCP1 content and intracellular lipolysis. Furthermore, treatment of mice with the peripheral CB1R antagonist AM6545 resulted in comparable lowering of body weight and activation of BAT. Taken together we concluded that the TG-lowering effect of rimonabant is due to peripheral blockade of the CB1R on BAT.

Part II of this thesis describes studies on the regulation of inflammation by the ANS, with focus on the cholinergic anti-inflammatory reflex. In this reflex, acetylcholine is released upon ANS activity and stimulates $\alpha 7$ AChR, which is highly expressed on immune cells and platelets, resulting in attenuation of NF- κ B-mediated gene expression of pro-inflammatory cytokines. In **Chapter 7**, we studied the effects of hematopoietic $\alpha 7$ nicotinic acetylcholine receptor ($\alpha 7$ nAChR) deficiency on inflammation, platelet activation status and atherosclerosis in *Ldlr*^{-/-} mice. To this end, bone marrow from *$\alpha 7$ nAChR*^{-/-} or wildtype mice was transplanted into *Ldlr*^{-/-} mice. Hematopoietic $\alpha 7$ nAChR deficiency increased the number of leukocytes in the peritoneum, lymph nodes, spleen and blood accompanied by increased expression of pro-inflammatory cytokines in spleen and peritoneal leukocytes. Additionally, we found increased activation status of platelets. Likewise, incubation of human platelets with an $\alpha 7$ nAChR agonist decreased aggregation. Despite the large effects of hematopoietic $\alpha 7$ nAChR deficiency on inflammatory status and platelet function, it did not affect atherosclerosis development or composition of lesions.

The cholinergic anti-inflammatory reflex is proposed to act mainly via the spleen. Therefore, in **Chapter 8**, we assessed the effects of selective parasympathetic and sympathetic denervation of the spleen on inflammation and atherosclerotic lesion development in APOE*3-Leiden.CETP mice. Selective parasympathetic denervation increased leukocyte counts in the spleen and increased gene expression of pro-inflammatory cytokines in the liver and in peritoneal leukocytes as compared to sympathetic denervation and sham surgery. Further, plasma levels of IL-6 and IL-1 β were increased in parasympathetically denervated mice. However, the increased pro-inflammatory status in parasympathetically denervated mice did not affect atherosclerotic lesion size or lesion composition.

Finally, we evaluated the results of this thesis in **Chapter 9** and discussed the potency of targeting the ANS for treatment of obesity and CVD, with special attention for BAT activation as a highly relevant and emerging pharmaceutical target. Collectively, the studies described in this thesis have increased our insight into regulation of energy metabolism and inflammation by the ANS.

NEDERLANDSE SAMENVATTING

Hart- en vaatziekten zijn de voornaamste doodsoorzaak in de wereld op het moment van schrijven. Zij zijn vaak het gevolg van vernauwing van bloedvaten door plaatselijke ontstekingen en ophopingen van vetten. Dit proces noemen ook wel aderverkalking of 'atherosclerose'. Onderzoek in de afgelopen jaren heeft aangetoond dat de hersenen, ofwel het 'centrale zenuwstelsel', een belangrijke rol spelen bij het aansturen van de verwerking van vetten door het lichaam en het moduleren van ontstekingen. Deze processen vinden onbewust plaats en worden gecontroleerd door het autonome zenuwstelsel, een onderdeel van het centrale zenuwstelsel. In dit proefschrift werd de manier waarop het autonome zenuwstelsel dit doet bestudeerd, wat mogelijk resulteert in nieuwe aangrijpingspunten in de preventie en behandeling van hart- en vaatziekten.

Hoofdstuk 1 geeft een algemene introductie op de onderwerpen die besproken worden in dit proefschrift. Hierin wordt onder andere beschreven dat obesitas een belangrijke risicofactor vormt voor het ontwikkelen van hart- en vaatziekten. Obesitas ontstaat door een 'positieve energiebalans', waarbij de voedselinname groter is dan het energieverbruik. Onderzoek aan systemen die voedselinname en energieverbruik regelen kan daarom belangrijke informatie opleveren die niet alleen gebruikt kan worden in de strijd tegen obesitas, maar ook in de strijd tegen hart- en vaatziekten. Daarnaast wordt de functie van bruin vet beschreven. Bruin vet is een uniek orgaan dat in pasgeboren kinderen en in kleine zoogdieren een cruciale rol speelt bij het handhaven van de lichaamstemperatuur. Omdat baby's een relatief groot lichaamsoppervlak hebben waardoor relatief veel warmte wordt afgegeven aan de omgeving dient bruin vet warmte te genereren. Bruin vet heeft de unieke eigenschap om energie die opgeslagen is in vet en suiker te verbranden tot warmte, ofwel 'thermogenese'. Hiertoe bevatten bruine vetcellen het ontkoppelingseiwit UCP1. Pas recent is ontdekt dat bruin vet ook aanwezig én actief is in volwassenen en geactiveerd wordt door blootstelling aan een lage omgevingstemperatuur.

Obesitas is in sommige gevallen erfelijk. Mutaties in het gen dat codeert voor de melanocortine 4 receptor (MC4R), wat leidt tot deficiënte voor dit eiwit, vormen de meest voorkomende erfelijke oorzaak van obesitas. Het niet goed functioneren of ontbreken van de MC4R in mensen resulteert niet alleen in verhoogde eetlust maar vermindert ook het energieverbruik. In **Hoofdstuk 2** onderzochten we in muizen het mechanisme waardoor MC4R-deficiëntie het energieverbruik vermindert door een remmer van de MC4R te infunderen in de hersenen. Infusie van de remmer resulteerde in snelle gewichtstoename wat gepaard ging met een toename van de voedselinname en een afname in het energieverbruik. We toonden aan dat de verlaging in het energieverbruik veroorzaakt werd door verminderde activiteit van

het sympathische zenuwstelsel, onderdeel van het autonome zenuwstelsel, vanuit de hersenen richting het bruin vet. Dit heeft tot gevolg dat het bruin vet minder actief is, wat bleek uit minder expressie van UCP1 en een ophoping van vet in het bruin vet weefsel, waardoor het minder vetten kon opnemen vanuit de bloedbaan. Om specifiek de bijdrage van het bruin vet in de gewichtstoename te onderzoeken hebben we muizen die behandeld werden met de MC4R remmer op dieet gezet waarbij de muizen precies evenveel aten als de muizen in de controlegroep. Uit dit experiment konden bleek dat remming van de MC4R gewichtstoename gaf onafhankelijk van de voedselinname, wat zeer waarschijnlijk werd veroorzaakt door een verlaagde activiteit van het bruin vet. We concludeerden dat het melanocortinesysteem, waarvan MC4R deel uitmaakt, een dubbele rol vervult: enerzijds reguleert het de eetlust en anderzijds reguleert het energieverbruik door de activiteit van bruin vet te moduleren.

Deze dubbele rol van het melanocortinesysteem maakt dit systeem een aantrekkelijk aangrijpingspunt voor medicatie. Het melanocortinesysteem wordt geactiveerd door onder andere hormonen die vrijkomen bij voedselinname, namelijk leptine, insuline en het zogenaamde *glucagon-like peptide 1* (GLP-1). Momenteel worden analoga van GLP-1 zoals 'exenatide' ofwel 'exendin-4' ontwikkeld voor de behandeling van type 2 diabetes (T2D). Het was al bekend dat deze middelen gewichtsafname geven, maar het precieze mechanisme was nog onbekend. Vanuit de resultaten die beschreven zijn in hoofdstuk 2 was onze hypothese dat exendin-4 bruin vet zou kunnen activeren. Om dit te onderzoeken hebben we in **Hoofdstuk 3** exendin-4 direct in de hersenen van muizen geïnfundeed. Dit resulteerde in een afname van lichaamsgewicht wat veroorzaakt werd door een selectieve afname van lichaamsvet, en ging gepaard met verlaging van de voedselinname en een toename in energieverbruik. Mechanistisch onderzoek toonde aan dat de sympathische signalering vanuit de hersenen naar bruin vet was verhoogd. Dit leidde tot een verhoogde aanwezigheid van UCP1 in bruin vet en verhoogde de opname van vetten en glucose uit het bloed door bruin vet. Deze gunstige resultaten vonden we niet alleen in slanke muizen, maar ook in obese muizen die insulineresistent zijn. Deze studie geeft aan dat de gunstige effecten van GLP-1 analoga op de stofwisseling in T2D patiënten deels verklaard zouden kunnen worden door activatie van het bruin vet.

Een ander belangrijk systeem in de hersenen, de centrale biologische klok, regelt het dag- en nachtritme van het lichaam dat ook wel het 'circadiane ritme' wordt genoemd. Verstoringen van dit ritme als gevolg van bijvoorbeeld ploegendiensten, zijn geassocieerd met de ontwikkeling van obesitas en hart- en vaatziekten. Mogelijke oorzaken hiervoor zijn het verstoren van het slaap-, activiteits-, en eetpatroon, dan wel blootstelling aan licht op ongebruikelijke tijdstippen. Een recent onderzoek heeft laten zien dat er een relatie is tussen blootstelling aan licht in de nacht en

het lichaamsgewicht van mensen, maar een oorzakelijk verband en onderliggende mechanismen waren nog niet aangetoond. Om dit te onderzoeken hebben we in **Hoofdstuk 4** muizen blootgesteld aan een verschillend aantal uren licht per etmaal: 12 uur, 16 uur of 24 uur. We toonden aan dat met een langere lichtperiode per etmaal de hoeveelheid lichaamsvet toeneemt terwijl de muizen niet meer aten of minder bewogen. Ook hier bleek activiteit van bruin vet een cruciale factor. Hoe langer de lichtperiode, hoe lager de sympathische signalering vanuit de hersenen naar het bruin vet en hoe minder het bruin vet in staat is om vetten en glucose uit de bloedbaan op te nemen en te verbranden. We concludeerden dat een optimaal dag- en nachtritme cruciaal is voor een hoge activiteit van bruin vet.

In mensen kan bruin vet zichtbaar gemaakt worden door opname van een radioactief glucose-analoog te detecteren met PET-CT scans die ook worden uitgevoerd voor diagnostische doeleinden in de oncologie. Interessant is dat, wanneer men PET-CT scans over het jaar heen bekijkt, bruin vet vaker detecteerbaar is in de winter- dan in de zomermaanden. Dit kan natuurlijk veroorzaakt worden door de lage temperatuur in deze maanden. Echter, de detecteerbaarheid van bruin vet bleek beter overeen te komen met de lengte van de lichtperiode dan met de buitentemperatuur. In **Hoofdstuk 5** onderzochten we de effecten van blootstelling aan een korte lichtperiode (8 uur per etmaal, overeenkomend met de winter) en een lange lichtperiode (16 uur per etmaal, overeenkomend met de zomer) op de activiteit van bruin vet in muizen. Terwijl blootstelling aan een lange lichtperiode de functie van bruin vet verminderde, overeenkomend met bevindingen uit **Hoofdstuk 4**, resulteerde blootstelling aan een korte lichtperiode in een verhoogde activiteit van het bruin vet. Deze observaties suggereren dat het korter worden van de dagen bij het naderen van de winter de activiteit van het bruin vet verhoogt om het organisme voor te bereiden op een lagere omgevingstemperatuur. Daarnaast onderzochten we de activiteit van bruin vet over de dag in de muizen en toonden aan we dat bruin vet het meest actief is als de muizen ontwaken aan het einde van de rustperiode.

Naast lichaamseigen eiwitten en de biologische klok werd onderzoek gedaan naar stoffen die bruin vet kunnen activeren. Rimonabant is een geneesmiddel dat op de markt was voor patiënten met sterk overgewicht en T2D. Rimonabant verlaagde niet alleen het lichaamsgewicht maar verbeterde ook risicofactoren voor hart- en vaatziekten. Binnen een jaar is rimonabant echter weer van de markt gehaald doordat het ernstige bijwerkingen had waaronder depressie. Desalniettemin is het interessant om te achterhalen hoe rimonabant deze gunstige effecten op de stofwisseling teweegbrengt. Hiertoe behandelden we obese muizen met rimonabant zoals beschreven in **Hoofdstuk 6**. Ook in muizen induceerde rimonabant een aanzienlijk gewichtsverlies en verbeterde het de bloedwaardes van vetten. Dit bleek het gevolg van een verhoogde opname van vetten door bruin vet weefsel. Deze effecten bleven zelfs aanwezig wanneer de signalering tussen hersenen en

bruin vet minimaal was: een zogenaamde 'thermoneutrale' omgevingstemperatuur waarbij bruin vet in principe geen warmte hoeft te genereren voor het handhaven van de lichaamstemperatuur. Deze bevinding suggereerde dat rimonabant bruin vet direct zou kunnen activeren. Inderdaad konden we aantonen dat het eiwit waar rimonabant aan bindt, de cannabinoïde 1 receptor (CB1R), niet alleen in de hersenen voorkomt maar ook in bruin vet. Om nog een stap verder te gaan gebruikten we in een nieuw experiment een ander middel dat op rimonabant lijkt maar de hersenen niet kan binnendringen. Ook dit middel activeerde bruin vet en veroorzaakte gewichtsverlies. We concludeerden dan ook dat het eiwit waar rimonabant aan bindt een veelbelovend farmacologisch aangrijpingspunt is voor de behandeling van obesitas en mogelijk ook hart- en vaatziekten.

In het tweede deel van dit proefschrift wordt dieper ingegaan op de controle van ontstekingsprocessen door het autonome zenuwstelsel. De $\alpha 7$ nicotinerge acetylcholine receptor ($\alpha 7$ nAChR) is een eiwit dat aanwezig is op verschillende cellen van het immuunsysteem en dat geactiveerd kan worden door signalen vanuit het autonome zenuwstelsel. Activatie van dit eiwit onderdrukt ontstekingsprocessen. In **Hoofdstuk 7** onderzochten we de gevolgen van het ontbreken van deze receptor op immuuncellen voor de ontwikkeling van aderverkalking in muizen. We toonden aan dat het aantal witte bloedcellen in verschillende organen verhoogd was en dat die cellen ook actiever waren. Daarnaast waren bloedplaatjes ook in een hogere staat van paraatheid. Ondanks deze effecten op het immuunsysteem, vonden we geen nadelige gevolgen voor aderverkalking.

De milt is een belangrijk orgaan waar signalen vanuit het autonome zenuwstelsel bestemd voor immuuncellen vrijkomen. Deze signalen bereiken de milt via twee typen zenuwbanen, namelijk sympathische zenuwbanen en parasympathische zenuwbanen. In de studie beschreven in **Hoofdstuk 8** onderzochten we de effecten van het chirurgisch verbreken van deze zenuwbanen op het immuunsysteem en de ontwikkeling van aderverkalking. Terwijl het verbreken van sympathische signalering nauwelijks effect had op immuuncellen, resulteerde het verbreken van parasympathische signalering in een verhoogd aantal immuuncellen in de milt. Verder resulteerde het verwijderen van zowel sympathische als parasympathische zenuwbanen tot een verhoogde productie van inflammatoire moleculen, zogenaamde cytokines. Echter, ook deze ingreep bleek geen gevolgen te hebben voor het ontstaan van aderverkalking.

Tot slot worden in **Hoofdstuk 9** alle resultaten bediscussieerd en de mogelijkheden besproken van nieuwe therapieën voor de preventie en behandeling van obesitas en verwante ziektebeelden als T2D en hart- en vaatziekten. Samenvattend hebben we aangetoond dat de hersenen, en meer specifiek het autonome zenuwstelsel, een belangrijke rol spelen bij de verwerking van vetten in het lichaam en de modulatie van ontstekingsreacties. Wanneer dergelijke processen verstoord worden kan

dit resulteren in obesitas en mogelijk in hart- en vaatziekten. Daarnaast laten we zien dat activatie van bruin vet een veelbelovend aangrijpingspunt kan zijn om het energieverbruik te verhogen en obesitas tegen te gaan. Recent hebben we ook in muizen aangetoond dat activatie van bruin vet aderverkalking kan voorkomen. Momenteel wordt zowel door anderen als door onze groep veel onderzoek gedaan naar de mogelijk gunstige effecten van activatie van bruin vet op de stofwisseling in de mens.

LIST OF PUBLICATIONS

1. Kazem S, van der Meijden E, [Kooijman S](#), Rosenberg AS, Hughey LC, Browning JC, Sadler G, Busam K, Pope E, Benoit T, Fleckman P, de Vries E, Eekhof JA, Feltkamp MC. Trichodysplasia spinulosa is characterized by active polyomavirus infection. **J Clin Virol** **2012**; 53: 225-230
2. Bruinstroop E, la Fleur SE, Ackermans MT, Foppen E, Wortel J, [Kooijman S](#), Berbée JFP, Rensen PC, Fliers E, Kalsbeek A. The autonomic nervous system regulates postprandial hepatic lipid metabolism. **Am J Physiol Endocrinol Metab** **2013**; 304: E1089-1096
3. Boon MR, Geerling JJ, [Kooijman S](#), Parlevliet ET, Havekes LM, Romijn JA, Meurs IM, Rensen PCN. Sympathetic nervous system control of triglyceride metabolism: novel concepts derived from recent studies (review). **J Lipid Res** **2014**; 55: 180-189
4. [Kooijman S](#), Boon MR, Parlevliet ET, Geerling JJ, van de Pol V, Romijn JA, Havekes LM, Meurs I, Rensen PCN. Inhibition of the central melanocortin system decreases brown adipose tissue activity. **J Lipid Res** **2014**; 10: 2022-2032
5. [Kooijman S*](#), Boon MR*, van Dam AD, Pelgrom LR, Berbée JFP, Visseren CAR, Van Aggele RC, van den Hoek AM, Sips HCM, Lombès M, Havekes LM, Tamsma JT, Guigas B, Meijer OC, Jukema JW, Rensen PCN. Cannabinoid 1 receptor blockade diminishes obesity and dyslipidemia via peripheral activation of brown adipose tissue. **FASEB J** **2014**; 28: 5361-5375
[* Authors contributed equally]
6. [Kooijman S](#), Meurs I, van der Stoep M, Habets KL, Lammers B, Berbée JF, Havekes LM, van Eck M, Romijn JA, Korpelaar SJ, Rensen PC. Hematopoietic $\alpha 7$ nicotinic acetylcholine receptor deficiency increases inflammation and platelet activation status, but does not aggravate atherosclerosis. **J Thromb Haemost** **2015**; 13: 126-135
7. Khedoe PPSJ, Hoeke G, [Kooijman S](#), Dijk W, Kersten S, Havekes LM, Hiemstra P, Berbée JFP, Rensen PCN, Boon MR. Brown adipose tissue takes up plasma triglycerides mostly after lipolysis. **J Lipid Res** **2015**; 56: 51-59
8. [Kooijman S*](#), Meurs I*, van Beek L, Khedoe PPSJ, Giezekamp A, Pike-Overzet K, Cailotto C, van der Vliet JW, van Harmelen V, Boeckxstaens G, Berbée JFP, Rensen PCN. Splenic autonomic denervation enhances inflammation does not aggravate atherosclerotic lesion development in APOE*3-Leiden.CETP transgenic mice **Am J Physiol Heart Circ Physiol** **2015**; 309: H646-654.
[* Authors contributed equally]
9. van Dam AD, Nahon KJ, [Kooijman S](#), van den Berg SM, Kanhai AA, Kikuchi T, Heemskerk MM, van Harmelen V, Lombès M, van den Hoek AM, de Winther MP, Lutgens E, Guigas B, Rensen PCN, Boon MR. Salsalate activates brown adipose tissue in mice. **Diabetes** **2015**; 64:1544-54
10. Berbée JFP, Boon MR, Khedoe PPSJ, Bartelt A, Schlein C, Worthmann A, [Kooijman S](#), Hoeke G, Mol IM, John C, Jung C, Vazirpanah N, Brouwers LP, Gordts PL, Esko JD, Hiemstra PS, Havekes LM, Scheja L, Heeren J, Rensen PCN. Brown fat activation reduces hypercholesterolemia and protects from atherosclerosis development. **Nat Commun** **2015**; 6: 6356

11. [Kooijman S*](#), van den Berg R*, Ramkisoensing A, Boon MR, Kuipers EN, Loef M, Zonneveld TC, Lucassen EA, Sips HCM, Chatzisprou IA, Houtkooper RH, Meijer JH, Coomans CP, Biermasz NR, Rensen PCN. Prolonged daily light exposure increases body fat mass through attenuation of brown adipose tissue activity. **Proc Natl Acad Sci USA** **2015**; 112:6748-6753
[* Authors contributed equally]
12. Rozema E, van Dam AD, Sips HCM, Verpoorte R, Meijer OC, Choi YH*, [Kooijman S*](#). Extending pharmacological dose-response curves for salsalate with natural deep eutectic solvents. **RSC Adv** **2015**; 5:61398-61401
[* Authors contributed equally]
13. Van Dam AD, [Kooijman S](#), Schilperoort M, Rensen PCN, Boon MR. Regulation of brown adipose tissue activity by AMP-activated protein kinase. **Trend Mol Med** **2015**; *in press*
14. Hoeke G, [Kooijman S](#), Boon MR, Rensen PCN, Berbée JFP. Role of brown fat in lipoprotein metabolism and atherosclerosis. **Circ Res** **2015**; *in press*
15. Coomans CP, Lucassen E, [Kooijman S](#), Fifel K, de Boer T, Rensen PCN, Michel S, Meijer JH. Plasticity of circadian clocks and consequences for metabolism. **Diabetes Obes Metab** **2015**; 14 Suppl 1:65-75
16. [Kooijman S*](#), Wang Y*, Parlevliet ET*, Boon MR, Edelschaap D, Snaterse G, Romijn JA, Rensen PCN. Central GLP-1 receptor signalling increases the uptake of plasma triglycerides and glucose by activated brown adipose tissue in mice. **Diabetologia** **2015**; *in press*
[* Authors contributed equally]
17. Van Beek L, Vroegrijk IOCM, Katiraei S, Heemskerk MM, van Dam AD, [Kooijman S](#), Rensen PCN, Koning F, Verbeek JS, Willems van Dijk K, van Harmelen V. Fcy-chain deficiency restricts the development of diet-induced obesity. **Obesity** **2015**; *in press*
18. [Kooijman S](#), van den Heuvel JK, Rensen PCN. Hypothalamic regulation of brown fat activity. **Trends Endocrinol Metab** **2015**; *in press*
19. Laurila P-P, Soronen J, [Kooijman S](#), Boon MR, Forsström S, van den Berg SAA, Coomans CP, Kaiharju E, -, Rensen PCN, Kovanen P, Suomalainen A, Jauhainen M. Deficiency of *Usf1* Protects against obesity, insulin resistance, dyslipidemia, and atherosclerosis, and leads to increased energy expenditure and brown adipose tissue activity in mice; *revision submitted*

CURRICULUM VITAE

Sander Kooijman werd op 10 januari 1987 geboren te 's-Gravenhage. In 2005 behaalde hij zijn VWO diploma aan het Erasmus College te Zoetermeer. In dat zelfde jaar begon hij met de studie Biomedische Wetenschappen aan de Universiteit Leiden, waarvan hij in 2009 het Bachelor of Science diploma behaalde. Direct aansluitend begon hij met de masteropleiding Biomedical Science, eveneens aan de Universiteit Leiden.

In het kader van zijn masteropleiding heeft Sander twee onderzoekstages gevolgd. De eerste stage werd uitgevoerd bij de afdeling Moleculaire Cel Biologie. Onder begeleiding van Dr. Valentijn werd de manier waarop het stollingseiwit von Willebrand factor uit endotheelcellen wordt uitgescheiden onderzocht. De tweede stage werd uitgevoerd bij de afdeling Medische Microbiologie onder begeleiding van Dr. Feltkamp. Hier was hij betrokken bij onderzoek naar een recent ontdekt polyomavirus.

In 2011 behaalde hij aan de Universiteit Leiden het Master of Science diploma Biomedical Sciences. Van augustus 2011 tot augustus 2015 voerde hij als onderzoeker in opleiding onder supervisie van Prof. dr. Patrick C.N. Rensen en Prof. dr. ir. Louis M. Havekes het in dit proefschrift beschreven onderzoek uit bij de sectie Endocrinologie van de Hoofdafdeling Interne Geneeskunde van het Leids Universitair Medisch Centrum. Sinds augustus 2015 is hij aangesteld als post-doctoraal onderzoeker binnen dezelfde vakgroep als waar het promotieonderzoek is uitgevoerd.

